Die approbierte Originalversion dieser Dissertation ist in der Hauptbibliothek der Technischen Universität Wien aufgestellt und zugänglich.
http://www.ub.tuwien.ac.at

The approved original version of this thesis is available at the main library of the Vienna University of Technology.
http://www.ub.tuwien.ac.at/eng

TECHNISCHE
UNIVERSITÄT
WIEN
Vienna University of Technology

DISSERTATION

Dynamics of One-Dimensional Bose Gases in Time-Dependent Traps

ausgeführt zum Zwecke der Erlangung des akademischen Grades
eines Doktors der technischen Wissenschaften

unter der Leitung von
o.Univ.-Prof. Dipl.-Ing. Dr. techn. Hannes-Jörg Schmiedmayer
Atominstitut (E141)

eingereicht an der
Technischen Universität Wien
Fakultät für Physik

von
Dipl. Ing. Wolfgang Rohringer
Matrikelnummer 0125883
Erdbergstraße 30/6
1030 Wien, Österreich

Wien, April 2014

Wolfgang Rohringer

Diese Dissertation haben begutachtet:

Jörg Schmiedmayer

Thomas Gasenzer

Referees:

Prof. Dr. Jörg Schmiedmayer (Technische Universität Wien)
Prof. Dr. Thomas Gasenzer (Universität Heidelberg)

CoQus Thesis Advisory Committee:

Prof. Dr. Jörg Schmiedmayer (Technische Universität Wien)
Prof. Dr. Martin Plenio (Universität Ulm)
Prof. Dr. Arno Rauschenbeutel (Technische Universität Wien)

Co - supervision:

Dr. Michael Trupke (Technische Universität Wien)

Abstract

Dynamics of One-Dimensional Bose Gases in Time-Dependent Traps

In the scope of this thesis, an experiment was prepared to reliably produce Bose-Einstein condensates in an atom chip trap. In this setup, the dynamics and relaxation processes within an ultracold cloud of ^{87}Rb in a time-dependent trapping potential were investigated. The system under scrutiny is a gas of interacting bosons in a highly elongated magnetic trap created by wire structures on the atom chip. Such a trap allows confining the gas to the motional ground state of the radial trapping potential, while still accommodating axial excitations at temperatures between 10 to 200 nanokelvins, constituting the one-dimensional realization of a Bose–Einstein condensate, called "quasicondensate". This scenario is described by the Lieb-Liniger model of weakly interacting bosons in a one-dimensional geometry. Both the Lieb-Liniger model as well as its effective low energy limit valid in the quasicondensate regime, the Luttinger liquid model, can be mapped to models describing the dynamics of 1d spin chains in solid state physics, which is why an understanding of their nonequilibrium dynamics is of interest beyond the field of cold atom physics.

The trapping potential is manipulated according to various different protocols in order to investigate the time evolution of excitations in the cloud. Specifically, a dynamical scale invariance present in the system allowing the exact calculation of time-dependent correlation functions, the feasibility of optimal control to engineer the cloud's state after a quench, as well as the 1d expansion of a quasicondensate are investigated. Experimental data is compared to numerical simulations based on a stochastic nonlinear Schrödinger equation and to analytical results.

The final part of the thesis describes the preparation of a new experiment combining an atom chip with optical nanofibers to create a novel atom-photon interface.

Zusammenfassung

Dynamik von eindimensionalen Bose-Gasen in zeitabhängigen Fallen

Im Rahmen dieser Arbeit wurde ein Experiment zur Produktion von Bose-Einstein Kondensaten in einer Atomchip-Falle vorbereitet. Damit erfolgten Untersuchungen zur Dynamik sowie zu Relaxationsprozessen in einer ultrakalten Wolke von ^{87}Rb–Atomen in einem zeitabhängigen Fallenpotential. Lithographisch gefertigte Drahtstrukturen auf dem Atomchip erlauben die Präparation eines Gases wechselwirkender Bosonen in einer stark elongierten magnetischen Falle bei Temperaturen zwischen 10 und 200 Nanokelvin, sodass die Dynamik auf den transversalen Grundzustand des Fallenpotentials beschränkt ist, während im axialen Potential viele Zustände besetzt werden können. Dieses System ist die eindimensionale Version eines Bose–Einstein-Kondensats und wird als ”Quasikondensat” bezeichnet, dessen theoretische Beschreibung durch das Lieb-Liniger Modell wechselwirkender Bosonen in 1d gegeben ist. Sowohl das Lieb-Liniger Modell als auch das Luttinger-Flüssigkeitsmodell, eine effektive Theorie für den Quasikondensat–Zustand, können auf die Dynamik von eindimensionalen Spin–Ketten abgebildet werden, wie sie in Problemstellungen der Festkörperphysik vorkommen. Daher ist das Verständnis von Nichtgleichgewichts-Phänomenen in diesen Modellen auch über das Feld der Physik kalter Atome hinaus von Interesse.

Das Fallenpotential kann im Rahmen unterschiedlicher Protokolle manipuliert werden, um die anschließende Zeitentwicklung des Systems zu durchleuchten. Im Besonderen wurde eine dynamische Symmetrie des Systems untersucht, die eine Berechnung von zeitabhängigen Korrelationsfunktionen erlaubt. Basierend darauf wurde die 1d–Expansion eines Quasikondensats diskutiert, sowie eine Methode entwickelt um die Zeitentwicklung nach einer schnellen Änderung des Fallenpotentials durch Optimal-Control-Techniken zu steuern. Die experimentellen Ergebnisse wurden mit analytischen Vorhersagen für die Form der zeitabhängigen Korrelationsfunkionen verglichen. Darüber hinaus wurden numerische Simulationen basierend auf einer stochastischen nichtlinearen Schrödingergleichung implementiert und durchgeführt, welche die experimentellen Ergebnisse und das analytische Modell zusätzlich validierten.

Den abschließenden Teil der Arbeit stellt die Planung und Mitvorbereitung eines neuen Experiments dar, das durch Integration von optischen Nanofasern auf einem Atomchip eine neuartige Atom-Licht Schnittstelle demonstrieren soll.

Contents

1. Introduction & Motivation 1
1.1. Motivation 1
1.2. Introduction 2
1.3. Structure 4

I. Basics 5

2. 1d Bose gases: Theoretical basics 7
2.1. Introduction 8
2.1.1. Bose-Einstein condensation of the ideal gas 8
2.1.2. Bosonic fields and correlation functions 11
2.1.3. Interacting Bose gases 12
2.2. The interacting Bose gas in 1d 14
2.2.1. Phase diagram of the homogeneous 1d Bose gas 15
2.2.2. Effect of the trap on the phase diagram 18
2.2.3. Excitation spectrum of the 1d Bose gas 19
2.3. The 1d quasicondensate 20
2.3.1. Luttinger liquid model 20
2.3.2. Correlation functions 22
2.4. The 1d-3d crossover regime 24
2.4.1. Thermal occupation of transverse states 24
2.4.2. Interaction-induced swelling of the radial wave function 25
2.5. Density correlations in free expansion 27
2.5.1. Density profile in free expansion 28
2.5.2. Density correlations and thermometry 28

3. Numerical techniques 31
3.1. Introduction and Overview 31
3.2. Gross-Pitaevskii equation 35
3.3. Stochastic Gross-Pitaevskii equation 37
3.3.1. Why SGPE? 38
3.3.2. Implementation 39
3.3.3. Choice of γ and growth of the quasi-BEC 40
3.3.4. Time evolution and temperature 41
3.3.5. Density matrix and mode occupation 42

3.3.6. SGPE in the 1d-3d crossover regime 44
3.3.7. Applications 44
3.4. Phase diffusion & Ornstein Uhlenbeck process 45

4. Experimental setup & techniques 47
4.1. Magnetic micro-traps on atom chips 47
4.1.1. Magnetic traps 48
4.1.2. Atom chip traps 49
4.2. Detection techniques 51
4.2.1. Absorption imaging 51
4.2.2. Fiber-based fluorescence detection 54
4.3. Experimental setup 55
4.3.1. Overview 55
4.3.2. The atom 56
4.3.3. Vacuum chamber, atom source and coils 57
4.3.4. Laser system 59
4.3.5. Chip mounting & copper structures 62
4.3.6. Atom chip 64
4.3.7. Evaporative cooling setup 66
4.3.8. Absorption imaging 67
4.3.9. Fluorescence detector 67
4.3.10. Experiment control and data acquisition 70
4.4. Bose-Einstein condensation in an atom chip setup 73
4.4.1. Laser cooling in a MOT. 73
4.4.2. Transfer to the macroscopic magnetic trap. 74
4.4.3. Evaporative cooling and trap compression. 75
4.4.4. BEC in macroscopic trap. 77
4.4.5. Transfer to the chip trap and quasi-BEC. 78
4.5. Trap characterization 79
4.6. Temperature measurement based on density ripples 81
4.6.1. Basics 81
4.6.2. Implementation 82

II. Physics 87

5. Quasi-BEC dynamics in time-dependent trapping potentials 89
5.1. Introduction 89
5.2. Trap quench: Breathing dynamics 90
5.2.1. Gross-Pitaevskii equation with time-dependent external potential 90
5.2.2. Experimental scheme 93
5.2.3. Characterization of the breathing mode 95
5.3. Excitation dynamics 100
5.3.1. Scaling solution for the many-body Hamiltonian 100

5.3.2. Scaling approach in the Thomas-Fermi regime 101
5.3.3. Temperature measurements in breathing clouds 104
5.4. Summary 115

6. Optimal control on quasi-BEC dynamics 117
6.1. Introduction 117
6.2. Control Scheme 119
6.3. Characterization measurements 123
6.4. Simulation results 124
6.5. Measurement results 129
6.6. Summary 133

7. Cold atoms in a magnetic guide 135
7.1. Introduction 135
7.2. Transport of quasi-BECs in a magnetic guide 137
7.3. Excitation spectrum of 1d-expanding quasi-BECs 141
7.4. Fluorescence detection of cold atoms 147
7.5. Summary 153

III. Outlook & Conclusion 155

8. Towards a novel light-matter interface 157
8.1. Overview 157
8.2. The nanofiber atom chip 160
8.2.1. Magnetic trap geometries. 161
8.3. Current state of the project and outlook 163

9. Conclusion 165

IV. Appendices 171

A. Nature constants 173
A.1. General constants 173
A.2. ^{87}Rb D2 line 173

B. Numerics: Odds and ends 174
B.1. Picking random points on a sphere 174
B.2. GPGPU with Matlab 174

C. Publications 175

1. Introduction & Motivation

1.1. Motivation

Although physics branches out into many different directions, the last decades have seen two frontiers that encompass much of the research effort taking place on a diverse amount of topics. One of them is elementary particle physics and cosmology; the other is the description of many-body quantum systems. For the former, the main challenge is still finding a consistent fundamental theory. In contrast, the second frontier is much about dealing with the vast complexity arising from systems that, in principle, can be microscopically described by a known "fundamental" theory - however, interactions between the many constituents render it very hard to make predictions for observables from said theory. For a long time, the main arena for the investigation of many-body quantum systems was solid state physics. Yet, technical progress has added other areas such as the behaviour of complex molecules in biological systems [1] or ultracold atomic vapours.

Cold atoms. The advent of cold atom experiments and the production of degenerate quantum gases from ultracold atomic vapours [2, 3, 4] has brought an intriguing new angle on the problem. For once, physicists had the chance to engineer interacting many-body quantum systems so that their theoretical description is tractable, or in such a way that they resemble other known scenarios (for instance from solid state physics) but offer to study formerly inaccessible observables, or to easily tune formerly inaccessible parameters. Consequently, fundamental open questions regarding for instance the nature of quantum phase transitions [5, 6] or the mechanisms behind thermalisation and relaxation in quantum mechanical systems [7, 8, 9] can be tackled in experiments with unprecedented control and flexibility.

1d Bose gases. An intriguing example is the 1d Bose gas. Initially devised as an exactly solvable toy model by Lieb and Liniger in 1964 [10, 11], it is possible today to create and manipulate this system with different experimental techniques [12]. While optical lattice experiments allow to easily tune interactions to study the transition from non-interacting ideal to strongly correlated systems [13], atom chip experiments allow to create single to few of these gases that can be precisely investigated to yield correlation functions [14, 15, 16, 17], encoding much of the information about the system's many-body state. The 1d Bose gas is unique in that its classical counterpart is integrable, allowing the investigation of quantum mechanical relaxation processes in a system that classically is not supposed to relax. Further, in the experiment the presence of the trapping potential [18, 19] allows to study the consequences of perturbations to the ideal 1d case in the context of integrability [20]. In addition, it is possible to implement efficient numerical simulations for comparison with both theory and experiment [21, 22, 23].

Non-equilibrium dynamics. Much has been learned about the equilibrium properties of 1d Bose gases in recent years [12]. Consequently, it is a good time to focus on the much less well-understood non-equilibrium dynamics: To which state does the system relax after perturbing it? What are the timescales involved? The goal of this work is to help elucidate these questions. Due to the well-known and controlled microscopic physics, it is possible to study the emergence of universal effective field theories and their limitations depending on the details of the system. Especially universal physics considering dynamical properties rather than the equilibrium states is of interest in this context.

Beyond cold atoms. This opens up ties to other branches of physics. In the case of the 1d Bose gas, the Lieb-Liniger-Hamiltonian can be mapped to that of a quantum Ising spin chain [24], making some results directly applicable to certain solid-state systems. While not topic of this thesis, adding coupling between two trapped Bose gases yields a system described by a Sine-Gordon Hamiltonian, which, similarly, can be mapped to the XY model [25]. On the other hand, the Gross-Pitaevskii Lagrangian dimensions can be described in terms of different effective metrics [26], depending on its dimensionality, making accessible several analogue-gravity models in experiment. A number of proposals exists on how to draw parallels between the role of quantum and thermal fluctuations in superfluids and in cosmological models [27, 28, 29].

1.2. Introduction

The aim of this thesis was to understand and control dynamics of cold 1d and quasi-1d Bose gases in time dependent traps and magnetic guides on an atom chip. An important tool towards this goal, thermometry for 1d quasicondensates based on density correlations in time-of-flight expansion, has been developed in the course of previous work within our group. This method is described in references [30, 15], and in detail within Stephanie Manz's thesis [31].

Preparing cold clouds. At the start of this thesis project, our setup allowed to prepare atom clouds with temperatures in the order of a few 10 microkelvins. Much interesting physics, however, like non-classical atom statistics, only becomes accessible at temperatures on the order of a few 10 nanokelvins, at which atoms undergo Bose-Einstein condensation, or are even restricted to the quantum mechanical ground state along the trap's tightly confining axes. In order to reliably achieve such conditions, several changes had to be implemented in the setup. With a stable laser system already in place, one of the key improvements was exchanging the experiment control with an up-to-date system yielding higher time resolution and less electronic noise, while at the same time allowing for much easier handling of input signal calibration, real-time data analysis, and automated parameter scans. Together with several other changes to reduce electrical noise and stray light as well as an optimization of the experimental cycle, cooling of atoms down to temperatures in the nanokelvin-regime and Bose-Einstein condensation have been achieved.

Quasi-BEC dynamics in time-dependent trapping potentials. Wire structures on our atom chip allow us to deform the trapping potential in a controlled way in order to induce dynamics, or 1d expansion along a magnetic guide. Consequently, the goal is to understand the dynamics of a quasi-1d superfluid in a time-dependent trap. For the overall shape of the density profile, the evolution in a time-dependent trap has been known since many years [32, 33]. Understanding the full many-body dynamics, or as an intermediate step, the multimode-dynamics of phononic phase and density fluctuations on top of a mean-field approximation, is a more difficult problem, up until recently only discussed for special cases [34, 35]. Surprisingly, a similar approach based on a dynamical symmetry of the underlying Hamiltonian can be extended to a full class of systems governed by a many-body Schrödinger equation with repulsive inter-particle interactions, allowing to solve the time-dependent equation with the help of a scaling transformation [36]. This yields predictions for correlation functions and corresponding observables, like the average coherence length in the system, that can be interpreted in terms of an effective temperature. We test these predictions in experiments performing a fast switch ("quench") between well-characterized initial and final trap geometries, and find good agreement between the scaling solution, numerical calculations and our data.

Optimal Control of quasi-BEC dynamics. Our experiment is not limited to fast quenches of the trap geometry or slow, adiabatic ramps. We can also implement much more complicated time-dependences. This allows us to perform compression or decompression protocols for the trap on non-adiabatic timescales, while suppressing the collective dynamics typical after a simple quench. Such 'shortcuts to adiabaticity' have recently been successfully implemented for 3d thermal clouds and 3d BECs [37]. Here, we demonstrate a similar scheme based on optimal control for 1d quasicondensates. In contrast to the 3d BEC, the limited phase-coherence allows us to directly probe the temperature of the phonon ensemble in the 1d quasicondensate. Such measurements provide evidence that the shortcut procedure does not induce excitations and is therefore indeed adiabatic with respect to the full observable excitation spectrum, up to the cutoff given by the finite optical resolution of our imaging system.

Cold atoms in a 1d magnetic guide. One of the tools available in the experiment is a fluorescence detector based on the integration of optical fibres on the atom chip, which has been employed for previous measurements on atoms in the microkelvin-regime as documented in references [38, 39, 40, 41, 42]. To make use of this device, atoms need to propagate from the central chip region, where the preparation of the cloud takes place, over a distance of 5.5 millimetres to the site where the fluorescence detector is mounted. At nanokelvin temperatures, this transport differs significantly from what has been observed in the microkelvin regime and poses several experimental challenges: Preparing clouds with sizeable atom numbers at low temperatures usually yields sufficient densities such that the propagation along the magnetic guide is not free, but rather hydrodynamic. The cloud is much more sensitive to irregularities of the trapping potential, which can inhibit the propagation from the initial trap to the fluorescence detector. Additionally, at low temperatures, it only takes a small number of photon scattering events to drastically influence the motion of an atom in the detection region. We use the results outlined above to characterize and engineer the transport to the detection site and analyse the interaction of cold atoms with the detector. Finally, for sufficiently long 1d expansion times, the observation of effects beyond the model based on scale invariance is predicted. Their discussion and prospects for future measurements are presented in the later sections of this thesis.

1.3. Structure

Part I contains a brief introduction to the theory of 1d Bose gases and some numerical methods suited to their simulation. A full treatment of these topics would be beyond the scope of this work, hence these sections should merely serve as a basis for each project's more detailed presentation later on.

Much of the experiment has already been set-up before the start of this thesis. Therefore, a presentation of the apparatus in part I focuses on the changes to the machine implemented in the scope of this project to achieve BEC, as well as on some experimental techniques relevant for later chapters.

Part II contains the measurement results and their analysis. It constitutes the core part of this thesis. It is split into three self-contained but interconnected projects, each presented within its own chapter.

Part III presents an outlook focusing on the ongoing construction of a new experimental setup, starting with a short overview, followed by the contributions made in the scope of this thesis project. I conclude with a summary of the main results and a short discussion of open questions and prospects for future experiments, with an emphasis on the new setup in preparation.

Part I.

Basics

2. 1d Bose gases: Theoretical basics

> *"A theory is something nobody believes, except the person who made it."*
>
> ALBERT EINSTEIN, IN A CONVERSATION WITH HERMANN MARK

The central part of this thesis as presented in chapters 5 and 6 deals with the dynamics of 1d quasicondensates in time-dependent trapping potentials and the description of fluctuations and coherence properties in the presence of such dynamics. While these chapters contain a presentation of the corresponding theoretical models, the latter are based on the detailed understanding of the equilibrium properties of trapped 1d Bose gases that has been achieved during the last decades. The goal of this chapter is to present a short overview of the physics involved and a compilation of important references, with a focus on the topics relevant for the later parts of this thesis: The description of phase fluctuations in terms of low-energy phononic excitations and corresponding correlation functions, and the manifestation of characteristic density fluctuations in free expansion providing observables that render these fluctuations experimentally accessible.

The chapter starts with a short discussion of Bose-Einstein condensation, bridging the well-known textbook case of an ideal Bose gas in a three dimensional box in the continuum limit to the experimental system at hand, a trapped 1d Bose gas with a finite number of particles. This is followed by the introduction of interacting Bose gases in terms of bosonic fields and corresponding correlation functions, a formalism that is used throughout the rest of this chapter.

Section 2.2 continues with a discussion of the different regimes that exist for the trapped interacting 1d Bose gas, followed by the core of this chapter, section 2.3, which puts focus on the 1d quasicondensate with weak interactions at finite temperature, as realized in our experiments. It develops the description of thermal phase fluctuations in terms of a universal Luttinger liquid model, containing a discussion of its limits and an outlook on current research dealing with effects beyond this picture. In particular, section 2.4 contains an analysis of the 1d-3d crossover regime and the influence of experimentally relevant 3d effects on the 1d physics presented in the previous sections. Finally, section 2.5 briefly summarizes the theory developed in reference [30] that is the basis of thermometry based on density fluctuations, also called *density ripples*, emerging during the free expansion of a phase-fluctuating quasicondensate.

2.1. Introduction

The attempt to derive Planck's radiation law [43, 44] purely on the grounds of the light quanta hypothesis and statistical mechanics led to the publication of Satyendra Nath Bose's seminal article in 1924 [45], published with the help of Einstein, and in further consequence to the realization that indistinguishable particles in quantum mechanics are not correctly described by classical Maxwell-Boltzmann statistics [46, 47]. As discovered only several years later, their statistical properties depend on spin [48, 49, 50, 51, 52]. Particles with integer spin, today called *bosons*, can accumulate and condense in the energetic ground state under certain conditions, forming a novel state of matter. The possibility of such a state was actually pointed out by Einstein already in [53]. Although the effects of Bose-Einstein statistics are apparent in a variety of physical systems, most prominently laser light, the experimental realization of a *Bose-Einstein condensate (BEC)* from a cold bosonic vapour was not achieved until the mid nineties [2, 3, 4]. Today, such experiments are a cornerstone of fundamental research in many-body quantum physics. The following sections sketch the mechanism of Bose-Einstein condensation, with a focus on the influence of dimensionality on the phenomenon.

2.1.1. Bose-Einstein condensation of the ideal gas

The textbook case to introduce BEC is the discussion of the ideal homogeneous Bose gas in three dimensions [54, 47]. The average particle number in a grand-canonical ensemble of bosons defined by a volume V, chemical potential μ and temperature T with $\beta = (k_B T)^{-1}$ and Boltzmann's constant k_B is given by the sum over the average occupation of each discrete momentum state $\boldsymbol{k}$ with corresponding energy eigenvalues $\epsilon_{\boldsymbol{k}} = \hbar^2 \boldsymbol{k}^2/(2m)$ as

$$\langle N \rangle = \sum_{\boldsymbol{k}} \langle n_{\boldsymbol{k}} \rangle = \sum_{\boldsymbol{k}} \frac{1}{e^{\beta(\epsilon_{\boldsymbol{k}}-\mu)} - 1} = \langle n_0 \rangle + \sum_{\boldsymbol{k} \neq 0} \langle n_{\boldsymbol{k}} \rangle = \langle n_0 \rangle + \langle n_{ex} \rangle . \tag{2.1}$$

Here, the ground state occupation number $\langle n_0 \rangle$ is considered separately from the excited state occupations $\langle n_{ex} \rangle$ since its contribution otherwise vanishes in the continuum limit taken below. It can be expressed as

$$\langle n_0 \rangle = \frac{1}{e^{-\beta\mu} - 1} = \frac{z}{1-z} \geq 0. \tag{2.2}$$

The quantity $z = e^{\beta\mu}$ is called *fugacity*. The chemical potential needs to fulfil $\mu < 0$ to prevent negative occupation numbers, restricting the fugacity to values between $0 \leq z < 1$. To discuss the behaviour of the system in the 'quantum mechanical' limit $T \to 0, z \to 1$, the volume is considered to be an n-dimensional box with periodic boundary conditions, and the continuum limit is taken, replacing the sum from equation 2.1 by the integral

$$\langle N \rangle = \frac{z}{1-z} + \int d\epsilon \, \mathcal{D}(\epsilon) \, \langle n(\epsilon) \rangle. \tag{2.3}$$

Here, $\mathcal{D}(\epsilon) = d\Omega/d\epsilon$ represent the density of states that depends on the volume of a phase space element Ω in this semi-classical approximation and therefore on the dimensionality of the system. This quantity determines the fate of the system in the quantum limit, as will be seen below.

BEC in 3 dimensions.

In a homogeneous three dimensional system, Ω can be expressed as

$$\Omega = \frac{1}{\hbar^3}\int d^3r\, d^3p = \frac{4\pi V}{\hbar^2}\int_0^\infty dp\, p^2 = \frac{V}{4\pi^2}\left(\frac{2m}{\hbar^2}\right)^{3/2}\int_0^\infty d\epsilon\sqrt{\epsilon}. \tag{2.4}$$

Hence, the total occupation number in excited states $\langle n_{ex}\rangle$ can be written as

$$\langle n_{ex}\rangle = \frac{V}{4\pi^2}\left(\frac{2m}{\hbar^2}\right)^{3/2}\int_0^\infty \frac{d\epsilon\sqrt{\epsilon}}{e^{\beta(\epsilon-\mu)}-1} \tag{2.5}$$

This integral can be solved analytically, yielding

$$\langle n_{ex}\rangle = \frac{V}{\lambda_{dB}^3}\cdot g_{3/2}(z)\,. \tag{2.6}$$

Here, $\lambda_{dB} = \sqrt{2\pi\hbar^2/(mk_BT)}$ denotes the thermal de Broglie wavelength and $g_{3/2}(z)$ the polylogarithm

$$g_{3/2}(z) = \sum_{m=1}^{\infty}\frac{z^m}{m^{3/2}}. \tag{2.7}$$

This series only converges for $|z| \leq 1$ and is bounded by Riemann's zeta function:

$$g_{3/2}(1) = \sum_{m=1}^{\infty}\frac{1}{m^{3/2}} = \zeta(3/2) \approx 2.612. \tag{2.8}$$

This means that the excited states can only accommodate a finite number of particles. Let us further assume a fixed average particle number $\langle N\rangle$ in the system. Upon lowering the temperature, the total particle number can be kept constant by raising μ. For $\mu \to 0$, however, the excited state population saturates, and equation 2.6 cannot account for the total particle content of the system any more. Consequently, an increasing occupation needs to accumulate in the ground state, constituting the phenomenon of Bose-Einstein condensation.

The critical temperature for the onset of this process can be defined at the point where saturation is reached:

$$T_c = \frac{2\pi\hbar^2}{m}\left(\frac{\langle N\rangle}{V\zeta(3/2)}\right). \tag{2.9}$$

Defining the average density $n = \langle N\rangle/V$, this leads to the condition for the onset of condensation:

$$n\lambda_{dB}^3 \approx 2.612. \tag{2.10}$$

The left side of equation 2.10 is also called the phase space density of the system.

It is instructive to also touch upon BEC in a trap. A trapping potential modifies the density of states. For the special case of an isotropic harmonic trap, for example, it is given by

$$\mathcal{D}\left(\epsilon\right) = \frac{1}{2\left(\hbar\omega\right)^3}\epsilon^2, \tag{2.11}$$

and the critical temperature turns out to be

$$T_c = \frac{\hbar\omega}{k_B}\left(\frac{\langle N\rangle}{\zeta\left(3\right)}\right)^{1/3}. \tag{2.12}$$

with $\zeta\left(3\right) \approx 1.212$.

In the typical experimental case of an anisotropic trapping potential, it is useful to adopt a local density approximation (LDA). Here, the chemical potential depends on the position in the trap as $\mu(r) = \mu - V(\boldsymbol{r})$, with a maximum value at the trap minimum. In such a scenario, condensation sets in at the trap centre first, as the local phase space density exceeds $\zeta\left(3/2\right) \approx 2.612$. While the condensation process and critical temperature is described rather well by the non-interacting model as discussed above, with interaction-induced shifts of T_C measured to be in the order of a few percent [55], the shape of the condensate and its dynamics is usually dominated by interactions. An appropriate model to describe the ground state and dynamics of an interacting Bose gas within a mean-field picture is presented in section 2.1.3.

BEC in one dimension.

As already mentioned, the density of states determines the behaviour of a bosonic gas in the quantum limit. The general scaling with the dimensionality d of the system is $\mathcal{D}\left(\epsilon\right) \propto \epsilon^{\frac{d-2}{2}}$. For the already discussed 3d case, it is proportional to $\sqrt{\epsilon}$, tending to zero in the limit $\epsilon \to 0$. In two dimensions it does not depend on energy at all, while in one dimension it scales as $1/\sqrt{\epsilon}$, showing divergent behaviour in the limit $\epsilon \to 0$. In a hand-waving picture, this means that there is an arbitrarily large number of low-energy states at decreasing level spacing that can be populated, and that intuitively, one should not expect condensation in the ground state. Indeed, the one-dimensional equivalent to equation 2.6 reads

$$n_{1d}\lambda_{dB} = g_{1/2}(z) = \sum_{m=1}^{\infty}\frac{z^m}{m^{1/2}}, \tag{2.13}$$

with the linear density n_{1d}. This polylogarithm actually diverges in the limit $|z| \to 1$, and the excited state population is not bounded, in contrast to the 3d case. This finding has its roots in the Mermin-Wagner-Hohenberg theorem[1] [57, 56], stating that spontaneous symmetry breaking at finite temperature in a system with short-range interactions is prohibited.

---

[1] Actually, the argument goes back to previously unpublished work of N. Bogolyubov and is a consequence of the Bogolyubov-k^{-2} theorem, as acknowledged in [56]. Sometimes also called Coleman-theorem.

However, as already demonstrated, the existence of a trap changes the density of states. While a harmonic confinement in 1d leads $\mathcal{D}(\epsilon)$ to be independent of ϵ, still prohibiting condensation at finite temperature, it was found that this argument is only valid in the continuum limit, while the discrete structure of levels in a system with a finite particle number allows macroscopic occupation of the ground state [58], although not in terms of a well-defined phase transition as in the 3d case, but as a smooth crossover, in accordance with the experimental realization of such systems in [59] and later work. A discussion of BEC of an ideal gas in various types of trapping potentials can be found in [60].

2.1.2. Bosonic fields and correlation functions

At this point, it is useful to introduce some notions used throughout the rest of the chapter. It is convenient to describe many-body states in terms of field operators

$$\hat{\Psi}^\dagger(\boldsymbol{r}) = \sum_i \psi_i^*(\boldsymbol{r})\,\hat{a}_i^\dagger, \qquad \hat{\Psi}(\boldsymbol{r}) = \sum_i \psi_i(\boldsymbol{r})\,\hat{a}_i. \tag{2.14}$$

They describe the creation or annihilation of a particle at position $\boldsymbol{r}$. Here, $\hat{a}_i$ and $\hat{a}_i^\dagger$ denote creation and annihilation operators for the single particle states defined by the wave functions $\psi_i(\boldsymbol{r})$. All operators fulfil bosonic commutation relations

$$\left[\hat{a}_i, \hat{a}_j^\dagger\right] = \delta_{ij}, \qquad \left[\hat{\Psi}(\boldsymbol{r}), \hat{\Psi}^\dagger(\boldsymbol{r}')\right] = \delta(\boldsymbol{r} - \boldsymbol{r}'). \tag{2.15}$$

In this notation, one can define several important quantities. The one-body reduced density matrix $\rho^{(1)}$, equivalent with the first-order correlation function $G^{(1)}$, is given by

$$\rho^{(1)}(\boldsymbol{r}, \boldsymbol{r}') = G^{(1)}(\boldsymbol{r}, \boldsymbol{r}') = \left\langle \hat{\Psi}^\dagger(\boldsymbol{r})\,\hat{\Psi}(\boldsymbol{r}')\right\rangle \tag{2.16}$$

It is a measure for the spatial coherence of the system. In particular, it can be used to provide criteria for Bose-Einstein condensation. If one eigenvalue (λ_0) of the density matrix is in the order of the total particle number $\langle N\rangle$ while the other eigenvalues are of order one, the system is called Bose-condensed, and the number of particles in the condensate is given by $\langle N\rangle = \lambda_0$ [61]. Equivalently, one can consider the normalized entity

$$g^{(1)}(\boldsymbol{r}, \boldsymbol{r}') = \frac{G^{(1)}(\boldsymbol{r}, \boldsymbol{r}')}{\sqrt{G^{(1)}(\boldsymbol{r}, \boldsymbol{r})}\sqrt{G^{(1)}(\boldsymbol{r}', \boldsymbol{r}')}}, \tag{2.17}$$

where

$$G^{(1)}(\boldsymbol{r}, \boldsymbol{r}) = \left\langle \hat{\Psi}^\dagger(\boldsymbol{r})\,\hat{\Psi}(\boldsymbol{r})\right\rangle = n(\boldsymbol{r}) \tag{2.18}$$

is simply the local density. This function can take values between 1 and 0. If $g^{(1)}(\boldsymbol{r}, \boldsymbol{r}') > 0$ for distances $|\boldsymbol{r} - \boldsymbol{r}'|$ in the order of the whole extension of the cloud, the density matrix is said to feature a property called off-diagonal long range order, implying coherence over the full cloud extension and the presence of a BEC. Note that the criterion given above can also be applied to characterize quasicondensates lacking coherence over the full sample size. In this case, the highest occupied mode, characterized by the largest eigenvalue λ_0 of $\rho^{(1)}$ is also called Penrose-Onsager mode and represents the phase-coherent fraction of the gas.

Similarly, the second order correlation function

$$G^{(2)}\left(\boldsymbol{r},\boldsymbol{r}'\right)=\left\langle\hat{\Psi}^{\dagger}\left(\boldsymbol{r}\right)\hat{\Psi}^{\dagger}\left(\boldsymbol{r}'\right)\hat{\Psi}\left(\boldsymbol{r}\right)\hat{\Psi}\left(\boldsymbol{r}'\right)\right\rangle, \tag{2.19}$$

as well as its normalized version

$$g^{(2)}\left(\boldsymbol{r},\boldsymbol{r}'\right)=\frac{G^{(2)}\left(\boldsymbol{r},\boldsymbol{r}'\right)}{n\left(\boldsymbol{r}\right)n\left(\boldsymbol{r}'\right)} \tag{2.20}$$

can be defined. They represent the joint probability to measure two particles at the respective positions $\boldsymbol{r}$ and $\boldsymbol{r}'$ and are of interest in the context of density ripple thermometry as outlined in section 2.5. Reordering the field operators in this expression allows to define a density correlation function.

2.1.3. Interacting Bose gases

In terms of the notation introduced in the previous section, we can now write down the Hamiltonian of an interacting Bose gas in second quantization as

$$\hat{H}=\int d\boldsymbol{r}\hat{\Psi}^{\dagger}\left(\boldsymbol{r}\right)\hat{H}_{sp}\hat{\Psi}\left(\boldsymbol{r}\right)+\frac{1}{2}\int d\boldsymbol{r}d\boldsymbol{r}'\hat{\Psi}^{\dagger}\left(\boldsymbol{r}\right)\hat{\Psi}^{\dagger}\left(\boldsymbol{r}'\right)V_{int}\left(\boldsymbol{r}'-\boldsymbol{r}\right)\hat{\Psi}\left(\boldsymbol{r}\right)\hat{\Psi}\left(\boldsymbol{r}\right), \tag{2.21}$$

where $\hat{H}_{sp}$ represents the single-particle Hamiltonian

$$\hat{H}_{sp}=-\frac{\hbar^2}{2m}\Delta+V_{ext}(\boldsymbol{r}), \tag{2.22}$$

while $V_{ext}\left(\boldsymbol{r}\right)$ and $V_{int}\left(\boldsymbol{r}'-\boldsymbol{r}\right)$ stand for the external trapping and interaction potentials of two atoms at distance $|\boldsymbol{r}'-\boldsymbol{r}|$.

To study the macroscopically occupied ground state of a BEC, it is a good approximation to replace field operators $\hat{\Psi}\left(\boldsymbol{r}\right),\hat{\Psi}^{\dagger}\left(\boldsymbol{r}\right)$ by a complex wave function $\Psi\left(\boldsymbol{r}\right),\Psi^{*}\left(\boldsymbol{r}\right)$. In addition, BEC occurs in the low-temperature limit, translating into low average kinetic energy per atom causing s-wave scattering to dominate the contribution from higher partial waves, and the usually complicated interaction potential governing scattering between two atoms can be replaced by a delta-function pseudopotential. Under these conditions, interactions can be treated in terms of a mean-field description, and the shape and time-evolution of the macroscopic wave function Ψ, taking the role of an order parameter for the BEC transition, are given by the Gross-Pitaevskii equation (GPE) [62]:

$$i\hbar\frac{\partial}{\partial t}\Psi\left(\boldsymbol{r},t\right)=\left(-\frac{\hbar^2}{2m}\Delta+V_{ext}\left(\boldsymbol{r},t\right)+g\cdot\left|\Psi\left(\boldsymbol{r},t\right)\right|^2\right)\Psi\left(\boldsymbol{r},t\right). \tag{2.23}$$

The coupling constant depends on the s-wave scattering length a_s, governing the interaction strength, as

$$g=\frac{4\pi\hbar^2 a_s}{m}. \tag{2.24}$$

In the limit of negligible interactions, the shape of $\Psi\left(\boldsymbol{r},t\right)$ corresponds to the single-particle ground state in the trap. For harmonic confinement, this is a Gaussian defined by the oscillator lengths $a^i_{ho}=\sqrt{\hbar/(m\omega_i)}$, where $\omega_i=(\omega_x,\omega_y,\omega_z)$ are the trap frequencies along each direction of the parabolic potential. For a sizeable interaction term, the behaviour of the ground state solution depends on the sign of a_s: If it is negative, there is a critical particle number beyond which the solution is not stable and describes a collapse of the condensate. For a positive scattering length, as is the case for ^{87}Rb in the absence of a Feshbach resonance, repulsive interactions will broaden the ground state profile. Throughout this thesis, the discussion is focused on a gas with short-range repulsive interactions. An important case is the limit where the interaction term dominates. Separating the condensate wave function into

$$\Psi\left(\boldsymbol{r},t\right)=\Psi\left(\boldsymbol{r}\right)e^{-i\frac{\mu t}{\hbar}}, \tag{2.25}$$

substituting it into equation 2.23 and dropping the kinetic term yields

$$\left|\Psi\left(\boldsymbol{r}\right)\right|^2=\frac{1}{g}\left(\mu-V_{ext}\left(\boldsymbol{r}\right)\right). \tag{2.26}$$

This is called the Thomas-Fermi approximation, and the density takes the shape of the potential.

So far, we have been concerned with the ground state profile. Note that the time-dependent GPE 2.23 allows to describe collective excitations. Further, small fluctuations around the ground state wave function $\Psi+\delta\Psi$ can be reintroduced and treated in terms of a Bogolyubov transformation [63]. A very similar method to treat fluctuations of a 1d quasicondensate is applied in section 2.3.

Finally, it is useful to introduce the hydrodynamic representation of the Gross-Pitaevskii equation, which is utilized in the discussion of the finite-temperature scaling solution for a 1d quasicondensate in chapter 5. One can separate the condensate wave function as

$$\Psi\left(\boldsymbol{r},t\right)=\sqrt{n\left(\boldsymbol{r},t\right)}\cdot e^{i\phi(\boldsymbol{r},t)}, \tag{2.27}$$

where $n(\boldsymbol{r},t)=:n$ and $\phi(\boldsymbol{r},t)$ represent density and phase, respectively. Substituting this ansatz into equation 2.23 and making use of the relation between phase gradient and velocity field $v := \boldsymbol{v}(\boldsymbol{r},t) = (\hbar/m)\nabla\phi(\boldsymbol{r},t)$ yields the hydrodynamic equations:

$$\frac{\partial n}{\partial t} + \nabla\left(nv\right) = 0 \tag{2.28}$$

$$m\frac{\partial v}{\partial t} + \nabla\left(V_{ext}\left(\boldsymbol{r},t\right) + gn - \frac{\hbar^2}{2m\sqrt{n}}\Delta\sqrt{n} + \frac{mv^2}{2}\right) = 0 \tag{2.29}$$

Here, 2.28 represents the continuity equation, while 2.29, neglecting the third term in brackets on the r.h.s. denoting the quantum pressure, hence again introducing the Thomas-Fermi approximation, reduces to the Euler equation for an ideal fluid.

2.2. The interacting Bose gas in 1d

Typically, 1d Bose gases are realized in a highly anisotropic cylindrical trap. Considering harmonic confinement as in previous sections, the trap is characterized by radial and axial trap frequencies ω_r and ω_a, with $\omega_r >> \omega_a$. The common 1d-condition is that both thermal energy and chemical potential are small with respect to the radial level spacing,

$$k_B T, \mu \ll \hbar\omega_r \tag{2.30}$$

with the result that the gas is restricted to the radial ground state of the trap, and all dynamics takes place along the axial direction. In this scenario, the transverse direction can be integrated out to arrive at a one-dimensional description, if an effective 1d-coupling constant can be found, as discussed in [64]. For a typical atom chip trap with radial trap frequencies ranging from $2\pi \times 1$ kHz to $2\pi \times 4$ kHz, the corresponding oscillator lengths are between $a_{ho,r} = (\hbar/m\omega_r)^{1/2} = 340$ nm and 170 nm, while the 3d scattering length is $a_s \approx 5$ nm. In this case, the scattering properties keep their 3d character and an effective 1d interaction constant results from averaging over the radial density profile [65]:

$$g_{1d} = \frac{g}{2\pi a_{ho,r}^2} = 2\hbar\omega_r a_s \tag{2.31}$$

with the 3d interaction constant g as defined in 2.24. With this, disregarding the axial trapping potential for the moment, we can consider the following Hamiltonian:

$$\hat{H} = -\frac{\hbar^2}{2m}\int dz\hat{\Psi}^\dagger\left(z\right)\frac{\partial^2}{\partial^2 z}\hat{\Psi}\left(z\right) + \frac{g_{1d}}{2}\int dz\hat{\Psi}^\dagger\left(z\right)\hat{\Psi}^\dagger\left(z'\right)\hat{\Psi}\left(z\right)\hat{\Psi}\left(z'\right). \tag{2.32}$$

This is the famed Lieb-Liniger Hamiltonian [10, 11] for an interacting 1d Bose gas in second quantization. It is one of the few many-body systems where ground state properties and the excitation spectrum can be calculated exactly regardless of interaction strength. Initially developed as a toy model, the experimental realization of 1d Bose gases revived the interest in theoretical studies of this Hamiltonian. One important question in this context is how to properly define integrability for quantum systems.

The classical counterpart of the Lieb-Liniger Hamiltonian describes a homogeneous[2] gas of particles confined to one spatial dimension. This system is integrable in the classical sense so that one can construct as many conserved quantities as there are degrees of freedom. For a quantum mechanical system, on the other hand, the notion of integrability still lacks a meaningful definition. The Lieb-Liniger problem, for instance, is mathematically 'integrable' in that one can find an exact solution, but a physical argument that connects to the definition of integrability in classical mechanics and allows to classify different systems and to predict mathematical 'integrability' still waits to be found, despite ongoing efforts [9].

In addition, the Lieb-Liniger model can be mapped to the XXZ-Heisenberg spin chain in the continuum limit, and shares a universal theory describing the low-lying elementary excitations with many other one-dimensional systems realized in solid state physics, from electrons in quantum wires formed by semiconductor heterostructures to carbon nanotubes [66]. This is the Tomonaga-Luttinger liquid description, a variant of which will be introduced in section 2.3.1. Comprehensive reviews on this topic can be found in [24] and [12].

2.2.1. Phase diagram of the homogeneous 1d Bose gas

In the following, we will define several quantities that allow us to categorize the different regimes encountered in the phase diagram of the 1d Bose gas, following references [67, 68, 69, 70, 71]. The characteristic length and energy scales associated with the interaction constant are

$$l_g = \frac{\hbar^2}{m g_{1d}}, \qquad E_g = \frac{m g_{1d}^2}{2\hbar^2} = \frac{\hbar^2}{2 m l_g^2} \tag{2.33}$$

In addition, one can define a dimensionless quantity characterizing the interaction strength, the so-called Lieb-Liniger parameter:

$$\gamma = \frac{m g_{1d}}{\hbar^2 n_{1d}} = \frac{1}{n l_g}, \tag{2.34}$$

where n_{1d} denotes the linear density. It is connected with the pre-factor c of the interaction term in the first-quantized version of the Hamiltonian 2.32 as $\gamma = c/n_{1d}$ [11]. It reveals a counter-intuitive peculiarity of the 1d Bose gas: In contrast to the 3d system, the interaction strength increases with decreasing linear density n_{1d}. Further, we can define the degeneracy parameter, below which quantum effects start to become important:

$$T_d = \frac{\hbar^2 n_{1d}^2}{2 m k_B} = \frac{E_g}{k_B \gamma^2}. \tag{2.35}$$

Finally, using T_d, a dimensionless temperature can be expressed as

$$t = \frac{T}{\gamma^2 T_d}. \tag{2.36}$$

---

[2] Here, the term homogeneous as used in classical statistical mechanics denotes a system of particles with identical masses.

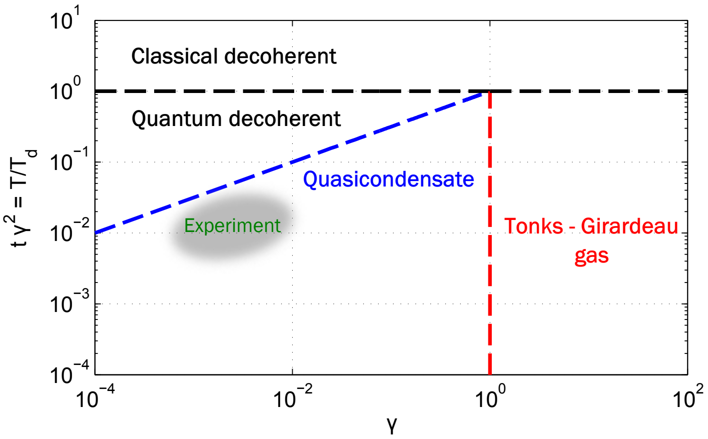

Figure 2.1.: Phase diagram of the 1d homogeneous Bose gas. The classical decoherent regime is found for $\gamma^2 t >> 1$ (black line). At weak interactions, it borders on the quantum decoherent regime ($\gamma^{1/2} \ll \gamma^2 t \ll 1$, blue and black line), where the blue line separates it from the quasicondensate regime. For $\gamma \ll 1$ and $\gamma^2 t \ll 1$, the system enters the strongly interacting Tonks-Girardeau regime. The grey-shaded region denotes the approximate parameter regime available to our experimental setup.

The two parameters γ and t can be used to construct the phase diagram of the homogeneous 1d Bose gas shown in figure 2.2.1. Based on the exact solution to the Lieb-Liniger problem and a model presented in [72] allowing to calculate thermodynamical properties at equilibrium, one finds several regimes distinguished by different excitation spectra, correlation properties and overall physical behaviour as described in [67] and [68].

Classical decoherent gas. For $T > T_d$ the gas is non-degenerate and hence governed by a classical Boltzmann distribution, and correspondingly, thermal correlations [73]:

$$g^{(2)}(z) = 1 + g^{(1)}(z) = 1 + \exp\left(-\frac{z^2}{2\pi\lambda_{dB}}\right), \tag{2.37}$$

where the characteristic length scale is governed by the thermal de Broglie wavelength λ_{dB} and the relation between first and second order correlation functions follows for Wick's theorem [74] and a Gaussian state.

Quantum decoherent gas. The onset of quantum degeneracy is found for temperatures below $\gamma^2 t \approx 1$. In the regime marked by $\gamma \ll 1$ and $\gamma^{-3/2} \ll t \ll \gamma^{-2}$, Bose-enhancement leads to increased coherence resulting in a non-Gaussian first-order correlation function [69, 70]

$$g^{(1)}(z) = \exp\left(-\frac{z}{l_\phi}\right) \tag{2.38}$$

with a coherence length

$$l_\phi = \frac{2}{n_{1d}\gamma^2 t} = \frac{\lambda_{dB}^2 n}{2\pi}. \tag{2.39}$$

The second-order correlation function, which cannot be obtained as easily by the Wick theorem as 2.37, is given by

$$g^2(z) = 1 + \exp\left(-\frac{2z}{l_\phi}\left[1 - \frac{4}{\gamma^3 t^2}\left(1 + \frac{2z}{l_\phi}\right)\right]\right) \tag{2.40}$$

.

Quasicondensate. In the limit of weak interactions and low temperature ($\gamma \ll 1$, $t \ll \gamma^{-3/2}$), the system forms a quasicondensate that shares many properties with the 3d BEC, such as suppressed density fluctuations, but long-range phase-coherence is destroyed by pronounced phase fluctuations, as discussed in section 2.1.1. Since most experiments presented in this thesis are performed in this regime, it will be described in detail within section 2.3. With respect to the phase diagram, it is interesting to note that the fluctuations dominating the coherence properties are thermal over much of the parameter range, with quantum fluctuations starting to dominate only for temperatures and linear densities $k_B T/g_{1d} n_{1d} \lesssim 0.1$ [75].

Tonks-Girardeau gas. For $\gamma > 1$ at degeneracy, the system enters the strongly interacting regime and forms a so-called Tonks-Girardeau gas [76]. In contrast to a coherent BEC-like state, the system is best described in terms of repelling single-particle wave packets mimicking in many respects fermionic behaviour, and in the limit of $\gamma \to \infty$ there exists an exact mapping to a system of free fermions by the so-called Jordan-Wigner transformation. While in our experimental setup, this parameter regime is out of reach for now, it is possible to create interaction strengths in the order of $1 < \gamma < 10$ in optical lattices arranged to realize an ensemble of cylindrical tubes with high radial confinement [77]. In addition, an atom chip experiment [16] also reported to achieve interaction strengths of $\gamma \approx 1.5$. This was made possible by creating a trap with AC currents using a modulation frequency of 200 kHz to smoothen out corrugations of the potential usually leading to fragmentation of the atom cloud for traps close to the chip allowing sufficient radial confinement to achieve strong interactions. Such a technique is feasible to introduce in future chips used in our experiment.

It is crucial to keep in mind that the different phases outlined above are not separated by sharp transitions. As mentioned in section 2.1.1, there is no mechanism, such as the saturation of the excited state population in 3d, that allows to define a clear BEC phase transition for the 1d Bose gas. Rather, one finds a large crossover region between the decoherent and quasicondensate regimes, where the condensation is usually induced by interactions [78] rather than in terms of a two-step process of initial radial and subsequent axial condensation that has been described for an ideal Bose gas in a trap [58]. Likewise, there exists no sharp transition between the weakly and strongly interacting regimes at $\gamma = 1$. Significant characteristic effects, for example sizeable deviations from the Bogolyubov-like excitations as discussed below, appear only for $\gamma \gg 1$ [79]. Similarly,

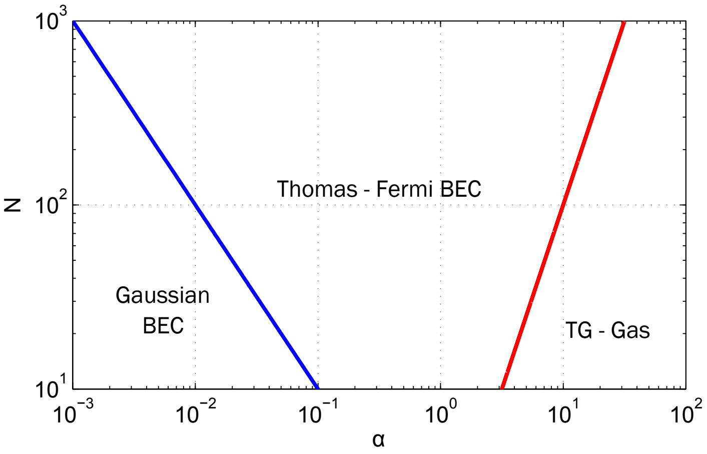

Figure 2.2.: Phase diagram of the trapped 1d gas at $T = 0$. $N \gg \alpha^{-1}$ separates the non-interacting Gaussian and interaction-dominated Thomas-Fermi regime, while the red line ($N \ll \alpha^2$) marks the transition to the strongly interacting Tonks-Girardeau regime. Note that for sufficiently high atom numbers, the system is always found in the Thomas-Fermi regime.

the break-down of the self-similarity present during the hydrodynamic expansion of a weakly interacting Bose gas, for instance, has its onset at γ well below unity [80].

Experimentally accessible parameter regime. The region of the phase diagram that can be realized with the experimental setup discussed in this thesis is marked by the grey-shaded area within figure 2.2.1, characterized by $10^{-3} < \gamma < 10^{-2}$ and temperatures corresponding to $10 < T < 200$ nK. The limitations on γ arise from the available radial trap frequencies below ~ 2 kHz and feasible atom numbers between a few hundred and 30000 within a 1d geometry. The temperature is bounded from below by the efficiency of evaporative cooling in 1d [81], and thus indirectly by the initial phase space density after loading the chip trap. The upper limit is again given by the maximal radial trap frequencies. In terms of energy, a frequency of 1 kHz roughly corresponds to a temperature of 50 nK. At temperatures significantly exceeding the radial trap frequencies defining the transverse level spacing, the dynamics is not confined to 1d any more and hence the 1d phase diagram loses its validity. In summary, these effects limit the exploration of 1d physics in our setup mainly to quasicondensates and, potentially, the quantum decoherent regime in future experiments with extremely dilute clouds.

2.2.2. Effect of the trap on the phase diagram

The characteristic length scale of an axial harmonic potential with trap frequency ω_a is the already introduced oscillator length $a_{ho} = \sqrt{\hbar/(m\omega_a)}$. For most regions in the phase diagram, correlation lengths are much smaller than this quantity, and the influence of the trap can be included in terms of a local density approximation (LDA). As such, the gas is treated as composed of slices, each of which obeys the same description as a homogeneous gas with local density $n_{1d}(z)$ [68]. In this picture, the biggest influence of the trap is expected in the limit of low temperatures, where correlation lengths and a_{ho} can become comparable.

As already noted above, the presence of a trapping potential alters the scaling of the density of states, and thus allows to realize a BEC in the limit $T \to 0$ at low interaction strengths, warranting a mean-field description of the 1d gas. Similar to the 3d case, we can write down a Gross-Pitaevskii equation

$$i\hbar\frac{\partial}{\partial t}\psi\left(z,t\right)=\left(-\frac{\hbar^2}{2m}\frac{\partial^2}{\partial_z^2}+\frac{m\omega_a^2 z^2}{2}+g_{1d}\cdot\left|\psi\left(z,t\right)\right|^2\right)\psi\left(z,t\right). \tag{2.41}$$

At negligible interaction strength, 2.41 reduces to a Schrödinger equation, and the density profile $n(z) = |\psi(z)|^2$ is given by the single-particle ground state, hence a Gaussian in the case of harmonic confinement.

To investigate the effect of interactions, it is useful to define the parameter [82]

$$\alpha = \frac{m g_{1d} a_{ho}}{\hbar^2}. \tag{2.42}$$

It can be interpreted as the ratio of a_{ho} and the interaction length introduced in equation 2.33. Together with the total particle number, it spans the phase diagram of the trapped degenerate gas at $T = 0$ [71] as shown in figure 2.2.2. For $N \gg \alpha^{-1}$ and $\alpha \ll 1$, the system enters the Thomas-Fermi regime, and the density profile takes the shape of an inverted parabola

$$n(z) = n_0\left(1-\frac{z^2}{R_{TF}^2}\right) \tag{2.43}$$

with the central density n_0 and the Thomas-Fermi radius

$$R_{TF} = \sqrt{\frac{2g_{1d}n_0}{m\omega_a^2}} \tag{2.44}$$

Only for $\alpha \gg 1$ and $N \ll \alpha^2$, the gas is in the Tonks-Girardeau regime. The profile is parabolic as well, but with a different radius $R_{TG} = \sqrt{2N}a_{ho}$.

With particle numbers exceeding $N = 1000$ and values of $\alpha \approx 0.1$, the experiments performed in the course of this thesis fall deeply into the Thomas-Fermi regime.

2.2.3. Excitation spectrum of the 1d Bose gas

The excitation spectrum of the homogeneous Bose gas can be calculated directly from the exact solution of the Lieb-Liniger model [11]. One finds two branches, typically labelled as type-I or 'particle' excitations, and type-II or 'hole' excitations, respectively, with different dispersion relations. The latter are restricted to the strongly interacting regime, while the former can be determined by application of the Bogolyubov theory

[63, 83] to the 1d gas [84]. Here, excitations are treated as small fluctuations $\delta\psi$ around the mean-field ground state ψ, in a basis of quasiparticles labelled by the momentum k. The dispersion relation writes

$$\epsilon_k = \sqrt{E_k\,(E_k + 2\mu)}, \tag{2.45}$$

with the free particle dispersion relation $E_k = \hbar^2 k^2/2m$ and chemical potential $\mu = g_{1d} n_0$. At low energies it can be approximated as $\epsilon_k \approx ck$, and the excitations correspond to phonons propagating at a speed of sound $c = \hbar/\sqrt{m\mu}$. At high energies, quasiparticles behave as free particles with a dispersion relation $\epsilon_k \approx E_k + \mu$. The crossover between these phonon- and particle-like regimes takes place at energies around the chemical potential μ, corresponding to momenta in the order of the inverse healing length $\xi^{-1} = mc/\hbar$.

Much of the physics observed in experiment can be captured by models taking only into account the low-energy phononic part of the spectrum, such as the Luttinger liquid approach presented in the following section.

2.3. The 1d quasicondensate

As introduced in the previous section, a quasicondensate is an entity that is similar to a BEC, but where long-range phase coherence is destroyed by excitations. While quasicondensates are not restricted to 1d and have been realized in both 2d [85] and in elongated 3d geometries [86], in a 1d geometry all dynamics is restricted to the axial direction, allowing a simplified description.

2.3.1. Luttinger liquid model

Following reference [87], the starting point is a hydrodynamic approach [88] as introduced in section 2.1.3 where we represent excitations in terms of density fluctuations $\delta\hat{n}(z)$ and a spatially varying phase $\hat{\phi}(z)$ on top of a mean-field in the Thomas-Fermi regime, relying on a local density approximation to include an external harmonic trapping potential. The fields $\delta\hat{n}(z)$ and $\hat{\phi}(z)$ are conjugate quadratures that can be described by the Hamiltonian

$$\hat{H} = \frac{\hbar}{2\pi} \int dz \left[v_N\,(z)\,(\pi\delta\hat{n}\,(z))^2 + v_J\,(z)\,(\partial_z\hat{\phi}\,(z))^2 \right] = \sum_j \epsilon_j \hat{b}_j^\dagger \hat{b}_j, \tag{2.46}$$

with the generalized velocities

$$v_N(z) = \frac{g_{1d}}{\hbar\pi}, \qquad v_J(z) = \frac{\hbar\pi}{2m} n(z) \tag{2.47}$$

and the parabolic mean-field density profile with a radius R_{TF}

$$n(z) = n_0 \left(1 - \frac{z^2}{R_{TF}^2}\right). \tag{2.48}$$

The generalized velocities are connected with the sound velocity $c(z)$ and the so-called Luttinger parameter as

$$c(z) = \sqrt{v_N(z)v_J(z)}, \qquad K(z) = \sqrt{\frac{v_J(z)}{v_N(z)}}. \tag{2.49}$$

Both the sound velocity and the Luttinger parameter are local quantities due to the inhomogeneity of the system.

The harmonic Hamiltonian 2.46 describes a Luttinger liquid in a trap, governed by 1d versions of the hydrodynamic equations 2.29 and 2.28, neglecting the quantum pressure term. Higher order contributions to the Hamiltonian that are not quadratic in $\delta\hat{n}(z)$ or $\hat{\phi}(z)$ are likewise neglected. Note that the physical a-priori assumption behind these approximations is that density fluctuations are small.

We can expand $\delta\hat{n}(z)$ and $\hat{\phi}(z)$ in a basis of uncoupled eigenfunctions [82]

$$\delta\hat{n}\left(z,t\right) = \sum_{j\geq 1}\sqrt{\frac{\epsilon_j}{2\hbar\pi v_N\left(z\right)R_{TF}}}\tilde{f}_j\left(z,t\right)\hat{b}_j + H.c. \tag{2.50}$$

$$\hat{\phi}\left(z,t\right) = -i\sum_{j\geq 1}\sqrt{\frac{\hbar\pi v_N\left(z\right)}{2\epsilon_j R_{TF}}}\tilde{f}_j\left(z,t\right)\hat{b}_j^\dagger + H.c. \tag{2.51}$$

with separable basis functions

$$\tilde{f}_j\left(z,t\right) = f_j\left(z\right)\exp\left(-\frac{i}{\hbar}\epsilon_j t\right). \tag{2.52}$$

In the weakly interacting Thomas-Fermi regime, one can choose a basis of Legendre polynomials $P_j(z/R_{TF})$

$$f_j\left(z\right) = \sqrt{j+\frac{1}{2}}P_j\left(\frac{z}{R_{TF}}\right), \tag{2.53}$$

and the energy spectrum is given by

$$\epsilon_j = \hbar\omega_j = \frac{\hbar\omega_a}{\sqrt{2}}\sqrt{j\left(j+1\right)}. \tag{2.54}$$

Since the Hamiltonian 2.46 is harmonic, there is no coupling between phase and density fluctuations. Since the occupation number of each mode j is conserved, the only dynamics that takes place after fixing the initial state is a rotation of each eigenstate in the phase space spanned by the quadratures $\delta\hat{n}$, $\hat{\phi}$ with frequency ω_j.

Using the operators 2.50 and 2.51, it is possible to calculate the mean square fluctuations $\langle\delta\hat{n}^2\rangle$ and $\langle\delta\hat{\phi}^2\rangle$ in the inhomogeneous system within this model. The corresponding expressions can be found in reference [82]. At this point, we limit ourselves to the remark

that the initial assumption of small density fluctuations is well justified for experimental parameters, since they are found to approximately scale as T/T_D. Since $k_B T_D$ is usually much larger than the radial energy level spacing $\hbar\omega_r$ for a typical atom chip trap, T/T_D is always small (usually on the percent level) as soon as the 1d regime is entered.
Descriptions beyond the Luttinger limit have been presented in the form of a functional integral approach including phase fluctuations exactly [89], and an extension of the Bogolyubov theory to quasicondensates [84]. The former has also been extended to accommodate an ab-initio treatment of phase fluctuations [90], and a comprehensive review can be found in [47]. The latter faces some subtleties, mainly involving the definition of the phase operator, and a detailed description of how to overcome these problems is found in references [84] and [91].

2.3.2. Correlation functions

We proceed to derive an expression for the first order correlation function $g^{(1)}(z, z')$ at finite temperature from a Luttinger liquid model as introduced above, before shortly commenting on density correlations in the quasicondensate regime.

First order correlation function

Neglecting density fluctuations, we can define a quasicondensate wave function analogous to 2.27:

$$\psi(z,t) = \sqrt{n(z)}e^{i\hat{\phi}(z,t)}, \tag{2.55}$$

and the first order correlation function as defined in equation 2.16 reduces to

$$g^{(1)}(z, z') \approx \sqrt{n(z)\, n(z')} \left\langle e^{i\left[\hat{\phi}(z)-\hat{\phi}(z')\right]} \right\rangle, \tag{2.56}$$

which can be rewritten with the help of Wick's theorem [74] as

$$g^{(1)}(z, z') \approx \sqrt{n(z)\, n(z')} e^{-\frac{1}{2}\left\langle\left[\hat{\phi}(z)-\hat{\phi}(z')\right]^2\right\rangle}, \tag{2.57}$$

with the phase variance $\langle[\hat{\phi}(z) - \hat{\phi}(z')]^2\rangle = \langle\delta\hat{\phi}^2\rangle$. For simplicity, following reference [71], this quantity will be calculated in the plane-wave basis of a homogeneous system, which is a good approximation to the inhomogeneous model from section 2.3.1 in the vicinity of the cloud centre. Expanding the phase operator as

$$\hat{\phi}(z) = \sqrt{2}\sum_{k>0}\left[\hat{\phi}_{ck}\cos(kz) + \hat{\phi}_{sk}\sin(kz)\right], \tag{2.58}$$

we have for the phase variance

$$\frac{1}{2}\left\langle\left[\hat{\phi}(z) - \hat{\phi}(0)\right]^2\right\rangle = \sum_{k>0}\left\langle\hat{\phi}_{ck}^2\right\rangle(\cos(kz)-1)^2 + \sum_{k>0}\left\langle\hat{\phi}_{sk}^2\right\rangle\sin^2(kz). \tag{2.59}$$

Assuming thermal equilibrium, the average energy stored in phase fluctuations for each mode is given by the equipartition theorem and the amplitudes are given by [71]

$$\left\langle \hat{\phi}_k^2 \right\rangle = \frac{m k_B T}{n_{1d} \hbar^2 k^2 L}. \tag{2.60}$$

Rearranging the sum and taking the continuum limit, we find

$$\frac{1}{2} \left\langle \left[\hat{\phi}(z) - \hat{\phi}(0) \right]^2 \right\rangle = \frac{m k_B T}{n_{1d} \hbar^2 \pi} \int_0^\infty dk \frac{1 - \cos(kz)}{k^2}. \tag{2.61}$$

Since

$$\frac{1}{2\pi} \int_0^\infty dk \frac{1 - \cos(kz)}{k^2} = \frac{z}{4}, \tag{2.62}$$

we find that the first order correlation function for a thermal state takes the form of an exponential:

$$g^{(1)}(z, 0) \approx e^{-\frac{m k_B T}{2 \hbar^2 n_{1d}} z}. \tag{2.63}$$

The characteristic scale of the exponential is called the thermal coherence length $\lambda_T = m k_B T / 2\hbar^2 n_{1d}$ and expresses the average extension of phase-coherent regions within the quasicondensate. For typical experimental parameters, it is in the order of a few to tens of microns, compared to Thomas-Fermi radii of roughly 200 μm. Nevertheless, if the ratio $k_B T/\mu$ becomes sufficiently small, λ_T can potentially grow to exceed the system size, establishing a phase-coherent 1d BEC. Under such conditions, however, the effect of quantum fluctuations offering a logarithmic contribution to the exponent of $g^{(1)}(z, 0)$, as considered for instance in reference [92], needs to be taken into account. For the experiments presented in this thesis, however, such a contribution is negligible and an exponential coherence function offers an excellent description.

By the Wiener-Khinchin theorem[3], one can identify the momentum distribution of the gas as the power spectral density corresponding to the autocorrelation function $g^{(1)}(\Delta z)$ via a Fourier transform:

$$n(k) = \mathcal{F}\left[g^{(1)}(z, 0) \right] \tag{2.64}$$

Substituting the expression 2.63, one finds a Lorentzian shape [93, 94].

$$n(k) \approx \frac{1}{2\pi} \int d(\Delta z) g^{(1)}(\Delta z) e^{-ik\Delta z} = \frac{1}{\pi} \frac{\lambda_T}{1 + \lambda_T^2 k^2}. \tag{2.65}$$

Second order correlation function

The in-situ non-local pair correlation function of the 1d Bose gas at finite temperature across the full 1d phase diagram has been calculated in references [69] and [70], and necessitates an approach beyond the Luttinger liquid description also for quasicondensates. For distances below the healing length $z < \xi$, the main contribution comes from particle-like Bogolyubov excitations, and the pair correlation function for a thermal quasicondensate reads

---

[3] Also called Wiener-Khinchin-Einstein theorem or Khinchin-Kolmogorov theorem.

$$g^2(z,0) = 1 + \frac{T}{2T_D\gamma^{3/2}} e^{-2z/\xi}, \tag{2.66}$$

decaying exponentially with the characteristic length scale ξ. At distances $z > \xi$, phononic excitations dominate and lead to an antibunching contribution

$$g^2(z,0) \xrightarrow[z>\xi]{} 1 - \frac{\pi T^2}{8T_D^2\gamma^{3/2}} e^{-\pi T z/T_D\gamma\xi}. \tag{2.67}$$

Picking $z/\xi = 2$ and a typical value of $\gamma \approx 5 \times 10^{-3}$, the maximum antibunching contribution is found at 5 nK, with a deviation of 0.0005 from the Poissonian value $g^2(z,0) = 1$. Together with required resolutions well below the healing length, a direct observation of non-local pair correlations in an atom chip setup is, to say the least, extremely challenging. Local correlations, via measurement of in-situ density fluctuations, however, have been investigated experimentally within [14, 95, 96].

2.4. The 1d-3d crossover regime

So far the only effect of the trap considered has been the axial potential. The radial confinement was integrated out to only enter via the 1d interaction constant $g_{1d} = 2\hbar a\omega_r$. Here, the underlying assumption is that radially, we have a Gaussian ground state wave function with a size given by the transverse harmonic oscillator length $a_{ho,r} = \sqrt{\hbar/(m\omega_r)}$ that is independent of the local density. While this is true deeply in the 1d regime, defined by $\mu, k_BT \ll \hbar\omega_r$, many atom chip experiments are performed in a regime where the transverse level spacing only slightly exceeds the chemical potential or temperature. In the following, methods to take into account effects in the thus arising 1d-3d crossover regime.

2.4.1. Thermal occupation of transverse states

If k_BT exceeds the radial level spacing, this will lead to thermal population of radial states. Assuming that the number of atoms in each state besides the ground state is low, the excited state population will be incoherent, warranting a description in terms of a set of ideal 1d Bose gases in each state. In this case, we can use an approach employed in reference [97]. The total atom number in excited states is assumed to obey

$$n_r(z;\mu,T) = \frac{1}{\lambda_{dB}} \sum_{j=1}^{\infty} (j+1)\, g_{1/2}\left(\tilde{z}_j\right), \tag{2.68}$$

where $g_{1/2}(\tilde{z})$ is the polylogarithm encountered already in section 2.1.1, and

$$\tilde{z}_j = \exp\left(\frac{\mu_j(z)}{k_BT}\right) \tag{2.69}$$

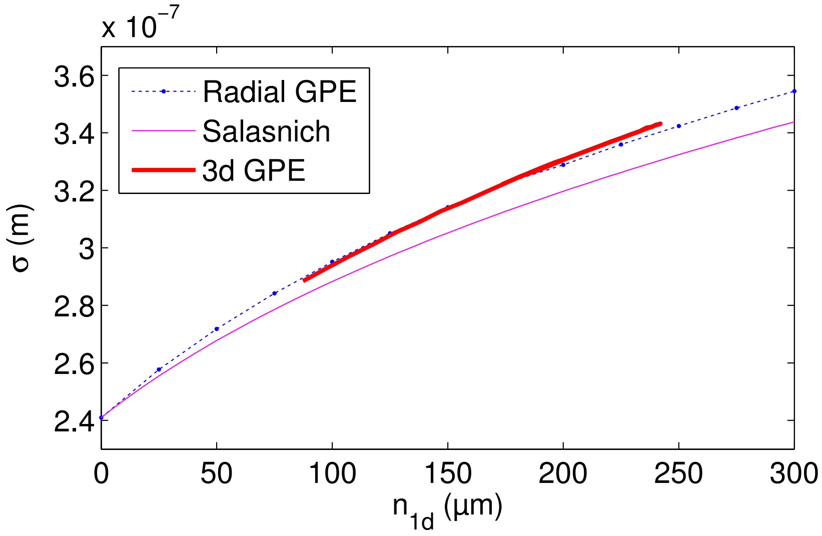

Figure 2.3.: Density dependence of the radial in-situ width of a quasi-1d condensate for a radial trapping frequency of $\omega_r = 2\pi \times 2$ kHz. Pink line: Equation 2.72. Blue dotted line: Results from a radial GPE simulation, as in reference [98]. Red line: Results from a 3d GPE simulation.

is a fugacity for each level j defined by a chemical potential $\mu_j(z)$, which can be calculated as

$$\mu_j(z) = \mu - V(z) - j\hbar\omega_r - 2g_{1d}\left[\left\langle|\psi(z)|^2\right\rangle + n_r(z)\right]. \tag{2.70}$$

Here, the term in square brackets allows to incorporate a mean-field shift by the ground state and overall excited state population, with the effect of pushing thermal atoms away from the axial center of the trap. While the ground state mean-field shift is usually sizeable, the excited state contribution can be neglected in good approximation for $k_B T$ in the order of the radial level spacing.

This approach can be easily implemented numerically. Assuming a fixed overall atom number N, one can start with ground state wave function of N atoms, calculate $n_r(z;\mu,T)$, and then iteratively lower the ground state atom number and update mean-field shifts until one arrives at $[\langle|\psi(z)|^2\rangle + n_r(z)] = N$. Note that we require $\mu_j(z) < 0$ $\forall\ z$, otherwise the polylogarithm $g_{1/2}(\tilde{z}_j)$ diverges. One finds that excited state populations are in the order of a few percent even at temperatures significantly exceeding the radial level spacing. An example can be found in figure 2.4.2.

2.4.2. Interaction-induced swelling of the radial wave function

When interactions seize to be negligible for the radial profile, a density-dependent deformation from a Gaussian shape is expected to be observed. This process is coherent in that it is contained in 3d GPE simulations of elongated trapped atom clouds, and analogous to the transition from a non-interacting Gaussian to a Thomas-Fermi solution for the axial density distribution that has been described in section 2.2.2. For experimental parameters as shown in figure 2.4.2, it actually starts to set in already at the lowest densities $\mu \ll \hbar\omega_r$. The effect is discussed in reference [65], and approximately described by a spatially varying chemical potential

$$\mu \approx \hbar\omega_r \left(\sqrt{1+4an_{1d}}-1\right) \tag{2.71}$$

as well as a ground state wave function that is assumed to be Gaussian, but with a correspondingly scaling density-dependent width

$$\sigma^2 = a_{ho,r}\sqrt{1+2an_{1d}}. \tag{2.72}$$

With increasing densities, this assumption is to gradually break down, however, as one slowly crosses over from a 1d to an elongate 3d system. The scaling of the chemical potential with linear density 2.71 together with the expected deviations from a Gaussian wave function at high densities have been measured within reference [99].[4] As outlined in reference [98] and chapter 5, this transition goes hand in hand with a change of axial breathing frequencies, in excellent agreement with the measurements presented in section 5.2.3.

We can compare the predictions from reference [65] with results from both radial and 3d Gross-Pitaevskii simulations for experimentally relevant parameters. Such a comparison is shown in figure 2.4.2 for a radial trap frequency of 2 kHz, and demonstrates both the validity of the model and its limitations at low and high densities, respectively.

The transverse swelling of the cloud due to a density-dependent chemical potential also affects the density distribution. This effect can be easily accounted for numerically by solving an adapted 1d GPE 2.41 containing the modified chemical potential 2.71:

$$i\hbar\frac{\partial}{\partial t}\psi\left(z,t\right) = \left[-\frac{\hbar^2}{2m}\frac{\partial^2}{\partial_z^2}+\frac{m\omega_a^2 z^2}{2}+\hbar\omega_r\left(\sqrt{1+4aN|\psi(z)|^2}-1\right)\right]\psi\left(z,t\right). \tag{2.73}$$

with total atom number N. The resulting ground state density profile can also be calculated according to [100][5]:

$$n(z) = \frac{\alpha}{16a}\left(1-\frac{z^2}{R^2}\right)\left[\alpha\left(1-\frac{z^2}{R^2}\right)+4\right] \tag{2.74}$$

Here, the radius is defined by $R = \sqrt{\alpha}a_{ho,z}^2/a_{ho,r}$, and the parameter α is given by

$$\alpha^3\left(\alpha+5\right)^2 = \left(\frac{15Naa_{ho,r}}{a_{ho,z}^2}\right)^2. \tag{2.75}$$

---

[4] Note that what is measured in this paper is the interaction energy released during expansion. The comparison with the incorrect ground state width from reference [100] as presented in the paper is in fact misleading.

[5] Note however, a missing prefactor of 1/4 as well as an incorrect result for the ground state radius in reference [100].

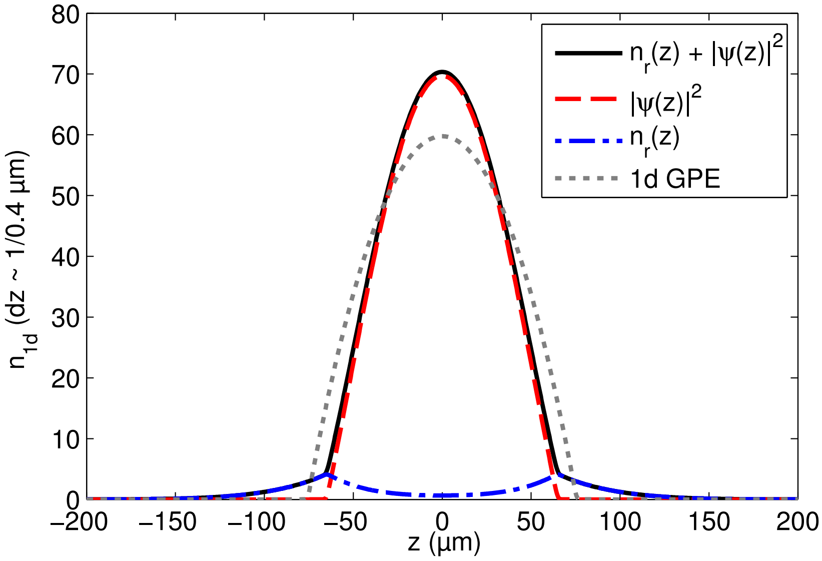

Figure 2.4.: Numerics in the 1d-3d crossover regime for a cloud of $\approx$ 15000 atoms at 75 nK in a trap with frequencies $\omega_a = 2\pi \times 8$ Hz and $\omega_r = 2\pi \times 1000$ Hz. Red dashed line: Ground state density from the modified 1d GPE 2.73. Blue dash-dotted line: Radial excited state population according to the iterative solution of equation 2.68. Black line: Sum of the two contributions. Grey dotted line: Ground state density calculated from the 1d GPE 2.41 for the same total atom number.

Note that numerically, density profiles including both the effect of interaction-induced swelling of the ground state as well as an incoherent excitation of radial excited states can be calculated. As an example, figure 2.4.2 shows the density profile obtained by solving the Gross-Pitaevskii equation 2.73, including a thermal occupation for a temperature of 75 nK at a total atom number of 15000 in a trap with radial and axial frequencies of $\omega_a = 2\pi \times 8$ Hz and $\omega_r = 2\pi \times 1000$ Hz, respectively. The thermal excited state population $n_r(z)$ amounts to approximately 7%. For comparison, the figure contains the ground state profile for the same atomnumber, obtained by the regular 1d GPE 2.41.

2.5. Density correlations in free expansion

The temperature measurements in chapter 5 and 6 use a thermometry method based on the analysis of density fluctuations in free expansion and has been developed and implemented in references [30] and [15], respectively, and the thesis [31] provides a detailed description. Here, the basic idea behind the method and the main results valid for a homogeneous 1d quasicondensate in a thermal state are shortly reviewed as a basis for later chapters.

2.5.1. Density profile in free expansion

The typical initial state of interest is a 1d quasicondensate in the harmonic trap in the radial ground state, and axially in the Thomas-Fermi regime as discussed in the previous section. Hence, the initial density profile is axially parabolic, with a radius of order 100 μm, and radially Gaussian with a width defined by the radial oscillator length $a_{ho,r} < 1$ μm. After switching off the trap, the cloud expands both along the radial and axial dimensions. Radially, the width scales as [101]

$$w_r = a_{ho,r}\sqrt{1+(\omega_r t_{exp})^2}, \tag{2.76}$$

up to small corrections in the 1d-3d crossover regime discussed in section 2.4. The expansion can be separated into a hydrodynamic stage, during which interaction energy is converted into kinetic energy and momentum transfer between axial and radial direction can take place, and a ballistic, non-interacting stage. The characteristic timescale for this separation is given by the inverse trap frequency $t_r = (\omega_r/2\pi)^{-1}$. During this timescale, axial fluctuations corresponding to a length scale of $\Delta z = \xi\mu/\hbar\omega_r$ [30], with the healing length ξ, are affected. For typical densities and trap frequencies in our setup it holds that $\Delta z \leq \xi$, with the result that for phononic excitations and length scales that are experimentally resolvable, the influence of the hydrodynamic stage on axial fluctuations can be neglected and the expansion can be treated as purely ballistic.

Since the interaction energy is almost exclusively converted into radial motion, at experimentally relevant expansion times of $t_{exp} \approx 10ms$, the average mean-field axial density profiles before and after expansion are in good approximation identical in the absence of collective breathing excitations. Phase fluctuations, in the trapped cloud, give rise to a local velocity field:

$$v(z,t) = \frac{\hbar}{m}\nabla\phi(z,t). \tag{2.77}$$

In the absence of interactions during expansion, this velocity field propagates freely, leading to characteristic correlations, also called *density ripples*, in the expanded profile.

2.5.2. Density correlations and thermometry

Since hydrodynamic effects and the transverse dynamics can be neglected, correlation functions after expansion

$$g^{(2)}\left(z_1, z_2; t_{exp}\right) = \frac{\rho\left(z_1, z_2; z_1, z_2; t_{exp}\right)}{n\left(z_1; t_{exp}\right) n\left(z_2; t_{exp}\right)} \tag{2.78}$$

are related to the two-particle density matrix of the trapped system

$$\rho\left(z_3, z_4; z_3', z_4'; 0\right) = \left\langle \hat{\Psi}^\dagger\left(z_3', 0\right) \hat{\Psi}^\dagger\left(z_4', 0\right) \hat{\Psi}\left(z_4, 0\right) \hat{\Psi}\left(z_3, 0\right) \right\rangle \tag{2.79}$$

by free propagators

$$\mathcal{G}_1(z - z'; t_{exp}) = \sqrt{\frac{m}{2\pi\hbar i t_{exp}}} \exp\left(\frac{im\left(z-z'\right)^2}{2\hbar t_{exp}}\right) \tag{2.80}$$

by the general expression given in reference [30]:

$$\rho\left(z_1, z_2; z_1, z_2; t_{exp}\right) = \int dz_3 \int dz_3' \int dz_4 \int dz_4'$$
$$\mathcal{G}_1(z_1 - z_3; t_{exp})\mathcal{G}_1(z_2 - z_4; t_{exp})\mathcal{G}_1^*(z_2 - z_4'; t_{exp})\mathcal{G}_1^*(z_1 - z_3'; t_{exp})\rho\left(z_3, z_4; z_3', z_4'; 0\right) \quad (2.81)$$

In principle, this relation holds for arbitrary known in-situ density matrices. Reference [30] contains the derivation of an analytical expression for $g^{(2)}(x; t_{exp})$ in the for our purposes relevant regime of a weakly interacting homogeneous 1d Bose gas. Using the translation invariance in the homogeneous system, the permutation invariance of the bosonic density matrix, the fact that the two particle-density matrix describing a phase-fluctuating gas can be decomposed in terms of 1-body density matrices by the Wick theorem and substituting the known expression for the thermal first-order correlation function 2.63 as derived in section 2.3.2, an expression for the power spectrum of density fluctuations in expansion is calculated as

$$\frac{\langle|\rho(q)|^2\rangle}{n_{1d}^2\xi} \approx \frac{\lambda_T q - e^{-2\hbar q t_{exp}/m\lambda_T}\left[\lambda_T q\cos\left(\hbar q^2 t_{exp}/m\right) + 2\sin\left(\hbar q^2 t_{exp}/m\right)\right]}{q\xi\left(1+\lambda_T^2 q^2\right)}, \quad (2.82)$$

which is related to the second order correlation function by a Fourier transformation

$$\left\langle|\rho(q)|^2\right\rangle = n_{1d}^2 \int_{\infty}^{\infty} dz\, e^{iqz}\left[g^{(2)}\left(x; t_{exp}\right) - 1\right] \quad (2.83)$$

Probing an approximately homogeneous region in the vicinity of the cloud centre with known density n_{1d} at a known expansion time t_{exp}, either $\langle|\rho(q)|^2\rangle$ or $g^{(2)}(x; t_{exp})$ can be measured as described in section 4.6 and compared to expressions 2.82 or 2.83, with the temperature as only left parameter. Note that this method constitutes a direct measurement of the temperature of phononic excitations within the degenerate system, as opposed to indirect temperature measurements based on the analysis of thermal clouds surrounding the quasicondensate, where equilibrium between the two components needs to be assumed.

Further, note that the method is valid throughout the quasicondensate regime, which is bounded by

$$\frac{k_B T}{\mu} \ll \frac{K}{\pi}, \quad (2.84)$$

where K represents the Luttinger parameter defined in section 2.3.1, which is not very stringent considering values of $K \approx 50$ for experimental parameters. Further, the method is not tied strictly to the 1d regime, since low-energy excitations also behave one-dimensional throughout the 1d - elongated 3d crossover regime, as long as the wavelengths of the considered modes is smaller than the radial oscillator length $a_{ho,r}$. However, hydrodynamic effects during expansion may require a treatment beyond free propagators [102, 86], significantly complicating the analysis.

3. Numerical techniques

> *"People think computers will keep them from making mistakes. They're wrong. With computers you make mistakes faster."*
>
> ADAM OSBORNE, PC PIONEER AND EPONYM FOR THE OSBORNE EFFECT.

Following early results based on the Hartree-Fock and Hartree-Fock-Bogolyubov approach, a review of which can be found in reference [103], and extensions such as the ZNG approach [104], a wealth of techniques to theoretically study both equilibrium properties and dynamics in finite-temperature ultracold Bose gases using a representation based on classical fields has been developed, among them but not limited to the stochastic Gross-Pitaevskii equation (SGPE) [105, 106, 107], the projected [108] and stochastic projected GPE [109] and the truncated Wigner (tW) approach [110, 111]. Some of these c-field methods, as will be seen, even allow to mimic quantum mechanical properties such as spontaneous scattering, although more sophisticated approaches are available for a proper treatment of such effects [112].

The goal of this chapter is to present the basic idea behind these techniques, introduce relevant literature and 'operationally' present the methods used in the context of this thesis, while a rigorous mathematical justification, or the derivation of these methods from the underlying quantum field theory, is left to the references. After a short introduction and overview, the Gross-Pitaevskii equation in 1 and 3 dimensions is briefly discussed, before focusing on the stochastic GPE in 1 dimension, its implementation within the context of this thesis and the calculation of important observables in this framework. Finally, the sampling of phase fluctuations based on an Ornstein-Uhlenbeck process as used for the thermometry scheme from section 4.6 is presented.

3.1. Introduction and Overview

In this section, we follow references [22] and [23], which provide comprehensive reviews of the different c-field techniques available for the simulation of ultra-cold Bose gases, while the latter also serves as a highly recommended pedagogical introduction to the topic. At the heart of these models lies an effective Hamiltonian in second quantization, written in terms of field operators:

$$\hat{H}_{eff} = \int d^3r \hat{\Psi}^\dagger\left(\boldsymbol{r},t\right)\hat{H}_{sp}\hat{\Psi}\left(\boldsymbol{r},\boldsymbol{t}\right) + \frac{g_{eff}}{2}\int d^3r \hat{\Psi}^\dagger\left(\boldsymbol{r},t\right)\hat{\Psi}^\dagger\left(\boldsymbol{r},t\right)\hat{\Psi}\left(\boldsymbol{r},t\right)\hat{\Psi}\left(\boldsymbol{r},t\right). \quad (3.1)$$

Here, the single-particle Hamiltonian is given by

$$\hat{H}_{sp} = -\frac{\hbar^2}{2m}\Delta + V_0(\boldsymbol{r}). \tag{3.2}$$

The usual starting point to treat condensates is to separate the bosonic field operator into two parts representing a condensate and non-condensed component

$$\hat{\Psi}\left(\boldsymbol{r}, t\right) = \phi_0\left(\boldsymbol{r}, t\right) + \hat{\delta}(\boldsymbol{r}, t) \tag{3.3}$$

where $\phi_0\left(\boldsymbol{r}, t\right)$ is treated as a classical object, while the non-condensed component remains represented by an operator. Subsituting this ansatz into 3.1 yields a lengthy Hamiltonian with various terms coupling the condensed and non-condensed components. Depending on which terms are kept and neglected, one arrives at different effective Hamiltonians defining limits with their respective validity range, like the Hartree-Fock or Hartree-Fock-Bogolyubov limits, as summarized for instance in [103, 23], allowing a self-consistent solution.

For quasicondensates, a separation like 3.3 is problematic, since one faces a situation with many highly occupied modes. Therefore, we are looking to treat the system in a picture where the field operator is represented in terms of an expansion

$$\hat{\Psi}\left(\boldsymbol{r}, t\right) = \sum_{n<n_\Lambda} \hat{a}_n \phi_n(\boldsymbol{r}, t). \tag{3.4}$$

Here, we have introduced a cut-off scale defined by the momentum:

$$\hbar k_\Lambda(\boldsymbol{r}) \approx \sqrt{2m\left(E_{max} - V_0(\boldsymbol{r})\right)}, \tag{3.5}$$

where E_{max} represents the corresponding maximum energy. By neglecting modes above the cut-off, in other terms below a certain length scale, the field operator defined by 3.4 is *coarse-grained.* Such a cut-off is inevitable since any numerical representation involves a discretisation of the problem at some scale.

Cut-off and effective coupling constant. In general, the effective coupling constant depends on the choice of the cut-off [74]. With respect to the problem at hand, this dependence is discussed in [111]. If the cut-off is taken far below the momentum scale defined by the inverse scattering length a^{-1}, this dependence can be neglected and the effective coupling constant can be chosen as $g_{eff} = 4\pi a\hbar^2/m$ as for the GPE [113]. Of course, the cut-off should be taken high enough not to remove modes with a sizeable population due to interaction or thermal energy, i.e. $E_{max} > k_B T, \mu$. Note that the most simple way to provide a cut-off is via the resolution of the numerical grid such that $\hbar k_\Lambda = 2\pi\hbar/\Delta x$. More refined methods involve an additional projector to split the mode spectrum below E_{max} into an incoherent and c-field region to explicitly select not only an energy scale but also a preferred basis for the projection, and allow to treat the incoherent region by a quantum kinetic approach as summarized in [22].

Equation of motion and c-field approximation. The Heisenberg equation for the field operator $\hat{\Psi}\left(\boldsymbol{r}\right)$, for the moment neglecting the subtleties introduced by finite-size effects on the definition of the δ function on a grid (see for instance [111, 22]), writes as

$$i\hbar\frac{\partial\hat{\Psi}(\boldsymbol{r},t)}{\partial t}=\left[\hat{H}_{sp}+g_{eff}\hat{\Psi}^{\dagger}\left(\boldsymbol{r},t\right)\hat{\Psi}\left(\boldsymbol{r},t\right)\right]\hat{\Psi}\left(\boldsymbol{r},t\right). \tag{3.6}$$

Simply replacing the field operator by a single complex wave function $\Psi(\boldsymbol{r})$ (see for example [32]) yields the 3d GPE. In a sense, this introduces the most simple, single-mode, c-field approach.

To include excitations in the treatment, the field operator can be approximated by a multimode classical field

$$\hat{\Psi}\left(\boldsymbol{r},t\right)\approx\Psi\left(\boldsymbol{r},t\right)=\sum_{n<n_{\Lambda}}a_{n}\phi_{n}(\boldsymbol{r}),t \tag{3.7}$$

where a_n are given by c-numbers. The use of the representation 3.7 to solve equation 3.6 is the common denominator of all the different c-field techniques.

Truncated Wigner (tW) approach. Starting point is the von Neumann equation for the time evolution of the system's density operator

$$i\hbar\frac{\partial\hat{\rho}}{\partial t}=\left[\hat{H},\hat{\rho}\right]. \tag{3.8}$$

By using the relation between density operator and the Wigner distribution as outlined in [111] and [22], 3.8 can be mapped to a equation of motion of the Wigner distribution. While the reader is referred to the references for these steps, in this context it is important that it is possible, by neglecting third-order derivatives, to map this equation on a Liouville equation for the Wigner distribution without diffusion term, or equivalently, on a 'stochastic' partial differential equation for a single realization of the field $\Psi(\boldsymbol{r},t)$. Solving the former is then reduced to solving the latter for a sufficiently large sets of different realizations of $\Psi(\boldsymbol{r},t)$, with initial conditions sampled from the Wigner distribution. This is the *truncated Wigner* approach, and the 'stochastic' equation has the same shape as the regular GPE:

$$i\hbar\frac{\partial}{\partial t}\Psi(\boldsymbol{r},t)=\left[H_{sp}+g|\Psi(\boldsymbol{r},t)|^{2}\right]\Psi(\boldsymbol{r},t) \tag{3.9}$$

Originally, this approach goes back to work presented in [110]. Different methods of sampling the Wigner distribution are presented in references [111] and [22]. A straightforward way for a homogeneous Bose gas is to perform the c-field expansion 3.7 in terms of Bogolyubov modes obtained by solving the Bogoliubov-de Gennes equations, ideally incorporating the external potential. For correctly sampled initial conditions, all modes below the cut-off are occupied with on average half a particle of 'quantum' noise. This allows to mimic spontaneous scattering by the fact that all modes contain a weak seed for stimulated scattering. On the flip side, time evolution with the Gross-Pitaevskii equation leads to thermalisation into a classical equilibrium state at higher temperature than the initial state due to this excess noise [111]. Depending on the parameter range and dimensionality of the system, this process limits the timescale of validity for the simulations.

Classical field method and PGPE. Here, one also uses a decomposition of the form 3.7. Initial sates are not sampled from a Wigner function, but from some classical distribution, and the propagation is performed with a GPE, as in the truncated Wigner approach. Historically, this method has been used in the limit of large occupation numbers for all modes (i.e. high temperature) [114], and for 3d systems, where fast equilibration rates due to mode mixing render the method fairly independent of the exact initial state. References [115] and [108, 116] constitute examples for this method. The latter introduces the so-called projected GPE (PGPE). Here, the c-field is split into a classical and incoherent region

$$\Psi\left(\boldsymbol{r},t\right)=\sum_{n<n_c}a_n\phi_n^{(c)}(\boldsymbol{r},t)+\sum_{n_c<n<n_\Lambda}a_n\phi_n^{(I)}(\boldsymbol{r},t), \tag{3.10}$$

and the time-evolution is performed with a GPE involving a projector onto the classical region to ensure a well-defined cut-off.

Stochastic GPE and stochastic projected GPE (SPGPE). Stoof and co-workers [105, 106] as well as Gardiner and co-workers [107, 109, 117] arrived independently at very similar stochastic generalisations of the classical field approach. Reference [107] presents a way to derive an evolution equation for the Wigner function including second-order terms, that in the truncated Wigner approximation reduces to a Fokker-Plank equation with diffusion term, and equivalently a stochastic differential equation including noise terms. In its most general form, a numerical implementation has only been realized recently [117]. A different approach promoted in reference [23] would be an explicit coupling of a quantum Boltzmann equation to replace the noise and damping terms in the SGPE, similar to the ZNG approach [104], where the former is coupled to a single-mode BEC. Such an approach would allow to include quantum noise and dynamics of the thermal component but has proven to be elusive so far.

The most simple, and so far most common approach consists of neglecting collisions between incoherent and coherent region without particle exchange, and leads to Stoof's SPGE as presented in [118], or equivalently the simple-growth SGPE [22] which will be introduced in section 3.3.

3.2. Gross-Pitaevskii equation

There are many different options to solve partial differential equations numerically (for examples from quantum optics, see [119]). In the following, simple ways to solve the 1d and 3d GPE are presented, serving as a basis for more sophisticated approaches if necessary. For ways minimizing the error per time-step or maximizing computational efficiency, for instance by higher order propagation methods, the reader is referred to literature, where possible.

Gross-Pitaevskii equation

As introduced in section 2.2.2, the 1d GPE has the form:

$$i\hbar\frac{\partial}{\partial t}\psi\left(z,t\right)=\left(-\frac{\hbar^2}{2m}\frac{\partial^2}{\partial_z^2}+V\left(z,t\right)+g_{1d}\cdot\left|\psi\left(z,t\right)\right|^2\right)\psi\left(z,t\right). \tag{3.11}$$

The GPE lends itself to a solution by a split-operator method. A discretised forward propagation is given by

$$\psi(x,t+\Delta t)=e^{-iH\Delta t/\hbar}\psi(x,t), \tag{3.12}$$

where $e^{-iH\Delta t/\hbar}=U(\Delta t)$ is the time-evolution operator. The Hamiltonian of interest is of the form

$$H=T(p)+V(z,t)+V_{int}(z,t), \tag{3.13}$$

with $V_{int}(z,t)=g_1d\cdot\left|\psi\left(z,t\right)\right|^2$. Here, $T(p)$ is diagonal in the momentum basis, while $V(z,t)+V_{int}(z,t)$ is diagonal in the momentum basis. While this complicates the direct calculation of 3.12, one can split the time evolution as follows,

$$\begin{aligned}\psi(z,t+\Delta t)=&\ e^{-i\Delta t(V(z,t)+V_{int}(z,t))/2\hbar}\\&\times\mathcal{F}^{-1}\left[e^{-i\Delta tT(p)/\hbar}\mathcal{F}\left[e^{-i\Delta t(V(z,t)+V_{int}(z,t))/2\hbar}\psi(z,t)\right]\right],\end{aligned} \tag{3.14}$$

alternating between propagation in position and momentum space for the potential and kinetic operators, respectively, where $\mathcal{F}\left[\psi\right]$ denotes the Fourier transform. The reasoning for the symmetrized splitting

$$U(\Delta t)\rightarrow U_V(\Delta t/2)U_T(\Delta t)U_V(\Delta t/2) \tag{3.15}$$

becomes clear when considering that $T(p)$ and $V(z)$ do not commute, and the decomposition of $H(z,p)$ is given by the Baker-Campbell-Hausdorff formula

$$e^Te^V=\exp\left(T+V+\frac{1}{2}\left[T,V\right]+\frac{1}{12}\left[T,\left[T,V\right]\right]+\frac{1}{12}\left[\left[T,V\right],V\right]\right), \tag{3.16}$$

with the result that the symmetrized version in principle yields an error of order $\mathcal{O}\left(\Delta t^3\right)$, while for the two-step splitting we have $\mathcal{O}\left(\Delta t^2\right)$ [119]. However, this is only true when disregarding the dependence of V_{int} on the wave function $\psi(z,t)$. Taking it into account yields an overall error of $\mathcal{O}\left(\Delta t^2\right)$ for the symmetric splitting. Note that higher-order methods for the GPE, among other types of equations, have been presented in reference [120]. The time-dependence of the potential (or also the interaction constant g_{1d}) is realized by simply updating it at each time-step.

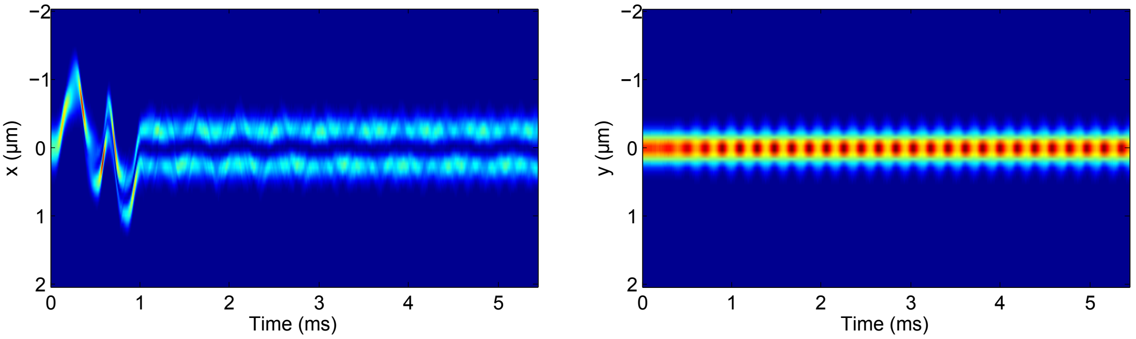

(a) Time evolution along x - direction (b) Time evolution along x - direction

Figure 3.1.: Dynamics of the transverse density profile calculated with a 3d GPE simulation during and after excitation into the second excited state along x-direction by an optimal control pulse on the trap position along the x-direction, similar to reference [121], but with shorter ramp times. (a) Carpet plot of the density profile along the x-direction parallel to the chip surface. One can see the minimum in the center characteristic for depletion of the ground state, and residual dynamics. (b) Carpet plot of the density profile along the y-direction normal to the chip surface. The excitation of a breathing mode is apparent. Parameters: 700 atoms, $\omega_x/2\pi = 1.83$ kHz, $\omega_y/2\pi = 2.58$ kHz, with a quartic contribution identical to [121]. Grid: $n_x = n_y = n_z = 64$ points, $(r_x, r_y, r_z) = (2, 2, 50)$ μm, $dt \approx 1$ μs.

Ground state calculation. The ground state can be calculated from an arbitrary initial state $\psi_0(z,t)$ by imaginary time evolution, performing the same steps as outlined above but with $\Delta t \rightarrow i\Delta t$. Effectively, the time-evolution operator becomes real, introducing losses depending on the local interaction and potential energy. Upon renormalization of the wave function at each timestep and iteration, the minimal-energy ground state profile is recovered. A good measure for convergence to the ground state is the overlap $\langle \psi(z,t), \psi(z,t+\Delta t) \rangle$ between wave functions at different timesteps converging against unity. In addition, subsequent real-time evolution in a stationary trap at constant atom number should yield a stationary wave function.

Note that both imaginary and real-time propagation are implemented in the same way for the quasi-1d GPE 2.73 presented in section 2.4. Proper choice of grid size and resolution is usually not as critical as for the 3d GPE or the SGPE discussed in later sections. Crosschecks for proper performance consist of tracking kinetic, interaction and total energy throughout the time evolution, or the overlap between initial and final wave function during real-time propagation in a static trapping potential at constant atom number. Examples for the use of 1d and quasi-1d GPE simulations are found within sections 2.4, to estimate the breathing dynamics in a time-dependent potential in section 5.2 and for the optimal control scheme presented in section 6.4.

3d Gross-Pitaevskii equation

For the 3d GPE 3.9, the same principles apply as for the 1d case. The only difference is that calculations are more memory-intensive since all quantities live on a 3d grid. In the context of this thesis, a 3d GPE simulation has been used to calculate the scaling of the trapped radial ground state width with the linear density n_{1d} for comparison with analytical results in section 2.4. Unrelated to the work presented in this thesis, 3d simulations of a atom cloud in a radially anharmonic, anisotropic trap that is subject to an optimal control pulse to transfer atoms from the radial ground state to the second excited state have been performed for comparison with corresponding transverse 1d simulations and experiment. Earlier experiments on this topic can be found in [121]. The goal was to identify whether a potential coupling between the transverse degrees of freedom influence the dynamics. Figure 3.1 show results for an excitation sequence at typical experimental parameters.

3.3. Stochastic Gross-Pitaevskii equation

In the context of this thesis, an easy-to-implement version of the SGPE as developed by Stoof in [105, 106], and subject as well as tool for ongoing studies in the group of Proukakis [114, 122, 123, 124, 125] in one dimension. It is equivalent to the so-called 'simple growth' SGPE as studied in [107, 109, 22] is given by a Langevin equation of the form

$$i\hbar\frac{\partial\psi(z,t)}{\partial t} = (1-i\gamma)\left[H_{GP}-\mu\right]\psi(z,t)+\eta. \tag{3.17}$$

Here, μ denotes the chemical potential, and H_{GP} is given by the regular 1d Gross-Pitaevskii Hamiltonian,

$$H_{GP} = -\frac{\hbar^2}{2m}\frac{\partial^2}{\partial z^2}+V(z,t)+g_{1d}|\psi|^2. \tag{3.18}$$

while γ and η are damping and noise coefficients that encode the coupling of the classical field to a thermal bath with chemical potential μ and temperature T. Within this approach, γ and η are related by a classical fluctuation-dissipation relation

$$\langle\eta^*(z,t)\,\eta(z',t')\rangle = 2\hbar k_B T\gamma\delta(t-t')\,\delta(z-z'). \tag{3.19}$$

A detailed discussion of the damping term's spatial dependence can be found in the thesis [126], based on the results from reference [127]. As discussed in the same thesis however, and in reference [22], the spatial dependence has little influence on an equilibrium state generated by the SGPE [22]. Therefore, it is common to neglect it and choose a constant bare rate

$$\gamma = \gamma_b = \kappa\frac{4mk_BT}{\pi}\left(\frac{a}{\hbar}\right)^2. \tag{3.20}$$

The pre-factor κ is not specified, whereas values of $\kappa \approx 3$ have been reported to yield good agreement with analytically calculated damping rates in different settings [22]. A discussion of γ in the context of our experiments is found in the following section.

Note that dropping the noise-term yields the dissipative GPE that has been previously used to study damping processes (see [23] and references therein).

3.3.1. Why SGPE?

The starting point for most experiments is a quasicondensate in a thermal state, which is experimentally generated by condensation from a 3d thermal cloud, where thermalisation takes place at least as long as the surrounding cloud is present. Once fulfilling the 1d conditions 2.30, the system is described by the integrable Hamiltonian 2.32, hosting a large number of conserved quantities. Even in the presence of a harmonic trap, which breaks the mathematical integrability of the Lieb-Liniger Hamiltonian, thermalization times are expected to be long in terms of experimentally relevant time-scales.

Preparation of a thermal state. For c-field calculations in 3d systems, it is often sufficient to provide initial fluctuations with the correct amount of energy, and rely on intrinsic thermalisation to provide a thermal state, as discussed for the example of the PGPE method in reference [23]. For the reasons stated above, this is not practicable for 1d systems. Having found that correlation functions used for thermometry as discussed in section 2.5 and 4.6 are very sensitive to non-thermal initial states, it is therefore crucial to avoid sizeable deviations from a thermal state for the initial conditions in simulations, which requires picking the correct basis to populate with thermally distributed quasiparticle excitations. While this is straightforward for the homogeneous system and the corresponding plane-wave basis, a trapped gas necessitates solving the Bogolyubov-de Gennes equations as proposed in [111, 22]. The SGPE, in constrast, intrinsically provides a correct thermal initial state by the simulated coupling to an external heat bath, for arbitrary trapping potentials. As discussed within section 3.3.3, such a state can then be propagated by a regular GPE-Hamiltonian just as in other c-field approaches.

Equilibrium state Taking into account the interaction of the c-field with the thermal bath by the fluctuation-dissipation theorem 3.19 leads to a classical Rayleigh-Jeans distribution. While in 1d, no ultraviolet divergence appears and the distribution is well defined in the high-energy limit, there still exists a cut-off dependent difference to the correct Bose-Einstein distribution. In contrast, sampling of the Wigner function as performed in the truncated Wigner approach yields the correct Bose-Einstein distribution of initial excitations, as mentioned in section 3.1. This difference is most strongly pronounced a scenario where a significant amount of atoms is distributed among many modes with low occupation numbers per mode, but at temperatures below T_D. Revisiting the phase diagram of section 2.2.1, this happens as one crosses over to the decoherent quantum regime. Within the quasicondensate regime, as will be seen in section 3.3.5, most atoms are in modes with average population numbers per mode $\langle n_j \rangle >> 1$, and the differences between Bose-Einstein and Rayleigh-Jeans distribution are usually negligible.

Accordingly, the SGPE accommodates only thermal population of modes, in contrast to the truncated Wigner method. This is important when considering simulations where scattering from the c-field into high-momentum modes k with $E_k \gg k_B T$ is important. As mentioned in section 3.1, the quantum noise present in the tW initial state provides a weak seed in each mode allowing to mimic spontaneous scattering, which will be suppressed for processes involving thermally unpopulated modes using an SGPE initial state. On the other hand, the classical state is the correct equilibrium state with respect to propagation with the GPE Hamiltonian. This means that exactly in scenarios where the 'quantumness' of the tW method is important, the effect of re-thermalisation into a classical equilibrium state will be sizeable [111], so care has to be taken that the time-scales in simulations, where this process becomes important, are not exceeded.

A detailed comparison between the SGPE as presented here, and a number-conserving truncated Wigner approach can be found in reference [123].

3.3.2. Implementation

For the actual implementation, in principle the use of a split-operator method as presented in section 3.2 is thwarted by the additive noise term in equation 3.17. In 1d, however, it is in good approximation possible to separate the time evolution of the dissipative part of 3.17 from the subsequent addition of noise to the wave function. For the dissipative time evolution step, note that there is no distinction between imaginary and real time evolution. Rather, due to the prefactor $(1 - i\gamma)$ on the r.h.s. of equation 3.17, the time evolution is promoted by

$$U\left(\Delta t\right) = e^{-(\gamma+i)\Delta t (H_{GP}-\mu)/\hbar}, \tag{3.21}$$

and hence complex, which does not hinder a decomposition as performed in equation 3.14, though. The noise term can be implemented as

$$\psi(z,t) = \psi(z,t) + \frac{\mathcal{R}(z) + i\mathcal{R}'(z)}{\sqrt{2}}\sqrt{\frac{\eta dt}{\hbar^2 dz}}, \tag{3.22}$$

with $\eta = 2\hbar k_B T \gamma$ [126], and $\mathcal{R}(z), \mathcal{R}'(z)$ denoting vectors containing Gaussian random numbers.

While for the 1d simulations performed in the course of this thesis, using a time-evolution in this manner created equilibrium states at correct temperatures for all used observables, implementations in 2d and 3d are expected to suffer from the approximate treatment of the noise term, and a proper implementation as outlined in the appendix of thesis [126] should be adopted.

Choice of grid parameters. For Stoof's SGPE approach, the cut-off is not explicitly defined in terms of a projector, but by the grid resolution. Due to the convergence of the Rayleigh-Jeans distribution in the UV limit, the 1d SGPE is fairly insensitive to the exact choice of the cutoff. However, following the analysis performed in [126], and the physical picture that the noise and damping terms encode scattering of the c-field with atoms from a thermal bath at temperature T, a reasonable choice is

$$E_g = \left(\frac{2\pi}{\Delta x}\right)^2 \frac{\hbar^2}{2m} = k_B T, \tag{3.23}$$

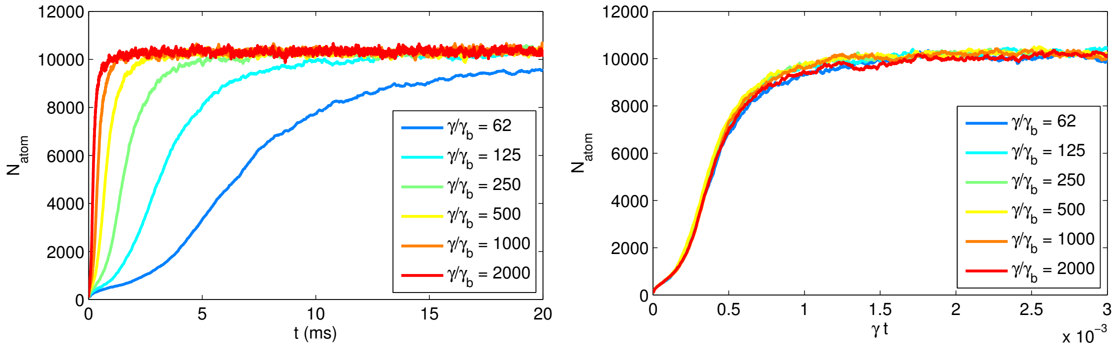

(a) Quasicondensate growth: real time (b) Quasicondensate growth: rescaled time

Figure 3.2.: Quasi-BEC growth at different values of γ in units of the bare rate 3.20 at $\kappa = 3$, atom number $N \approx 10000$, temperature: $T = 50$ nK and trap frequencies of $\omega_r = 2\pi \times 1000$ Hz, $\omega_a = 2\pi \times 12$ Hz in (a) real time, (b) rescaled time units $\gamma \cdot t$.

where E_g denotes the maximum energy corresponding to a grid with a resolution of Δx, which consequently is given by the thermal de Broglie wavelength

$$\Delta x_\Lambda = \lambda_{dB}. \tag{3.24}$$

The grid size L for a trapped system is simply chosen to accommodate the full atom cloud on the grid, or in other words, so that the density at the edge of the grid is vanishing. These choices are used for all the simulations presented within this thesis.

3.3.3. Choice of γ and growth of the quasi-BEC

Equation 3.17 does not take into account the full interaction between c-field and thermal bath, neglecting scattering terms contained in the SPGPE [117]. Further, neither is a full ab-initio calculation of γ for the interaction of a 1d quasicondensate with a surrounding 3d thermal cloud available, nor a corresponding model taking into account the dynamics of the thermal cloud. While one could possibly match γ by the prefactor κ to experimentally observed damping rates, a cleaner approach consists of using the SGPE only to provide an initial equilibrium state, while performing the subsequent time-evolution of the c-field with the regular GPE Hamiltonian, without noise or damping. Experimentally observed sources for damping can then be discriminated from the internal dynamics of the simulated c-field. For such an approach, which is dubbed $SGPE_{eq}$ in the thesis [126] and which has been previously used for instance to study the dynamics of condensate formation in atom chip traps [114], it is interesting to note that the choice of the damping rate γ only determines the time-scale of equilibration, but not the general growth dynamics or the resulting equilibrium state [126]. As a consequence, as long as the goal is purely to prepare an equilibrium state, one is free to choose a value of γ leading to equilibration within the shortest amount of computation time for any given trapping geometry. To demonstrate this, figure 3.2 shows a comparison for the

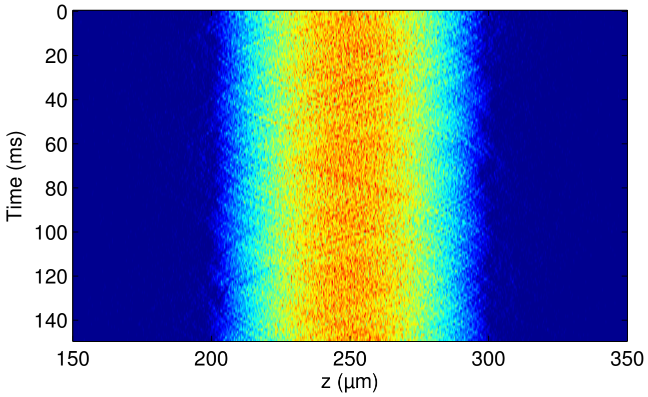

Figure 3.3.: Density profiles during time evolution of a single state generated by the SGPE. Parameters: $\omega_a = 12$ Hz, $\omega_r = 1000$ Hz, $N \approx 10000$, $T = 50$ nK.

quasi-BEC growth at different values of γ, given in units of the bare value 3.20 at $\kappa = 3$, with an equilibrium atom number of $N \approx 10000$, a temperature of $T = 50$ nK and trap frequencies of $\omega_r = 2\pi \times 1000$ Hz and $\omega_a = 2\pi \times 12$ Hz. Plotting the atom number in the quasi-BEC against real time yields the growth curves from figure 3.2(a), while rescaling time with γ reveals the universal growth behaviour from figure 3.2(b). Temperature measurements as presented in the next section yield the same results regardless of the exact value of γ.

3.3.4. Time evolution and temperature

As stated in the previous section, initial states created by the SGPE are propagated without damping or noise for the simulations performed in the context of this thesis, analogous to other c-field methods. Figure 3.3 shows a carpet plot of in-situ density profiles corresponding to a state propagated for 150 ms with the same parameters as used for the growth-simulations presented in the previous section ($\omega_a = 12$ Hz, $\omega_r = 1000$ Hz, $N \approx 10000$, $T = 50$ nK).

To estimate the temperature, we employ two different methods. First, the thermometry scheme used to analyse experimental data based on density correlations in free expansion as presented in sections 2.5 and 4.6 can be employed. Performing time-evolution with a free propagator for experimental free expansion times and convolution with the imaging system's point spread function yields density profiles that can be subjected to the same analysis as experimental data. The results of such a procedure for a set of 240 different realisations at identical parameters is shown in figure 3.4(a), plotting the temperature against propagation time, where 0 denotes the point in time where the coupling to the heat bath given by γ and η is removed. It shows that the temperature indeed corresponds to the set value, and that it is stationary during propagation, apart from small random fluctuations. The inset contains the density correlation functions of the

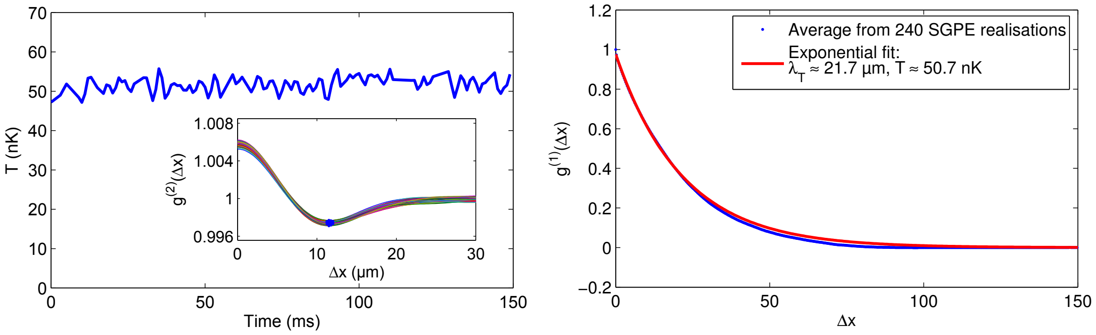

(a) Temperature: Density ripples. (b) Temperature: $g^{(1)}(\Delta z)$ in-situ

Figure 3.4.: Temperature estimation for c-fields. (a) Results of density ripple thermometry over 150 ms of time evolution for a set of 240 independent realisations generated by the SGPE (blue line). Inset: Corresponding density autocorrelation functions $g^{(2)}(\Delta z)$ of simulated profiles after 10 ms of free expansion. Parameters: ($\omega_a = 12$ Hz, $\omega_r = 1000$ Hz, $N \approx 10000$, $T = 50$ nK). (b) First order autocorrelation function $g^1(z, 0)$, for a single point in time at otherwise identical parameters as in (a) (blue dots), fitted by an exponential (red line) for comparison with the theory presented in section 2.3.2. The temperatures estimated by both methods agree within fluctuations.

expanded profiles used to extract the temperature. Alternatively one can calculate the first order correlation function $g^{(1)}(z = 0, z') = g^{(1)}(\Delta z)$ and compare it with the analytical result for the homogeneous case 2.63, substituting an average density

$$\bar{n} = \frac{1}{2R_{TF}} \int\limits_{|z|<R_{TF}} dz\, n(z). \tag{3.25}$$

A typical result of this method is shown in figure 3.4(b), comparing the averaged first order correlation function obtained from 240 SGPE realizations with an exponential fit for a single time-step, yielding a temperature consistent with density ripple thermometry and the set temperature.

3.3.5. Density matrix and mode occupation

In addition to the first order correlation function $g^{(1)}(z = 0, z') = g^{(1)}(\Delta z)$, it is also possible to extract the one-body reduced density matrix defined by equation 2.16

$$\rho^{(1)}\left(z, z'\right) = \left\langle \hat{\Psi}^{\dagger}\left(z\right) \hat{\Psi}\left(z'\right) \right\rangle \tag{3.26}$$

from a sufficiently large set of independent realisations of SGPE solutions at identical parameters. Let us revisit the definition of the c-field as superposition of eigenmodes given by equation 3.7, that writes for the 1d system under consideration:

$$\Psi\left(z, t\right) = \sum_{n<n_{\Lambda}} a_n \phi_n(z, t). \tag{3.27}$$

Here, $\phi_n(z,t)$ denote a set of orbitals with constant occupation numbers, diagonalising the classical representation of the field operator $\Psi(z,t)$. Now consider an ensemble of random realisations of fields $\psi_n^r(z,t)$ generated by the SGPE. Such a set can also be considered as basis that can be used to construct $\Psi(\boldsymbol{r},t)$. Considering an arbitrary point in time, we can hence construct the instantaneous density matrix

$$\rho^{(1)}(z,z') = \left\langle \hat{\Psi}^\dagger(z)\,\hat{\Psi}(z') \right\rangle \approx \langle \Psi^*(z)\,\Psi(z') \rangle \tag{3.28}$$

simply by writing $\Psi(z)$ as a matrix containing all realisations $\psi_n^r(z)$ and substituting into the r.h.s of equation 3.28. Diagonalising $\rho^{(1)}(z,z')$ then yields its representation in terms of the orbitals $\phi_n(z,t)$ and corresponding occupation numbers $|a_n|^2$. According to the Penrose-Onsager criterion introduced in section 2.1.2, the highest occupied orbital can be identified as the phase-coherent condensate mode, and is in good approximation given by [123]

$$n_{PO}(z) = n(z)\sqrt{2 - g^{(2)}(0,z)}\,g^{(1)}(0,z). \tag{3.29}$$

with the total density profile $n(z)$.

To obtain the quasicondensate fraction, one can rely on the definition of the component of the field for which density fluctuations are suppressed, given in [128] and defined by

$$n_{qc} = \sqrt{2\left\langle |\Psi(z)|^2 \right\rangle^2 - \langle |\Psi(z)|^4 \rangle}, \tag{3.30}$$

again adopting the definition of $\Psi(z)$ in terms of the initial random realisations $\psi_n^r(z)$. Note that this expression contains the Penrose-Onsager mode. The thermal fraction simply corresponds to the residual atoms.

Figure 3.5 presents such a decomposition obtained from an ensemble of 1200 independent realisations of SGPE solutions. Figure 3.5(a) contains the spatial distribution of atoms in the Penrose-Onsager mode, in quasicondensate modes different from the PO-mode, and the residual thermal fraction for a cloud of 10000 atoms at a temperature of 100 nK in a trap characterised by $\omega_a/2\pi = 10$ Hz and $\omega_r/2\pi = 1000$ Hz. Even though the thermal coherence length $\lambda_T \ll R_{TF}$, as extracted by the analyses presented in the previous section, is much smaller than the spatial extension of the cloud given by the Thomas-Fermi radius, more than half of the atoms actually form a true condensate. Most of the residual atoms occupy a comparably small number of modes forming the quasicondensate fraction $n_{qc} - n_{PO}$, whereas only 3% can be considered as fully incoherent atoms due to quantum depletion or sufficiently high kinetic energy.

Since sizeable deviations from a classical Rayleigh-Jeans distribution as discussed in section 3.3.1 are only expected for the small decoherent component, SGPE states can be considered an excellent approximation to experimentally created quasicondensates in a typical atom chip trap.

For completeness, figure 3.5(b) shows the 10 highest occupied modes in the density matrix decomposition of the same cloud as analysed in figure 3.5(a). Note that the

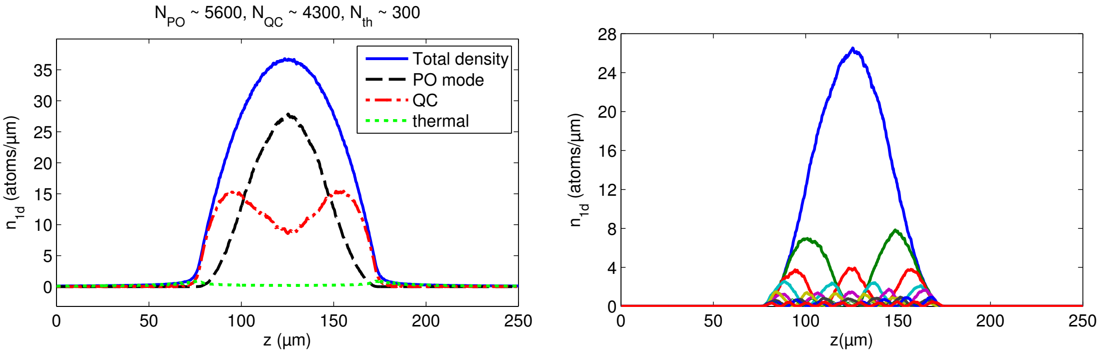

(a) Density matrix: Eigenmode distribution (b) Density matrix: First 10 eigenmodes

Figure 3.5.: Eigenmodes and occupation numbers of the diagonalised simulated one-particle density matrix 3.28 for 10000 atoms at a temperature of 100 nK in a trap characterised by $\omega_a/2\pi = 10$ Hz and $\omega_r/2\pi = 1000$ Hz. (a) Spatial distribution of atoms in the Penrose-Onsager mode (black dashed), in the quasicondensate component without Penrose-Onsager mode (red dot-dashed) and the decoherent component (green dotted). The total density is given by the blue line. (b) Density distribution in the 10 highest populated modes. The blue line again corresponds to the Penrose-Onsager mode. The eigenbasis is well-described by a set of Legendre polynomials as used in section 2.3.1.

eigenmodes are described in good approximation by a basis of Legendre polynomials as obtained in terms of the inhomogeneous Luttinger liquid description introduced in section 2.3.1.

3.3.6. SGPE in the 1d-3d crossover regime

Section 2.4 introduced the modified GPE 2.73 to take into account broadening of the radial ground state profile at high linear densities and its effect on the axial density distribution. As presented in [124] and discussed in detail within the thesis [129], it is straightforward to modify the SGPE 3.17 by introducing the modified interaction term from equation 2.73 into the Hamiltonian 3.18:

$$H_{GP}^{1d3d} = -\frac{\hbar^2}{2m}\frac{\partial^2}{\partial z^2} + V(z,t) + \hbar\omega_r\left[\sqrt{1+4a|\psi|^2} - 1\right]. \qquad (3.31)$$

As discussed within the references cited above, also thermal occupation of transverse excited states can be included by the same method outlined in section 2.4. Due to the already noted low expected atom number in radial excited states at typical experimental parameters, they are neglected for the simulations performed in connection to measurements presented within this thesis.

3.3.7. Applications

Within the context of this thesis, SGPE-based c-field simulations are used to validate the extension of the density ripple thermometry method (see section 2.5) to breathing clouds, as presented in section 5.3.3. In addition, similar simulations are directly compared with experimental data and an analytical model based on the dynamical scale invariance of the 1d GPE in the Thomas-Fermi regime in section 5.3.3. Optimal control ramps as demonstrated within chapter 6 are applied to initial states created by the SGPE to investigate the adiabaticity of these ramps with respect to the excitation spectrum in section 6.5. Finally, the SGPE is used to study the hydrodynamic expansion of quasicondensates in 1d waveguides in 7.

Beyond the scope of this thesis, the approach presented here has been used to study the effect of experimental imperfections on the observation of generalized Gibbs states in coherently split 1d Bose gases [130], evaporative cooling in 1d [81], and the effect of breathing on the analysis of data considering thermalisation in coherently split 1d Bose gases beyond the dynamics predicted by the Luttinger liquid theory [131].

3.4. Phase diffusion & Ornstein Uhlenbeck process

Creating a single solution of the c-field approach presented in the previous section, such as shown in figure 3.3, takes at the point of writing this thesis between a few seconds and a minute, depending on temperature, and therefore grid resolution. Consequently, the time needed for the generation of a set of $\mathcal{O}(100)$ realisations to provide enough statistics for the calculation of correlation functions amounts to several minutes to hours. While this is acceptable for many applications, it is prohibitive for fitting experimental data to extract temperature information. To this end, a simpler and more efficient procedure can be used. Exploiting the circumstance that for thermal excitations, the fluctuations of the phase $\Phi(z)$ are Gaussian [1], the phase profile along z can be described by a stochastic diffusion process first described by Ornstein and Uhlenbeck in 1930 in the context of Brownian motion [132]. Basically, it describes a standard Wiener process with a mean-reverting contribution, preventing long-time (or in our case long-distance) drifts from a certain equilibrium state. A phase profile corresponding to this process can be generated by an updating formula [133]

$$\Phi(z + \Delta z) = \Phi(z) + \sqrt{\frac{\Delta z}{\lambda_T(z)}}\mathcal{R}, \tag{3.32}$$

where $\mathcal{R}$ is given by a Gaussian random number. Starting with an arbitrary phase at some point in the cloud, a set of $\mathcal{O}(100)$ realistic phase profiles can be created within seconds or less. While density fluctuations are neglected in this approach, this is not crucial if the goal is not to propagate the created states by a GPE, but only by free evolution to create time-of-flight profiles, since the strongly suppressed in-situ density fluctuations have little influence on density ripples in expansion. The mean-reverting nature of the Ornstein-Uhlenbeck process prevents long-distance drifts from the average phase coherence length $\lambda_T(z)$. However, this method allows to include the density dependence in the case of inhomogeneous profiles, improving upon the homogeneous result from section 2.3.1.

---

[1] Note that this is consistent with the δ-correlated noise term in the fluctuation dissipation theorem 3.19.

Just as the states generated by the c-field technique, time-of-flight density profiles created by the updating formula can be convoluted with the PSF of the imaging system, so that resulting autocorrelation functions $g^{(2)}(\Delta z; t_{exp})$ can be directly compared with experimental data and hence be used for fitting. More information about this method can be found in [75], which also discusses its application to the case of tunnel-coupled quasicondensates as investigated within our group.

4. Experimental setup & techniques

> *"An experiment is something everybody believes, except the person who made it."*
>
> Albert Einstein, in a conversation with Hermann Mark

After introducing the main concepts of how to trap (4.1) and detect (4.2) ultracold atomic clouds in a typical atom chip setup, this chapter provides a short description of the experimental apparatus used to perform the measurements presented in chapters 5, 6 and 7. The final sections introduce some experimental techniques relevant to these measurements, mainly the characterization of magnetic micro-traps on atom chips (4.5) as well as thermometry of 1d quasi-condensates based on density correlations in free expansion (4.6).

In the course of this thesis, Bose-Einstein condensation has been achieved with this machine. Section 4.4 outlines the experimental sequence leading to condensation in both a macroscopic magnetic trap and a chip trap, discussing the points that were particularly crucial for these steps and presenting early characterisation measurements.

4.1. Magnetic micro-traps on atom chips

The appealingly simple concept of trapping neutral atoms with a single wire [134, 135] and subsequent successful experimental demonstrations [136, 137] have soon led to more advanced designs based on microstructured surfaces, so-called atom chips [138, 139], allowing for high current densities and tight confinement. The realisation of Bose-Einstein condensation in such traps [140, 141] established these devices as one of the main design choices for atom traps. Much information about the fabrication of atom chips as used for the experiments in our group can be found in references [142, 143].

Modern atom chips support wire structures with diameters of a few tens of microns and allow to achieve the tight confinement that is needed to freeze out radial degrees of freedom and realize a 1d system of ultracold atoms. Magnetic trapping with atom chips is an established technique by now, and for detailed information on this topic, the reader is referred to [144, 145, 146, 147, 141, 71]. This section briefly summarizes the basics of magnetic trapping and the different types of traps commonly realized within atom chip experiments.

4.1.1. Magnetic traps

In the following, we consider the interaction of a neutral atom with an external magnetic field. If the field is weak enough to cause a Zeeman shift that is small in comparison with the hyperfine level splitting, F remains a good quantum number and the total angular momentum of the atom is given by $\hat{\boldsymbol{F}}$. The corresponding atom-field interaction Hamiltonian reads:

$$\hat{H}_{int} = -\hat{\boldsymbol{\mu}} \cdot \boldsymbol{B} = g_F \mu_B \hat{\boldsymbol{F}} \boldsymbol{B}, \tag{4.1}$$

with the magnetic moment of the atom $\hat{\boldsymbol{\mu}}$, the Landé-factor g_F, Bohr-magneton μ_B and a magnetic field $\boldsymbol{B} := \boldsymbol{B}(\boldsymbol{r}, t)$. If, further, the atom sees a magnetic field that changes slowly compared to its Larmor frequency, $\dot{\boldsymbol{B}}/|\boldsymbol{B}| \ll \gamma_L$, with $\gamma_L = m_F g_F \mu_B |\boldsymbol{B}|/\hbar$, it will stay in its magnetic sub-state characterized by the quantum number m_F, while the time-dependence of the field only causes an adiabatically varying linear Zeeman-shift. In this case, the interaction Hamiltonian, reduces to

$$\hat{H}_{int} = m_F g_F \mu_B |\boldsymbol{B}| = V_{int}. \tag{4.2}$$

Depending on the sign of $m_F \cdot g_F$, this quantity is minimized either in small or big external fields. Wing's theorem [148] states that the Maxwell equations don't allow the existence of a magnetic field maximum in a source-free region of space, in analogy to Earnshaw's theorem [149] for electrostatics. Hence, atoms can only be trapped in a potential minimum, hence in states satisfying $m_F \cdot g_F > 0$.

Many different technical implementations of magnetic traps have been introduced, as listed in [101]. Most of them address a problem arising in the most simple trap design, consisting of a quadrupole field with a potential minimum at $B = 0$, as created by a pair of coils in anti-Helmholtz configuration. As apparent from the quantity $\dot{\boldsymbol{B}}/|\boldsymbol{B}|$, for $|\boldsymbol{B}| \to 0$ the adiabaticity condition is easily broken, and for $B = 0$, no quantization axis is defined whatsoever. Hence, atoms in the vicinity of such a trap minimum can undergo spin-flips into untrapped m_F states [150]. While loss rates for temperatures far from degeneracy are low, close to the BEC transition when most atoms accumulate near the trap minimum, they become significant. Therefore, different solutions to 'plug' such a hole in the trap have been proposed. One trap that is stable against Majorana losses is the so-called Ioffe-Pritchard trap [151, 152]. It can be described by the field configuration [153]

$$\boldsymbol{B} = B_0 \begin{pmatrix} 0 \\ 0 \\ 1 \end{pmatrix} + B' \begin{pmatrix} x \\ -y \\ 0 \end{pmatrix} + \frac{B''}{2} \begin{pmatrix} -xz \\ -yz \\ z^2 - \frac{1}{2}\left(x^2 + y^2\right) \end{pmatrix}. \tag{4.3}$$

Note that in close vicinity to the minimum, the confinement is always dominated by the second order term of the potential's Taylor expansion, and can be treated as being harmonic. The most commonly used atom chip trap, characterised by a H or Z-shaped wire configuration as shown below, is an example of a Ioffe-Pritchard trap.

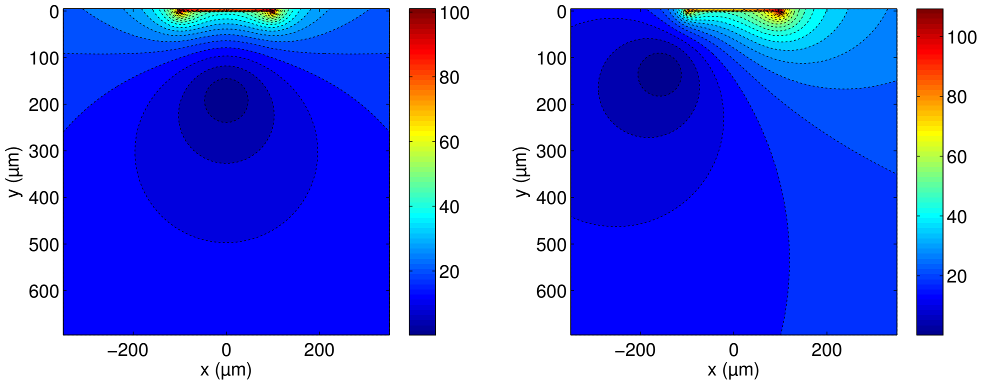

(a) Central trap, $B_b \parallel \boldsymbol{x}$ (b) Edge trap, $B_b \nparallel \boldsymbol{x}$

Figure 4.1.: Side-guide potentials for different bias fields. (a) Cut through a side-guide potential for a rectangular wire with a width of 200 μm, a thickness of 2 μm, a current of $I = 2$ A, and external fields $B_x = 20$ G and $B_y = 0$ G. (b) As (a), but $(B_x, B_y) = (7.07, 7.07)$ G, displaying the minimum shifted towards the edge of the wire structure.

4.1.2. Atom chip traps

A current flowing through a straight wire, in the following assumed along the z-direction of the coordinate system, generates a magnetic field

$$\boldsymbol{B_w}(r) = \frac{\mu_0}{2\pi}\frac{I}{r}\boldsymbol{e_\phi}, \tag{4.4}$$

where ϕ and r denote polar coordinates in the plane perpendicular to the wire and μ_0 the vacuum permeability. In addition, let us impose an additional homogeneous external bias field $\boldsymbol{B_b}$. This will create a region (r_0, ϕ_0), where $\boldsymbol{B_w}$ is exactly offset by the bias field so that $\boldsymbol{B_w(r_0, \phi_0)} + \boldsymbol{B_b(r_0, \phi_0)} = 0$. An atom with magnetic moment $\boldsymbol{\mu}$ in a low-field seeking state, assuming the conditions discussed in section 4.1.1, sees a potential $V = g_F m_F \mu_B |\boldsymbol{B}|$ with a minimum at (r_0, ϕ_0), and hence, a trap. This configuration of an infinitely extended thin wire and a homogeneous bias field is called a *side-guide*, and the trap minimum is a line parallel to the wire at the distance

$$r_0 = \frac{\mu_0}{2\pi}\frac{I}{B_b}. \tag{4.5}$$

Figure 4.1 shows a slice through a realistic side-guide-like potential of a rectangular wire in the (r, ϕ)-, or, equivalently, the (x, y)-plane at an arbitrary axial coordinate z. The wire has a width and thickness of $\delta x = 200$ μm and $\delta y = 2$ μm and is situated at the upper edge of the plots. Colors show absolute field values $|\boldsymbol{B}|$ in Gauss, as indicated by the colorbars. Figure 4.1(a) displays the commonly used case of bias field oriented in parallel to the chip plane, in our case corresponding to the x-axis.

In figure 4.1(b), the bias field is rotated to exhibit a finite y-component. This shifts the trap minimum towards the edge of the wire. Such a configuration allows to create traps with tight confinement in the vicinity of the edge regions of macroscopically big current carrying structures, which will be useful in a new experimental setup built in our laboratory at the moment of writing this thesis, and introduced in chapter 8.

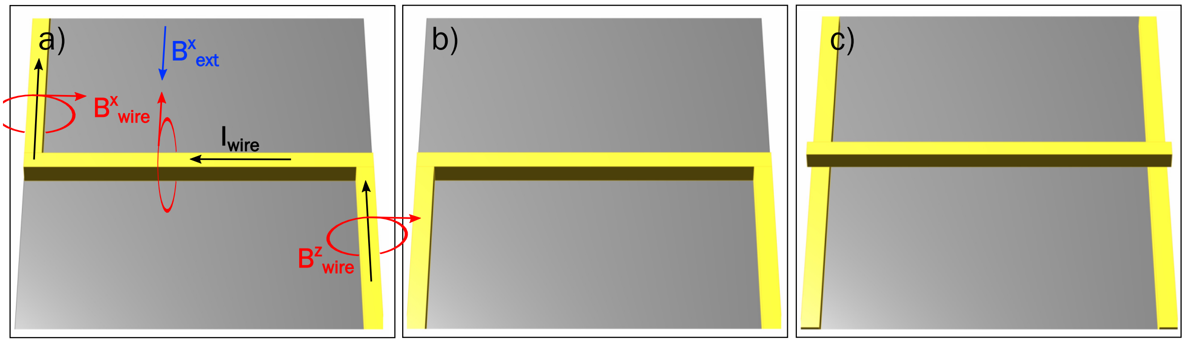

Figure 4.2.: Common wire traps. (a) Z-trap. The central wire piece together with the offset field B^x_{ext} creates a side-guide like potential. The two bent pieces acting as leads generate an inhomogeneous field contribution along the axial (z)-direction, providing axial confinement and possible an offset (Ioffe) field to lift the trap bottom from 0 to a finite value. (b) U-trap. Similar to Z-trap, but the counter-propagating currents in the leads provide fields that cancel in the center, creating a field-zero at the trap-bottom. (c) H-trap. As indicated, this trap can be provided by wires arranged in a multi-layer structure. Depending on the current direction in the leads, it can act similar to both a Z-or U-trap. Axial and radial confinement can be tuned independently.

As described so far, the side-guide lacks axial confinement and, as a trap, suffers from Majorana losses for the reasons mentioned in section 4.1.1. The latter problem can be cured by applying an additional bias field along the z-direction, while the former is addressed by additional wire segments orientated perpendicular to the main trapping wire. Examples of such traps can be found in figure 4.2. Especially the Z-trap (4.2a), also containing a schematics of the contributing currents and fields), and H-shaped traps (4.2c)) consisting of wire segments in different chip layers [154] are commonly used. For the Z-trap, the fields generated by the collinear wire segments point along the same direction and hence add up. This effect by itself lifts the trap minimum to a finite value, which, depending on the spatial extension of the central wire and the currents involved, can render the application of an external field along z redundant. In the case of the macroscopic Z-trap used in the intermediate stages of a typical experimental cycle (see sections 4.3.5 and 4.4), this effect can be so strong that it is advantageous to apply a reverse field to increase the trap's confinement [155]. In the chip trap used for the experiments described in this thesis, on the other hand, the effect is not big enough to prevent significant losses, necessitating an additional external field.

4.2. Detection techniques

A number of detection schemes for ultracold atoms have been developed over the years, and most of them are based on atom-light interaction [156]. Although several interesting complementary methods based for instance on electron microscopy [157], photo-ionization and detection by a channel-electron multiplier [158], and, most notably, direct detection of metastable Helium on microchannel-plates [159] have been implemented, optical imaging is well suited to most experiments for many reasons: The typically used Alkali atoms feature quasi-closed transitions yielding high scattering rates, suitable light-sources for detection are normally already necessary for laser cooling and therefore come 'for free', highly sensitive cameras and detectors for the usual near-infrared wavelengths involved are readily available, and optical imaging can be adapted to cover the full regime of atomic densities from dilute magneto-optical traps to highly confined trapped Bose-Einstein condensates. An overview discussing the most commonly used imaging methods based on absorption, fluorescence and phase-contrast detection can be found in [101]. More recent methods enabled optical detection at the single-atom level mediated by fluorescence [160, 161, 162, 121, 40, 163]. In addition, highly sensitive detection methods based on exploiting the coupling to optical cavities have been developed [164, 165, 166, 167, 168, 169].

In our experiment, absorption imaging in free expansion and a single-atom sensitive fluorescence detector based on optical fibers integrated on an atom chip are available.

4.2.1. Absorption imaging

In the following, the basics of absorption imaging, as used to perform the measurements presented in chapter 5 and 6 are briefly summarized. A comprehensive review on this technique with a focus on atom chip experiments can be found in references [55] and [170].

Figure 4.3 shows an illustration of absorption imaging. Illuminating an atom cloud with a directed, short laser pulse of intensity I_0, tuned to be in the vicinity of a suitable optical transition, leads to photon scattering and attenuation of the transmitted laser pulse as described by Beer-Lambert's law:

$$I_t = I_0 e^{-\sigma n_c(x,z)}. \tag{4.6}$$

Here, σ denotes an effective scattering cross section depending on the used transition and intensity, while $n_c(x,z)$ corresponds to the atomic density profile integrated along the direction of transmission, in this case $\boldsymbol{y}$. This *column density* is consequently given by

$$n_c(x,z) = \int dy\, n(x,y,z) = \sigma \ln\left(\frac{I_0\,(x,z)}{I_t(x,z)}\right). \tag{4.7}$$

The transmitted intensity distribution $I_t(x,z)$ is recorded by a camera. A realistic detector with a finite pixel size given by an area A_p will measure a density $n_p(x_i, z_j)$ in

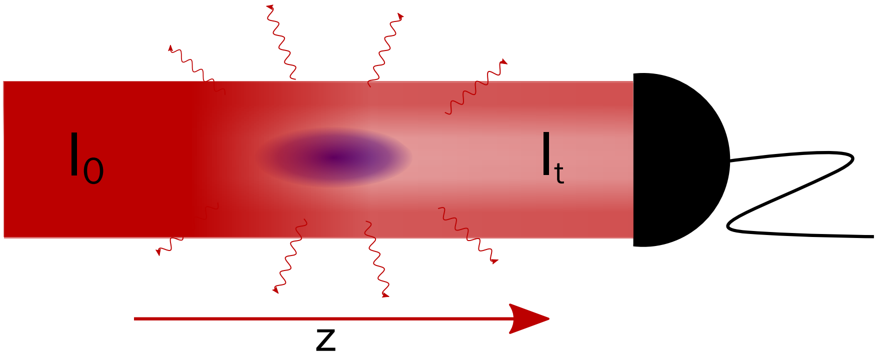

Figure 4.3.: Basic scheme of absorption imaging. An incoming beam with an intensity profile I_0 interacts with an atom cloud, and photons are resonantly scattered out of the incident beam into 4π, attenuating it according to equation 4.6. The transmitted intensity profile is imaged by a suitable detector.

each pixel i, and a total atom number

$$N = \frac{A_p}{M^2} \sum_p n_p \left(x_i, z_i\right), \tag{4.8}$$

with the magnification M of the imaging system, with the result that A_p/M^2 corresponds to an effective pixel size in object space. M can be measured during characterizing the imaging system with the help of suitable resolution targets before integrating it within the experiment (see for example [170]). Additionally, structures of known size on the chip can be used as a cross-check after integration, in addition to position measurements of free-falling atom clouds at different fall times, as in [171].

The effective scattering cross section σ is harder to identify, as it depends on a variety of experimental parameters. For the remainder of the discussion, we will consider ^{87}Rb, as used in our experiments. The most important properties of ^{87}Rb are summarized in appendix A. A well-defined value for the resonant scattering cross-section σ_0 can be provided for an atom in the $|F = 2, m_F = 2\rangle$-state, a quantization axis defined by a magnetic field with a strength so that the Larmor frequency γ_L exceeds the coupling to the light field, and σ_+-polarized light resonant with the transition between $|F = 2, m_F = 2\rangle$ and $|F' = 3, m_F = 3\rangle$ in the limit of low intensities $I_0 < I_{sat}$. Disregarding losses to the $F = 1$-manifold that are negligible for the number of $\mathcal{O}(100)$ scattered photons per atom during imaging, this scenario constitutes an effective two-level system, and the resonant scattering cross section reads

$$\sigma_0 = \frac{\hbar\omega_0\Gamma}{2I_{sat}} = \frac{3\lambda^2}{2\pi} \tag{4.9}$$

with a wavelength λ, a saturation intensity

$$I_{sat} = \frac{\hbar\omega_0^3\Gamma}{12\pi c^2}, \tag{4.10}$$

where $\omega_0 = (E_2 - E_1)/\hbar$ is defined by the energy difference between ground and excited state, and $\Gamma = 1/\tau$ by the lifetime of the transition $\tau = 26.24$ ns. Substituting numbers yields $I_{sat} = 1.699 \frac{mW}{cm^2}$ and a resonant cross section $\sigma_0 = 0.291\ \mu m^2$ [172]. These values mark the maximum scattering rates that can be achieved on this transition.

In the experiment, after switching off the trapping fields, the m_F-states are not well defined. In a field-free environment, the imaging pulse defines an inherent quantization axis, and ideally, after a few scattering events the rate for each atom converges against σ_0. However, already the presence of small stray fields can significantly reduce the steady-state scattering rate [173]. Therefore, it is advantageous to apply a well defined homogeneous offset field aligned to the imaging axis to replicate the ideal case discussed above. Note that a magnetic field causes a differential Zeeman shift

$$\Delta_m = (m_{F'} g_{F'} - m_F g_F) \frac{\mu_B}{\hbar} B \tag{4.11}$$

between the ground and excited states involved in the transition. Usually, trap switch-off and offset field application will lead to a distribution of atoms among the different m_F states, and if the differential Zeeman shift Δ_m exceeds the linewidth of the laser, optical pumping to the correct $|F = 2, m_F = 2\rangle$ ground state of the cycling transition is suppressed, leading to a loss of signal.

Similarly, any source of detuning between imaging laser and atomic transition Δ leads to a reduction of the scattering rate given by

$$\sigma = \frac{\sigma_0}{1 + \left(\frac{2\Delta}{\Gamma}\right)^2 + \frac{I_0}{I_{sat}}}. \tag{4.12}$$

Polarizations deviating from σ_+ lead to a change both the effective scattering cross section and the saturation intensity due to optical pumping between different m_F-states driven by the σ_- and π-components.

The coil setup in our experiment makes the application of an offset field for regular absorption pictures impractical (see section 4.3). Switching external fields between the values needed for a trap and the offset field, respectively, induces current oscillations for durations of several 10 ms. By optimal control techniques using the approach presented in [174], however, these oscillations were suppressed for one specific switch-off procedure, allowing to perform calibration measurements with a well-defined external field of 1.5 G and σ_+-polarization for a set of quasi-BECs in a trap with known trapping frequencies. A comparison of measured and simulated density profiles was used as a validation of the atom number calculated from the resonant scattering cross-section, and further comparison with the usual imaging setup without offset field and linear polarization allows to perform a calibration, finding $\sigma/\sigma_0 \approx 0.5$. This is consistent with calculations presented in [173], with σ/σ_0 ranging from 0.5 to 0.55 for the limiting cases a quantization axis aligned parallel and normal to the imaging beam direction, respectively.

The duration of the imaging laser pulses in our experiment is typically between 50 and 80 μs. Two pictures are taken for each absorption image. They contain the transmitted intensity distribution in the presence of atoms $I_t(x, z)$, and without atoms $I_t(x, z)$, respectively. Since the imaging process is destructive due to momentum transfer of photons to the atom cloud, and since gravity leads to atoms falling out of the illuminated region, the second picture can be taken typically $5 - 50$ ms after the initial one, depending on the size and density of the atom cloud. An additional constraint on the minimum time between pictures might be imposed by the shift- or readout speed of the camera. To correct for stray light, two background pictures taken without the imaging beam at a later point of the experimental cycle can be subtracted from the initial pictures, at the disadvantage of adding the corresponding additional camera readout noise.

As mentioned, the discussion in this section is tailored to absorption imaging in the limit of low intensities. As I_0 approaches I_{sat}, nonlinear effects and increased forward scattering start to set in. An imaging method situated in this regime is presented in reference [175].

4.2.2. Fiber-based fluorescence detection

Simply put, the difference between absorption and fluorescence detection is given by the position of the detector. In the regime of validity of the Beer-Lambert law 4.6, the intensity scattered out of the imaging beam as indicated in figure 4.3 is

$$I_f = I_0 - I_t = I_0 \left(1 - e^{-\sigma n_c(x,z)}\right) . \tag{4.13}$$

Assuming the same conditions as in the previous section, all statements about the scattering rate σ carry over to fluorescence imaging. Nevertheless, one fundamental difference between the two methods is that in the limit of low atom numbers N, the minimal number of atoms detectable with fluorescence detection at a given signal-to-noise ratio scales favourably as compared to absorption detection [39]. Other differences are of mostly technical nature: In fluorescence imaging, the detector is not illuminated by the full detection beam, allowing high intensities to maximize the number of scattered photons, while at the same time employing highly sensitive detectors, as for example EMCCD cameras. Using the same intensities in an absorption imaging setup would lead to the destruction of the detector. On the other hand, the detected photon intensity

$$I_F^{det} = \eta_{coll} I_0 \left(1 - e^{-\sigma n_c(x,z)}\right) \tag{4.14}$$

is suppressed by the collection efficiency $\eta_{coll} = A_{det}/4\pi$ given by the fraction of solid angle the detector is covering, assuming isotropic scattering on average. Maximizing η_{coll} necessitates, in optical terms, a detector with a large numerical aperture which is often hard to implement and has the added disadvantage of higher sensitivity to collect background photons from spurious light sources.

The use of an miniaturized, integrated fluorescence detector close to the atomic scatterers provides an elegant solution to maximize the numerical aperture while minimizing the background, and has been shown to allow single-atom sensitive detection [40, 42]. A detailed presentation can be found in [39]. A short overview of the detection geometry is presented in section 4.3.9. Within the scope of this thesis, the detection efficiency for atom clouds close to degeneracy has been studied. The results are presented in chapter 7.

4.3. Experimental setup

The apparatus described here consists of over 60 devices coordinated by a central experimental control system and many more passive optical, opto-mechanical and electronic elements, and a full description involving each single device is beyond the scope of this work. Therefore, the following section only provides an overview discussing the most important components, concentrating on the status-quo as of 2012 and 2013, at the time when the measurements presented within this thesis have been performed. Where it is useful, experimental parameters are included as reference values. A focus lies on the modifications that have been applied in order to prepare the machine for the routinely generation of degenerate Bose gases. Many components have already been selected and installed during the first iteration of the experiment at the university of Heidelberg, a detailed description of which can be found in reference [38]. Other changes have been made during the reconstruction of the machine after the group's move to the Vienna labs and are documented in reference [39].

4.3.1. Overview

The goal of each experimental sequence is the trapping and manipulation of a bosonic atom cloud that is in a cold thermal or Bose-condensed state in a magnetic micro-trap. To achieve this, each experimental sequence needs to go through several stages, necessitating specific working conditions and devices. In the following, an overview of the most important devices and components is given, while the different stages to go through to generate a 1d quasi-BEC in an atom chip trap are discussed in section 4.4. Figure 4.4 starts with a sketch outlining the structure of the experiment, containing the components discussed below. Most of the setup is built on top of a pneumatically supported optical table to decouple it from environmental mechanical shocks and vibration. Power supplies and control electronics are stored below the table and on shelves above it, with the exception of the laser control electronics that is housed within a separate rack besides the table. Many devices are connected to a central experimental control, which itself is linked to a dedicated computer with an interface to steer the experiment's operation. Two different PCs are connected to cameras and photon counters for the fiber detection

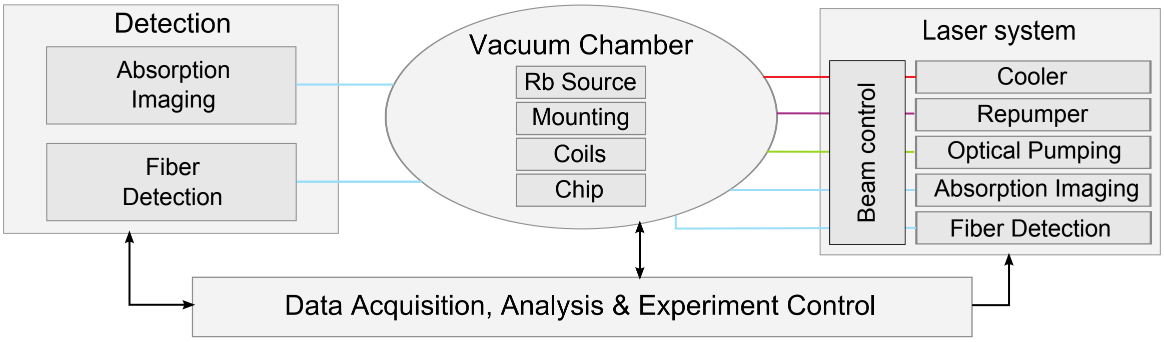
Detection
Absorption Imaging
Fiber Detection
Vacuum Chamber
Rb Source
Mounting
Coils
Chip
Laser system
Beam control
Cooler
Repumper
Optical Pumping
Absorption Imaging
Fiber Detection
Data Acquisition, Analysis & Experiment Control

Figure 4.4.: Sketch of the experiment's basic structure. The different components discussed throughout section 4.3 are sorted into categories belonging to the laser system, vacuum chamber setup, detection, as well as data acquisition and control. All components, except the computers belonging to the latter category are mounted on and around a single optical table in the laboratory.

setup, respectively.

4.3.2. The atom

The standard procedure to reach the temperatures necessary to allow magnetic trapping of neutral atoms is laser cooling [176, 177] in a magneto-optical trap, which is also used in this setup. While an increasing number of elements can be laser cooled as of now [178, 179, 180], the choice in our experiment is ^{87}Rb. It is one of the most commonly used elements and isotopes in cold atom experiments, partly due to the good availability of the needed wavelengths in the vicinity of 780.24 nm for the D2 line in terms of diode lasers and, more recently, frequency doubling of high-power Telecom-wavelength sources [181]. Figure 4.3.2 shows the level scheme and the relevant transitions of the D2 line. The lasers used to drive these transitions in the different stages of the experiment are discussed below (4.3.4). It was mentioned in section 4.1.1 that an atom needs to be in a low-field seeking state for magnetic trapping. For ^{87}Rb, one can choose between the $|F=2, m_F=1,2\rangle$ and $|F=1, m_F=-1\rangle$ states. For all the experiments presented in the chapters 5 and 6, the $|F=2, m_F=2\rangle$ state has been used. It has the advantages of a higher confinement by a factor $\sqrt{2}$ as compared to state $|F=1, m_F=-1\rangle$, and no need for repumping to the $F=2$ manifold for detection. For the demonstration of state selective detection with the integrated fluorescence detector, the $|F=1, m_F=-1\rangle$ has been used. A very recent measurement of the s-wave scattering lengths for the $F=1$ and $F=2$ states can be found in [182], with previous results referenced therein.

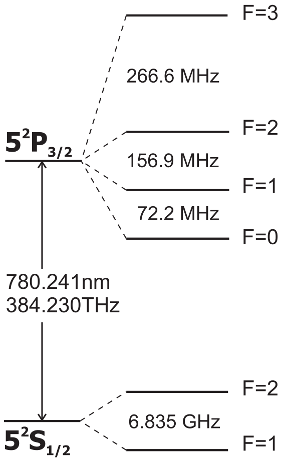
F=3
266.6 MHz
F=2
5²P3/2
156.9 MHz
F=1
72.2 MHz
F=0
780.241nm
384.230THz
F=2
6.835 GHz
5²S1/2
F=1

Figure 4.5.: ^{87}Rb D2 line: Level scheme.

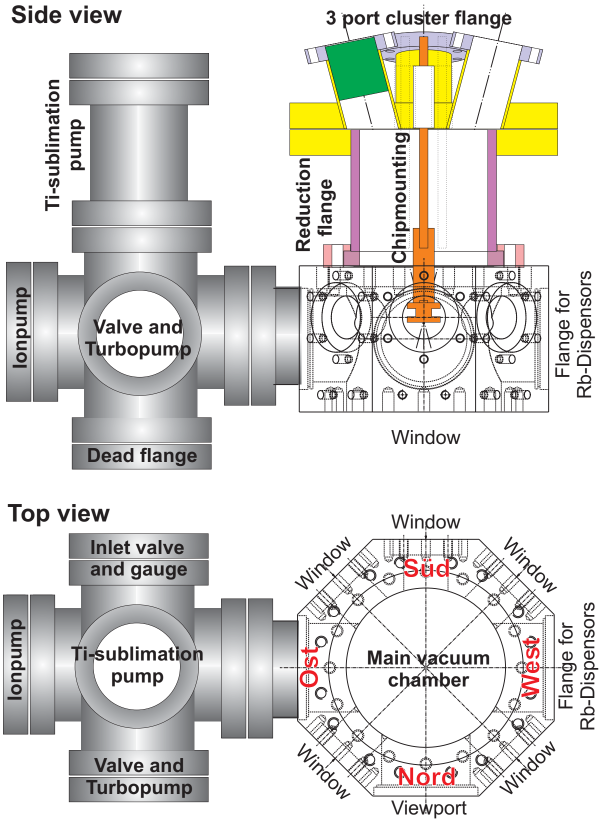
Side view
3 port cluster flange
Ti-sublimation pump
Reduction flange
Chipmounting
Ionpump
Valve and Turbopump
Flange for Rb-Dispensors
Window
Dead flange
Top view
Inlet valve and gauge
Window
Window
Süd
Window
Ionpump
Ti-sublimation pump
Ost
Main vacuum chamber
West
Flange for Rb-Dispensors
Valve and Turbopump
Window
Nord
Window
Viewport

Figure 4.6: Vacuum chamber. Upper panel: Side view. On the right side, the main chamber is displayed. On top, the chip mounting attached to a three-port cluster flange installed on top of a reduction flange that is connected to the upper orifice of the vacuum chamber. The cluster flange features feedthroughs for electric connections for chip wires and copper structures, as well as Swagelok-feedthroughs for optical fibers. On the left side, the 6-way cross connecting the chamber to the installed vacuum pumps. Lower panel: Top view. On the six-way cross, the valve leading to the vacuum gauge is visible. The top view of the chamber reveals the optical access an beam paths. The axis pointing from north-west to south-east, as labelled in the figure is used for MOT beams, while the orthogonal axis (north-east to south-west) is used for imaging. At the north, south, east and west positions, two pairs of identical coils. An additional coil is situated at the top of the chamber, mounted around the reduction flange. At the bottom of the chamber, a big window is used for MOT beams and additional optical access for imaging. Drawings adapted from [38].

4.3.3. Vacuum chamber, atom source and coils

Since laser cooling is selective to the specific element and isotope chosen, it is necessary to work with a good vacuum of at least $p \approx 10^{-8}$ to 10^{-9} mbar. Reaching lifetimes in the order of many seconds, as needed to achieve BEC in a magnetic trap, enforces even more stringent conditions, necessitating ultra-high vacuum (UHV) of $p \approx 10^{-11}$ mbar. We achieve such pressures in a steel vacuum chamber, as outlined in figure 4.6 (detailed drawings can be found in reference [38]). Pumping down is performed by a combination of a turbo-molecular pump[1] and heating of the vacuum chamber to at least $100°C$, while an ion-getter pump[2] keeps the pressure during regular operation with the additional use of a titan-sublimation pump[3] at regular intervals of a few weeks to months.

Source. As a Rubidium source, suitable alkali metal dispensers[4] can be mounted within UHV and allow the implementation of a closed, single-chamber experiment. The dispensers contain a mixture of Rubidium chromate and a reducing agent on a Tungsten wire. Upon heating the dispenser by applying a suitable current to the wire, usually around $4 - 7A$ during regular operation, the reducing agent reacts with the chromate, leading to the release of Rubidium by evaporation. For our experiments, pulsed operation of 12 to 16 seconds at the beginning of the experimental sequence, for a cycle time between 30 and 35 seconds, has shown to yield both a sufficient number of atoms in the MOT, and at the same time sufficiently low background pressure during the magnetic trapping stages to guarantee long enough lifetimes. According to our experience, the Rubidium stored in the dispensers under these conditions is sufficient to allow several years of operation.

---

[1] Pfeiffer Vacuum Gmbh, Asslar, Germany.

[2] VacIon Plus (55 l/s), Varian Inc. (now Agilent), Torino, Italy.

[3] Mini-Ti Ball, Varian Inc. (now Agilent), Torino, Italy.

[4] SAES Getters S.p.A., Milan, Italy

Coils. Two symmetric pairs of coils are mounted at the 'North' / 'South' and 'East' / 'West' positions as denoted in figure 4.6. An additional coil on top of the chamber creates a field perpendicular to the chip. In contrast to other experiments within the group, these coils are used to generate all external fields used throughout the experimental cycle[5]. This is easily possible, since the mounting and chip is aligned at an angle of 45 degrees with respect to the coil axes in such a way that the direction of bias and Ioffe fields can be reversed without having to change the direction of current within the coils. This setup simplifies especially the copper-structure based magnetic trap (see section 4.4 that necessitates reversing the direction of the Ioffe field to improve confinement, as discussed in 4.1.1. On the other hand, this setup also leads to the fact that the small Ioffe field is generated by subtraction of two strong fields along the z-direction, if at the same time a big transverse bias field is needed for a sizeable confinement. This translates to significant current noise on the trap bottom. An additional pair of coils along the Ioffe-direction, designed to create small fields, would alleviate this problem and in addition allow current stabilization schemes that improve stability of the trap bottom [183], while a similar additional pair of bias coils would facilitate applying a suitable offset field for absorption imaging. Hence, implementing such coils is planned for the next iteration of the experiment.

Periphery. Externally controlled power supplies are used to drive both the currents for the Rubidium source[6] as well as for the coils[7]. The latter need to be switched rapidly at several points during the experimental cycle. Since this cannot be accomplished with the power supplies themselves, resulting in current oscillations directly after switchoff, external switches dissipating the power stored in the coils by Darlington transistors built at the institute's workshop are used. They also contain current sensors that are used to monitor the proper operation of both switches and power supplies.

The power supplies used for the coils feature both a constant current (CC) and a constant voltage (CV) mode. Connecting both current and voltage control channels to the corresponding input plug of the power supply allows to freely switch between these operation modes by changing the corresponding signals in the experiment control. This can be used to control the switch-on behaviour of the coils to allow short current rise times

---

[5] The exception is a set of big compensation coils around the whole setup running a constant current to compensate for earth's magnetic field.

[6] Kepco ATM 6-10M, Kepco Inc., N.Y., USA

[7] HP 6552A (now Agilent) / Agilent 6652A, Agilent Technologies, Santa Clara / CA, USA.

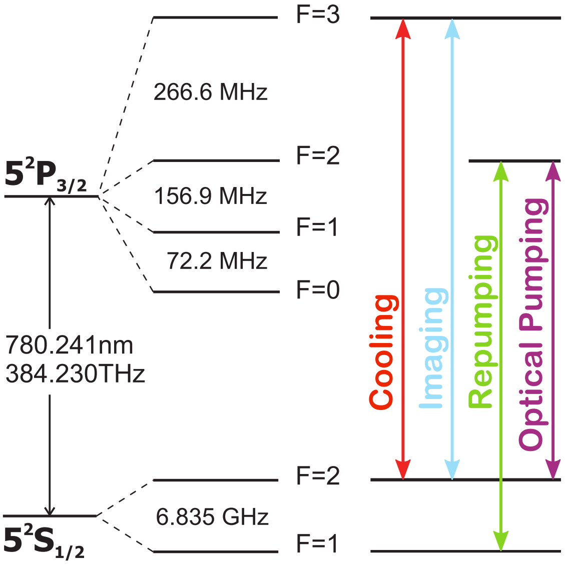

Figure 4.7: ^{87}Rb D2 line: Level scheme and used transitions.

while suppressing subsequent current oscillations. Measurements performed within the group show that the CV mode features less current noise than the CV mode. This suggests that it is preferable to CC during the chip trap. However, since the coil resistance can vary with temperature, the CV mode has been observed to current drifts without proper external stabilisation as mentioned above. Therefore, in contrast to the suggestions from noise measurements, the CC mode is preferable during the chip trap in our experimental setup.

4.3.4. Laser system

Lines. In order to cool, trap and detect ^{87}Rb, a number of lasers stabilized to operate on specific transitions of the D2-line are necessary, as shown in figure 4.7. For *cooling*, cyclic transitions between $F = 2$ and $F' = 3$ are utilized. The $F' = 3$ state can decay to the $F = 1$ state that is dark with respect to the cooling light, with a branching ratio of approximately 1/1000. Therefore, an additional *repumping* laser tuned to the $F = 1 < - > F' = 2$ is necessary to return these atoms to the cyclic transition. These lines are sufficient for the generation of a magneto-optical trap and optical molasses. Switching on a magnetic trapping field provides a quantization axis and a distribution of atoms among different m_F states between $-2 < m_F < 2$, and only the $m_F = 1, 2$ states are trapped. To improve the transfer efficiency, an *optical pumping* laser on the $F = 2 \leftrightarrow F' = 2$ transition, σ_+-polarized with respect to the quantization axis defined by the initial trapping field is used to accumulate most atoms in the trapped $|F = 2, m_F = 2\rangle$ state. Detection, again, operates on the cycling transition, as discussed within section 4.2.

Structure. The basic structure of the laser setup has not been changed since the initial rebuilding of the experiment after its move to Vienna. A detailed description can be found in [39], while an overview is presented in figure 4.3.4. To generate all

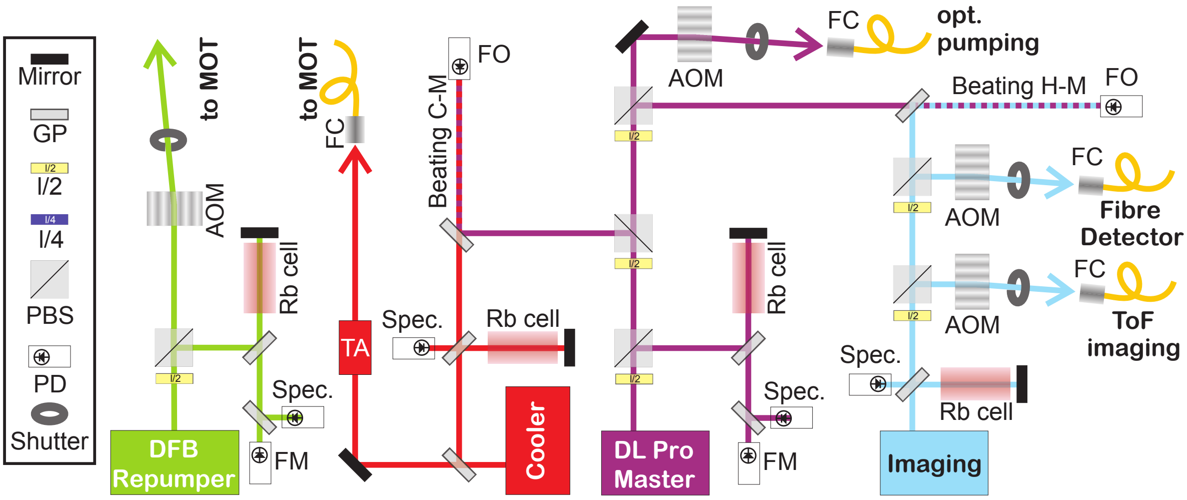
Mirror
GP
l/2
l/4
PBS
PD
Shutter
to MOT
AOM
Rb cell
Spec.
FM
DFB Repumper
to MOT
FC
TA
Spec.
Rb cell
Cooler
Beating C-M
FO
AOM
FC
opt. pumping
Beating H-M
FO
DL Pro Master
Rb cell
Spec.
FM
FC
AOM
Fibre Detector
FC
AOM
ToF imaging
Spec.
Rb cell
Imaging

Figure 4.8.: Laser setup. All necessary wavelengths are produced by a set of four lasers. A reference laser (master) and a repumping laser are locked via FM-locks directly to doppler-free saturation spectroscopy setups. The other two lasers (cooler, imaging) are stabilized by an FO-lock with respect to the master laser. Optical pumping is provided by the master, while the imaging beam is split into two paths providing light independently for regular (ToF) imaging and fibre detection. The cooler pumps a tapered amplifier providing ≈ 400 mW of optical power for the MOT beams. Drawing adapted from [39].

wavelengths in the vicinity of 720.24 nm needed to drive the transitions of the D2-line, frequency stabilized diode lasers are used.

Lasers and frequency control. One so-called *master* laser is stabilized on the $F = 2 \leftrightarrow F' = 2,3$ crossover peak of a doppler-free saturation spectroscopy setup by a frequency modulation (FM)-locking technique. It is a self-built external cavity diode laser (EDCL) in Littrow configuration. A fraction of the output beam is used as a reference for frequency offset (FO)-locking [184] both the *cooling* and the *imaging* laser, while most of the power is directed towards an acusto-optical modulator, acting as a switch and shifting the frequency by -133.3 MHz into resonance with the $F = 2 \leftrightarrow F' = 2$ transition for optical pumping. The FO-lock for the cooling and imaging lasers yields to a tunability on a range of 100 MHz without influencing the beam direcation (as for a single-pass AOM setup) or the output power (as for a double pass AOM setup). The imaging beam is split and directed to two different single-pass AOMS providing a redshift of 80.7 MHz and 110.7 MHz, respectively. The first AOM directs light for the time-of-flight imaging setup, the other to the fiber detection. Depending on which is used, the FO lock is tuned to shift one of the two beams in resonance with the $F = 2 \leftrightarrow F' = 3$ transition, accordingly. The use of two AOMs at different frequencies reduces crosstalk and corresponding beating effects.

The cooling laser consists at the point of writing this thesis, of a commercial ECDL[8], driven with control electronics manufactured in the institute's electronic workshop to allow the use of an FO lock, that seeds a tapered amplifier (TA) chip providing the power necessary for the magneto-optical trap. The TA has been constructed in the course of the thesis [39]. The output beam transmits a single-pass AOM applying a red-shift of 92 MHz, while again the FO-lock can be used to tune the beam to an overall redshift between 10 to 70 MHz from the $F = 2 \leftrightarrow F' = 3$ as used in the MOT and molasses phases. The *repumping* laser is, similar to the master, stabilized by an FM-lock to the $F = 1 \leftrightarrow F' = 1, 2$ crossover peak and shifted into resonance with the $F = 1 \leftrightarrow F' = 2$ transition by a single-pass AOM. Initially a commercial ECDL[9], it has been replaced by a distributed feedback (DFB) diode laser. Such diodes do not rely on external gratings for mode selection and stabilization, but feature an Bragg resonator directly manufactured into the active region of the laser diode by spatially modulating the refractive index. They have the advantage of mode-hop free operation, greatly improving stability of the experiment since mode-hops induced by small temperature changes on the laser table limited the time over which the rempumping laser, and thus the experiment, could be stabilized in the previous setup. A detailed description of the used locking techniques can be found in [185].

The overall output powers of the different lasers correspond to 15 mW of repumping light, and a few mW of total imaging and optical pumping power at the vacuum chamber. The cooler features seeding powers of up to 20 mW for the TA chip, which emits approximately 900 mW of total optical power. Since the beam profile of TA chips is rectangular and modified by diffraction at the output surface, it is usually badly matched to the input of a polarization-maintaining single-mode fiber that has to be used to transmit the light to the vacuum chamber for best stability, leading to a maximum total power of roughly 480 mW at the vacuum chamber.

Periphery. All laser power supplies together with temperature control and locking electronics are mounted within a rack connected to a USV-backed up power line that is reserved for low-noise equipment. The only externally controlled devices from this rack are the VCOs to tune the frequency offset of the FO locks. The AOM drivers[10] are quite noisy and connected to a different power line. Here, the amplitude is externally controlled, and digital TTL triggers to switch them can be applied, while the frequency of all AOMs stays at a fixed value. As an interesting sidenote, it was found that the intensity of light leaking through the AOMs varies depending on both TTL level and set amplitude. Only using the digital trigger led to significant transmitted residual intensities, while negligible leakage has been observed with both amplitude and TTL switched down. In this configuration it was possible to create BECs without the use of additional mechanical shutters, with the exception of the high-power cooling laser.

---

[8] Toptica DL PRO, TOPTICA Photonics AG, Munich, Germany.

[9] Toptica DL 100, TOPTICA Photonics AG, Munich, Germany.

[10] Lingam Wildsau, Innsbruck.

Two different types of shutters are used. Within the laser box, small devices that do not introduce significant mechanical vibrations are utilized as to adversely affect the stability of the laser locks. They have small plastic blades that are prone to be burnt through at even modest intensities, and also likely to get stuck if switched in rapid intervals. Since they were a frequent error source, a replacement solution for the next iteration of the experiment is highly recommended. For the repumper and MOT beams, big metal blade shutters[11] mounted outside the laser box were used. They induce significant mechanical vibrations, but are unlikely to be damaged by even intense, focused beams. Care has to be taken that proper mechanical insulation of the laser box and the table is guaranteed.

Future improvements. In its current iteration, the laser setup allows continuous runtime of the experiments of a few days under ideal conditions. Further improvements to be considered within the next iteration of the experiment encompass removing the separate repumping laser altogether, and replacing it by a microwave modulation [cite modulation papers] of a DFB-based cooling laser seeding a TA chip. Such a setup is built and tested at the moment of writing this thesis. On the one hand, this allows to shift the ratio between cooling and repumping light by the MW modulation amplitude. This is useful, since at 15 mW of total repumping power, a total saturation of the atom number in the magneto optical trap has still not been observed and higher powers would be advantageous. In addition, one less laser means one less independent error source, and the DFB diode would additionally improve stability as compared to the ECDL-laser in the current configuration. Further, the master laser could be replaced by the commercial model acting to seed the TA chip as of now. Using an FM lock with the electronics shipped with the laser allows remote control of the lock-point, further reducing direct intervention necessary to keep the apparatus running. Finally, a new fiber-coupled TA has been ordered recently[12], offering higher output powers of up to 2W, to replace the ageing chip, offering additional power reserve and temperature stability.

4.3.5. Chip mounting & copper structures

Mounting. To allow time-of-flight imaging, the atom chip needs to be mounted upside down in the vacuum chamber. Consequently, the chip mounting is attached to a three-port cluster flange screwed to a reduction flange on the upper orifice, protruding into the chamber from above. It consists mainly of a number of copper rods connecting current feedthroughs at the flange to a set of copper structures and pins to connect the chip, fixed within a Shapal[13] plate with suitable recesses that allow precise positioning of both the copper structures and the chip. This is important to guarantee correct alignment of the copper structures with respect to the wires, and good thermal contact between mounting and chip. Shapal, a composite sintered ceramic made of Aluminium Nitride

---

[11] Uniblitz Shutter Systems, Vincent Associates, Rochester, USA.

[12] Toptica BoosTA, TOPTICA Photonics AG, Munich, Germany.

[13] Tokuyama Corporation, Tokyo, Japan.

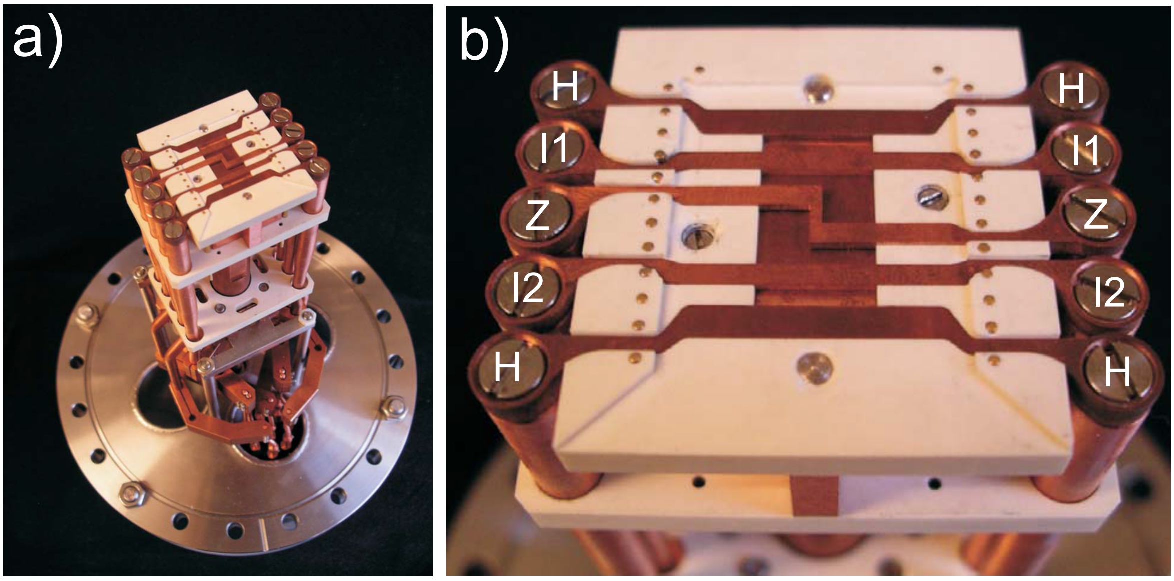

Figure 4.9.: Chip mounting and copper structures. (a) Overview picture of the mounting attached to the 3 port cluster flange. The copper rods providing the macroscopic wire structures with current, copper block and Shapal stabilization plates are shown. (b) Close-up picture of the Shapal plate accommodating copper structures and the chip. The connections to the copper wires are labelled as explained in the text. Along the sides of the recess for the chip, the pins for bonding to the chip wires are visible.

and Boron, is an ideal choice for this since it features good electrical isolation but at the same time a high thermal conductivity[14]. The Boron admixture facilitates machining of the otherwise hard and rigid ceramics. Additional Shapal pieces are used to stabilize the copper rods at different positions. Figure 4.9a) shows the chip mounting attached to the cluster flange before assemblage of the vacuum chamber, and 4.9a) contains a close-up of the Shapal plate and the copper structures.

Copper structures. The copper structures need to support currents of up to 60 A, driven by external power supplies[15] without significant heating. Most important are the copper plate centred within the mounting and connected via the rods labelled by H within the figure, and the Z-shaped structure crossing it centrally, used to create the inhomogeneous fields needed for the MOT and the subsequent macroscopic magnetic trapping phase respectively (see section 4.4). An additional pair of copper wires is present, labelled as $I1$ and $I2$ in figure 4.9. For the experiments presented within this thesis, it has not been used. Great care has to be taken that the connection screws are properly tightened, so that all connections are supported by as much surface as possible. Point-like connections heat up significantly during operation, leading to evaporation of attached pollutants and consequently to an increased background pressure, reducing lifetime. To prevent this, optionally the copper connections on the flange-end can be water cooled, which was, however, not necessary in our setup.

---

[14] Thermal conductivity: ~ 100 W/(m·K); Volume resistivity: $\sim 10^{14}$ Ω·cm.

[15] Agilent 6551A, Agilent Technologies, Santa Clara, USA.

Periphery. Two power supplies[16] act as current sources for the copper structures. The currents need to be switched on and off on the μs scale to allow reliable transfer from MOT to magnetic trap and to chip trap. As for the coils, switching the power supplies directly is not fast enough, and an external solution is necessary. For the major operation time throughout this thesis, the same high-power switches based on Darlington transistors[17] have been used as for the coils. However, due to the low resistance of the copper structures, the power supplies are likely to produce current spikes during switching, with a chance to damage the Darlington transistors. This necessitated frequent maintenance. Therefore, suitable high-power relays have been tested and used during the later stages of the experiment. They have proven to withstand continual operation under experimental conditions and are a cheap and reliable alternative.

4.3.6. Atom chip

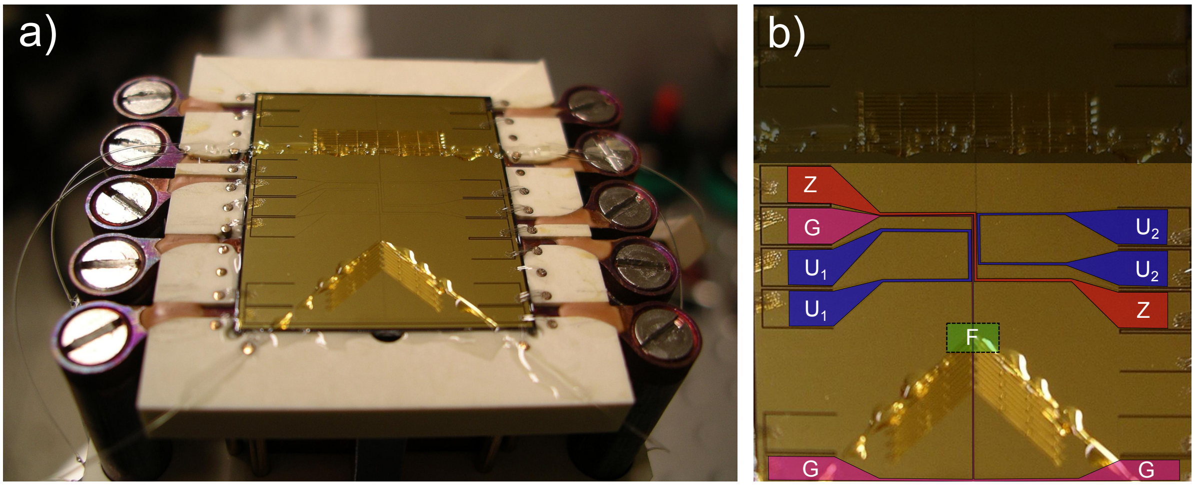

Figure 4.10.: Atom chip. (a) Overview picture of the chip glued to the Shapal plate displayed in figure 4.9(b), with attached bond wires and optical fibers. (b) Top view of the chip surface. The colored overlays correspond to wire structures used within this thesis. Red: Central trapping wire. Blue: Control wires used to tune the confinement. Pink: Magnetic guide wire allowing atoms to propagate from the chip centre to the fluorescence detection region (green). The V-shaped patterns in the lower part of the picture correspond to SU-8 holding structures for optical fibers. The upper greyed-out part of the picture contains other fibre detectors described in [38] and not used within this thesis.

The atom chip is the heart of the experiment. It is consists of a 2.5 cm × 3 cm big silicon substrate with a thickness of typically 700 μm covered by a 2 μm thick Gold layer. The function of the layer is twofold: On the one hand it acts as a highly reflective mirror surface to reflect beams used in the U-MOT setup [186]. On the other hand, the surface can be structured by lithographic techniques. More precisely, the silicon substrate is coated by photo-resist. Exposing the resist with UV light in regions defined by a suitable lithography mask and subsequent development results in a silicon layer with hardened resist structures on top. Now, the Gold is applied by evaporation. Lift-off removes the resist and the Gold on top, resulting in a silicon substrate with a structured Gold surface. In this way, wire structures as presented in section 4.1.2 are created that allow current densities in excess of 10^7 A/cm^2. Further details about the fabrication process of the chip used within this thesis can be found in [143, 38].

---

[16] Built by the electronic workshop at Heidelberg University.

[17] Built by the electronic workshops at Heidelberg University and the ATI.

Wire structures and dimensions. An overview picture of the chip is found in figure 4.10a), wile the wire structures used in this thesis are outlined in 4.10b). The central trapping wire used to prepare cold thermal clouds and quasi-BECs has a thickness of 200 μm and is labelled by the connections Z. The central wire piece spans a length 4.5 mm. Likewise, the U-shaped control wires, indicated in the figure by the labels U_1 and U_2 are 200 μm thick. In addition, the wire denoted as G constitutes the guide wire that allows to transport atoms from the central chip region to the fluorescence detector marked by F. This wire has a thickness of 50 μm, and the distance between the chip centre and the detector amounts to 5.5 mm. Note that a second guide wire exists that leads towards the greyed-out upper region of the chip. Here, additional detectors are situated that have been characterized in [38]. At the start of this thesis, the second guide wire has found not to conduct current at all, indicating some sort of damage rendering it dysfunctional during some stage of the experiment's move from Heidelberg to Vienna. Hence, the additional detectors have not been used in the scope of this thesis.

Currents. Using the supported current densities of 10^7 A/cm^2, these wire structures are expected to withstand currents of 40 A and 10 A for a thickness of 2 μm and widths of 200 μm and 50 μm, respectively. However, the thin bond wires connecting the chip to the pins represent a more sensitive bottleneck. As to not evaporate them, 2 A of continuously applied current are not exceeded during operation of the experiment. The used power supplies to drive these currents have been developed within the electronics workshops in Heidelberg and Vienna. To prevent electric noise generated by outside sources to couple to the chip currents, a 10 V car battery is used as voltage source.

Fiber holding structurs. On top of the Gold surface, our chip supports holding structures for optical fibers, as apparent in figure 4.10. These structures are applied within an additional fabrication step, consisting of spin-coating the chip with a layer of SU-8[18] photo-resist, and another step of UV-exposure and development. With SU-8, it is possible to build stable structures with a height in excess of 100 μm. By varying the process parameters, it is possible to influence the shape, going from rectangular to slightly undercut structures that can be used as funnels to precisely align and hold optical fibers.

---

[18] Microchem Corporation, Massachusetts, USA.

To prevent any additional movement, the fibers are fixed with a vacuum-proof epoxy-based glue. A detailed description of the SU-8 structures can be found in [38], while in the scope of [187], the SU-8 fabrication steps have been reproduced within Vienna, and details about the process are contained here. Note that in preparation of the experiment's next iteration, a modified process has been developed that allows to fabricate even bigger SU-8 structures that can hold fibers with a diameter exceeding 125 μm. It involves a multi-layer SU-8 fabrication and an additional thin SiO_2 layer between Gold and SU-8 to improve the adherence of the latter. A detailed description is expected to be published in future and to be contained in Dominik Fischer's Ph.D. thesis [188].

4.3.7. Evaporative cooling setup

Some information about the physics of forced RF cooling can be found in section 4.4. As an RF source, two frequency generators[19] are used in our experiment. One of them (labelled 'RF1') is used to cover a frequency range from 0 to 20 MHz, the other one ('RF2') is restricted to 0 to 3 MHz. The reason is that we use an analog signal between 0 and 5 V to control the frequency output of the RF generator. Since internally, this voltage range is mapped to a finite number of frequency steps, a bigger range corresponds to a lower resolution. This is disadvantageous in the final steps towards condensation. Therefore, one generator is used to perform pre-cooling within the copper-structure generated magnetic trap, while the final steps to condensation are performed with the second generator.

In general, analog control yields a broader, more noisy output signal. A digital solution with the current equipment is prohibited by the fact that in this mode the RF-generator cannot be externally triggered properly, and all workarounds yield random delays between trigger signals and response of the device in the order of a few to a few tens of ms. An additional disadvantage is that the amplitude of the signal cannot be controlled externally. At the moment we use two different amplitudes for precooling and condensation, but a certain amount of power broadening in the order of tens to a few hundreds of Hz cannot be prevented. Therefore, for the next iteration of the experiment, an advanced RF source allowing full digital control of both frequency and amplitude, that allows to reduce the latter during the final cooling steps, as well as control over the phase, would constitute a big improvement. Such sources have started to see use in other experiments within the group recently[20].

The RF signal is fed by BNC cables to the H-like copper structure that can be seen in figure 4.9 via externally triggered RF switches[21]. Since the exact field strength at the position of the atom cloud is not known exactly, the amplitude is chosen to yield the shortest cooling times to degeneracy.

---

[19] Agilent 33220A, Agilent Technologies, Santa Clara, USA.

[20] Tabor Electronics Ltd., Tel Hanan, Israel

[21] Mini-Circuits, N.Y., USA.

	Main imaging	Overview imaging
Camera	Andor iKon M	Pixelfly QE
Magnification	5.62 ± 0.13	1.72 ± 0.02
Effective pixel size	2.32 μm	3.76 μm
Field of view	2.37×2.37 mm^2	5.23×3.85 mm^2
Diffraction limited resolution	5.22 μm	-

Table 4.1.: Parameters of the main and overview absorption imaging systems.

4.3.8. Absorption imaging

A detailed presentation of the absorption imaging setup can be found in [171]. One camera[22] together with suitable optics is employed as an overview imaging with a field of view sufficient to image the compressed MOT and the early stages of the copper-structure based magnetic trap. A second camera[23] is designed to yield high resolution images of cold thermal clouds and quasi-BECs. The imaging optics has been designed and tested in the course of the thesis [171]. Within the coordinate system introduced in 4.1.2, both imaging systems observe atom clouds integrated along the x direction, transversely to the weakly confined axis of the magnetic traps generated in the experiment. While much of the system's characterization has been performed prior to its integration within the setup, proper focussing has to be accomplished with atoms as an imaging targes. Two useful techniques employed, based on the shape of diffraction patterns from optically dense clouds, the other using an MTF-induced effective cutoff on the spectrum of density ripples in free expansion (see section 4.6) developed within the group [121] are found in [170, 171]. Table 4.1 presents the most important parameters of both imaging systems needed for the analysis of the data this thesis is based upon.

4.3.9. Fluorescence detector

The integrated fluorescence detector was the main tool to acquire the data analyzed and presented in [39]. It is therefore thoroughly described within this reference. The detector itself is best explained by means of the microscope picture shown in figure 4.11a). It consists of two optical fibers at an angle of 90 degrees with respect to each other, and each at 45 degrees with respect to a guide wire that allows atoms to propagate from the central chip trap to the detection region pictured. Both fibers have a diameter of 125 μm and are held in place by SU-8 structures as described in section 4.3.6. The fibers enter the vacuum chamber through the upper 3 port cluster flange via swagelok-feedthroughs housing teflon plugs that enclose the fibers. Upon tightening the feedthroughs, the teflon plugs provide proper sealing to ensure UHV conditions without damaging the fibers.

---

[22] Pixelfly QE, PCO AG, Kelheim, Germany.

[23] Andor iKon-M DU934N-BR-DD, Andor Technology PLC, Belfast, UK.

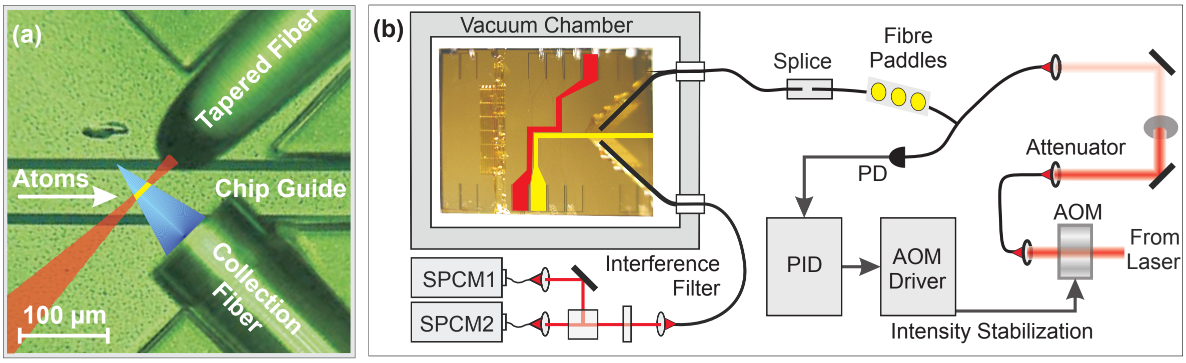

Figure 4.11.: Flourescence detection. (a) Microscope picture of the integrated fluorescence detector. Atoms propagate along the central guide wire, crossing a pair of orthogonally arranged fibres. A tapered detection fibre delivers light with a total power of picowatts to nanowatts into the red-coloured region, focussed centrally with respect to the guide wire. The blue-coloured cone indicates the region of maximum probability to scatter photons into the core of a multimode collection fiber at the bottom end of the pictures. The yellow-coloured overlap corresponds to the optimal detection region. (b) Sketch of the overall detector setup. An attenuated beam is coupled to a fibre-Y setup splitting the path to both an intensity stabilization setup and the vacuum chamber to deliver excitation light. Fluorescence light from atoms is guided out of the chamber to an interference filter and a Hanbury-Brown Twiss setup of a beam splitter and two SPCMs to resolve signals beyond the dead-time of the photodetectors.

Fibre detector. One of the fibers is single-mode and tapered[24], delivering excitation light at a distance of 62.5 μm from the chip surface, with a focus centred below the guide wire. The beam waist in focus is 5 μm. The second fiber multimode, and collects fluorescence light scattered into the fiber core. The region of maximum detection efficiency is marked by the blue cone in figure 4.11a). Outside this cone, the detection probability is not identically zero, but drops rapidly with the spatial distance of the cone border. Most of the signal will be collected from a small intersection within the detection cone that is illuminated by the light from the excitation fiber. This is the yellow-coloured region in figure 4.11a). Each scatters a number of photons in the detection region, the average of which depends on the effective scattering cross section and an interaction time that is either given by the motional dynamics or by loss into dark states (as for example the $F = 1$ state), a fraction of which is collected by the multimode fiber.

Detection setup. The rest of the detection setup, situated outside the vacuum chamber, can be divided into preparation of the excitation light, and collection of the fluorescence and is schematically shown in figure 4.11b). A fraction of light from the imaging laser passes an AOM and an attenuator before being coupled into a fiber-Y 50-50 beam splitter. One of the output ports leads to a set of fibre paddles to control the polarization. Afterwards, this fibre piece is spliced the actual excitation fibre

---

[24] Nanoptics, Inc. Gainesville, USA.

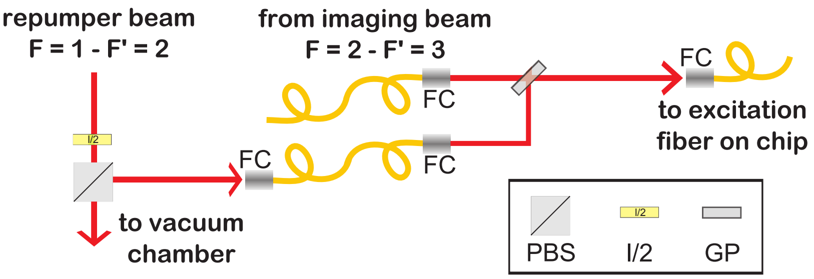

Figure 4.12.: Setup to guide additional light on the repumping ($F = 1 <-> F' = 2$) transition to the excitation fiber, enabling detection of atoms in the $F = 1$ hyperfine state.

entering the vacuum chamber. The other output port leads to an amplified photo diode, monitoring the transmitted power. The photo diode signal is used by a PID-regulator to close the feedback loop to the amplitude control of the AOM driver in order to stabilize the intensity to a fixed value. Note that the power needed to reach the saturation intensity within the detection region amounts to 325 pW. Typical powers used for experiments range between a fraction of this value up to a few nW.

The light collected by the multimode fibre is guided to an interference filter[25] and from there into a Hanbury-Brown Twiss (HBT) type setup consisting of a beam splitter and two single photon counting modules (SPCM)[26]. This setup allows to investigate photon correlations for time intervals below the SPCM dead time of approximately 50 ns and has been used to validate single atom detection within the setup [41].

While for many fluorescence detection schemes, background light is a problem, the miniaturized nature of the fibre detector leads to a negligible amount of background. Measurements of the fraction of light detected as a function of the intensity coupled into the excitation fibre in the absence of atoms scattering photons show a suppression of $10^{-}8$, or only 30 counts per second for each nW of power emitted by the excitation fibre[39]. Stray light at different wavelengths is suppressed even further due to the interference filter in the detection setup.

Detection efficiency. The total photon detection efficiency $\mathcal{N}_{ph}$, is the product of the collection-, all transmission-, as well as the SPCM detection probabilities within this setup [39, 189]:

$$\mathcal{N}_{ph} = R_{coll} \cdot f_f \cdot f_s \cdot f_g \cdot f_{SPCM}. \tag{4.15}$$

Here, $R_{coll} = 0.019$ denotes the photon collection ratio, $f_f = 0.96$ corresponds to Fresnel losses due to reflection at the multimode fiber tip, $f_s = 0.998$ stems from losses at the splice, $f_g = 0.84$ summarizes all reflection losses within the HBT setup (fiber coupler facets, filter transmission), and $f_{SPCM} = 0.564$ denotes the SPCM detection efficiency. With these numbers, the total photon detection efficiency amounts to $\mathcal{N}_{ph} = 0.0086$. It is also possible to bypass the HBT and only use the interference filter at the output. This slightly reduces the loss contribution of the filter gap f_g, to yield $\mathcal{N}_{ph} = 0.0091$.

---

[25] Semrock, Inc. Illinois, Lake Forest / IL, USA.
[26] Perkin Elmer SPCM-AQR-12-FC, Perkin Elmer, Inc., Waltham / MA, USA.

The total atom detection efficiency, on the other hand, depends on the number of scattered photons per atom and is therefore influenced by a number of parameters like the laser detuning, magnetic field gradient, polarization of the detection light or the motional dynamics of atoms in the detection region. A detailed analysis for thermal atoms at temperatures exceeding $\mathcal{O}(10)$ μK is found in [39]. An analysis for temperatures in the nK-regime is presented in the thesis [188], some aspects of which are discussed in chapter 7.

State selective detection. As discussed so far, only atoms in the $F = 2$ hyperfine state can be detected, while atoms trapped in the $|F = 1, m_F = -1\rangle$ state are dark. Since the $F = 1$ manifold does not offer a closed transition that our detection scheme is relying on, a solution based on superimposing repumping light coupling to $F = 1 <-> F' = 2$, while detecting on the closed $F = 2 <-> F' = 3$ transition. Such a scheme has been demonstrated to achieve atom detection efficiencies comparable to the numbers measured for atoms in the $F = 2$ state [42]. The simple setup to add repumping light is sketched in figure 4.12. Assuming a mixture of atoms in $F = 1$ and $F = 2$, it is possible to count the total atom number (imaging and repumper on), the $F = 2$ component (imaging on, repumper off) or the $F = 1$ component (external imaging pulse to remove $F = 2$ component, imaging and repumper on for fibre detection). Detecting both components independently within a single atom cloud, however, would necessitate an arrangement of two detectors so that the first counts the $F = 2$ component, and the second the atoms in $F = 1$.

4.3.10. Experiment control and data acquisition

The control and acquisition system is an often-times underestimated part of the experimental apparatus. While each single component is crucial to the operation of an experiment, after the initial setup of the hardware one is confronted with finding an experimental sequence leading to the desired result, such as production of a BEC, or a manipulation procedure transferring an atom cloud into a desired target state. In essence, this is a big optimization problem over the parameter space defined by the input of each controlled component. At the point of writing this thesis, 60 devices are subject to the experiment control, each of which has to perform a certain temporal sequence of action, amounting to over 1000 parameters. Of course, this is not a black box: knowledge of the applied techniques and a certain experience considering how to choose physically sensible parameters is important; nevertheless, many quantities still have to be found by performing parameter scans and evaluating the results. Likewise, troubleshooting for dysfunctional devices requires parameter scans and easy access to many different output

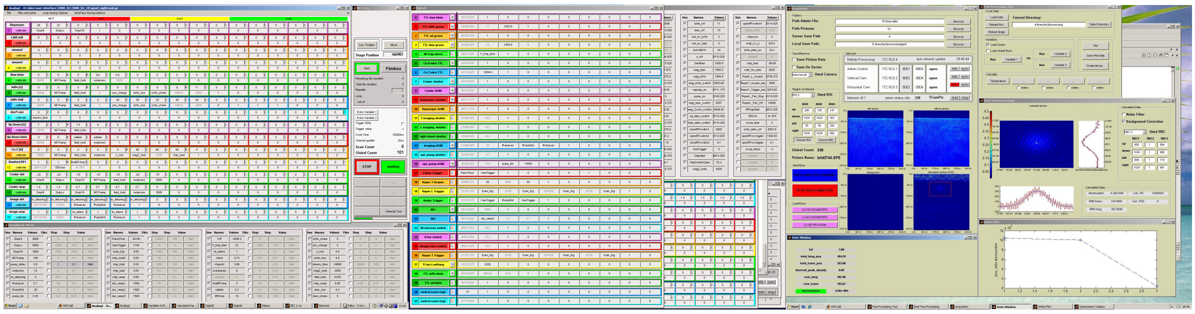

Figure 4.13.: Left and middle panels: Screenshots of the experiment control software written in Matlab and communicating with a real-time control system as described in the text. Each coloured line corresponds to a device, different columns to timesteps throughout an experimental cycle. Right panel: Acquisition software to store and pre-evaluate pictures and data from the experiment, also written in Matlab.

signals, which have to be monitored and recorded. The amount of time needed to do so greatly depends on the simplicity and ease of use of the control and real-time analysis.

In the early stages of this thesis, the initial LabView-based control has been exchanged by a modular real-time system of type AdWin-Pro II[27]. A previous version of this system has been in use within other experiments in our group before. The change to the new system brought several advantages. From a technical point of view, the main gain is a lower noise floor, an improved time resolution down to 9 μs, and a higher number of both analog and digital output channels. A Matlab-based software interface integrating control and real-time analysis that had been developed for another experiment [190, 191] could be adapted. Screenshots from the software are shown in figure 4.13. One of the main advantages is the comfortable calibration of control voltages to physical units such as magnetic fields in Gauss. Another comfortable feature is the online analysis, that can be easily set to log, store and automatically analyse and plot different measurement observables. Both of these features save a big amount of time when dealing with parameter scans in the process of optimization. Additionally, an automatic parameter optimization scheme based on a genetic algorithm was refined and adapted to this experiment [174, 192].

Beyond this, several features have been added over time. In hindsight, two have been especially useful. One of them is the option to define an arbitrary time during the experimental cycle and have a working imaging sequence determined and applied automatically, including correct switching of all lasers, fields and RF sources. The ability observe the atom cloud at any point during the cycle without having to perform lengthy changes on the timing drastically reduced the time spent looking for errors and faulty devices. The second feature was the implementation of a comfortable remote control for the machine, allowing parameter scans over nights and weekends, and monitoring the operation remotely.

---

[27] Jäger Computergesteuerte Messtechnik GmbH

Technical details about the control-system and further information about the software can be found in [174].

4.4. Bose-Einstein condensation in an atom chip setup

The basic structure of a typical experimental cycle can be roughly parted into three stages: Magneto-optical trap, magnetic trapping within a macroscopic trap generated by the copper structures (4.3.5), and the chip trap. Figure 4.4 visualizes a typical experimental cycle in terms of these stages. The total duration usually ranges between 30 and 35 seconds. 16 to 20 seconds of this time is consumed by the MOT phase, including loading and a short optical molasses phase, alone. Capturing the cloud in the macroscopic magnetic trap and pre-cooling takes around 6 seconds, while cooling to degeneracy in the chip trap needs 3 to 4 seconds. The rest of the time is taken up by further manipulation of the cloud, or propagation in the 1d magnetic guide towards the detection region. The following, the different stages of the experimental cycle are briefly described, with emphasis on the points that have been found to be crucial for the reliable generation of a BEC.

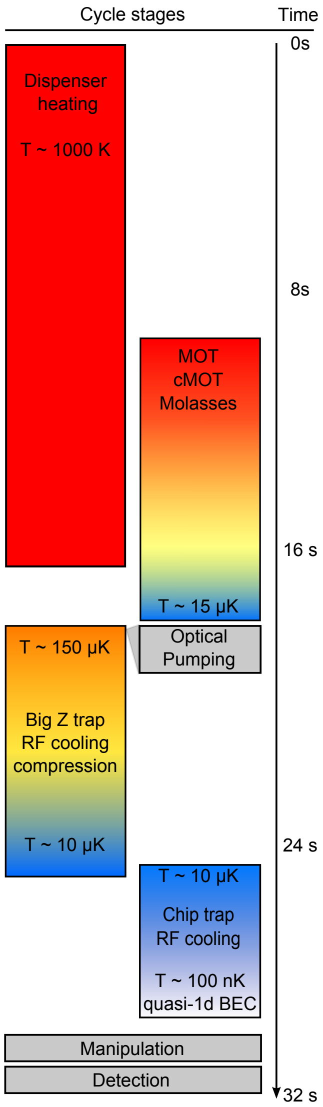

Figure 4.14.: Sketch of a typical experimental cycle, illustrating the different stages described within this section.

4.4.1. Laser cooling in a MOT.

As already introduced in section 4.3.4, the transition used for laser cooling of ^{87} is the $F = 2 \rightarrow F' = 3$ transition, while an additional repumping laser on the $F = 1 \rightarrow F' = 2$ line prevents the accumulation of atoms in the dark $F = 1$ state. Using a setup involving only a single vacuum chamber, one of the beam directions used for a classical 6-beam arrangement is blocked, necessitating the use of an U-MOT setup [186], where two beam pairs are mirrored on the chip surface, instead.

Dispenser heating. Before the start of the actual laser cooling stage, the Rubidium dispensers are heated by a current between 5 to 7 A for a time of 12 to 16 seconds. Note that these values can vary between the different experiments within the group even for identical dispensers, since the relation between current, pulse duration and temperature depends strongly on the thermal contact between the mount and dispensers, and on whether the mounting is actively cooled. The fact that for longer cycle times the dispensers have more time to cool down needs to be accounted for, too. Therefore, optimization of the dispenser timing is rather empirical, and often the last stepping stone to achieve BEC after a thorough optimization of the cycle's later stages.

MOT. After 10 seconds of dispenser heating, the lasers and fields for the magneto-optical trap are switched on. The cooling laser is redshifted by 20 MHz with respect to resonance, and bias fields along the x and y direction of 10.8 and 7 G, respectively, as well as a small field along the z-direction of 3.1 G are applied. Loading of the trap until saturation usually takes 5 to 10 seconds. During the last 2.5 seconds of the MOT phase, the dispensers are switched off so that they can suffiently cool down as to not cause an increased background pressure of hot Rubidium during the following magnetic trapping phase. The final 120 ms of the MOT phase are governed by a compression and shift of the MOT position closer to the chip surface by ramping the fields to $(B_x, B_y, B_z) = (18.8, 7.8, 1.6)$ G, to guarantee good overlap with the magnetic trapping potential.

Molasses. After the MOT, fields are switched off and the detuning is increased to a redshift of 50 MHz to employ polarisation gradient cooling in an optical molasses for 12 ms, yielding several 10^7 atoms at temperatures of $T \approx 15$ μK. At this stage, precise beam balance adjustment and compensation against stray fields is crucial. Ideally, the molasses is clearly visible, without any shift of the center-of-mass position.

4.4.2. Transfer to the macroscopic magnetic trap.

While directly loading a micro-trap on an atom chip from the molasses is possible, the mismatch between trap shape and cloud volume leads to large losses, heating and low phase space density after transfer. Therefore, an intermediate magnetic trapping stage in a macroscopic trap (see 4.1.1) is used. As described in section 4.1.1, the $F = 2, m_F = 2$ hyperfine and Zeeman substates are used for magnetic trapping. As many atoms as possible have to be collected in this state at the switch-on of the magnetic trap for an efficient transfer from the molasses. Therefore, the following procedure is used:

1. At the end of the molasses phase, the cooling lasers are switched off.

2. One of the fields (in our case the North-South (NS) coil field (see 4.3.3)) is ramped towards its set value for the magnetic trap to provide a quantization axis for optical pumping.

3. To transfer most atoms to the trapped $m_F = 2$ magnetic substate of the $F = 2$ manifold, the optical pumping laser resonant with the $|F = 2, m_F = 2\rangle \rightarrow |F' = 3, m'_F = 3\rangle$ transition, σ_+-polarized with respect to the quantization axis defined by NS coil field mentioned above, applies a pulse with a duration of a 750 μs during switching on this field.

4. Only after optical pumping, the repumping laser is switched off. This ensures that most atoms are transferred to the $F = 2$ hyperfine state.

5. Now, the other magnetic fields from the East-West (WO) coil pair and the central Z-shaped copper structure are switched on.

Optical pumping. The power, detuning and timing of the optical pumping pulse are optimized to yield the maximum number of atoms in the magnetic trap. Without optical pumping, the atoms in three of the 5 m_F states are not trapped and lost from the trap. Therefore, an additional factor of 2.5 to 3 in atom number is expected from optical pumping. Sometimes, slightly higher gains can be seen, since atoms in the $m_F = 1$ states see a trapping potential with weaker confinement, possibly not correctly mode-matched to the molasses position.

Field switch-on. It is also of utmost importance to provide a fast and smooth switch-on of the coils. Switching by the power supply, relying on its internal current regulation is usually slow. Therefore, a trick is used. During the molasses phase, the external switches between power supplies and coils are off, and the circuit is open. For switch-on, the power-supplies are tuned into CV mode, leading them to use the maximum available power trying to establish a defined voltage. Then, the circuit is closed, leading to a fast current- and therefore field-rise time in the order of 5 ms. The disadvantage of this method is an oscillatory behaviour of the current after switch-on. This can be counteracted by properly controlling the set current in CC mode after the switchoff. The resulting ramps should exhibit only minimal residual oscillations. A typical switch-on procedure is illustrated in figure 4.4.2.

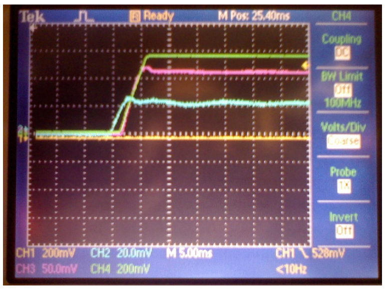

Figure 4.15.: Currents for switch-on of coils and Z-structure during transfer from the optical molasses to the macroscopic magnetic trap. Blue: NS-field. Red: WO-field. Green: Z-structure.

The initial Z-trap is governed by bias and Ioffe fields of $B_x = 23$ G and $B_z = -15.5$ G, respectively, as well as a current of $I_Z = 52$ A in the Z-shaped copper structure. This corresponds to trap frequencies of $(\omega_x, \omega_y, \omega_z) = 2\pi \times (31, 39, 16.3)$ Hz. A good benchmark atom number in the magnetic trap directly after transfer ~ 2 to 3×10^7 atoms. Compression leads to initial temperatures between 100 μK and 200 μK.

4.4.3. Evaporative cooling and trap compression.

To increase the cloud's phase space density and to allow matching of the macroscopic and chip traps for efficient transfer, forced radio-frequency evaporative cooling [193, 194] is employed. Application of a RF-field with a frequency that corresponds to the ground state Zeeman-splitting of atoms in a magnetic field couples the m_F states, leading to transfer atoms into untrapped states expelled from the trap. The Zeeman splitting of each atom depends on its position in the trap. Only atoms with a high total energy can probe regions far from the trap minimum, corresponding to high potential energy and a certain Zeeman splitting. Applying an RF field coupling to these high energy atoms will selectively remove them, and the remaining atoms can rethermalize at a lower temperature. In a 3d Bose gas, this rethermalization is established after around

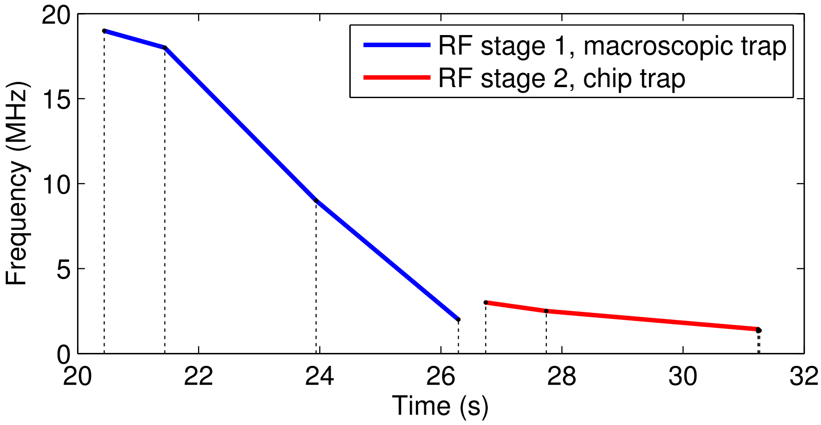

Figure 4.16.: Sketch of the RF-cooling ramps as explained within the text. The blue line corresponds to the first cooling stage within the macroscopic trap generated by copper structures below the chip. The red line indicates the final cooling steps within the chip trap. Two different RF-generators are employed to ensure optimal frequency range and resolution, although the final ramp piece within the macroscopic trap can already be performed with the high-resolution source labelled 'RF2' within the text, especially to create a condensate in this trap. The gap corresponds to the stage of transferring atoms between the macroscopic and chip traps.

4 collisions per atom [195].

For a perfect, otherwise loss-less system, the most efficient evaporation, in terms of the energy change over the number of removed particles $\Delta E_th/\Delta n$, is reached for a stationary RF-knife situated at the potential corresponding to the total system energy, and, as such, diverging evaporation time. This corresponds to the most extreme case of a system in a state where a single particle absorbs the total energy by a sequence of unlikely scattering events [101]. In a real system, however, other loss processes such as background gas collisions and 3-body recombination [196, 197, 198, 199] are always present and there is a trade-off between these losses and forced evaporation that yields an ideal rate for the frequency change $d\eta_{RF}/dt$ of the RF knife. To find this trade-off, the cooling ramp is divided in several segments, and optimization is performed by scanning their duration and the frequency of each support point. Note that this is a problem that lends itself well to an automatic optimization based on an algorithm, as demonstrated in [192].

The experimental sequence during evaporation is as follows: Directly after loading the macroscopic magnetic trap, the fields are held constant at their initial values for 100 ms to allow for a short plain evaporation phase. Afterwards, the coil fields and Z-structure current are ramped to values $(B_x, B_y, B_z) = (53, -30, 0)$ and $I_Z = 60$ A over a period of 6 seconds, while at the same time a three-stage evaporative cooling ramp is applied by the RF source labelled 'RF1' in section 4.3.7, covering a range of 20 MHz to 2 MHz, as displayed by the blue line within figure 4.16. From here, two options are available: To generate a BEC within the macroscopic trap, or to transfer atoms to the chip. Figure 4.16 shows the latter case.

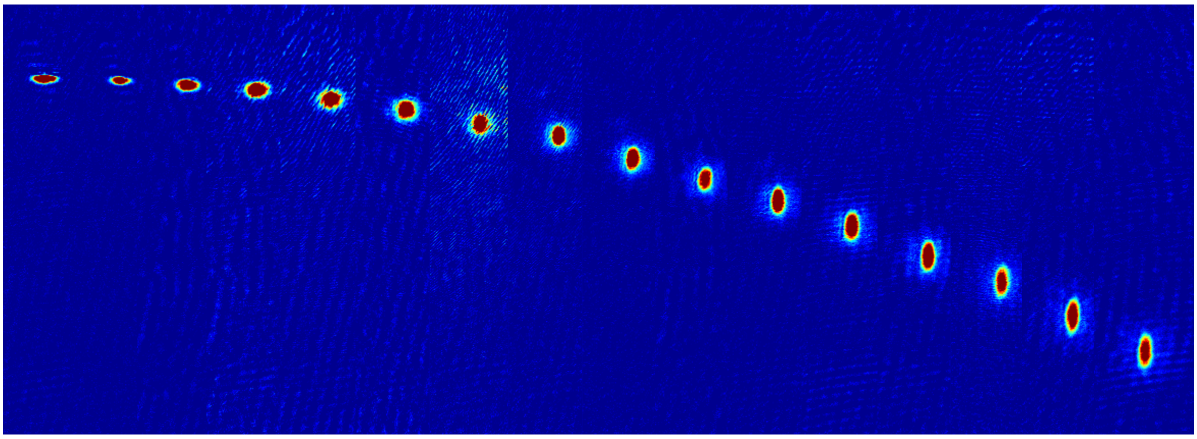

Figure 4.17.: Time-of-flight expansion of a 3d BEC generated in the macroscopic magnetic trap. Different pictures correspond to expansion times 2 to 17 ms in steps of 1 ms. The pictures demonstrate the inversion of aspect ratio during free expansion which is the typical 'smoking gun' evidence for the presence of a hydrodynamically expanding BEC, governed by an anisotropic momentum distribution in accordance with Heisenberg's uncertainty principle.

4.4.4. BEC in macroscopic trap.

The compressed macroscopic trap features trapping frequencies of $(\omega_x, \omega_y, \omega_z) \approx 2\pi \times (110, 115, 40)$ Hz and supports a cigar-shaped, elongated 3d BEC. To reach degeneracy, RF1 is switched down by its external RF-switch, while RF2 is turned on, continuing the ramp from 2 MHz down to 0.35 MHz over 1 to 2 seconds. The transition to the condensed state is marked by a sharp increase of the central density, and inversion of the profile's aspect ratio during free expansion as expected for the anisotropic momentum distribution in a hydrodynamic fluid, the iconic 'smoking gun' signature for the realization of a BEC [2]. As a demonstration, figure 4.17 shows the free expansion of a BEC from $\approx 3 \times 10^4$ atoms generated in the macroscopic trap, at times between 2 and 17 ms after release, in steps of 1 ms. A thermal cloud, in contrast, always shows a ballistic, isotropic expansion [101].

Depending on the final position of the RF-knife, the BEC can coexist with significant residual fraction of atoms in thermal states. Due to the different densities and momentum distributions, this leads to clearly identifiable bimodal density profiles in free expansion. Figure 4.18 shows such a profile integrated along the y-axis, together with a Gaussian fit to the thermal fraction. Measuring its width for different expansion times allows to estimate its temperature [101]. Assuming equilibrium between condensed and thermal atoms, suggests to assign this temperature also to the BEC. This notion is not completely unproblematic, though, with experimental results [200, 37] indicating that the dynamics of thermal atoms and condensed fraction in a 3d geometry after inducing collective excitations is uncoupled, without signs of thermalization over a timespan of several tens of ms. More related to the content of this thesis, 1d quasi-BECs allow to measure the temperature of both thermal and condensed fractions independently. Also

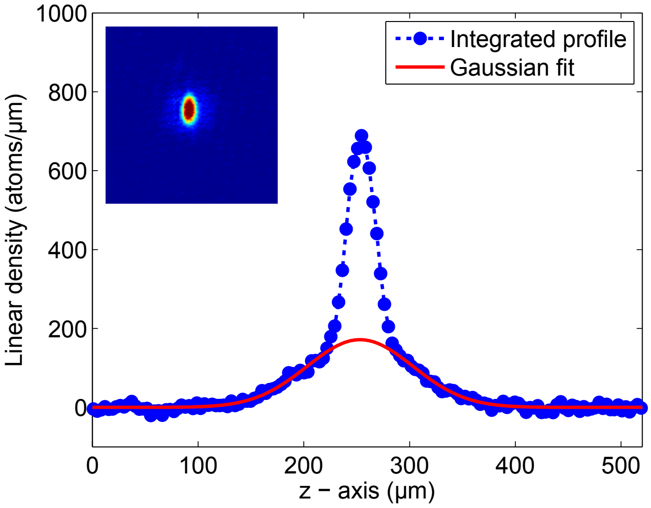

Figure 4.18.: Bimodal profile of a BEC and a surrounding thermal cloud. The plot is integrated from the picture shown in the inset, taken at a time-of-flight of 12 ms. The profile features the typical bimodal shape caused by the central parabolic density profile of a BEC and a surrounding Gaussian thermal atom cloud at lower density. Fitting the width of the thermal component during expansion allows thermometry of the system, given the assumption of thermal equilibrium as discussed in the text.

here, evidence for a lack of thermalization between the two subsystems on times exceeding 800 ms has been found [31], suggesting that care has to be taken when applying the notion of thermal equilibrium.

4.4.5. Transfer to the chip trap and quasi-BEC.

A good benchmark for efficient cooling in the chip trap has found to be an atom number exceeding 2×10^5 at temperatures between 10 and 15 μK at the end of evaporation in the macroscopic trap. To transfer atoms to the chip, source RF1 is switched down, and the fields and currents in the Z-structure I_Z and chip I_C are ramped within two steps from $I_Z = 60$ A to $I_Z = 0$ A, $B_x = 53$ G to $B_x = 17$ G, $B_z = -30$ G to $B_Z = 4$ G, and $I_C = 0$ A to $I_C = 2$ A during a time of 400 ms. The transfer is usually lossless and doesn't significantly change the temperature. After this ramp, the trap is compressed over a time of 4.5 s by changing the fields to $(B_x, B_y) = (17, 3.3)$ G, and source RF2 performs the final evaporative cooling stages to a frequency corresponding only a few kHZ above the trap bottom defined by the Ioffe field.

Figure 4.19a) shows a picture of a quasi-1d BEC of ≈ 14000 atoms after 10 ms of free expansion from a trap with a confinement governed by $\omega_a \approx 2\pi \times 8$ Hz and $\omega_r \approx 2\pi \times 1000$ Hz. The cloud clearly features density fluctuations along the longitudinal z-axis, characteristic for a quasicondensate with phase fluctuations impeding coherence over the full extension of the system (see section 2.3). These density fluctuations are random, forming a different pattern in each realisation, and averaging over many shots yields a

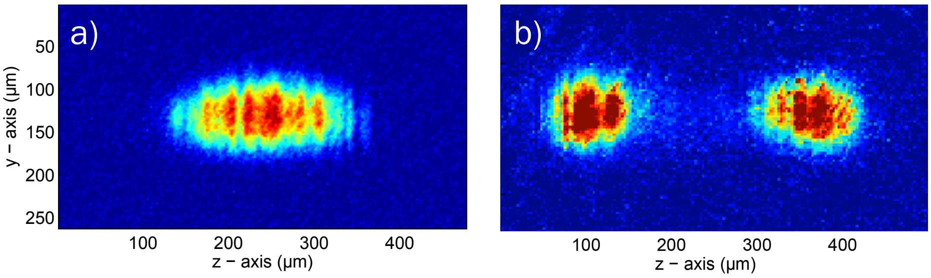

Figure 4.19.: Quasi-1d BECs at different distances from the chip surface. (a) Quasicondensate of ≈ 14000 atoms after a free expansion of 10 ms from a trap characterized by the frequencies $\omega_a \approx 2\pi \times 8$ Hz and $\omega_r \approx 2\pi \times 1000$ Hz, at an external bias field of $B_x = 26$ G. The distance of the trapped cloud from the chip exceeds 120 μm, and the density profile is in good approximation parabolic, indicating a harmonic trap an negligible influence of wire corrugations. (b) Quasicondensate of ≈ 10000 atoms after a free expansion of 10 ms from a trap at an external bias field of $B_x = 35$ G. Due to the influence of corrugations, the potential is split into two wells filled by independent quasicondensates.

smooth profile that for experimental parameters is governed by the shape of the trapping potential. Any irregularities that don't vanish with averaging hint at corrugations of the trap wire causing an irregular potential, an effect that becomes more pronounced for smaller distances between trap and surface. The influence of such corrugations is apparent in all of the group's experiments at the time of writing the thesis [201, 183], and the chip presented here is no exception. The parameters listed in the previous paragraph result in a distance between chip surface and trap minimum exceeding 120 μm. In contrast, 4.19b) depicts a cloud released from a trap with a bias field $B_x = 35$ G and otherwise identical parameters, the minimum situated less than 100 μm away from the surface. As an effect of wire corrugations, the potential splits into two distinct wells. For any experiment depending crucially on a harmonic trapping potential or good control over the trap shape, the influence of corrugations has to be avoided, putting a limit on the minimal distance, and as a consequence on the possible confinement in such a chip trap. Note, however, that it is possible to implement time-orbiting potentials (TOP traps) [183], or even more sophisticated schemes to smooth the potentials based on fast modulation of trap current and external bias fields [202, 203] to alleviate this problem. Such methods either require RF-dressing techniques or a specialized chip design and have therefore not been used in the scope of this thesis.

4.5. Trap characterization

In traps where the effects of wire corrugations can be avoided, and if there are no RF dressing techniques used to explicitly introduce anharmonic contributions to the potential, chip traps are in good approximation of Ioffe-Pritchard type (see 4.1.1), and the confinement around the potential minimum is described by axial and radial trap frequencies ω_a and ω_r. To measure them, a straightforward method consists of introducing dipole oscillations of a cloud, since the dipole oscillation frequency along

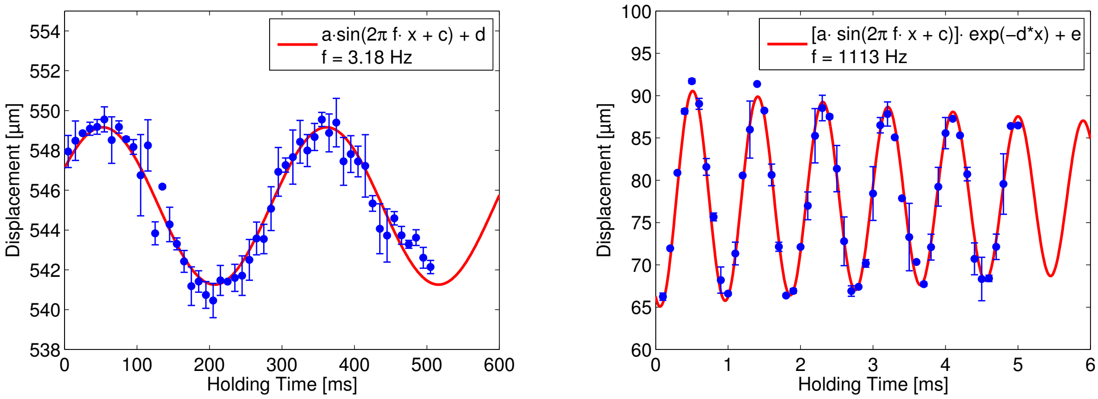

(a) Trap frequency measurement, axial direction. (b) Trap frequency measurement, radial direction.

Figure 4.20.: Dipole oscillations of quasicondensates for trap frequency determination. (a) Axial dipole oscillation induced by an axial shift of the trap via a small current in the guide wire. Errorbars correspond to the standard deviation from 5 pictures at identical parameters. (b) Radial dipole oscillation induced by a transverse shift of the trap via a current step for the central trapping wire. As in (a), errorbars are given by the standard deviation from a 5-shot average.

each trap axis equals the corresponding trap frequencies for both thermal clouds and quasicondensates. The excitation is performed by a displacement of the trap. Along the radial direction, the easiest way to accomplish this is condensation within a potential differing from the final trap by a fraction of 1% of the total current, in the order of a few mA. Upon realization of a quasi-BEC in a stationary state, the current is rapidly changed to the final value, causing the cloud to 'slosh' normal to the chip surface (the y-direction in the coordinate system used throughout this chapter.). Depending on the point in time of a subsequent trap switch-off, the momentum of this collective sloshing motion will point either against or into the direction of gravity, shifting the position of the expanded cloud as detected by absorption imaging. Such a measurement for the trap where the first condensates in our setup have been produced is shown in figure 4.20(b), yielding a value of $\omega_r = 2\pi \times 1113 \pm 4$ Hz.

To shift the trapping potential along the axial direction, one of the L-shaped guide wires featured on our chip can be used in a similar manner, keeping a current of roughly 0.1 mA during condensation, and ramping it down over 10 ms thereafter, fast enough to introduce axial sloshing but adiabatic with respect to the radial degrees of freedom. Figure 4.20(a) contains a measurement of the axial frequency corresponding the same trap as investigated in figure 4.20(b). The frequency is measured to be 3.18 ± 0.08 Hz.

An alternative method to measure radial trap frequencies is parametric heating. Here, the current used to generate the trapping potential is modulated in the expected trap frequency range. At resonance, this leads to parametric excitation of atoms and a sharp increase of losses that can easily be detected. An example for the use of this technique

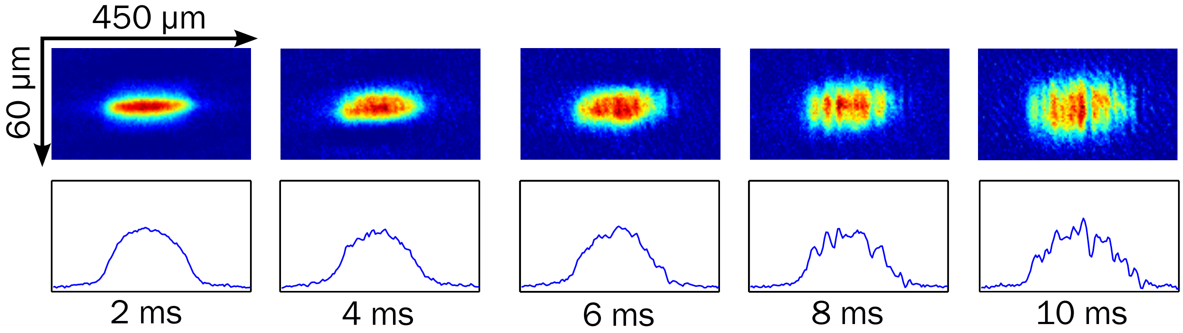

Figure 4.21.: Free expansion of a quas-1d BEC containing $\simeq 13000$ atoms from a trap characterized by $\omega_r \approx 2\pi \cdot 1000$ Hz and $\omega_a \approx 2\pi \cdot 8$ Hz. Upper panels show pictures of single atom clouds at expansion times between 2 and 10 ms, while lower panels contain corresponding density profiles integrated along the transverse direction. Both demonstrate the formation of an interference pattern caused by phase fluctuations within the trapped system.

in an atom chip experiment can be found in [31].

4.6. Temperature measurement based on density ripples

Thermometry of 1d quasi-BECs based on density correlations in free expansion as developed in reference [30] (see also section 2.5) and experimentally demonstrated in [15] is comprehensively described in the thesis [31]. Since this technique is central to the work presented here, this section discusses its implementation for the data analysis throughout chapters 5 and 6. In addition, a fast and robust way to estimate the temperature without explicitly fitting autocorrelation functions is outlined.

4.6.1. Basics

While it is possible to create a phase-coherent true BEC in one dimension in a trap at a finite number of particles, as discussed in section 2.3.2, the necessary conditions are hard to achieve in experiment. At realistic temperatures in an atom chip trap, remaining low-energy phononic excitations cause fluctuations that prevent phase coherence over the full extension of the system, forming a quasicondensate, as introduced in section 2.3. Section 2.5 discussed how in free expansion, phase gradients present in the cloud lead to the formation of interference patterns, and hence density fluctuations. As an example, figure 4.21 shows pictures and corresponding density profiles for the free expansion of a quasi-1d BEC of approximately 13000 atoms from a trap with $\omega_r \approx 2\pi \cdot 1000$ Hz and $\omega_a \approx 2\pi \cdot 8$ Hz. At the smallest expansion time of 2 ms, the density profile is still smooth on the scales resolved by our imaging optics. Only later, density fluctuations arise and become increasingly pronounced for longer expansion times. In contrast, for even later times of order ω_a^{-1}, these interference patterns would disappear, the expanded profile corresponding to the axial in-situ momentum distribution. As such, the observed interference patterns can be interpreted in analogy to near-field diffraction [31].

Section 2.5 discussed how the spectrum of phase fluctuations in the trapped system is governed by temperature through the first order correlation function, establishing a thermometry method that gives direct information about the phonon occupation numbers within the condensate, as opposed to indirect thermometry via thermal 'wings', requiring the assumption of equilibrium between condensed and non-condensed components of the cloud. In the following, the experimental implementation of this thermometry method is presented.

4.6.2. Implementation

Measurement principle. In the experiment, the temperature measurements work as follows. After preparation of the condensate, the trap is switched off, and the atom cloud undergoes a free expansion of 10 ms, sufficient for the formation of sizeable density fluctuations. This process is repeated at identical parameters to collect a set of $\mathcal{O}(100)$ pictures. Each of this pictures is summed along the transverse y-direction to yield an integrated linear density profile $n(z)$. The averaged normalized autocorrelation function $g^2\left(z-z'\right)$ for this dataset is calculated as

$$g^2\left(z-z'\right)=\frac{\left\langle \int dz' n\left(z'\right) n\left(z+z'\right)\right\rangle_i}{\int dz' \left\langle n\left(z'\right)\right\rangle_i \left\langle n\left(z+z'\right)\right\rangle_i}, \tag{4.16}$$

with $\langle\ldots\rangle_i$ denoting the average over a set of pictures, each with index i. For the experimental case of images with a discrete density n_m in each pixel m, this reduces to

$$g^2\left(\Delta z=\left(z_{n+1}-z_n\right)\right)=\frac{\left\langle \sum\limits_{n=0}^{N-m-1} n_{n+m} n_n \right\rangle_i}{\sum\limits_{n=0}^{N-m-1} \left\langle n_{n+m}\right\rangle_i \left\langle n_m\right\rangle_i}, \tag{4.17}$$

where N stands for the total number of pixels contributing to each profile. The blue circles in figure 4.22(b) correspond to such an autocorrelation calculated from a dataset of 250 pictures.

Finite-size model and imaging resolution. To estimate the temperature, the measured averaged autocorrelation function can be compared with the analytical result from equation 2.83. However, since this expression is strictly valid only for a homogeneous system, the model based on a parabolic density profile and stochastically generated phase fluctuations by an Ornstein-Uhlenbeck process from section 3.4 is used to take into account finite-size effects. Further, it is important to regard the finite resolution of our imaging system. For diffraction limited optics, point spread function (PSF) is given by a corresponding Airy-function [204], that is however well approximated by a Gaussian with a certain HWHM σ_{PSF}. The theoretical value from the Rayleigh-criterion determines a lower limit for the spatial separation that can be achieved. It can be validated

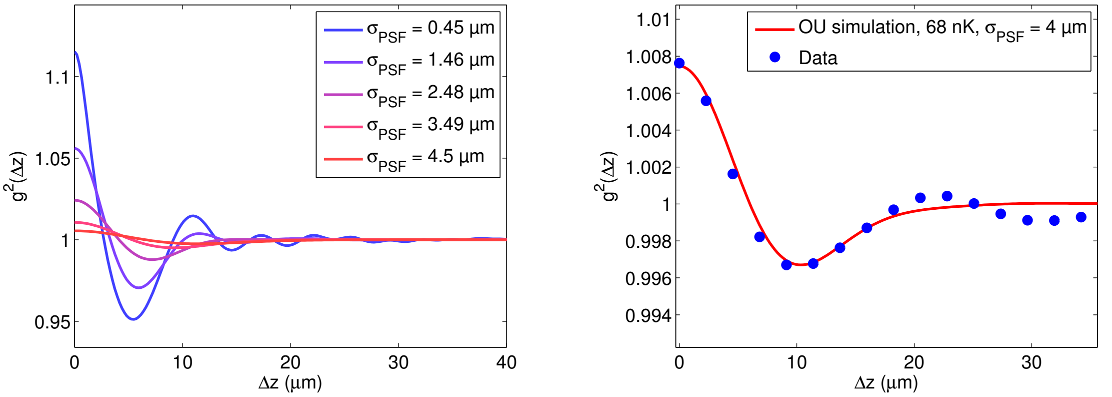

(a) Simulated g^2-functions and PSF.

(b) Measured and simulated g^2-function.

Figure 4.22.: Autocorrelation functions of density fluctuations in time of flight for thermometry. (a) Comparison of simulated g^2-functions for 10 ms expansion time, $T = 70$ nK, $n_0 = 200$ atoms per micron and $R_0 = 140$ μm for different PSFs as denoted in the legend. (b) Example: Comparison of simulated and measured g^2-functions for a dataset with $T = 68$ nK. Blue circles correspond to an average of 250 shots.

by independent measurements of the modulation transfer function on resolution targets [204, 170, 171]. Note that the transverse size of the expanded cloud might exceed the depth of focus of the imaging system, introducing another limit for the effective PSF width. Therefore, an additional independent estimation via the MTF-induced cut-off on the observed spectrum of density fluctuations needs to be performed [121], preferably on each dataset. For this, the presented analysis relies on the method outlined in [205]. According to these analyses, the PSF of our imaging system ranges between $\sigma_{PSF} \approx 4 \pm 0.1$ μm to $\sigma_{PSF} \approx 4.5 \pm 0.12$ μm, depending on the cloud's position in the field of view and diameter along the imaging axis. Convolution of the simulated expanded density profiles with the Gaussian PSF yields the final calculated autocorrelation, as given by the red line for the example shown in figure 4.22(b). For comparison, simulated autocorrelation functions at different PSF widths are plotted in figure 4.22(a).

Fitting based on the finite size model. It is instructive to briefly discuss some qualitative properties of this function. The position of the minimum at a given PSF is determined by the expansion time. This is clear in the treatment of the interference as near-field diffraction on a randomly spaced target, leading to Talbot-conditions for different frequency components at corresponding times of flight [15]. The height of the central peak is proportional to temperature, as apparent from equation 2.83, and can be used for thermometry as in reference [15]. However, a common error source was found to stem from the normalization of g^2-function. Here, slight shifts in the centre of mass position, residual shape oscillations of the cloud and shot-to-shot atom number fluctuations lead to offsets on the y-axis or overall slopes on the function. To minimize these spurious influences, a region of interest containing the cloud is defined on each picture

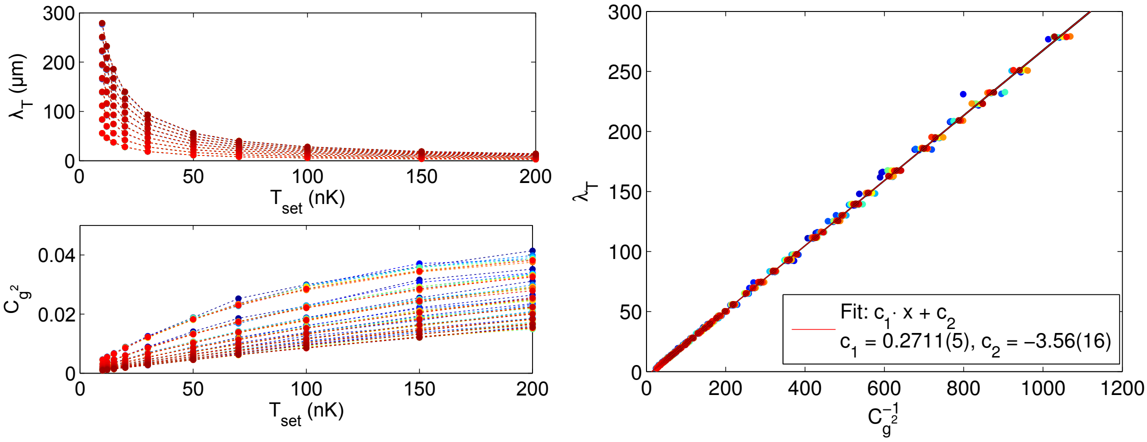

(a) λ_T and C_{g^2} versus temperature.

(b) λ_T plotted against C_{g^2}.

Figure 4.23.: The g^2 function contrast and thermometry. (a) Thermal coherence length λ_T (see equation 4.18) at the cloud center and contrast C_{g^2} as defined within the text, resulting from an Ornstein - Uhlenbeck simulation for peak densities and cloud radii ranging from $30 < n_{1d} < 300$ atoms/μm and $30 < R_{TF} < 300$ μm, respectively, plotted against the preset temperature, taking into account an experimental point spread function with a radius of $\sigma = 4.5$ μm. (b) Plotting the coherence lengths for all parameters as shown in the upper panel of (a) against the corresponding inverse g^2 contrast $C_{g^2}^{-1}$, a linear functional relationship is revealed, allowing a temperature calibration independent of cloud radius or density by a fit that is depicted together with confidence limits (red curve and grey area).

and shifted to centre the peak of the density distribution determined by fits along each axis. In addition, post-selection to minimize atom number fluctuations can be applied. Still, residual offsets render the peak value of the $g^2(\Delta x)$ to be a rather unreliable temperature measure. The best results are gained from a comparison of measurements with a set of pre-calculated autocorrelation functions for measured densities, cloud widths and a temperature range between 30 and 200 nK in terms of a least-squares fit of the full g^2-function, taking into account possible residual shifts along the y-axis. The correct temperature minimizes the χ^2-value of the fit. This analysis is very similar to what is presented in the thesis [201].

Temperature estimation from the g^2-function contrast. For datasets encompassing a large parameter range, fits based on the numerical calculation of phase distributions are time-consuming. To improve performance, on the one hand a fully vectorized version of the updating formula 3.32 has been implemented. On the other hand, a stable temperature measure that doesn't rely on explicit fitting has been found in terms of the *contrast* of the g^2-function $C_{g^2} = g^2(\Delta z = 0) - \min(g^2(\Delta z))$ that by construction is insensitive to offsets on the g^2-function. The prefactor of expression 2.82, determining this contrast, only depends on the thermal phase coherence length λ_T via a linear relationship $C_{g^2} \propto \lambda_T^{-1}$. The exact proportionality depends on the PSF, but was found to be universal with respect to the density or the cloud radius also for the finite-size problem as presented in figure 4.23. Comparing the contrast of simulated g^2-functions with the thermal phase coherence length in the trap center

$$\lambda_T = \frac{2\hbar n_0}{mTk_B}, \tag{4.18}$$

where n_0 represents the cloud's peak linear density, for an experimental PSF width of $\sigma_{PSF} = 4.5\ \mu$m, yields the proportionality

$$\lambda_T = \frac{0.2711}{C_{g^2}} - 3.56, \tag{4.19}$$

with λ_T given in microns. Using this calibration to calculate temperatures from the contrast C_{g^2} of simulation runs covering a range of densities between 25 and 250 atoms per micron and cloud radii from 30 to 300 μm yields the results shown in figure 4.24. Data points are plotted against the set temperatures for the OU-algorithm used to generate the phase profiles. Errorbars correspond to the standard deviation across all densities and radii at a given set temperature, while the black dotted line represents unity slope. For better visibility, the inset shows $T_{fit} - T_{set}$. The results indicate no significant dependence on any parameter except temperature. In practice, this calibration is used to estimate the approximate temperature of the cloud, allowing to narrow down the range covered by the full fitting procedure.

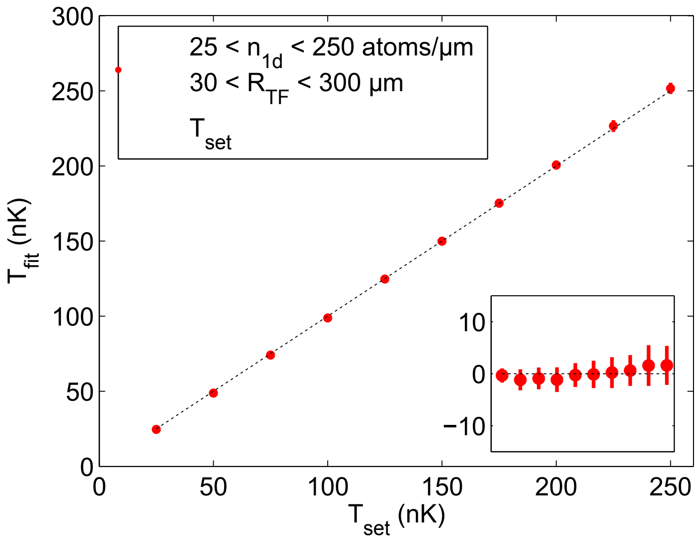

Figure 4.24.: Temperature and g^2-contrast: Simulation results. Temperature estimated from C_{g^2} by the calibration 4.19 and 4.18 from profiles generated by an Ornstein-Uhlenbeck process. Red circles correspond to an average over results T_{fit} for peak densities ranging from $25 < n_{1d} < 250$ atoms per micron as well as Thomas-Fermi radii between 30 μm and 300 μm. Errorbars correspond to standard deviations corresponding to the averages, while the black dotted line indicates unity slope, representing the expected results T_{set}. For better visibility of the absolute uncertainty, the inset shows $T_{fit} - T_{set}$.

Uncertainty. Residual relative fit errors are contributed by experimental shot-to-shot temperature variations, fluctuations in the cloud shape, the fit uncertainty as well as the temperature spread of the stochastic model. The standard deviation of the latter is in the order of 1 %, and the resulting error on the mean temperature can be suppressed to a level of $\approx 10^{-4}$ by averaging over a number of 500 simulated phase distributions. To estimate the relative error contributed by the other factors, a bootstrapping-based resampling method [206, 207] is used. Instead of calculating the average autocorrelation function from a dataset once, a number of $\mathcal{O}(100)$ picture subsets are generated by random drawing with replacement. The standard deviation of the resulting temperatures for each subset is an estimator for the RMS spread of the measurement, if the temperature distribution is Gaussian. For the measurements presented in this thesis, a number 150 subsets is used unless stated otherwise, and errorbars on temperatures are a result of the bootstrapping method. The uncertainty on the effective PSF radius in the order of 3 % introduces the main systematic contribution to the absolute measurement error of $\sim 10\%$.

Part II.

Physics

5. Quasi-BEC dynamics in time-dependent trapping potentials

This chapter discusses the behaviour of phononic excitations in breathing 1d quasi-condensates. A dynamical symmetry of the underlying Hamiltonian allows to derive a scaling solution, predicting the time-dependence of correlation functions for a given initial state. The results of this theory are compared to temperature measurements for different initial conditions, and to numerical simulations.

5.1. Introduction

As discussed in chapter 2, a 1d quasi-BEC behaves in many respects as an ideal fluid that can be described in terms of hydrodynamics, similar to the corresponding 3d system. In such a picture, low-lying collective excitations of the mean-field density profile are well understood since many years [98]. In contrast to a 3d BEC, however, fluctuations destroy the long-range order of the system. These fluctuations can be understood in terms of phononic excitations, with a thermal occupation number distribution if the system is in an equilibrium state. These modes are well-defined in terms of the Luttinger liquid model of a trapped system presented in chapter **??**. This model, however, has been developed for static density profiles and does not capture the description of phononic excitations in the presence of collective dynamics of the mean-field density a priori.

As outlined in sections 2.5 and 4.6, the loss of phase coherence due to phononic excitations leads to characteristic interference patterns (”density ripples”) emerging during free 3d expansion. For a thermal state in a static cloud, we can calculate the shape of the spectrum, or equivalently the average autocorrelation function of these interference patterns. A comparison between predicted and measured correlations allows us to extract the temperature associated with the phonon ensemble.

The aim of this section is to understand how these phononic excitations affect - and, more importantly, are affected by - low-lying collective modes. In particular, the quadrupole oscillation, also called ”breathing” in the literature, is studied. Its frequency has been calculated throughout the phase diagram of the 1d Bose gas [98], and it can be excited easily in our experimental setup without introducing other collective modes. Finally, since the breathing mode consists of a repeated compression and decompression of the cloud, an understanding of phononic excitations for this case lays the ground for rapid adiabatic compression and decompression schemes presented in chapter 6 as well as the description of a continuous 1d expansion of a quasicondensate - a scenario presented in chapter 7 and which is interesting for many proposals to use cold atoms as a toy model for effects in cosmology [208, 27, 28, 29, 26, 209, 210, 211].

Section 5.2 introduces the concept of a scaling transformation to describe the time dependent ground state wave function of the corresponding Gross-Pitaevskii equation (GPE) that can be used to describe a system in the presence of breathing, before presenting the experimental protocol used to induce the mode in a controlled manner together with several necessary characterization measurements. The second section generalizes these results and presents a solution for the corresponding many-body dynamics that has been found recently. We use this approach to derive the rescaled phase correlation function for a quasi-1d Bose gas in the Thomas-Fermi regime, considering an initially thermal state within a Luttinger liquid description. The rescaled function can be expressed in terms of a temperature that changes adiabatically with the spatial extension of the system. This temperature is an observable that can be measured in our experiments, and we present a comparison of theory, data and numerical calculations.

5.2. Trap quench: Breathing dynamics

Any collective dynamics can be considered as an answer of the system to a non-adiabatic change of an external parameter, also called 'quench' in the field of many-body quantum physics. In this section, a model of the breathing dynamics resulting of a trap quench with respect to the axial confinement in terms of a scaling solution to the time dependent GPE is presented. A discussion of the experimental scheme, the trap geometry and technical constraints is given, followed by a characterization of the breathing mode induced by our protocol.

5.2.1. Gross-Pitaevskii equation with time-dependent external potential

In order to describe the low-lying collective excitations of a BEC, fluctuations can be neglected and a mean-field description in terms of a Gross-Pitaevskii equation is sufficient:

$$i\hbar\frac{\partial\Psi_0}{\partial t} = -\frac{\hbar^2}{2m}\Delta\Psi_0 + \frac{m\omega_a^2(t)z^2}{2}\Psi_0 + \bar{U}\left|\Psi_0\right|^2\Psi_0, \tag{5.1}$$

with the mean-field wave function depending on time and spatial coordinates as

$$\Psi_0 = \Psi_0\left(\boldsymbol{r}, t\right).$$

This equation is explicitly time-dependent by the trap frequency $\omega_a(t)$. Under certain conditions discussed below, this equation can be solved exactly, as demonstrated in [32, 33]. In the following, this solution is discussed, using the notation adopted in [32], with emphasis on the Thomas-Fermi limit, as outlined in [212].

Scaling solution for the mean-field Hamiltonian

The goal is to find a scaling transformation acting on the wave function ψ_0 that keeps the form of the GPE intact, but yields a Hamiltonian that does not explicitly depend on time, but only implicitly due to rescaled distances and times $\boldsymbol{\rho}(\boldsymbol{r},t) = r/b(t), \tau(t)$ with a scaling parameter $b(t)$. Indeed, such a transformation exists and has the form

$$\Psi_0(\boldsymbol{r},t) = \frac{1}{b(t)^{d/2}} \chi_0\left(\boldsymbol{\rho},\tau\right) e^{i\Phi(\boldsymbol{r},t)} \tag{5.2}$$

with d denoting the spatial dimension of the system, and a phase

$$\Phi(\boldsymbol{r},t) = \frac{mr^2}{2\hbar} \frac{\dot{b}(t)}{b(t)}.$$

Substituting the ansatz (5.2) into equation (5.1) yields:

$$i\hbar \frac{\partial \chi_0}{\partial t}\left[\frac{d\tau}{dt} b^2(t)\right] = -\frac{\hbar^2}{2m}\Delta_\rho \chi_0 + \frac{m}{2}\left[\left(\omega_a^2(t) + \frac{\ddot{b}(t)}{b(t)}\right) b^4(t)\right]\rho^2\chi_0 + \frac{\bar{U}}{b(t)^{d-2}}\left|\chi_0\right|^2\chi_0 \tag{5.3}$$

To recover the form of the initial GPE (5.1), the expressions in square brackets, as well as the $b(t)$-dependence in the interaction term need to vanish. Note that for $d = 2$, this dependence vanishes identically. This case has been discussed in detail in [34] and is an instance of a hidden dynamical SU(1,1) symmetry, the existence of which is the reason behind the applicability of a scaling solution as outlined here [36]. It is present in many interesting systems, among them the quantum mechanical harmonic oscillator [213].

Turning to our case of $d = 1$, the interaction term scales as $\bar{U}b(t)$. Here, the following options exist to restore the symmetry:

- $\bar{U} = 0$, i.e. the noninteracting case.
- $\bar{U}b(t) = const$, which implies tuning interactions via the scattering length or the radial trap frequency.
- $\bar{U}b(t) \to \infty$, the Tonks-Gireardeau gas in the hard-core limit. For this system, a scaling approach has been used in [35] to construct an exact solution for the time-dependent many-body problem.
- Vanishing kinetic term, as valid deeply in the Thomas Fermi-regime. This is the usual scenario for quasi-1d BECs in atom chip experiments, and the regime investigated in this thesis.

In the 1d Thomas-Fermi approximation, the transformed equation reduces to:

$$i\hbar \frac{\partial \chi_0}{\partial t}\left[\frac{d\tau}{dt} b(t)\right] = \frac{m}{2}\left[\left(\omega_a^2(t) + \frac{\ddot{b}(t)}{b(t)}\right) b^3(t)\right]\rho^2\chi_0 + \bar{U}\left|\chi_0\right|^2\chi_0 \tag{5.4}$$

This implies the following conditions fixing $\tau(t)$ and the relation between $\omega(t)$ and $b(t)$:

$$\tau(t) = \int_0^t \frac{dt'}{b(t')}$$

$$\ddot{b}(t) + \omega_a^2(t) b(t) = \frac{\omega_0^2}{b^2(t)}, \tag{5.5}$$

the latter being a variant of the Ermakov equation [214, 215]. In the new variables τ and ρ, the problem is reduced to finding an initial state $\bar{\Psi}_0\left(z,0\right)$ that is a solution of the GPE with constant frequency $\omega_a\left(0\right)$, and solving equation 5.5 to find the correct scaling $b\left(t\right)$. Then, the solution at any time t reads

$$\Psi_0(r,t) = \frac{1}{\sqrt{b(t)}} \bar{\Psi}_0\left(\frac{r}{b(t)}, 0\right) \exp\left(\frac{imz^2}{2\hbar}\frac{\dot{b}(t)}{b(t)} - i\mu\tau(t)\right). \tag{5.6}$$

For the density profile, this ansatz predicts the well-known self-similar time-evolution

$$n\left(z,t\right) = \frac{1}{b}\bar{n}\left(\frac{z}{b},0\right).$$

For a parabolic profile in a harmonic trap, this becomes

$$n\left(z,t\right) = \left(\frac{\bar{n}_0}{b}\right)\left(1 - \frac{z^2}{R_0^2 b^2}\right)\Theta\left(1 - \frac{z}{R_0 b}\right), \tag{5.7}$$

where the scale parameter can be defined as

$$b(t) = \frac{R(t)}{R_0}, \tag{5.8}$$

with $\bar{n}_0$, R_0 and $R(t)$ denoting the initial peak density, Thomas-Fermi radius and the time-dependent cloud radius, respectively. Given knowledge of the trap-frequency behaviour $\omega_a(t)$ in the experiment, this constitutes a full description of the breathing dynamics.

Modified Ermakov equation for time-dependent interactions

Equation 5.5 has been derived with a time-independent interaction constant $\bar{U} = g_{1d} = 2a\hbar\omega_r$ in mind, where a denotes the 3d scattering length of ^{87}Rb as defined in appendix A. As will be discussed in section 5.2.2, however, ω_r is coupled to ω_a in our experiment, and therefore time-dependent. Expressing $\omega_0 = \omega_a(0)$ in terms of the initial Thomas-Fermi radius

$$R_0 = \sqrt{\frac{2g_{1d}\bar{n}_0}{m\omega_0^2}},$$

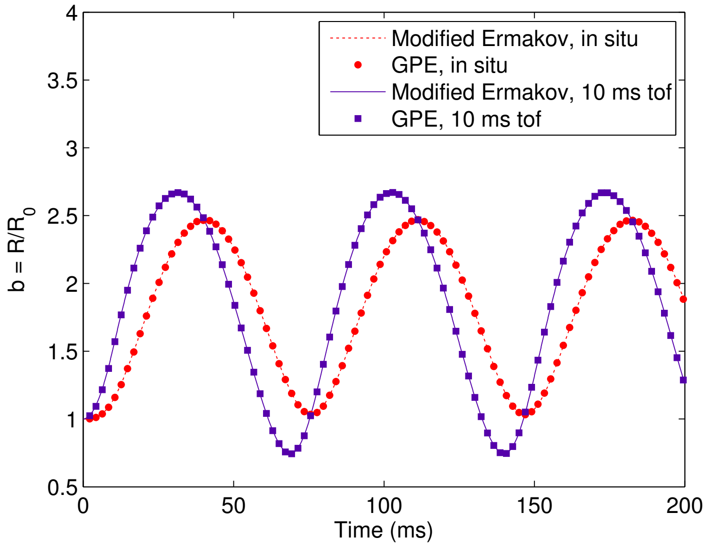

Figure 5.1: Modified scaling equation compared to GPE simulations. The in situ scale parameter $b = R(t)/R_0$ calculated from a GPE simulation (red dots) and equation 5.9 (red dotted line) is plotted against time for a ramp with duration $\tau = 10$ ms between an initial trap characterized by $\omega_a = 13.5$ Hz and $\omega_r = 630$ Hz and a final trap at $\omega_a = 8$ Hz and $\omega_r = 990$ Hz. Purple dots and straight line represent results from the GPE simulation and equation 5.9, respectively, for the scale parameter in free expansion $b_{tof} = b + t_{exp}\dot{b}$

one can substitute

$$\omega_0 = \sqrt{\frac{4\hbar a\omega_r\left(t\right)\bar{n}_0}{mR_0^2}} =: \sqrt{k_0\omega_r\left(t\right)}$$

into equation 5.5 to arrive at

$$\ddot{b}(t) + \omega_a^2(t)b(t) = \frac{k_0\omega_r\left(t\right)}{b^2(t)}. \tag{5.9}$$

To check whether this equation describes the correct scaling of the density profile, it can be compared with a 1d GPE simulation. Figure 5.1 shows the results for such a comparison of the scale parameter $b(t)$ in situ and after free expansion,

$$b_{tof}\left(t, t_{exp}\right) = b\left(t\right) + t_{exp}\dot{b}\left(t\right),$$

respectively, yielding excellent agreement and demonstrating the validity of the modified scaling equation.

5.2.2. Experimental scheme

The basic protocol for the measurements discussed in this chapter is as follows: First, a quasi-1d BEC in the Thomas-Fermi regime at thermal equilibrium is prepared, in a trap with well defined axial and transverse confinement. Then, we change the confinement in a controlled way to induce a breathing oscillation or 1d expansion. We let the cloud evolve for a time t, then switch off the trap and probe the cloud's density profile after a free expansion time t_{tof} by standard absorption imaging techniques as discussed in chapter 4.

Chip layout and constraints

As shown in chapter 4, axial and transverse confinement of an atom chip trap as well as the position of the trap minimum are governed by the spatial dimensions and shape of the used wire structures, the direction and magnitude of the currents in these wires, and the direction and magnitude of external bias fields. Any rapid change of these parameters will cause deformation and (or) displacement of the trap and induce collective excitations. For our measurements, we only want to excite an axial breathing mode. This places several constraints on our protocol: The axial trap minimum needs to stay at a fixed position. Additionally, the transverse trap minimum and confinement must be either constant, or any change needs to be slow compared to the time scale associated with the radial trap frequency $(\omega_r/2\pi)^{-1}$ to prevent the introduction of transverse dynamics.

Further, in order to use the model presented in the next subsection, we want to ensure a harmonic potential along all directions. For a regular Z-shaped wire trap, the transverse potential is always harmonic and isotropic[1], characterized by a radial trap frequency ω_r. Also, the axial potential is in general not harmonic throughout the parameter range. Additionally, wire corrugations can lead to irregularities in the current flow for small distances between trap minimum and chip surface, deforming the axial potential.

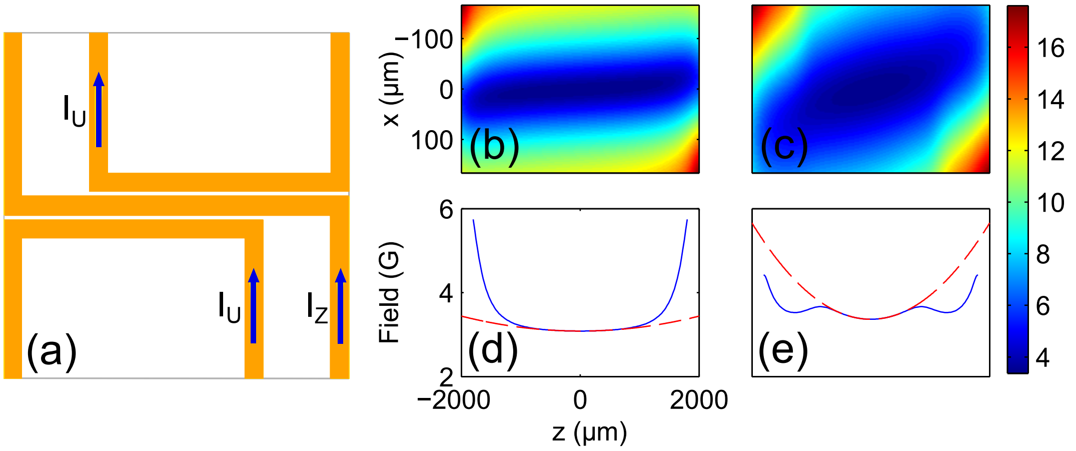

Figure 5.2.: Time dependent potentials on an atom chip. (a) The current ratio between a central Z-shaped wire and two U-shaped control wires allows us to precisely tune the trap geometry. For a symmetric current flow, the trap minimum is positioned below the center of the Z-wire, with the long trap axis aligned to the horizontal direction. (b) 2d cut through the trapping potentials for $I_Z = 2A, I_U = 0A$ and (c) $I_Z = 1.5A, I_U = 1A$ at a constant external bias field of $B = 26G$, respectively. (d,e) Cuts through the radial trap minimum of the same potentials to show the axial trap deformation.

To accommodate for these constraints, we use a combination of currents through a Z-shaped trap wire and two U-shaped control wires, as shown in figure 5.2a. The potential landscape generated by such a configuration is very flexible, allows the implementation of harmonic axial traps governed by an axial trap frequency ω_a, and can be calculated in a straightforward way by numerically solving the Biot-Savart equation for rectangular wire pieces and adding up the contributions. Figure 5.2b-e show cuts through the calculated 3d potential in the xz-plane, and along the z-direction respectively for two different current combinations. In a symmetric configuration, running identical currents through both control wires, the axial trap minimum stays always at a fixed central position. At distances between trap minimum and chip bigger than ∼80 μm, wire corrugations, which become visible as deviations from a parabolic density profile of the condensate, can be neglected and the calculations give an excellent description of our trap geometry. In order to prevent radial excitations, the effect of changes in the wire currents on the trap position and confinement could be counteracted by adjusting the external bias fields accordingly. However, this is impractical in our setup since these fields are produced by macroscopic coils, and fast changes in the set current lead to an oscillatory behaviour of the field. While this effect can be cancelled by a suitably designed control pulse, as shown in chapter 4, the minimum time scale for pulses that we have achieved is on the order of 7 ms. For linear current ramps of such a duration, the radial dynamics was shown to be adiabatic, while for the optimal control ramps presented in chapter 6, we would need a much higher time resolution. Therefore, external fields are kept fixed throughout our experiments.

---

[1] Note that RF-dressing techniques realized in other atom chip experiments allow to introduce both anharmonicity and anisotropy of the transverse potential

	I_Z (A)	I_U (A)	B_B (G)	B_I (G)	ω_a (Hz×2π)	ω_r (Hz×2π)
Initial trap	1.5	1	26	0.89	12.1 ± 0.25	630 ± 6
Final trap	2	0.3	26	0.89	8.23 ± 0.12	989 ± 5

Table 5.1.: External parameters and measured frequencies corresponding to the initial and final traps used throughout section 5.2 and 5.3.

Trap frequency calibration

Taking all discussed effects into account, we pick two trap configurations and now turn to their characterization in the experiment. For each trap, we prepare a quasi-BEC, measure the radial and axial trap frequencies by inducing a 'sloshing' dipole oscillation as outlined in chapter 4 and track the center-of-mass position of the cloud. Table 5.1 shows parameters and the results of trap frequency measurements for an initial and final trap as used for throughout section 5.2.

5.2.3. Characterization of the breathing mode

So far we have discussed how to induce the breathing mode, and the trap geometry. Here, the mode is characterized, taking into account heating of atoms in chip traps, and the impact of deviations from the 1d-description given section 5.2.1 arising in the 1d/3d crossover regime.

Breathing and RF Shield

Figure 5.3 shows the time evolution of an atom cloud after inducing a breathing mode by a linear ramp between the initial and final trap currents given in table 5.1. The first column shows density profiles as well as axial and radial cloud extensions for the dynamics after switching off evaporative cooling. This dataset demonstrates depletion of the condensate and build-up of a thermal cloud due to heating processes that dominates the dynamics after 200 ms of evolution time. Heating of 1d Bose gases in a chip trap, as the inverse process of evaporative cooling in 1d investigated in our group at the time of writing this thesis [81], is not completely understood yet. Different effects contribute, including atom loss due to collisions with background gas atoms, 3-body recombination [196, 197, 198, 199], direct heating of atoms in the ground state due to fluctuations of the magnetic trapping fields, [31, 216] and heating of thermal atoms in transverse excited states of the trap and their back-action on the quasicondensate by two-body collisions. Especially the interaction between condensate and thermal atoms lacks a theoretical description, and numerical tools to deal with these processes in a satisfactory way have only started to emerge recently [117].

For our measurements, it is important to approach the ideal case of a closed system as good as possible. One option is the application of a radio-frequency field (”RF shield”) to remove hot thermal atoms, preventing secondary collisions and ensuing additional heating. The middle and right columns in figure 5.3 show data for RF shields at frequencies of 1.16 MHz and 1.06 MHz, corresponding to a distance in frequency of 150 and 10 kHz with respect to the chemical potential. For these values, we don't expect direct evaporative cooling of the quasicondensate fraction. At 1.16 MHz (middle column), the axial breathing mode is still visible beyond 200 ms of evolution time, but the transverse ground state dynamics is hidden by the thermal component at late times (see also references [59] and [99]). At 1.06 MHz, the breathing mode survives over the full 400 ms of evolution time, with some residual damping.

In order to minimize the influence of thermal atoms without risking direct evaporative cooling of the condensate, all measurements are thus performed with an RF shield at 10 kHz distance from the chemical potential, and the evolution time is restricted to the first 200 ms after the trap quench. The overall atom loss rate during this period is discussed in section 5.3 on the basis of the datasets used for temperature measurements on breathing clouds.

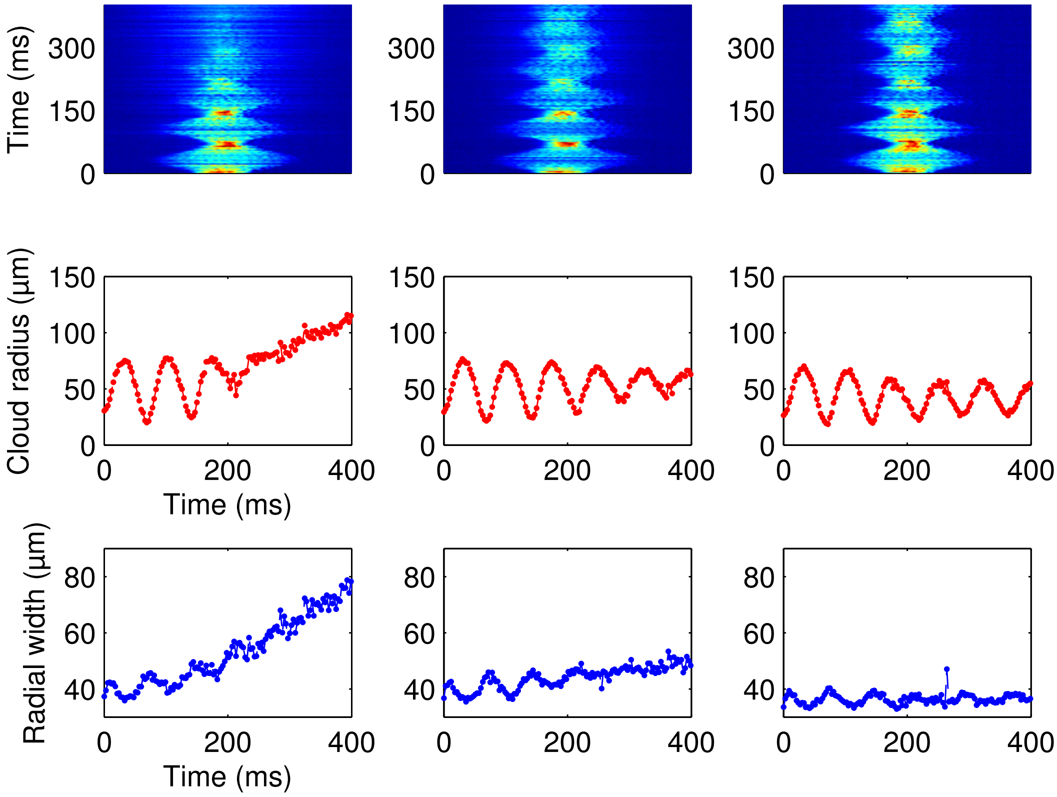

Figure 5.3.: Breathing mode and RF knife. The left, middle and right columns correspond to data taken for no RF shield, an RF shield at 1.16 MHz, and an RF shield at 1.06 MHz, respectively. The upper panels show density profiles for the time evolution of a cloud after the quench. Each profile is integrated from a single picture taken after an evolution time ranging between 0 and 400 ms in steps of 3 ms, and after 10 ms of free expansion. The middle panels depict the axial Thomas-Fermi radius from fits to these density profiles over time, whereas the lower panels show the RMS width of Gaussian fits to density profiles integrated along the axial direction. Results are discussed in the main text.

Characterization measurements

To characterize the breathing dynamics in our experiment, 11 datasets similar to the ones shown in figure 5.3 are analysed. Figure 5.2.3 shows the Thomas-Fermi radius, determined from a fit to each profile as described in section 2.4, plotted against time for a quench of duration τ =12.5 ms as an example. The time evolution of the radius during breathing $r(t)$ is of the form

$$r\left(t\right) = ae^{-\lambda t}\sin\left(ft + c\right) + d \qquad (5.10)$$

with a, f, λ, c and d denoting amplitude, frequency, damping rate, phase shift and an offset given by the average cloud radius, respectively.

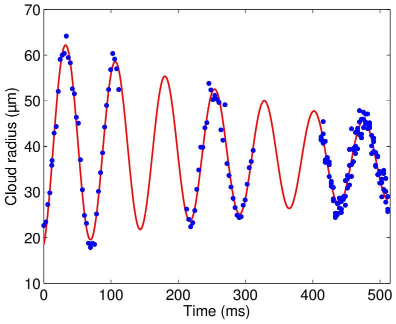

Figure 5.4.: Example of a breathing mode induced by a trap quench during a time τ = 12.5 ms and a fit as given in equation 5.10.

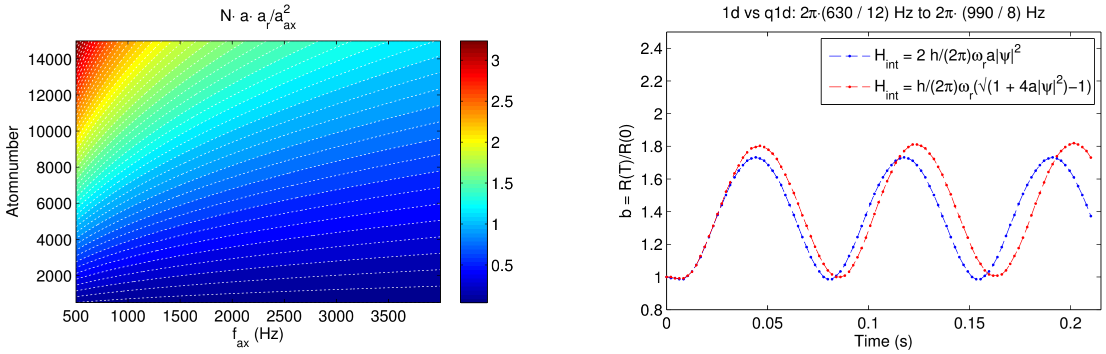

(a) Naa_r/l_a^2 over atom number and radial trap frequency

(b) Breathing: 1d vs. q1d GPE

Figure 5.5.: (a) The quantity Naa_r/l_a^2 governing the breathing frequency shift in the 1d-3d crossover regime as discussed in [98] for the typical accessible parameter range in atom chip traps ranging from 500 to 15000 atoms, and radial trap frequencies $f_r = 500$ to 4000 Hz. (b) Comparison of the breathing mode induced by a quench from $\omega_a = 2\pi \times (12)$ Hz and $\omega_r = 2\pi \times (630)$ Hz to $\omega_a = 2\pi \times (8)$ Hz and $\omega_r = 2\pi \times (990)$ Hz and 16000 atoms ($Naa_r/l_a^2 \approx 2$) in a time $\tau = 10$ ms, numerically calculated by a regular time-dependent 1d-GPE (blue) and a 1d GPE modified by a correction to the interaction term derived for the 1d/3d crossover regime [65, 100]. The observed frequency $(\omega_b/\omega_a)^2 \sim 2.6$ is consistent with an estimation based on the results calculated in [98] for our parameters, as discussed in the main text.

Frequency. For a weakly interacting 1d Bose gas, the breathing frequency should universally follow the relation $\omega_b/\omega_a = \sqrt{3}$ [217], consistent with the scaling equation 5.5, that only predicts small deviations from this value for large breathing amplitudes. In the 1d-3d crossover regime however, as discussed in reference [98], the ratio ω_b/ω_a is expected to interpolate smoothly between the 1d limit of $\omega_b/\omega_a = \sqrt{3}$ and the elongated 3d regime characterized by $\omega_b/\omega_a = \sqrt{2.5}$, over a broad range of the parameter Nal_r/l_a^2, where l_r and l_a denote the radial and axial harmonic oscillator lengths

$$l_r = \sqrt{\hbar/m\omega_r},$$

$$l_a = \sqrt{\hbar/m\omega_a}.$$

Section 2.4 discussed how the equilibrium density distribution of trapped atoms is affected in the 1d-3d crossover regime, and that this effect can be described in terms of a modified interaction term in the GP equation. This modification also affects the breathing dynamics. While, as outlined in the following, the self-similar time evolution of the density distribution is conserved in good approximation, the breathing frequency is shifted significantly with respect to the ideal 1d limit.
Figure 5.5(a) plots this parameter for atom numbers and radial trap frequencies that are accessible in our setup and shows it to range between 0.04 and 3.3, where, according to [98], deviations from the 1d limit are expected. As an example, figure 5.5(b) shows simulated breathing modes induced by a quench for typical experimental parameters as defined in the figure caption, where the time evolution is calculated with a 1d and

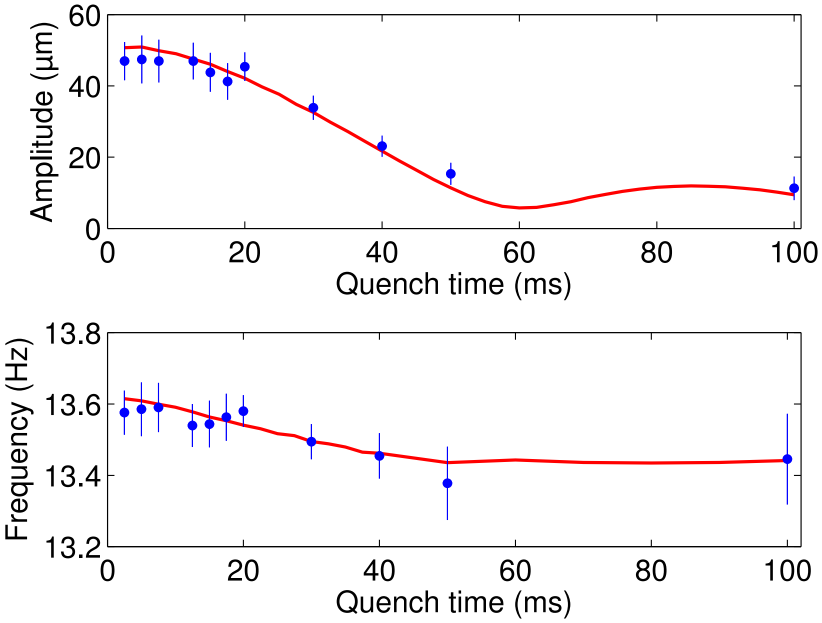

Figure 5.6.: Breathing amplitude and frequency plotted against quench time τ. Error bars correspond to 95 % confidence intervals of fits as shown in figure 5.2.3. The theoretical calculations (red lines) are based on numerically solving a 1d GPE with modified interaction term to account for deviations from the 1d regime.

modified interaction term, respectively, illustrating the frequency shift with $(\omega_b/\omega_a)^2 \sim 2.6$ for the quasi-1d case, consistent with what is expected from reference [98].

Amplitude and cloud shape. As frequencies, amplitudes follow the scaling equation 5.5 in the 1d-limit, while deviations in the 1d/3d crossover regime are covered by a modified GP equation. One might suspect that the shape of the density profile is also distorted during time-evolution, breaking self-similarity. In order to estimate the influence of this effect, one can compare the maximum difference in local density between simulated and rescaled initial profiles as given by equation 5.8. For the parameters used in figure 5.5(b), a maximum difference of <4% is found. Note that for simulations in the 1d limit, where the scaling solution is exact, the residual numerical difference amounts to 0.7%.

Results. Figure 5.2.3 summarizes amplitudes and frequencies extracted from data taken for different quench times between 2.5 and 100 ms, comparing them to quasi-1d GPE simulations as presented in this section, including the effect of a 10 ms time-of-flight expansion. For this parameter range, both frequencies and amplitudes are well described by our mean-field model without any free parameters. To account for damping, resorting to fits is still necessary and yields a characteristic time scale of $\tau_b = 500 \pm 56$ ms, averaged over all 11 datasets.

5.3. Excitation dynamics

5.3.1. Scaling solution for the many-body Hamiltonian

In the previous section, we have discussed the dynamics of the mean-field wave function in the presence of a time-dependent external potential in terms of a scaling solution. However, a similar ansatz can be invoked to gain a scaling transformation that solves a time-dependent many-body Schrödinger equation:

$$\frac{\partial\psi(\boldsymbol{x}_1,\ldots,\boldsymbol{x}_N;t)}{\partial t} = H(t)\psi(\boldsymbol{x}_1,\ldots,\boldsymbol{x}_N;t). \tag{5.11}$$

Here, ψ denotes a wave function which depends on the spatial coordinates $\boldsymbol{x}_i$ of each trapped particle. A special case found to be amenable for a scaling solution is the Tonks-Girardeau gas at infinite interaction strength, as discussed in reference [35]. Another instance for the application of a scaling solution is a Fermi-gas at unitarity [218]. An extension of this method to provide a general formalism covering a large class of systems is presented in reference [36]. The corresponding Hamiltonian is given by:

$$H(t) = \frac{1}{2m(t)}\sum_{i=1}^{N}\Delta_{x_i}^{(D)} - \mu(t)N + \lambda(t)\sum_{i=1}^{N}\boldsymbol{x}_i + \frac{m(t)\omega_a^2(t)}{2}\sum_{i=1}^{N}\boldsymbol{x}_i^2 + \sum_{i\neq j}V(\boldsymbol{x}_i - \boldsymbol{x}_j;t). \tag{5.12}$$

Here, $m(t)$, $\mu(t)$ and $\lambda(t)$ denote a time-dependent mass, chemical potential and linear potential, respectively, while $\omega_a(t)$ represents the time-dependent axial trap frequency as in previous sections. The scaling solution is given by

$$\psi(\boldsymbol{x}_1,\ldots,\boldsymbol{x}_N;t) = \frac{1}{R^N(t)}\Phi(\boldsymbol{y}_1,\ldots,\boldsymbol{y}_N;\tau)\exp\left(i\left[F(t)\tilde{\phi}(\boldsymbol{x}_i^2,\boldsymbol{x}_i,t)\right]\right), \tag{5.13}$$

where the coordinates $[\boldsymbol{y}_1,\ldots,\boldsymbol{y}_N]$ are given by a scale transformation $\boldsymbol{y}_i = (\boldsymbol{x_i}/L(t) + \boldsymbol{S}(t))$ at a spatial dimension of the system N.

The interaction potential needs to be homogeneous to order α

$$V\left(\lambda\boldsymbol{x}\right) = \lambda^{\alpha}V\left(\boldsymbol{x}\right),$$

where α is defined by the dimensionality and type of the interaction potential. This condition is fulfilled by a large class of interaction potentials [36], including our case of repulsive s-wave interactions $V(\boldsymbol{x}) \propto \delta(\boldsymbol{x})$. Additionally, there is a number of time-dependent parameters in the Hamiltonian, such as the mass $m(t)$ and chemical potential $\mu(t)$ and corresponding constraints that are discussed in detail within reference [36]. When fulfilled, the Schrödinger equation for the transformed wave function $\Phi(\boldsymbol{y}_1,\ldots,\boldsymbol{y}_N;\tau)$ is time-independent, and solving the dynamics reduces to defining the initial many-body wave function $\psi(\boldsymbol{x}_1,\ldots,\boldsymbol{x}_N;t)$. While this is a daunting task by itself, reference [36] shows how to exploit the form of the transformation 5.13 to relate time-dependent and initial-state correlation functions which can, in many cases, be described in terms of experimental observables. The authors demonstrate this by calculating the momentum distribution of a weakly interacting Bose gas with tunable interactions.

In the following, we will cast the many-body problem into a description that fits our system, a weakly-interacting Bose gas in the Thomas-Fermi regime. The many-body wave function is described in terms of a set of eigenmodes and corresponding quasiparticle occupation numbers, and rescaled first- and second order correlation functions for the case of an initial thermal state are derived. We will show how an approximate scaling solution holds in the Thomas-Fermi regime for a stationary 1d-interaction constant, and constraints for the validity of these solutions are discussed.

5.3.2. Scaling approach in the Thomas-Fermi regime

We start with the hydrodynamic representation of the 1d Gross-Pitaevskii equation, neglecting quantum pressure:

$$\frac{\partial v}{\partial t} + v\frac{\partial}{\partial z}v + \frac{1}{m}\frac{\partial}{\partial z}V(z,t) = -\frac{g_{1d}}{m}\frac{\partial}{\partial z}n \tag{5.14}$$

$$\frac{\partial}{\partial t}n + \frac{\partial}{\partial z}(nv) = 0. \tag{5.15}$$

Here, $n := n(z,t)$ and $v := v(z,t)$ denote the density and velocity profiles along the longitudinal axis, with an external harmonic potential $V(z,t) = m\omega_a^2 z^2/2$ and 1d interaction constant $g_{1d} = 2\hbar\omega_r a$. In the Thomas-Fermi regime, the ground state density profile is parabolic and exhibits self-similar scaling [32, 80] described by

$$n(z,t) = \left(\frac{n_0}{b}\right)\left(1 - \frac{z^2}{R_0^2 b^2}\right)\Theta\left(1 - \frac{|z|}{R_0 b}\right). \tag{5.16}$$

As in the previous section, $b(t) = R(t)/R_0$, R_0 and n_0 represent the scale factor, initial Thomas-Fermi radius and peak density, respectively. In this framework, excitations enter as density and velocity fluctuations $\delta n := \delta n(z,t)$ and $\delta v := \delta v(z,t)$ on top of the mean field n, v. Their dynamics can be described by linearized equations

$$\frac{\partial}{\partial t}\delta v + \frac{\dot{b}}{b}\delta v + \frac{\dot{b}}{b}z\frac{\partial}{\partial z}\delta v = -\frac{g}{m}\frac{\partial}{\partial z}\delta n \tag{5.17}$$

$$\frac{\partial}{\partial t}\delta n + \frac{\dot{b}}{b}\delta n + \frac{\dot{b}}{b}z\frac{\partial}{\partial z}\delta n = -n_0\frac{1}{b}\frac{\partial}{\partial z}\left[\left(1 - \frac{z^2}{R_0^2 b^2}\right)\delta v\right], \tag{5.18}$$

where expression 5.16 has already been substituted for $n(z,t)$.

Similar to the discussion of the equilibrium problem in reference [82], an ansatz of rescaled Eigenmodes can be defined:

$$\delta n = \frac{1}{b} \sum_{l=1}^{\infty} P_l\left(\tilde{z}\right) A_l \cos \eta_l \tag{5.19}$$

$$\delta v = -\sqrt{\frac{1}{b}} \sum_{l=1}^{\infty} \frac{g}{m R_0 \omega_l(0)} \frac{d}{d\tilde{z}} P_l\left(\tilde{z}\right) A_l \sin \eta_l, \tag{5.20}$$

with the Legendre polynomials $P_l(\tilde{z})$, interaction constant g, initial Thomas-Fermi radius R_0, rescaled coordinates $\tilde{z} = z/R = z/(R_0 b)$, and time-dependent amplitudes $A_l \sin \eta_l$ and $A_l \cos \eta_l$, where η_l denotes the frequency of the oscillation between the quadratures of the mode with index l. The spectrum at $t = 0$ is given by [82]

$$\omega_l\left(0\right) = \frac{\omega_a}{\sqrt{2}} \sqrt{l\left(l+1\right)} = \frac{c_0}{R_0} \sqrt{l\left(l+1\right)}, \tag{5.21}$$

with the initial sound velocity c_0. For $t > 0$, it scales as

$$\omega_l(t) = \omega_l(0) b^{-3/2},$$

due to the time-dependence of the sound velocity $c(t) = c_0/\sqrt{b}$ and Radius $R(t) = R_0 b(t)$. Substituting this ansatz into the equations 5.17 and 5.18 yields the set of equations:

$$\dot{\eta}_l = \omega_l\left(t\right) - \frac{1}{2}\frac{\dot{b}}{b} \sin \eta_l \cos \eta_l \tag{5.22}$$

$$\frac{\dot{A}_l}{A_l} = -\frac{1}{2}\frac{\dot{b}}{b} \sin^2 \eta_l. \tag{5.23}$$

This equation system is still coupled. Indeed, a similar derivation put forward in reference [29] yields a set of decoupled equations only for suitable tuning of the interaction constant $g_{1d}(t) = g_{1d}(0) b(t)$, identical to the case of exact scale invariance of GPE for the mean-field dynamics. Such a tuning is also assumed in reference [36].

Nevertheless, this ansatz yields decoupling of modes in good approximation also for the TF regime discussed here. Since the characteristic inverse time scale of the breathing mode $(\dot{b}/b)_{max} = \omega_a/2$ is small compared to the characteristic frequencies $\omega_l\left(0\right)$ of the phonon modes with $l > 2$, these expressions reduce to $\dot{\eta}_l \simeq \omega_l\left(t\right)$ and $A_l \simeq A_l\left(0\right) \left(R_0/R\right)^{1/4}$, and the phonon modes are expected to scale adiabatically. Under adiabaticity conditions, the initial number of phonons in a thermal state

$$\mathcal{N}_l(t) = \frac{1}{\exp \frac{\hbar \omega_l(t)}{k_B T(t)} - 1} = \mathcal{N}_l(0) \tag{5.24}$$

is conserved, resulting in

$$\frac{\omega_l\left(t\right)}{T\left(t\right)} = \frac{\omega_l\left(0\right)}{T\left(0\right)}, \tag{5.25}$$

which leads to the temperature scaling:

$$T\left(t\right)=T\left(0\right)b^{-3/2}. \tag{5.26}$$

The density correlations in free expansion that our thermometry scheme relies on are governed by the coherence function. For a thermal state with homogeneous density, as realized in the vicinity of the cloud center, it has the form [82, 71]:

$$g^{(1)}(z,0)\simeq n\left(z,0\right)\exp\left(-\frac{mk_BTz}{2n(z,0)\hbar^2}\right), \tag{5.27}$$

where $n(z,0)$ denotes the density at time $t=0$ and k_B the Boltzmann constant. Based on our model, it is expected to scale as

$$\tilde{g}^{(1)}(z,t)\simeq\frac{n\left(z,0\right)}{b}\exp\left(-\sqrt{\frac{1}{b}}\frac{mk_BT\left(0\right)z}{2n\left(z,0\right)\hbar^2}\right). \tag{5.28}$$

This expression can also be obtained directly from the scaling solution, based on the derivation for the equilibrium system provided in reference [84]. We can express phase fluctuations in terms of velocity fluctuations by the relation

$$\delta\phi_l\left(z,t\right)=R\sqrt{\frac{1}{b}}\frac{m}{\hbar}\int_0^{\tilde{z}}d\tilde{z}'\delta\tilde{v}\left(\tilde{z}'\right)A_l\sin\eta_l$$

with

$$\delta\tilde{v}=\frac{g}{mR_0\omega_l(0)}\frac{d}{d\tilde{z}}P_l\left(\tilde{z}\right)$$

and $A_l\simeq A_l\left(0\right)\left(R_0/R\right)^{1/4}$. Therefore, the relation between initial and time-dependent modes $\delta\phi_l$ reads

$$\delta\phi_l\left(z,t\right)=b^{1/4}\delta\phi_l\left(z/b,0\right)\frac{\sin\eta_l\left(t\right)}{\sin\eta_l\left(0\right)}. \tag{5.29}$$

The time-dependent one-body reduced density matrix can be expressed as

$$\rho\left(z,z',t\right)=\sqrt{n\left(z\right)n\left(z'\right)}\exp\left[-\frac{1}{2}\left\langle\delta\phi_{zz'}^2\right\rangle+\frac{im\dot{b}}{2\hbar b}\left(z^2-z'^2\right)\right] \tag{5.30}$$

with

$$\left\langle\delta\phi_{zz'}^2\right\rangle=\left\langle\left[\delta\phi\left(z,t\right)-\delta\phi\left(z',t\right)\right]^2\right\rangle.$$

Using $\delta\phi=\sum_l\phi_l$, we can write the density matrix (5.30) in terms of the modes (5.29). Substituting and following the steps in reference [84], we find that near the cloud center, where the density is practically uniform and we can use trigonometric approximations for the Legendre polynomials P_l [219],

$$\rho\left(z,z',t\right)\simeq\frac{\sqrt{n\left(z\right)n\left(z'\right)}}{b}\exp\left[-\frac{|z-z'|}{\sqrt{b}\lambda_T}+\frac{im\dot{b}}{2\hbar b}\left(z^2-z'^2\right)\right] \tag{5.31}$$

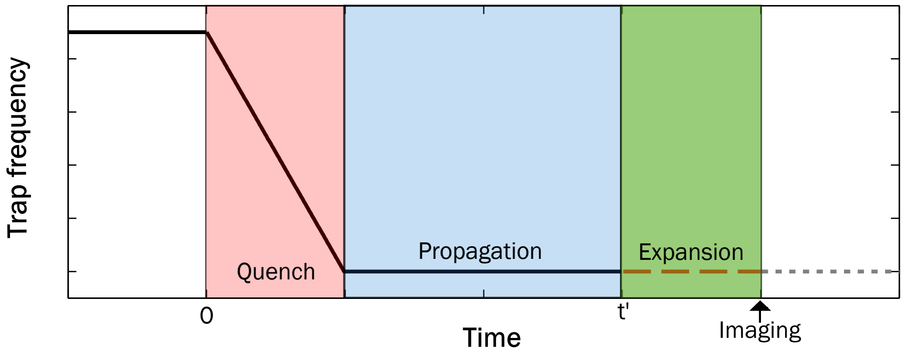

Figure 5.7.: Illustration of the measurement timing discussed in section 5.3.3.

with a coherence length $\lambda_T = \frac{2n(z)\hbar^2}{mk_BT(0)}$. This corresponds to a transformation of a form

$$\rho\left(z, z', t\right) = \frac{1}{b}\rho\left(\frac{z}{\sqrt{b}}, \frac{z'}{\sqrt{b}}, t\right) \exp\left[-iF(t)\left(z^2 - z'^2\right)\right], \tag{5.32}$$

as predicted in reference [36], with the difference that the spatial coordinates scale with $b^{-1/2}$ instead of b^{-1}. This difference is attributed to the Thomas-Fermi regime at constant 1d coupling strength, again as opposed to a suitable tuning of interactions imposed in reference [36], where the scaling solution is valid for initial states at arbitrary interaction strengths. Since our thermometry method, as discussed in section 4.6, is based on density correlations in time of flight that are derived from a second order correlation function expressed in terms of $\rho(z, z', t)$ [30], our measurements are not sensitive to the imaginary part of the exponent, yielding the observation of a temperature scaling given in equations (5.26) and (5.28). This point is also discussed in detail within section 4.6.

5.3.3. Temperature measurements in breathing clouds

In the following, three different datasets, labeled S1, S2 and S3, are discussed. For all datasets, initial and final traps are characterized by the same external parameters as given in section 5.2.2. Each set contains absorption images of atom clouds corresponding to evolution times t' between $t = 0$ ms and $t = 200$ ms in intervals $\Delta t = 10$ or 20 ms, with a certain number of repetitions at identical parameters, depending on the respective set. Here, $t = 0$ marks the point in time directly before the quench ramp. At each of these time steps, the trap is switched off, and an image is taken after $t_{exp} = 10$ ms of free time-of-flight expansion. The timing of the measurement is illustrated in figure 5.7. The datasets differ in quench duration τ, atom number and time resolution as stated in table 5.2, and the available statistics given by the number of repetitions at identical parameters.

	τ (ms)	Atom number	Time resolution (ms)	Repetitions
S1	10	16000 ± 1000	20	330
S2	10	11000 ± 1000	10	200
S3	30	16000 ± 1000	20	330

Table 5.2.: Overview of the three different datasets analyzed to probe the temperature scaling in a breathing cloud. The uncertainty of the atom number corresponds to the standard deviation within each set.

Scale parameter

To compare temperature measurements with the derived scaling law, knowledge of the in-situ scale parameter $b(t, t_{exp} = 0)$ is necessary. In-situ-imaging in our setup is restricted by wire bonding structures at the chip edges, as shown in chapter 4. However, the excellent agreement of our breathing measurements presented in section 5.2.3 with parameter-free calculations allows to infer this quantity from the scale parameter in time-of-flight $b(t, t_{exp})$ to high accuracy. An assessment of possible additional distortions of our measurements due to hydrodynamic effects in the initial time-of-flight expansion phase, as well as the amount and influence of thermal atoms in transverse excited states, is given at the end of section 5.3.3.

Overall, 10600 pictures contribute to these measurements. At a cycle time of 30 s for each picture, the measurement time amounts to over 88 hours spread over three weeks, with set S2 taken several weeks after S1 and S3. To account for possible small environmentally caused drifts of the trap geometry between the different datasets at identical wire currents and bias fields, we fit the axial cloud radii measured for each dataset with simulation results as described in section 5.2.3. For this fit, we allow the initial and final axial trap frequencies ω_a^0, ω_a^f to deviate from the values measured in 5.2.2. Figure 5.8 presents the results of these fits.

Temperature analysis for breathing clouds

Thermometry on breathing clouds relies on the same scheme as presented in section 4.6. After switching off the trap, phase fluctuations lead to the emergence of an interference pattern in the density profile that can be observed by imaging the cloud in free expansion. Calculating the autocorrelation function of each density profile, averaging and normalizing yields second-order correlation functions $g^2(\Delta z, t', t_{exp})$. Given a single-particle coherence function of the form 5.31, the breathing is expected to enter as a rescaling of the thermal coherence length $\lambda_T(t') = \sqrt{b}\lambda_T(t = 0)$ and an additional quadratic phase factor, as summarized in equation 5.32. For the description of second-order correlations within the trap, this phase factor cancels out. While the experiment also detects only second-order correlations, this phase becomes apparent as a quadratic velocity field leading to defocusing or partial focusing in free expansion, as sketched in figure 5.9.

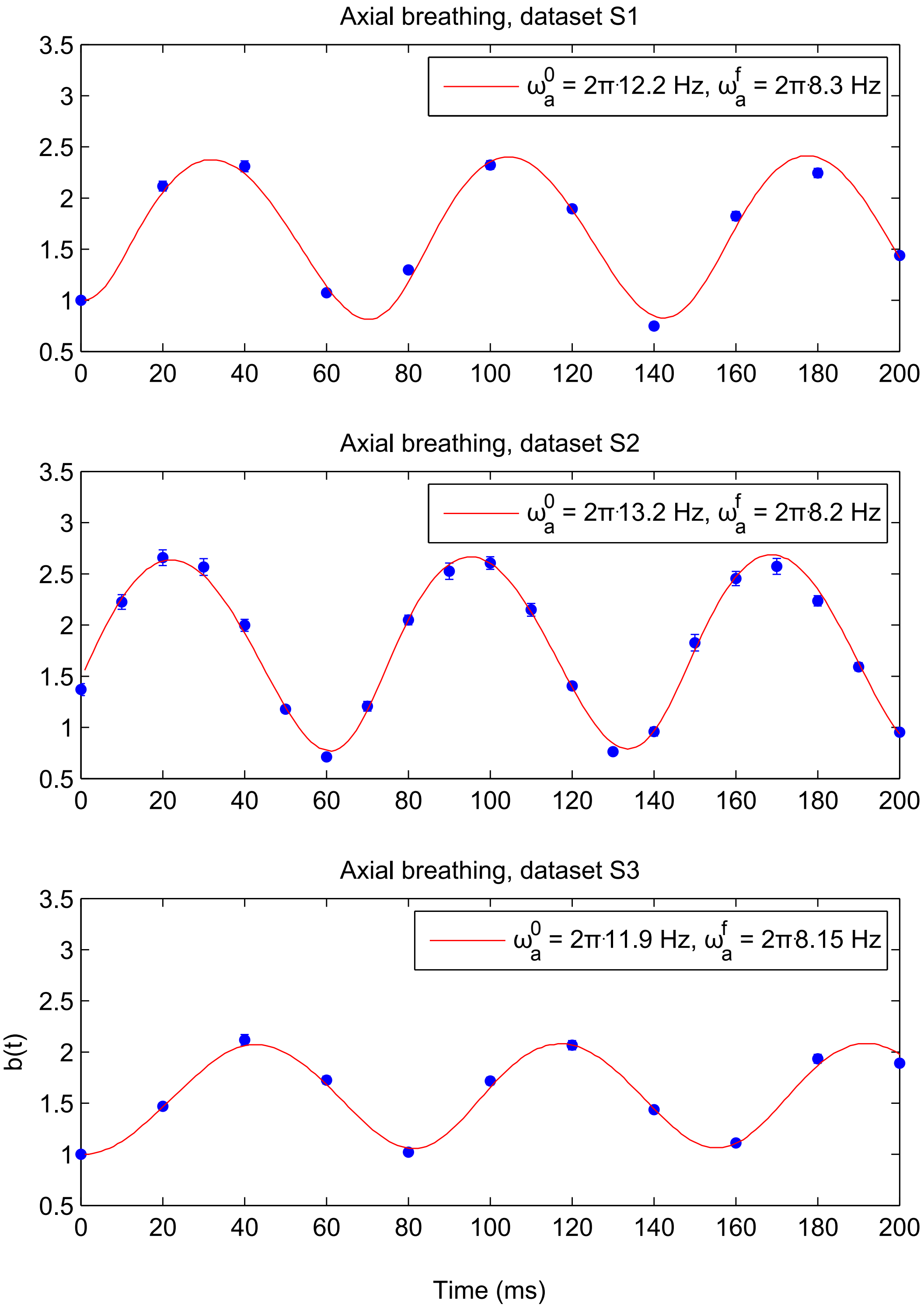

Figure 5.8.: Axial breathing for the datasets used for the datasets (a) S1, (b) S2 and (c) S3. Blue circles represent data. Errorbars are given by the standard deviation of the measured scale parameter for 330 (a and c), or 200 (b) repetitions at identical parameters, respectively. The solid red line shows a fit using the GPE as described in section 5.2.3.

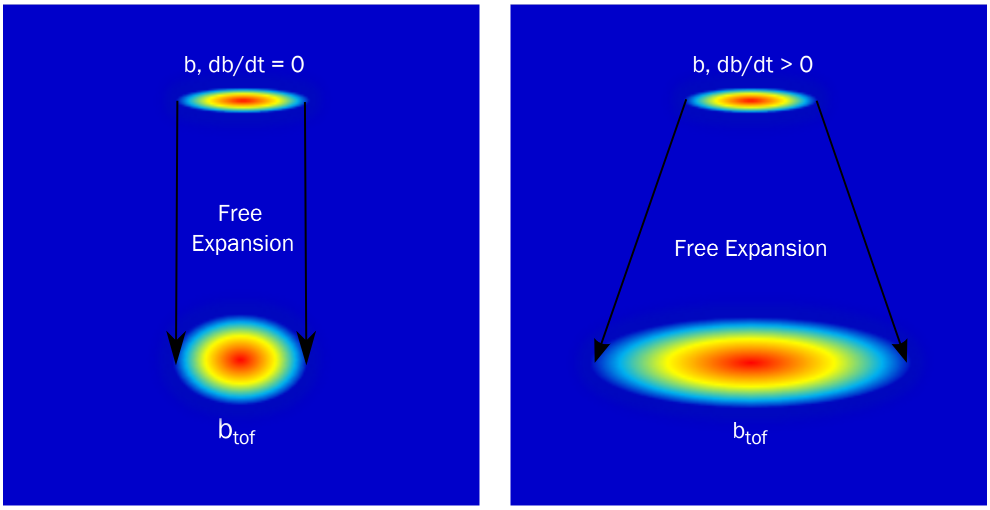

(a) Stationary cloud, $\dot{b} = 0$ (b) Breathing cloud, $\dot{b} > 0$

Figure 5.9.: (a) Stationary and (b) breathing clouds during free expansion.

Such a velocity field can be easily integrated in our temperature analysis. Using the knowledge of the in-situ scale parameter b and the corresponding velocity $\dot{b}$ from the measurements presented in the previous paragraph, we can define

$$\Psi(z,t) = \psi(z,t)\exp\left(\frac{im}{4\hbar}\frac{\dot{b}}{b}\left(z^2 - z'^2\right)\right). \tag{5.33}$$

Here, $\psi(z,t)$ is a wave function characterized by the total atom number, the radius bR_0 with the stationary Thomas-Fermi radius R_0, and phase fluctuations generated by an Ornstein-Uhlenbeck (OU) process for a certain temperature, as described in section 3.4, while the exponential expresses the velocity field governed by $\dot{b}/b$. Free expansion of the wave function Ψ yields correspondingly focused or defocused density profiles.

To shed light on how this (de-)focusing affects the shape of the autocorrelation function after free expansion, figure 5.10(a) presents a comparison of preset temperatures used in the Ornstein-Uhlenbeck algorithm and corresponding results of an analysis of the simulated density profiles after 10 ms of free expansion, based on the assumption that the temperature can be defined as

$$T = \frac{2\hbar n_0}{m\lambda_T k_B} = \frac{2\hbar n_0^{TOF}}{m\lambda_T^{TOF} k_B}. \tag{5.34}$$

Here, n_0^{TOF} and λ_T^{TOF} denote the peak density and an effective coherence length in free expansion, respectively. Under this assumption, the velocity field does not affect the temperature measurement beyond changing the peak density n_0, and we use the

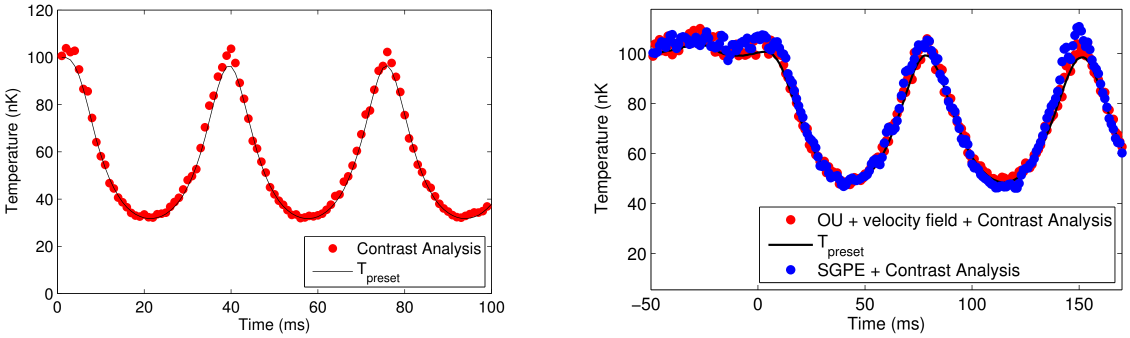

(a) Test of simple OU analysis.

(b) OU and velocity field compared to SGPE

Figure 5.10.: (a) Test of simple OU temperature analysis for breathing clouds. The black line corresponds to preset temperatures fed to an Ornstein-Uhlenbeck algorithm to simulate a trapped wave function with phase fluctuations. Red circles represent analysis results based on autocorrelation functions of density profiles generated from the same wave functions, incorporating breathing by an overall phase factor as given in equation 5.33. Temperatures result from formula 5.34, where λ_T^{TOF} is proportional to the inverse contrast of the autocorrelation function $1/C_{g^2}$, $C_{g^2} = g^2(\Delta z = 0) - \min(g^2(\Delta z)$. The proportionality is identical to the calibration given in section 4.6 for the case of a stationary atom cloud. (b) Comparison of OU and quadratic velocity field with SGPE simulations. Black line: preset temperatures as in (a). Red circles: Simple OU analysis as in (a). Blue circles: temperatures from an SGPE simulation with an initial set temperature of 100 nK. Autocorrelation functions from the SGPE simulation are subject to the same analysis as the red set. A stationary stage between $t = -50$ ms and $t = 0$ ms to ensure the preparation of an equilibrium state by the SGPE evolution is included.

same linear relationship between the contrast of the autocorrelation and the inverse coherence length that has been determined in section 4.6, which only depends on the point spread function of the imaging system. The comparison shown in figure 5.10(a) uses parameters $b(t)$ and $\dot{b}(t)$ as determined from dataset S1 and temperatures corresponding to the theoretical scaling $T = T_0 b^{-3/2}$, and shows excellent agreement between analysis and preset temperatures.

However, this simple description has to break down for certain combinations of b and $\dot{b}$. For an infinite time-of-flight, the expansion maps the momentum distribution of the trapped system onto the density profile, yielding a Lorentzian shape [93, 94], as discussed in section 2.3.2. The same can be achieved at finite expansion times by focusing of the condensate [220, 97, 221]. As already pointed out, partial focusing is exactly what happens during the inward directed breathing phase. As a consequence, especially during this phase, the breathing is expected to violate the assumption of short expansion times that guarantees the observation of mainly a density profile, as opposed to a convolution between in-situ density- and momentum distribution. To stress this point, figure 5.11 repeats the comparison from figure 5.10(a) and 5.10(b) for a wider variety of values for $\dot{b}$, crossing the focusing conditions for the set expansion time of 10 ms, at constant preset temperature.

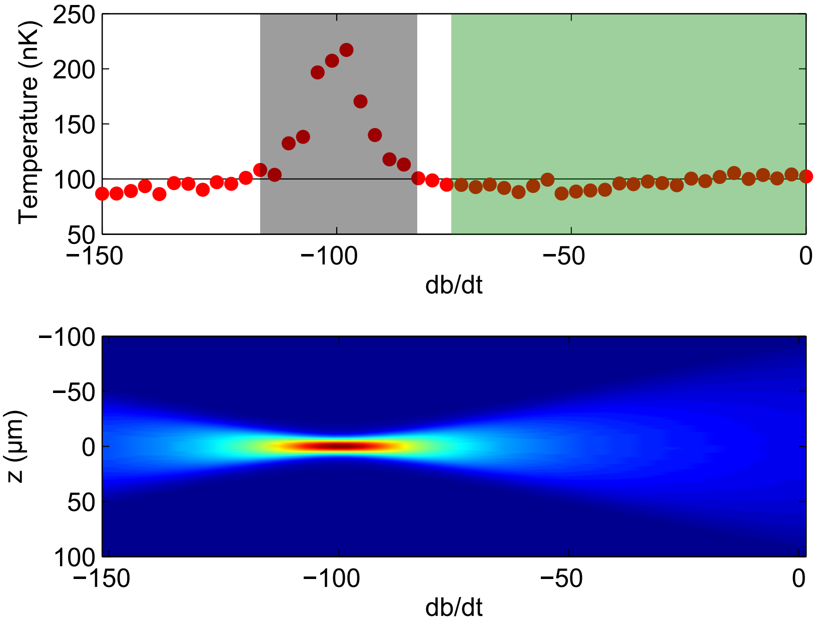

Figure 5.11.: Temperature measurements and focusing condition. (a) Temperature estimated from the OU analysis plotted against $\dot{b}$ for a free expansion time of $t_{exp} = 10$ ms. The plot shows the breakdown of the thermometry method around the focusing condition, marked by the grey shaded area, while for the rest of the parameter range, only small deviations from the preset temperature are observed. The green shaded area denotes the range covered by breathing experiments presented in this thesis. (b) Simulated time-of-flight density profiles, showing the focussing condition to be fulfilled for $\dot{b} \approx -100$, coinciding with the breakdown of the thermometry method.

Nevertheless, for the parameters relevant to our temperature measurements, even equation 5.34 together with the g^2-contrast calibration for the stationary case as presented in section 4.6 already represents a thermometry method with an accuracy that is better than our overall measurement uncertainty. This is of course under the assumption that 5.33 correctly captures the phase field in the presence of breathing. To further test this assumption, we compare our thermometry with simulations based on a SGPE (see section 3.17). Here, the breathing is induced directly by a change of the axial trap in the simulation, and the intitial temperature is a preset parameter. Figure 5.10(b) shows the result of a comparison between the OU-based model and the results of the SGPE simulation. The agreement indicates that equation 5.33 yields a good representation of the density profile in free expansion within our parameter range.

Results

Based on the findings of the previous section, an analysis of the datasets S1, S2 and S3 can be performed. Figure 5.12 shows a comparison between measured and simulated autocorrelation functions from dataset S1 for an evolution time of $t' = 20$ ms. Data points correspond to the average measured autocorrelation function calculated from pictures as shown in the inset, while errorbars are given by the standard deviation estimated by

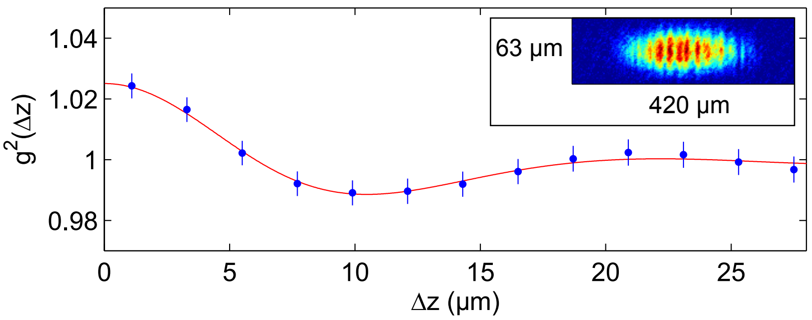

Figure 5.12.: Example for the autocorrelation analysis from dataset S1, at an evolution time of $t' = 20$ ms. Blue circles represent data, while errorbars show the standard deviation estimated by bootstrapping. The red line is the result of our temperature fit based on an Ornstein-Uhlenbeck simulation, with a best fit of $T = 62$ nK.

the bootstrapping method presented in section 4.6. The red line is calculated from a wave function where phase fluctuations are prepared by an Ornstein-Uhlenbeck process, taking into account breathing by equation 5.33, 10 ms of free expansion and the finite resolution of our imaging system, as described in section 4.6. The only parameter to be varied is the preset temperature T for the OU-algorithm, with a best fit for $T = 62$ nK.

The same analysis is performed for each evolution time t'. To illustrate the results, figure 5.3.3 shows contour plots of measured average and corresponding simulated autocorrelation functions for dataset S1.

Fitting the temperature for each subset and plotting it against the evolution time t' allows for a comparison with the scaling model developed in section 5.3.2. Figure 5.14(a) shows the time evolution of the measured temperature for dataset S2. While an oscillatory behaviour is apparent, the data also exhibits an overall rise in temperature over time. This is attributed to heating processes, as mentioned in section 5.2.3. While parametric heating processes have been observed in RF-dressed potentials in the presence of a pronounced anharmonicity in the transverse trapping potential at low atom numbers [31, 216], heating in atom chip traps usually leads to a linear increase in temperature within the system over time. To incorporate the influence of heating into our analysis, a general temperature scaling $T(t) = T_0 b(t)^{\epsilon_{sc}}$ is considered. The model presented in section 5.3.2 predicts ϵ_{sc} = -3/2, but for the purpose of this analysis, it is left as a free parameter. The mentioned temperature scaling solves the equation

$$\frac{\dot{T}}{T} = \epsilon_{sc}\frac{\dot{b}}{b} \tag{5.35}$$

An additional linear temperature increase can be represented by adding a constant term:

$$\dot{T} = \epsilon_{sc}\frac{\dot{b}}{b}T + \alpha T_0. \tag{5.36}$$

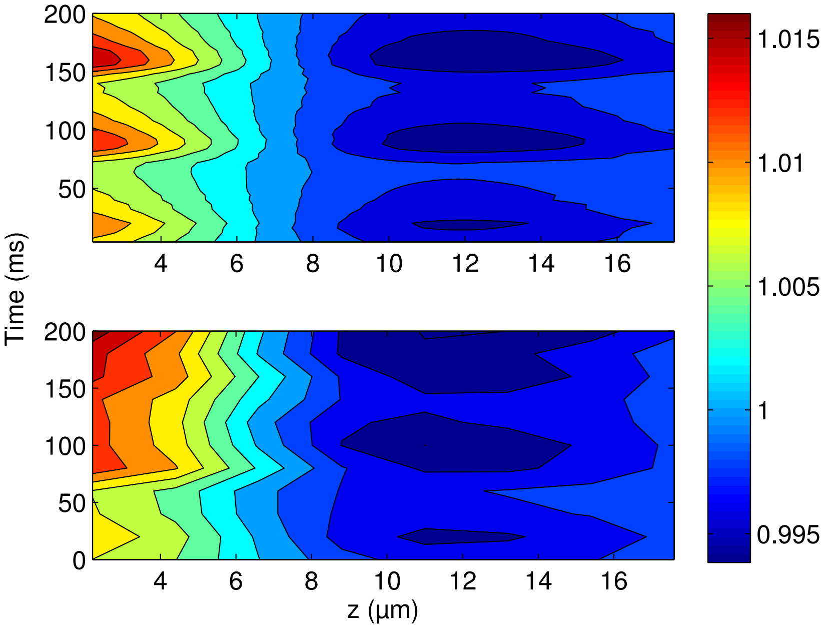

Figure 5.13.: Contour plots comparing simulated (upper panel) and measured (lower panel) average autocorrelation functions for dataset S1.

This equation is solved by

$$T = T_0 h(t) b^{\epsilon_{sc}}, \tag{5.37}$$

where $h(t)$ is given by

$$h(t) = 1 + \alpha \int_0^t dt' b(t')^{-\epsilon_{sc}}. \tag{5.38}$$

Note that in the stationary case of a constant $b = 1$, this reduces to $h(t) = 1 + \alpha t$, such that α corresponds to the regular heating rate in units of the initial temperature.

The black line in figure 5.14(a) corresponds to a least squares fit to equation 5.37, with parameters ϵ_{sc} and α. Figure 5.14(b) shows the corresponding χ^2-value of the fit plotted against the values of the two parameters. Best fitting is achieved in a region between $0.2 < \alpha < 0.3$ nK/ms, and around $\epsilon_{sc} \propto -1.6$, compatible to the theoretical prediction. The values for the fit in 5.14(a) are $\epsilon_{sc} = -1.7$ and $\alpha = 0.26$ nK/ms.

In the following, our data is compared with the theoretical prediction $\epsilon_{sc} = -3/2$. Figure 5.15 contains the temperature measurements from all three datasets, plotted against time, together with fits of the form 5.37, where the scaling exponent is fixed to $\epsilon_{sc} = -3/2$ such that the linear heating rate is the only free parameter. In addition, the figure plots the same data, corrected for the heating rate determined for each dataset, compared to the theoretical prediction in the absence of heating $T(t) = T_0 b^{-3/2}$. Overall, we find good agreement between the data and the model consisting of a linear heating process and the theoretically predicted scaling for each dataset.

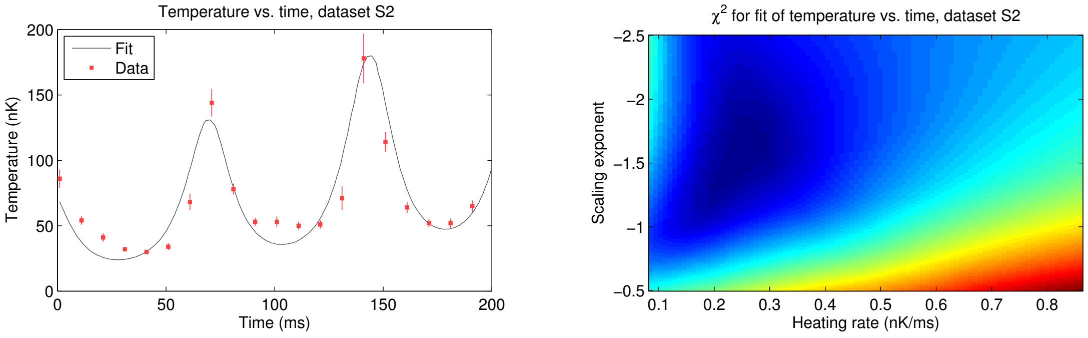

(a) (b)

Figure 5.14.: Estimation of heating rate and scaling exponent. (a) Measured temperature values from dataset S2 (red squares) with errorbars corresponding to the standard deviation for each subset estimated by bootstrapping. The black line represents a fit of the form 5.37, with both the heating rate α and the scaling exponent ϵ_{sc} as free parameters. (b) Goodness of the fit shown in (a), represented by the mean square deviation χ^2 in arbitrary units, plotted against αT_0 and ϵ_{sc}. The best values correspond to $\epsilon_{sc} = -1.7$ and $\alpha T_0 = 0.26$ nK/ms, with the theoretical prediction $\epsilon_{sc} = -1.5$ situated in an area yielding good agreement with the data.

The predicted scaling is universal in a sense that there is no dependence on other quantities characterizing the system, as density, absolute extent of the atom cloud or temperature or the details of the quench inducing the breathing. To illustrate this for our results, figure 5.16 combines the data from all three sets in a plot of the temperature normalised to each respective T_0 over the scale parameter b. For comparison, the inset contains the same plot, but in absolute units for each dataset. Note that datasets S1 and S3, while covering a similar range of temperatures and cloud radii, correspond to different quench times. The normalised data collapses onto a single region distributed around the prediction of the scaling model. In addition, the plot contains a power law fit of the combined data, yielding a scaling exponent of $\epsilon_{sc} = 1.4 \pm 0.2$, again in good agreement with the prediction.

As an additional cross-check for our results, classical field simulations based around the $SGPE_{eq}$-method described in section 3.17 have been performed. After preparation of a set of thermal initial states by the SGPE, in this case 120 realisations with a temperature of 100 nK, each of these states is propagated with a time-dependent GPE. We use the same trap parameters as in our experiment, and include both the 10 ms of free expansion time and our finite imaging resolution to yield density profiles that can be analysed in the same way as the data from experiment. In addition, the simulation allows the direct calculation of the time-dependent in-situ coherence functions defined in equation 5.27 as an independent thermometry method. The results of these simulations is included in figure 5.16, and show excellent agreement with the scaling model.

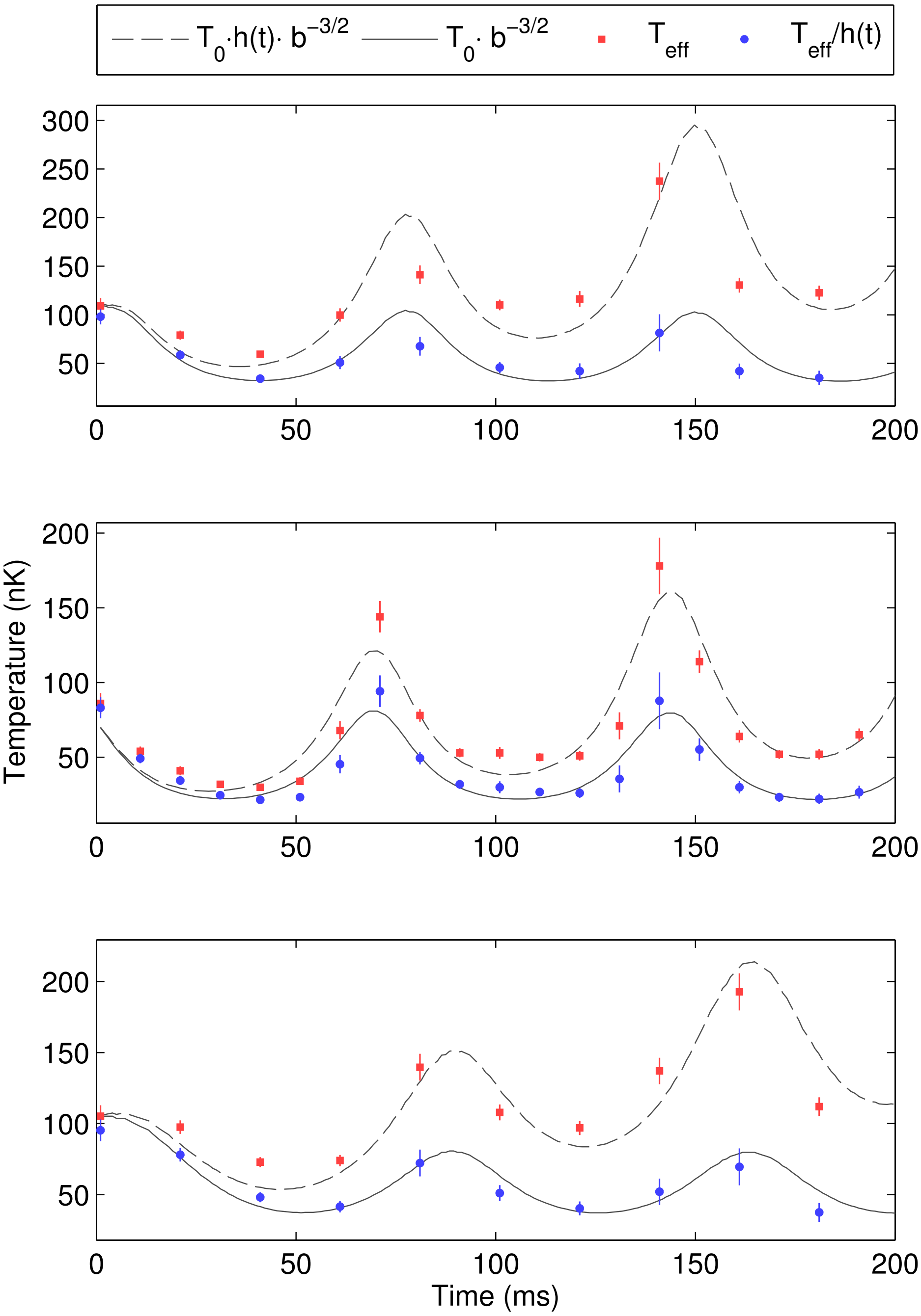

Figure 5.15.: Temperature plotted against evolution time during a breathing oscillation.. (a) Quench time $\tau = 10$ ms, ~16000 atoms. Red squares: Temperatures measured from density correlations in free expansion. Dashed line: scaling law taking into account linear heating as shown in the legend, fitted for a heating rate of $\alpha \cdot T(0) \approx 0.54$ nK/ms. Blue circles: Temperatures corrected for heating rate. Line: scaling law $T(t) = T(0) \cdot b^{-3/2}$ as discussed in the main text. Error bars represent one standard deviation estimated by a bootstrapping technique. (b) Quench time $\tau = 10$ ms, ~11000 atoms, heating rate $\alpha \cdot T(0) \approx 0.28$ nK/ms. (c) Quench time $\tau = 30$ ms, ~16000 atoms, heating rate $\alpha \cdot T(0) \approx 0.54$ nK/ms.

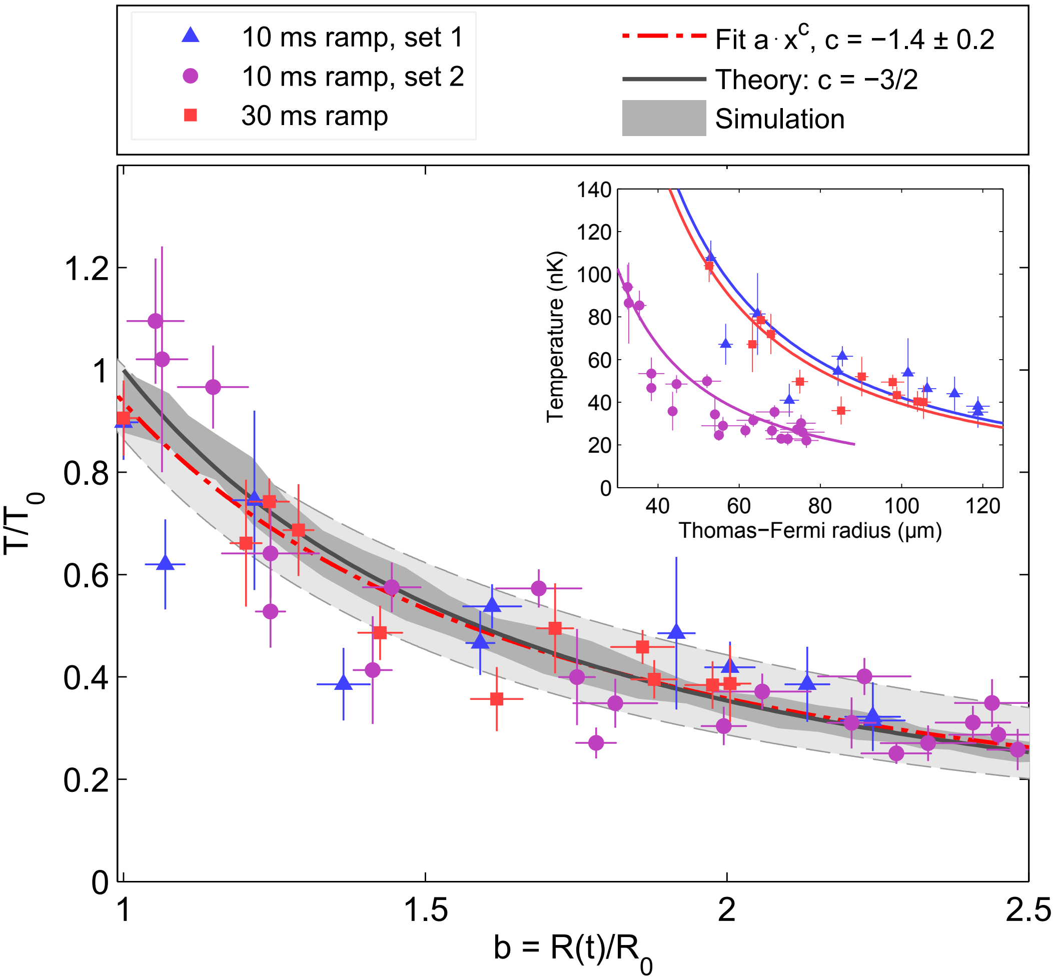

Figure 5.16.: Temperature as a power law of the scaling factor. The main figure shows all temperature measurements in units of the initial temperature of each dataset as a function of the scaling factor. For comparison, the inset depicts corresponding absolute temperatures and cloud lengths. Vertical errorbars are a result of a bootstrapping method as in [222]. Horizontal errorbars correspond to the standard deviation of measured cloud widths, normalized to the initial width. The dashed-dotted line shows a power law fit to the data, with the lightly shaded area representing the fit's 95 % confidence bounds. Data and fit are compatible with the scaling model discussed in the main text (black line), as well as with the results of a classical field simulation with 120 sets of stochastic initial conditions generated by a SGPE (dark shaded area).

Discussion

Overall, good agreement is found between data and both the scaling model as well as the numerical simulations, as long as the heating is properly corrected for. While the presented results suggest that heating leads to an additional linear increase in temperature that does not affect the scaling exponent, an independent validation of this conjecture is called for in future measurements. To achieve this, either a full understanding of heating in atom chip traps, or measurements where heating is negligible, are necessary. As already briefly mentioned in the beginning of section 5.2.3, many different effects contribute to heating, some of which are already under study within our group. In [31], it was found that heating of thermal atoms and a 1d condensate, in this case with low atom numbers, happens at different rates, in contrast to the assumption of thermal equilibrium between the two subsystems. On the other hand, in reference [201] thermalization processes in a 1d system are studied that are either intrinsic within a beyond-Luttinger liquid description, or mediated by interactions between atoms in radial excited states. Such measurements could lead to models for the interaction between ground state and radially excited atoms, which would be an important step towards a full understanding of heating in quasi-1d BECs.

As for the experimental reduction of heating, several options are available. On the one hand, measurements as presented within this chapter could be performed in an experiment with RF-dressed potentials, which have been observed to exhibit significantly smaller heating rates compared with static chip traps as used for our measurements. Further, interactions with radially excited atoms have shown to be suppressed when operating sufficiently far in the 1d regime [31, 131]. Novel atom chips that allow higher radial trap frequencies without compromising control over the axial potential due to wire corrugations could address this issue. The chip used in the new setup under construction, as described in section 8, could already allow to achieve this goal.

5.4. Summary

In this chapter, the excitation spectrum of a 1d quasicondensate in the presence of collective breathing dynamics has been analysed. Based on a Luttinger liquid model with a time-dependent set of basis functions, an adiabatic rescaling of initial eigenmodes has been identified for a self-similar time evolution of the overall density profile. This leads to a prediction for the scaling of the density matrix and the coherence function $g^(1)(z, z', t)$, in close correspondence to the predictions of reference [36]. For an initially thermal state, the temperature corresponding to phononic excitations scales with the spatial extension $b = R(t)/R_0$ of the cloud as $T(t) = T_0 \cdot b^{-3/2}$. This prediction has been compared to measurements and to numerical simulations based on the c-field approach presented in chapter 3. Both the scaling model as well as the numerical simulations have been found to agree well with measurements at different initial conditions, if heating in the atom chip trap is accounted for.

On the one hand, the results presented in this chapter constitute the first direct experimental demonstration of the presence of such a scaling law for the excitation spectrum of the 1d Bose gas. On the other hand, these results provide a means to perform thermometry in the presence of collective excitations, which is of significant practical importance for other measurements with atom chip experiments, where the excitation of collective excitations cannot be avoided. Note that the validity of the results presented here is not limited to thermal states. If correlations in the initial states are known, the time evolution can be calculated from the scaling model.

From our model, adiabaticity follows only approximately in the limit of low expansion speeds $\dot{R}/R(t)$ and moderate scale factors. The consequences arising from the breakdown of adiabaticity, as expected for the 1d expansion of a 1d condensate to sufficiently large scale factors, will be discussed in chapter 7.

6. Optimal control on quasi-BEC dynamics

This chapter presents the implementation of shortcuts to adiabaticity for the expansion or compression of 1d quasicondensates by optimal control on the external trapping potential and temperature measurements on the initial and final states, providing evidence that adiabaticity holds not only for the external dynamics, but also for the phononic excitation spectrum.

6.1. Introduction

In chapter 5, the breathing dynamics of a quasi-1d BEC after a quench of the trapping potential was studied and found to agree very closely with the predictions of the time-dependent Gross-Pitaevskii equation, or, equivalently, of a suitable scaling solution. Naturally, the question arises whether this agreement can be used to control the dynamics in a more sophisticated way than just altering the breathing amplitude by the quench duration. A control problem that is interesting from different angles is to speed up an adiabatic state change.

In quantum mechanics, adiabaticity is defined by vanishing transition probabilities between the instantaneous eigenstates of an underlying Hamiltonian. According to the adiabatic theorem [223, 224, 225], this implies either a time-independent Hamiltonian, or a time-dependence that is sufficiently slow. More explicitly, considering a system in an instantaneous eigenstate $\psi_n(t)$ of a Hamiltonian $\hat{H}(t)$, it has to hold that

$$\frac{\left\langle \psi_m(t) \left| \frac{d}{dt}\hat{H} \right| \psi_n(t) \right\rangle}{E_n - E_m} \ll 1, \tag{6.1}$$

with E_n and E_m denoting the energy eigenvalues corresponding to the states $\psi_n(t)$ and $\psi_m(t)$, or, equivalently, that any change of the Hamiltonian happens on a timescale $\tau \gg \hbar/\Delta E$. In this case, the system stays in the eigenstate $\psi_n(t)$ throughout the time evolution, only possibly picking up dynamical and geometrical phases. In the context of the previous chapter, the time-dependence of the Hamiltonian is given by the external trapping potential, and adiabaticity corresponds to changing the trap without inducing collective excitations in the process. Especially with respect to the longitudinal axis, characterized by trap frequencies in the order of a few Hz, many operations are not adiabatic. Splitting of atom clouds, for instance, as performed routinely in our group, happens on much shorter time-scales and thus induces collective excitations, a suppression of which would facilitate many measurement and analysis schemes. As such, the speed-up of adiabatic processes or tools to control or stop collective excitations constitutes a valuable experimental tool.

An example from quantum information physics, where adiabatic processes are of interest, is adiabatic quantum computation [226, 227]. The starting point of an operation is the known ground state of a precisely initializable Hamiltonian. Tuning a set of control parameters, this state is made to evolve to the unknown ground state of a desired complex target Hamiltonian. For the system to always stay in the instantaneous ground state, adiabaticity throughout the operation is necessary, limiting the possible speed. However, in an experimental setting, decoherence usually gives an upper limit for the allowed duration of a coherent operation. Thus, methods to speed up adiabatic control problems would be a valuable tool in this field.

Interestingly, the scaling symmetry of the Gross-Pitaevskii equation provides a method to manipulate the trap without inducing collective excitations of a BEC. The rescaled equation 5.3, together with the two constraints in form of an Ermakov-equation as 5.5 and the definition of a rescaled time constitute a time-independent problem. Under these conditions, adiabatic processes involving the external potential as control field can in principle be performed arbitrarily fast, and the corresponding time-dependence of the trap can be directly calculated from the Ermakov-equation. This scheme, dubbed *shortcut to adiabaticity* for BEC dynamics, has been devised in [212, 228], and experimentally implemented in [229, 200, 37].

For our system, a direct implementation is hindered by the fact that in our experiment, axial and transverse trap frequencies are coupled and cannot be tuned independently. For such a case, other methods, such as counter-diabatic driving, recently presented in [230], may be used to analytically derive a control ramp. The approach taken in this thesis revolves around a stochastic scheme based on the solution of the time-dependent Gross-Pitaevskii equation to calculate suitably parametrised control ramps, and a genetic algorithm that performs a minimization of the breathing amplitude by searching the parameter space for an optimum.

In the previous chapter, it was found that a scaling solution can not only be used to describe the ground state dynamics of a BEC, but also to calculate full time-dependent correlation functions of the system. Specifically, it was established that the scaling leads to an adiabaticity condition for the occupation numbers of phonon modes with respect to expansion or compression of the system. This carries over to shortcuts, with the consequence that an STA for the expansion of a quasi-1d BEC by construction is both an implementation of a quantum dynamical microscope for correlations, as proposed in [231], and of fast frictionless cooling [232].

In the following, the stochastic scheme used to implement shortcuts to adiabaticity for

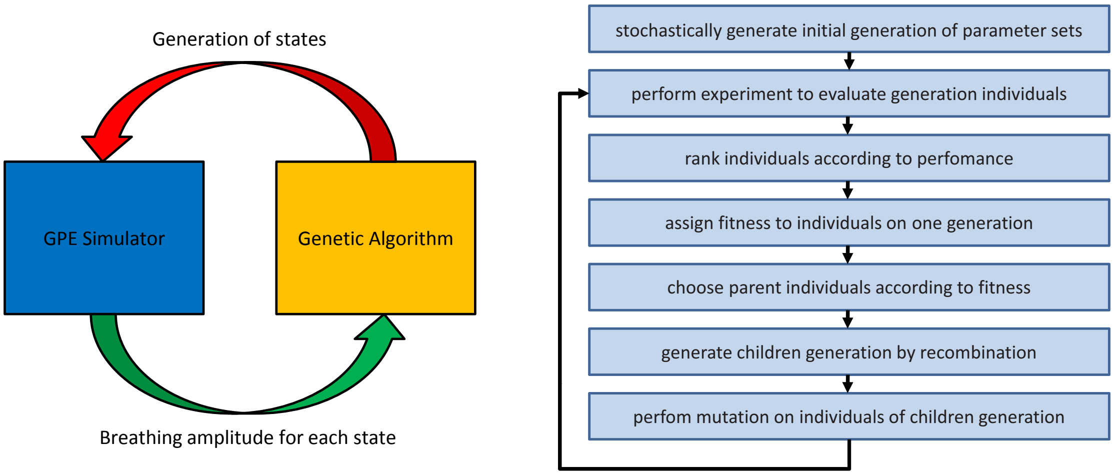
Generation of states
GPE Simulator
Genetic Algorithm
Breathing amplitude for each state
stochastically generate initial generation of parameter sets
perform experiment to evaluate generation individuals
rank individuals according to perfomance
assign fitness to individuals on one generation
choose parent individuals according to fitness
generate children generation by recombination
perfom mutation on individuals of children generation

(a) (b)

Figure 6.1.: Sketch of the optimal control scheme. (a) The 1d GPE in a time-dependent external potential is solved to evaluate a cost function that is represented by the breathing amplitude induced by a set of suitably parametrized control ramps changing the trap parameters. The parameters and the cost function value are fed to a genetic algorithm that, based on the results, generates a new set of ramps to be evaluated by the GPE simulation. Iterating this process leads to convergence against a set of ramps in a certain region of the paramter space, ideally in close vicinity to an optimum corresponding to vanishing breathing amplitude. (b) Steps preformed by the genetic algorithm during each iteration.

the expansion or compression of a quasi-1d BEC is presented, and the implementation in the experiment is discussed. A comparison between data and simulation results is given, and temperature measurements of the cloud during the process are presented. Although heating prevents the direct verification of fast frictionless cooling, the measurements indicate that the heating rates during shortcuts and during a subsequent hold time are identical, suggesting that the STA does not introduce additional excitations.

The chapter ends with a short outlook on the possibilities of engineering non-equilibrium states with the help of the presented control scheme.

6.2. Control Scheme

The control scheme used for the work presented in this chapter is briefly sketched in figure 6.1(a) and 6.1(b). Numerically solving the time-dependent 1d Gross-Pitaevskii equation allows to calculate the dynamics of an initially stationary atom cloud after a set of suitably parametrised control ramps that change the axial and radial trap frequencies $\omega_a(t)$ and $\omega_r(t)$, taking into account the experimental constraints outlined in section 5.2.2. The ramp parameters and the cost function, in our case the resulting breathing amplitude, are passed to a real coded genetic algorithm (RCGA), that iteratively performs an evaluation of the cost function and generates new ramp parameters that are fed to the GPE simulation, ideally minimizing the breathing amplitude within several tens of iterations. The RCGA used here has been developed to achieve closed-loop optimization within an experimental setting [174]. A very similar optimal control scheme that has been proposed more recently is the *Chopped Random Basis* (CRAB)-method [233], demonstrated experimentally in [234]. Both methods rely on a stochastic optimization algorithm - here a GA, in the case of CRAB a Nelder-Mead simplex method. The advantage of the CRAB method is a parametrization of the control ramps in the frequency domain. Estimating the minimal number of Fourier components necessary to encode a certain control ramp, it usually works on the smallest possible search space, minimizing the runtime. Our implementation foregoes this step in favour of an easy portability of the calculated results to the experiment control.

In the following, only a brief discussion of some important concepts of stochastic optimization as well as the methods used is given, while the reader is referred to reference [191] and references therein for a detailed description regarding the implementation, and to [192] for additional experimental results and benchmarks.

Choice of algorithm

It can be questioned whether a genetic algorithm is a sensible choice. In this context it is interesting to consider the so-called no-free-lunch theorems for search and optimization [235, 236]. They state that, averaged over all possible optimization problems which can be defined on a finite search space, the performance of each algorithm is identical. To be more precise, let $P\left(d_m|f,m,a\right)$ be the conditional probability of finding a particular set of states d_m by iterating a search algorithm a_1 m times on a cost function f. Given both a finite problem space and finite space of objective function values, [236] shows that for any two chosen algorithms a_1 and a_2 it holds that

$$\sum_f P\left(d_m|f,m,a_1\right) = \sum_f P\left(d_m|f,m,a_2\right). \tag{6.2}$$

This means that in principle, an algorithm has to be chosen to match the optimization problem at hand. A smooth search space without any local optima, for instance, lends itself to a simple gradient search while in a noisy problem space with one delta-spiked optimum, it is hard to do better than random search. However, in reality not all cost functions f are equally likely, and most problems will be situated between these extreme cases.

Interestingly, studies on quantum control problems carried out within the last decade have shown the search space of such problems to feature a universally simple structure [237, 238]. According to these studies, no local optima exist for unconstrained quantum control problems. If there are several optima, they all yield the same objective function value and are equally optimal. Recent years have already seen experimental efforts to confirm this conjecture [239]. Still, for many realistic quantum control problems, constraints on the control fields that reintroduce local extrema cannot be avoided. In addition, for closed-loop operation in an experiment, noise influences the performance of simple deterministic search methods. Stochastic optimization algorithms [240] have proven to operate well in complex and noisy problem spaces, however at the expense of guaranteed convergence to the global optimum.

There are many stochastic optimization algorithms to choose from. However, they all rely on both *exploration* and *exploitation* of the parameter space. The former is achieved by introducing randomness, while the latter is based on estimating and following gradients. The main differentiator is whether the algorithm is local or global, thus probing a limited region or sampling different parts of the search space within one iteration.

Out of these methods, a real coded genetic algorithm has been chosen due to the extensive literature on the subject and the ease of implementation. By assigning probabilities to the random elements of the algorithm, it is possible to tune the ratio of gradient estimation and random search to adapt it to specific optimization problems. A comparison of RCGAs with other optimization methods can be found in [241].

Implementation

The control ramp for the axial trap frequency ω_a is parametrized in terms of piecewise cubic splines

$$f_i(t) = c_0^i + c_1^i t + c_2^i t^2 + c_3^i t^3, \tag{6.3}$$

uniquely defined by support points p_i connecting the pieces $f_i(t)$ and the constraints of matched first derivatives between the pieces, and vanishing first derivatives $f'(0) = f'(\tau) = 0$ at the end points of the ramp at $t = 0$ and $t = \tau$, connecting to segments of constant frequency, for example $\omega_a(t < 0) = 2\pi \times 11.5$ Hz and $\omega_a(t > \tau) = 2\pi \times 7.5$ Hz for a decompression ramp. A set of support points p_i constitutes a state vector corresponding to a single ramp. An example for the parametrization is given in figure 6.2. Here, the "state vector" consists of 4 points. The advantage of this representation is a technical one: The experimental control system, described in section 4.3.10, directly supports the output of cubic splines and needs only the polynomial coefficients $c_{0,1,2,3}$ to identically reproduce the calculated control ramps via its analogue output channels, controlling the power supply for the currents through the chip structures.

In contrast to traditional genetic algorithms, an RCGA works directly on the search space spanned by such a state vector. For the example shown in figure 6.2, this space is of dimension $d = 4$. At the beginning of a typical optimization run, an initial set of $N_p = 24$ states $S_j = \{p_i\}$, is randomly chosen, the GPE simulation is performed for the corresponding ramps, and the resulting breathing amplitudes are determined. This set constitutes the first *generation* of states, and N_p is usually called the *population number*. Afterwards, the algorithm will go through the steps outlined in figure 6.1(b).

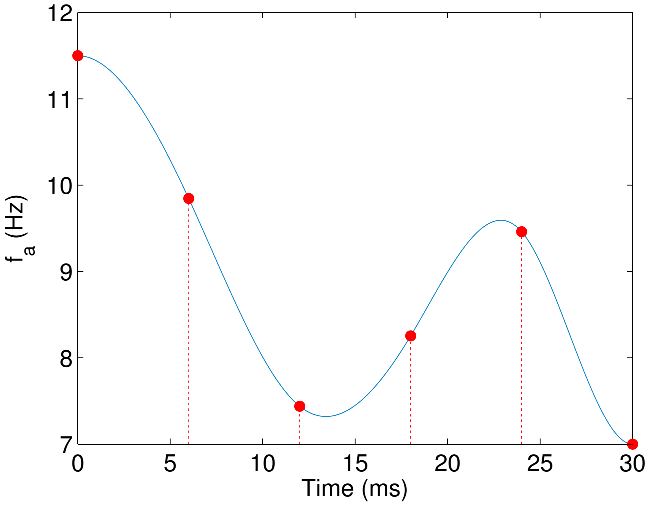

Figure 6.2.: Parametrisation of the control ramp. In experiment and corresponding simulations presented within this chapter, initial and final states characterized by axial trap frequencies $\omega_a(0) = 2\pi \times 11.5$ Hz and $omega_a(\tau) = 2\pi \times 7$ Hz at a ramp duration of $\tau = 30$ ms are used. The ramp segment connecting these values is defined by a set of $d+1$ piecewise cubic splines of form 6.3 that are uniquely fixed by d support points and boundary conditions on the derivatives of the spline segments.

Fitness assignment. The ranked states S_j, $j \in \{1...N_p\}$ are assigned a ranking-based *fitness* value, independent of the absolute value of the objective function (the breathing amplitude) that is given by

$$F\left(S_j\right) = \frac{2}{N_p}\left(1 - \frac{j-1}{N_p - 1}\right) \tag{6.4}$$

Such a ranking-based assignment has been observed to be less prone to premature convergence against local optima than a fitness assignment proportional to the objective function value for most test problems under consideration [241].

Selection. Generating a new population of states relies on two mechanisms: *recombination* and *mutation*. The selection of states for recombination based on their fitness value is performed by a variant of Roulette selection, called *stochastic universal sampling* (SUS) [242, 243]. Considering a mapping of each state's fitness value to a correspondingly long line section with a total length given by the sum of fitness values, SUS corresponds to a set of n_{pt} equidistant pointers distributed equally along the line with a random offset to select n_{pt} states for recombination. For the population size of $N_p = 24$ as used here, 12 parent states are selected. Compared to standard Roulette selection, SUS promotes the inclusion of states with low corresponding objective function value, promoting diversity and hence counteracting premature convergence against local optima.

Recombination Recombination constitutes the gradient search component of the algorithm. If there is an exploitable gradient towards an optimum present within the problem, the two selected parent states span a parameter subspace that is on average more optimal than a randomly chosen region. If an optimum is within this subspace, interpolating between these states provides better states. Here, we use intermediary recombination in the form of a BLX-α *blend crossover* method [241]. The new (child) state v_i^C, with variable index $i \in 1, ..., d$ is generated by the parent states $v_i^{P_{1,2}}$ as

$$v_i^C = v_i^{P_1} a_i + v_i^{P_2} (1 - a_i) \,, \tag{6.5}$$

where a_i is picked randomly by a uniform distribution from the interval $[-\alpha/2, 1 + \alpha/2]$ for each variable. The subspace under consideration forms a hypercuboid with a volume of

$$V_{PS}^C = (1 + \alpha) \prod_{i=1}^{d} l_i, \tag{6.6}$$

where l_i denotes the distance between the vector components $v_i^{P_{1,2}}$. To conserve the volume under interpolation [244, 241], a value of $\alpha = 0.5$ is chosen. 23 new states are created by recombination of the 12 parent states. In order not to lose already found good states, the best state from the previous generation is preserved, a practice called *elitism* in literature.

Mutation Mutation corresponds to a random change of the state vector components v_i. In our case, this is expressed by a non-uniform distribution of mutation steps favouring small deviations from the initial value [245, 246]:

$$v_i^{mut} = v_i + s_i \cdot r D_i \cdot 2^{-u\kappa_m} \tag{6.7}$$

with the mutated and source states v_i^{mut} and v_i, random sign s_i, the mutation range r and the definition domain D_i. The random number u is uniformly distributed in the interval $[-1, 1]$ and κ_m is called mutation precision, defining a lower limit of $\frac{1}{2}^{-\kappa_m}$ for the mutation step size. From runs on test problems, with population sizes between 20 and 30, a choice of $\kappa_m = 10$, $r = 0.2$ and a mutation rate of 10 percent has given the best convergence rates.

6.3. Characterization measurements

Before turning to the simulation of realistic ramps, it is necessary to exactly know the relation between the chip currents and trap parameters. To simplify the control problem, for the following simulations and experiments only the current in the U-shaped control wires I_U is subject to variation, while the current in the central Z-shaped structure is kept at a constant value of $I_Z = 1.5A$. This is in contrast to the measurements presented in the previous chapter, where both I_Z and I_U are varied in the course of a ramp.

A change of I_U tunes both the axial and radial trap frequencies ω_a and ω_r. Figure 6.3(a) shows the relation between I_U and $f_a = \omega_a/(2\pi)$ extracted from measurements based on axial sloshing of the atom cloud as described in section 4.5 that is used as a calibration for the experiment. With exception of the highest axial trap frequencies in the region around $f_a = 15$ Hz, the relation is linear to good precision. Figure 6.3(b) presents the results of corresponding transverse sloshing measurements to estimate the radial trap frequency ω_r. Here, also the data is well described by a linear fit. The coupling of trap frequencies as determined by this measurement is taken into account for the 1d GPE simulations presented below. Note that for axial trap frequencies $\omega_a < 2\pi \times 7$ Hz, slight deviations of the equilibrium density profile from a parabolic shape appear, hinting at anharmonicity of the trap due to the effect of wire corrugations deforming the potential. Therefore most measurements are performed in the range $2\pi \times 7 < \omega_a < 2\pi \times 13$ Hz.

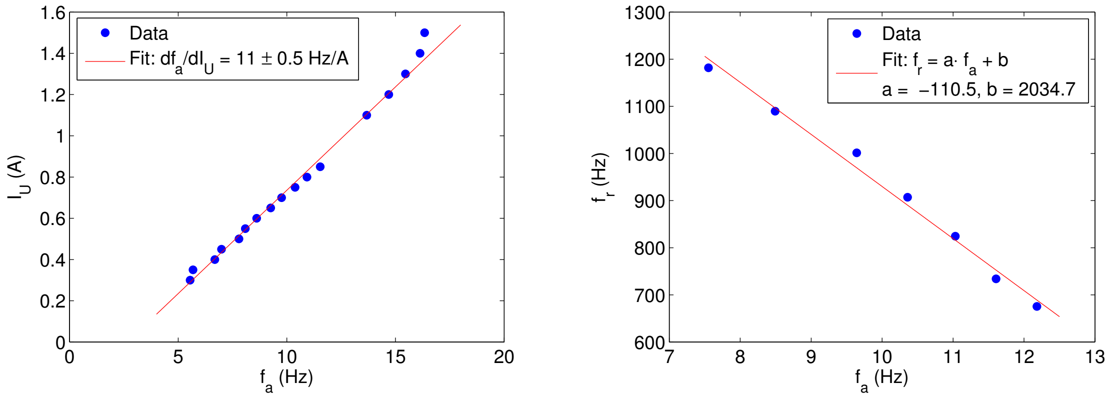

(a) (b)

Figure 6.3.: Trap frequency calibration. (a) Current through the control wire I_U over measured axial trap frequency $f_a = \omega_a/(2\pi)$. The linear relation extracted from these measurements is used as a calibration between I_U set in the experimental control and ω_a as calculated by the optimal control scheme. (b) Radial trap frequency $f_r = \omega_r/(2\pi)$ plotted against f_a. The linear relation recovered for the observed parameter range is taken into account in the 1d-GPE simulation that is part of the optimisation scheme.

6.4. Simulation results

Based on the trap frequency calibrations presented in section 6.3, the time-dependent 1d GPE

$$i\hbar\frac{\partial\Psi}{\partial t} = -\frac{\hbar^2}{2m}\frac{\partial^2\Psi}{\partial z^2} + \frac{m\omega_a(t)^2 z^2}{2}\Psi + 2\hbar\omega_r(t)\,a|\Psi|^2\Psi, \tag{6.8}$$

with scattering length a, ^{87}Rb-mass m and mean-field wave function $\Psi := \Psi(z,t)$ depending on time and the axial coordinate z can be solved for realistic trap frequencies $\omega_a(t)$ and $\omega_r(t)$. As a reference and for comparison with corresponding measurements,

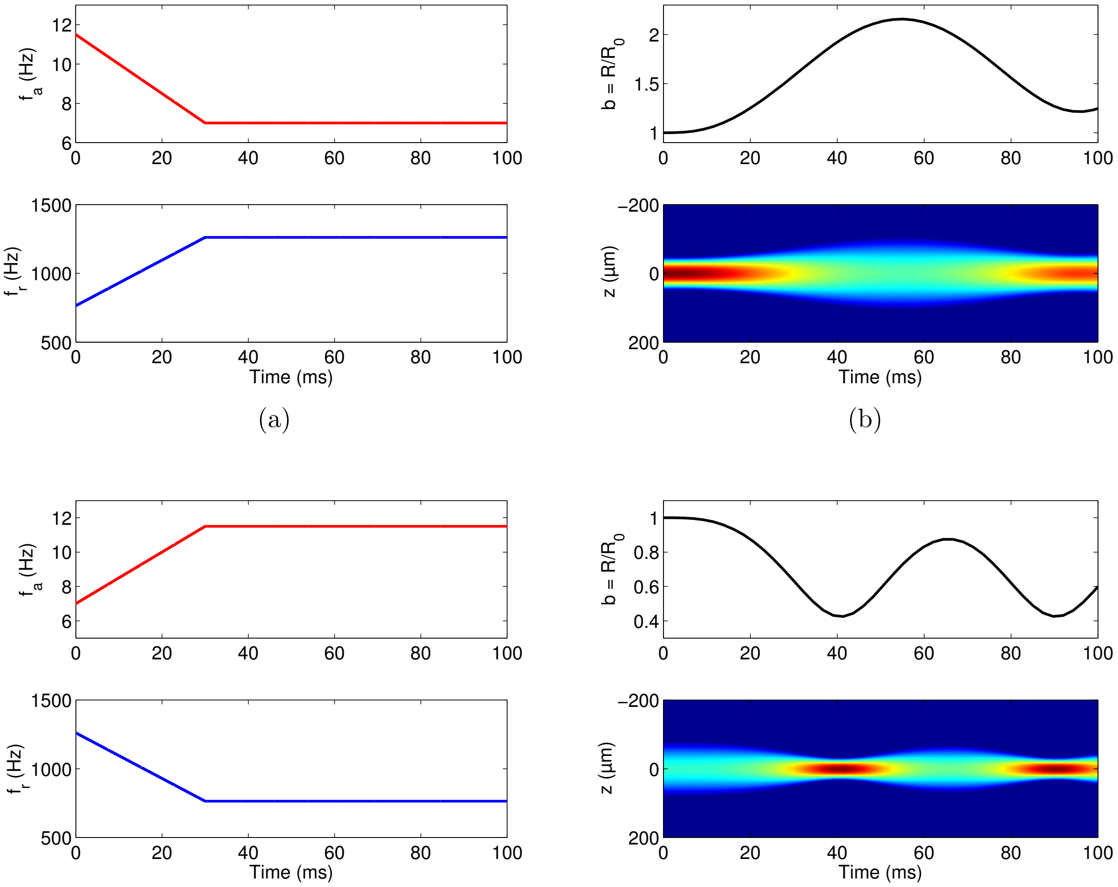

(a) (b)

(c) (d)

Figure 6.4.: Simulated breathing after linear trap frequency ramps. (a) Axial (upper panel) and radial (lower panel) trap frequency during the simulated time evolution in the course of an axial decompression or from $\omega_a(0) = 2\pi \times 11.5$ Hz to $\omega_a(\tau) = 2\pi \times 7$ Hz and (c) for the inverse compression process. (b), (d): Corresponding time evolution of the scale parameter (upper panels) and density profiles (lower panels).

figure 6.4 presents results from a simulation of a simple linear trap frequency ramp for a cloud with 10000 atoms. The simulations are performed with a grid size of 1000 points on a spatial interval of 400 μm. The ground state in the initial trap defined by $\omega_a(0)$ and $\omega_r(0)$ is found by imaginary time evolution of an arbitrary initial state, as described in chapter 3. In this case, a flat profile with a linear density of $n = 100/\mu$m is used. The subsequent dynamics is calculated by real time evolution in the time-dependent external potential.

Figure 6.4(a) contains the time-dependence of the axial and radial trap frequencies. In this example, an axial decompression from $\omega_a(0) = 2\pi \times 11.5$ Hz and $\omega_r(0) = 2\pi \times 764$ Hz to $\omega_a(\tau) = 2\pi \times 7$ Hz and $\omega_r(\tau) = 2\pi \times 1262$ Hz is considered, with a ramp time $\tau = 30$ ms. The resulting dynamics, tracked for a period of 100 ms, are shown in figure 6.4(b).

In the lower panel, a carpet plot of density profiles against axial coordinates and time is depicted. Correspondingly, the upper panel contains a plot of the scale parameter $b(t) = R(t)/R_0$ versus time. The breathing amplitude, used as a cost function F_c for the optimal control sequence, can be simply defined as

$$F_c = \max\{R(t)\} - \min\{R(t)\}, \tag{6.9}$$

with $t > \tau$, if at least one breathing period is tracked by the simulation.

Similarly, the inverse problem of an axial compression of a cloud initially prepared in a trap with $\omega_a(0) = 2\pi \times 7$ Hz and $\omega_r(0) = 2\pi \times 1262$ Hz to $\omega_a(\tau) = 2\pi \times 11.5$ Hz and $\omega_r(\tau) = 2\pi \times 764$ Hz can be analysed. The results are summarized in figure 6.4(c) and 6.4(d). Consistent with the breathing measurements and corresponding simulations presented in chapter 5, the linear ramps with a duration of 30 ms induce significant breathing. Even for ramp durations exceeding 100 ms, residual breathing in the order of 10% of the cloud radius has been observed. This is expected, considering that the adiabatic limit should be reached roughly in the limit marked by $\tau \gg 1/f_a \approx 150$ ms for $f_a = 7$ Hz.

In the following, the results for the optimized ramps found by the optimal control sequence for the same initial and final trap frequencies as considered above are discussed. Figure 6.5(a) shows the optimized ramps generated by the algorithm, and figure 6.5(b) summarizes the results for the decompression problem within the same time $\tau = 30$ ms and an atom number of 10000 as used for the linear ramps shown above. The optimization has been performed for a fixed population size of $N_p = 24$ states and 4 support points, resulting in 5 spline segments. The ramp found by the GA performs excellently and suppresses the residual breathing amplitude down to a level of 0.5 μm or 6 ‰ of the cloud radius R in the final potential.

Similar results are achieved for the inverse problem of an axial compression. Again considering the same initial and final trap frequencies of $\omega_a(0) = 2\pi \times 7$ Hz and $\omega_r(0) = 2\pi \times 1262$ Hz as well as $\omega_a(\tau) = 2\pi \times 11.5$ Hz and $\omega_r(\tau) = 2\pi \times 764$ Hz as for the linear ramp shown previously, the optimal control approach achieves excellent suppression of breathing. The absolute residual breathing amplitude is, as in the above case ≈ 0.6 μm, in this case corresponding to 1.2 % of the cloud radius. For this optimization run, the same population size of $N_p = 24$ states, but in contrast to the decompression example, 5 support points and 6 spline segments have been used. The generated ramps are depicted in figure 6.5(c), while the breathing dynamics is shown in figure 6.5(d).

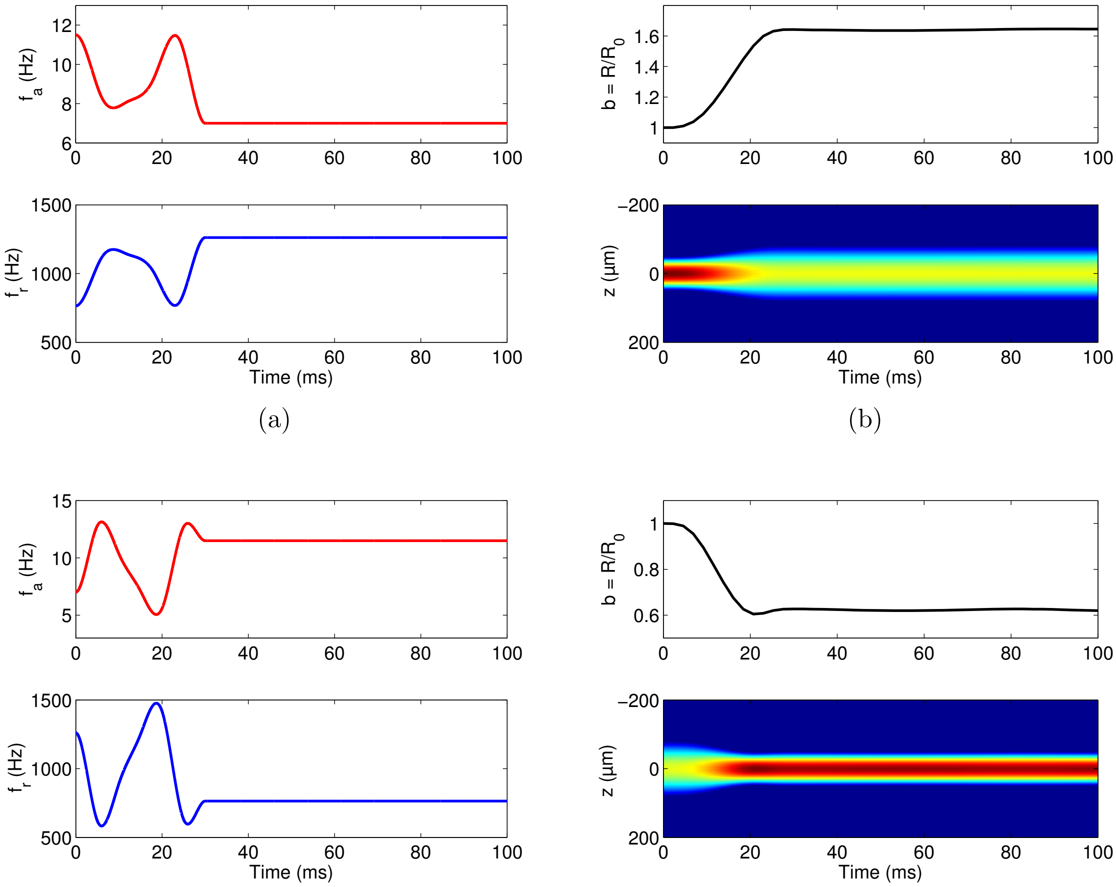

(a) (b)

(c) (d)

Figure 6.5.: Simulated breathing after optimized trap frequency ramps. (a) Axial (upper panel) and radial (lower panel) trap frequency during the simulated time evolution in the course of an axial decompression or from $\omega_a(0) = 2\pi \times 11.5$ Hz to $\omega_a(\tau) = 2\pi \times 7$ Hz and (c) for the inverse compression process. (b), (d): Corresponding time evolution of the scale parameter (upper panels) and density profiles (lower panels).

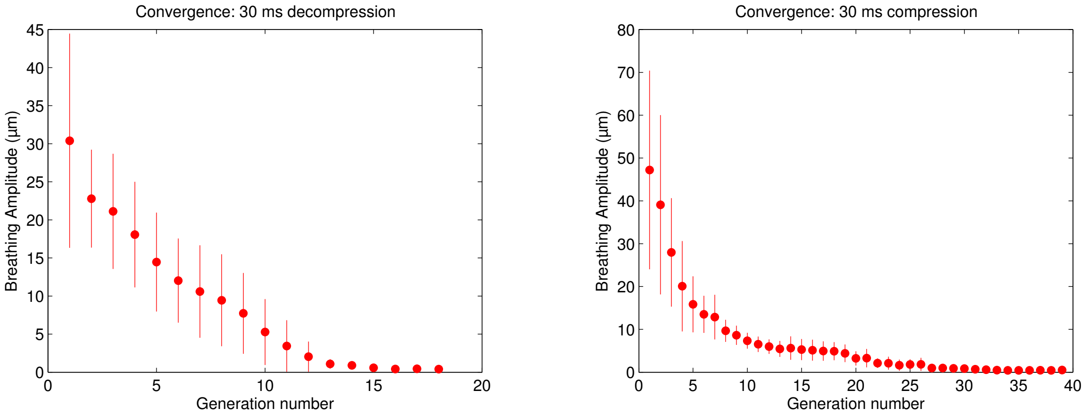

(a) (b)

Figure 6.6.: Convergence of the RCGA for the optimization runs resulting in the control ramps shown in figure 6.5. (a) Average breathing amplitudes and corresponding standard deviation (errorbars) within each generation of $N_p = 24$ states, each representing a decompression ramp. The dimensionality of the search space is given by the number of support points $d = 4$. (b) Average breathing amplitudes and standard deviation within each generation of 24 states, each representing a decompression ramp. In this case, $d = 5$. The onset of convergence is seen around generation 15 (a) and 30 (b), respectively.

Convergence and runtime

To characterize the convergence towards a good control ramp, the average fitness of each population's states and the corresponding spread can be tracked. Since the optimization relies on stochastic elements, the number of iterations needed to converge towards an acceptable solution varies between different optimization runs. For the stated control problem, the algorithm has been found to typically converge towards a solution within 10 to 30 generations. The population size of $N_p = 24$ has been chosen due to the observed behaviour in several test runs and is consistent with previous tests of the algorithm on toy models, as presented in [192]. For smaller population sizes, premature convergence towards a suboptimal state is likely. Larger population sizes, on the other hand, extend the average runtime.

The absolute runtime obviously depends on the computational resources available. The optimization runs discussed within this chapter have been performed on a workstation computer[1] using Matlab, allowing us to parallelize the problem to 12 processor cores. An optimization run from start to convergence in this configuration has a typical duration of 30 minutes. Running multiple runs (up to 3 without significant slowdown) within different Matlab sessions on the same machine can effectively cut this duration down to 10 to 15 minutes. While this is short enough to perform test runs to roughly evaluate the performance, acquiring sufficient statistics for a quantitative evaluation and tuning of algorithm parameters to improve performance would already require exceedingly large computation times.

---

[1] 4×AMD Opteron 6272 CPUs, 256 GB RAM.

Figures 6.6(a) and 6.6(b) show the convergence towards the optimized control ramps discussed within this chapter in terms of the average breathing amplitudes achieved across all 24 states within each generation, while error bars are given by the corresponding standard deviation. Note that for the compression problem, the dimensionality of the control space is 5 in contrast to 4 as for the decompression problem, consistent with a longer convergence time.

Note that all the simulations shown within this chapter so far have been performed before studying the scaling equations discussed in the previous chapter. Of course, for this particular control problem, replacing the GPE simulation by a numerical solution of the modified scaling equation 5.9 is much faster. In order to study the minimal achievable ramp times that still allow the suppression of the breathing dynamics in the following section, this approach is taken. On the other hand, the GPE allows to include modifications to the interaction term and the generalization to control problems for which scaling solutions do not hold, especially anharmonicity in the axial trapping potential that often cannot be avoided. Therefore, the optimal control scheme including the GPE is the more interesting tool for future applications within the group.

6.5. Measurement results

The goal of the work presented in this chapter is the demonstration of optimal control within an experimental setting. On the one hand, the experiment is subject to external perturbations leading to shot-to-shot fluctuations of the atom numbers, drifts of the trap parameters, imperfections of the axial trapping potential and similar disturbances. On the other hand, experimentally trapped atom clouds differ from simulations due to deviations from pure 1d physics, finite temperature and interaction with thermal atoms. Fortunately, simulations indicate that the control ramps are robust with respect to changes in atom number in the order of a factor 2. Additionally, the comparisons between simulated and measured breathing dynamics for the simple ramps presented in the previous chapter show good agreement and indicate that finite temperature has little effect on collective excitations within our parameter range. Additionally, small deviations can be accounted for by small adaptations of the experimental control fields. Since the same GA is implemented within the experimental control, also closed-loop adaption is feasible in our setup.

Nevertheless, it is interesting to observe that no adaptions were necessary to recover the results presented in figure 6.7. It shows the measured cloud radii after a short time-of-flight expansion phase of 5 ms throughout an axial decompression (figure 6.7(a)) and compression (figure 6.7(b)). The radii are determined by parabolic fits to imaged density profiles as shown in figure 6.8(b) and 6.8(d). Each data point corresponds to an average over 5 shots at identical parameters. Errorbars indicate the corresponding

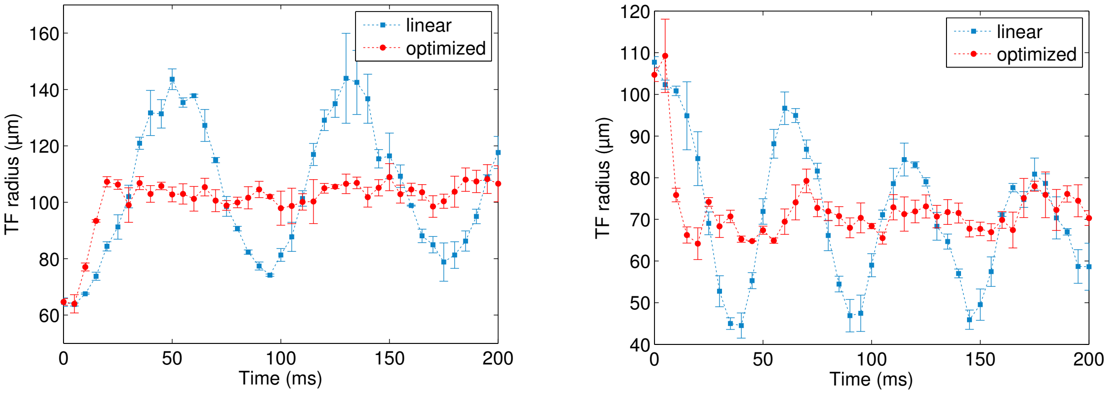

(a) (b)

Figure 6.7.: Measured cloud width for shortcuts and linear ramps. (a) Time evolution of the Thomas-Fermi radius for an optimal axial decompression (red circles and line) from $\omega_a^0 = 2\pi \times 11.5$ Hz, $\omega_r^0 = 2\pi \times 764$ Hz to $\omega_a^f = 2\pi \times 7$ Hz, $\omega_r^f = 2\pi \times 1262$ Hz compared with the Thomas-Fermi radius for a corresponding linear ramp (blue squares and dashed line). Errorbars represent the standard deviation of 5 shots at identical parameters. (b) Time evolution fo the Thomas-Fermi radii for an optimal axial compression (red circles and line) and a corresponding linear ramp (blue squares and dashed line). The compression process is inverse to the decompression, changing $\omega_a^0 = 2\pi \times 7$ Hz, $\omega_r^0 = 2\pi \times 1262$ Hz to $\omega_a^f = 2\pi \times 11.5$ Hz, $\omega_r^f = 2\pi \times 764$ Hz.

standard deviation.

The dynamics are triggered by the same control ramps as presented in section 6.3 based on the characterization measurements for the trap frequency calibration discussed above. For comparison, figure 6.7 shows the radius of a breathing cloud after linear ramps between the same initial and final trap configurations, in analogy to the simulation results depicted in figure 6.4. For both protocols, the optimized ramps lead to an excellent suppression of the breathing dynamics. Figure 6.8 contains an additional comparison between measured density profiles and simulation results for the breathing dynamics after decompression by a linear ramp, shown in figure 6.8(a) and 6.8(b) as well as after an optimized ramp in figure 6.8(c) and 6.8(d), underlining the excellent agreement between the calculated and measured mean-field dynamics.

Of course, in the light of the results presented in the previous chapter, it is interesting to track the temperature of the phonon ensemble throughout the shortcut. For a stationary cloud in thermal equilibrium, as outlined in section 5.3.2, the phonon spectrum is given by [82]

$$\omega_l = \frac{\omega_a}{\sqrt{2}} \sqrt{l\,(l+1)}, \tag{6.10}$$

with mode index l, depending only on the axial trap frequency ω_a. For an adiabatic state change within time τ, as discussed in the previous chapter, it holds that $T(0)/T(\tau) = \omega_l(0)/\omega_l(\tau)$, and consequently $T(0)/T(\tau) = \omega_a(0)/\omega_a(\tau)$. If the shortcut

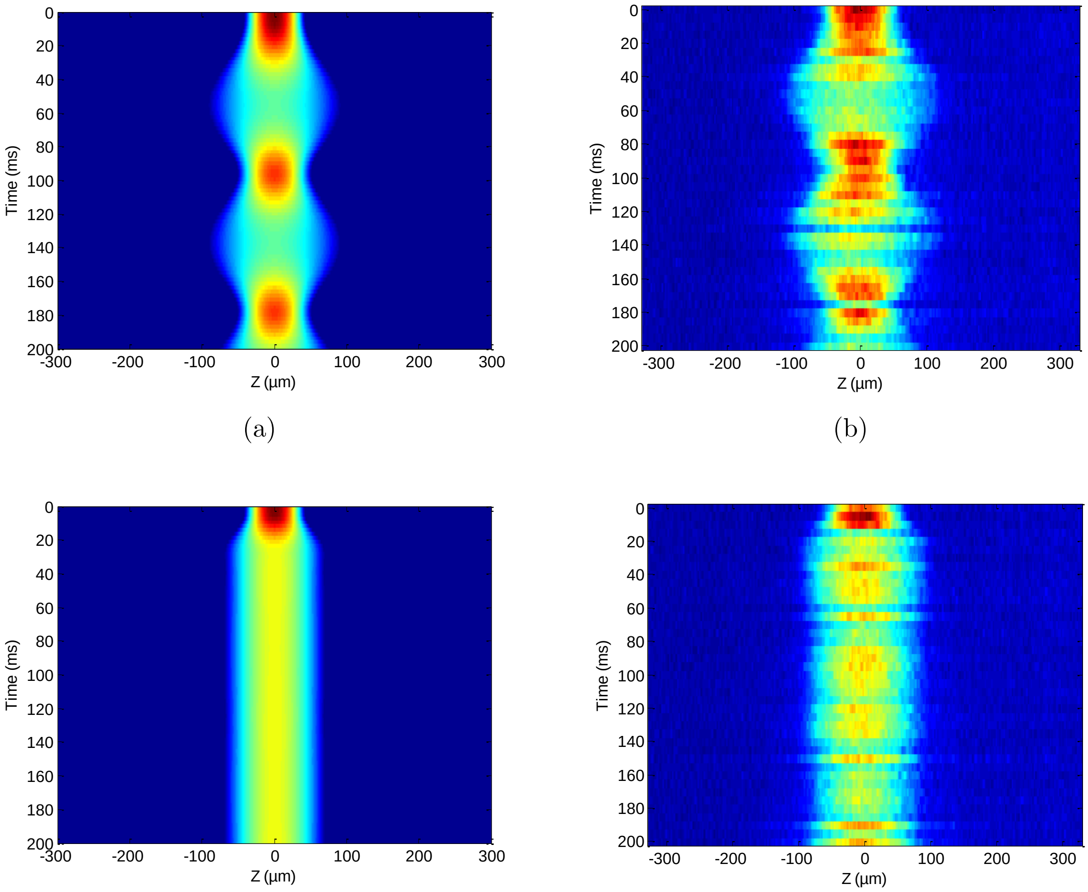

(a) (b) (c) (d)

Figure 6.8.: Comparison of simulated and measured density profiles for linear axial decompression. (a), (c): Simulation results for the linear and optimal decompression, as in figures 6.4 and 6.5. (b), (d): Imaged density profiles from the dataset evaluated in figure 6.7(a), averaged over 5 shots at identical experimental parameters.

is adiabatic not only with respect to the mean-field dynamics, but also the whole phononic excitation spectrum, as suggested by the scaling model developed in the previous chapter, the measured temperature ratio between initial and final state should behave as argued.

As a first check of this conjecture, an additional dataset for the decompression shortcut ramp has been recorded. Sets of 250 pictures at identical parameters for the times $t = 0$ ms (before the shortcut ramp), $t = \tau$ (directly after the shortcut ramp) and after a hold time $t = \tau + 30ms$ have been taken. The statistics and a free expansion time of 10 ms allow to apply density ripple thermometry as used in chapter 5 and described in section 4.6. All measured density profiles are depicted in figure 6.9(a), while the respective averaged profiles together with parabolic fits are shown in figure 6.9(b).

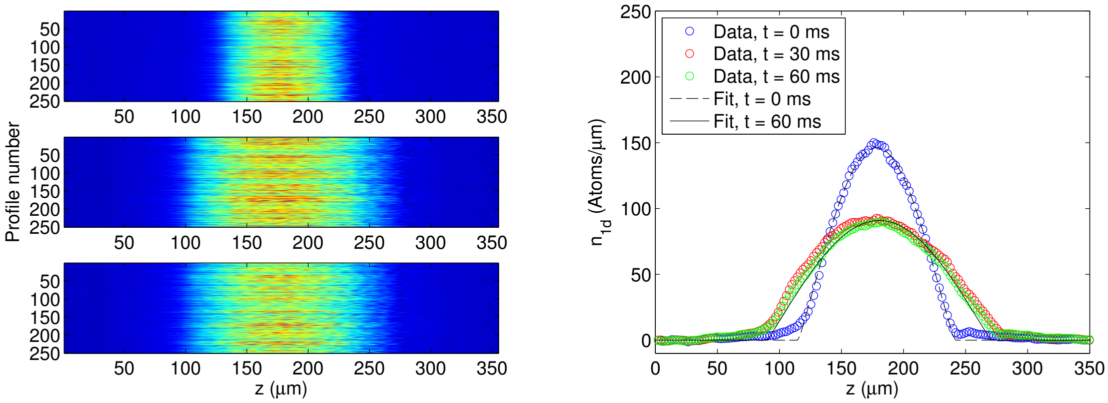

(a) (b)

Figure 6.9.: Density profiles from the dataset used for the temperature measurements discussed in the text and shown in 6.5. (a) Carpet plots of all density profiles involved in the temperature estimation for $t = 0$ ms (before the shortcut, upper panel), $t = 30$ ms (directly after the shortcut, middle panel) and $t = 60$ ms (after an additional hold time of 30 ms, lower panel). (b) Averaged density profiles at $t = 0$ ms (blue circles), $t = 30$ ms (red circles) and $t = 60$ ms (green circles), compared to parabolic fits at $t = 0$ ms (dashed black line) and $t = 60$ ms (black line). The parameters and ramp are identical to those used for simulations and measurements for the axial decompression as presented previously in this chapter.

Analysing density correlations, we find an initial temperature of 109 ± 6 nK as well as 78 ± 4 nK and 102 ± 5 nK directly after the shortcut and after the additional hold time of 30 ms, respectively. These results are summarized within figure 6.5. Clearly, heating is observed and prevents the direct verification of an adiabatic temperature change. However, correcting for an experimental heating rate of 0.5 nK/ms yields temperatures of 62 nK after the shortcut and 63 nK after the 30 ms hold time, in close agreement with the adiabatic prediction of 65 nK for our trap geometry. The fact that the temperatures before and after the shortcut are related according to the adiabatic prediction, if corrected for a regular experimental heating rate that leaves the temperature stationary during the hold time after the shortcut, at least suggests that the ramp itself provides a negligible contribution to the overall heating rate in the system. To illustrate this argument, figure 6.5 also contains the mentioned corrected temperature values. In addition to these measurements, the figure features a plot of numerical results for the temperature evolution from simulations based on stochastic initial conditions generated by a SGPE and subsequent evolution with a GPE in a time-dependent potential, subject to the shortcut ramp. The numerical results are in close agreement with the adiabatic prediction, and also the heating-corrected temperature measurements.

Of course, a clear demonstration of fast frictionless adiabatic cooling in a 1d quasi-BEC requires at least more temperature measurements throughout shortcuts between different

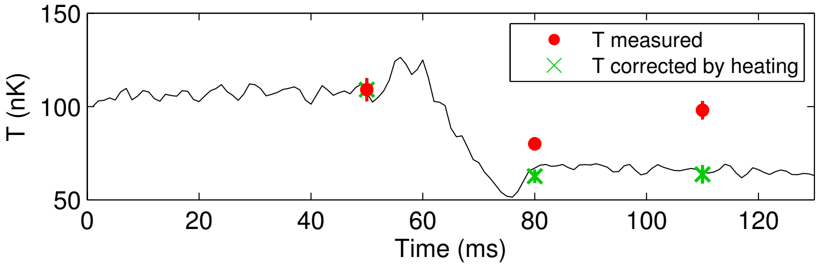

Figure 6.10.: Time evolution of the temperature in the course of a decompression STA. Red circles represent the measured temperature values for the dataset shown in figure 6.5. Green crosses correspond to temperatures corrected for an experimental heating rate of 0.5 nK/ms, comparable to what has been determined for the measurements presented in chapter 5. The black line shows results from numerical simulations based on the SGPE$_{eq}$-method, averaged over a set of 480 stochastic initial conditions, and evolved for the shortcut ramp employed in the measurements. Both the corrected temperatures as well as the numerical results are in close agreement with the adiabatic prediction discussed in the main text.

ramps, and ideally to probe a system with negligible heating rates in the future.

6.6. Summary

Summarizing, an optimal control approach for the mean-field dynamics of a 1d BEC based on the combination of a stochastic optimization algorithm and numerical simulations of the Gross-Pitaevskii equation has been presented in this chapter. Simulation results show that the control scheme allows to suppress the breathing dynamics typically induced by a fast change of the trap geometry, implementing a shortcut to adiabaticity. Further, it has been demonstrated that the control ramps obtained by the algorithm allow the suppression of breathing dynamics in a corresponding experimental implementation with quasi-1d BECs without any additional adaptations needed. The results hold in the presence of environmental perturbations present in the experiment, finite temperature, and deviations from the pure 1d model adopted in the numerics. The presented approach is expected to be useful as a tool to control the external dynamics of quasi-1d BECs within other atom chip experiments, for instance the investigation of Josephson physics [247], interferometry based on double well traps [248] or even optimal control experiments performed on the transverse state of the atom cloud [216], which also induce axial collective excitations.

It has been shown that quasi-1d BECs, allowing direct thermometry on the phononic excitations within the condensed atom ensemble, allow to probe the temperature throughout an optimal control sequence. Making use of this feature, the temperature measurements during a shortcut to adiabaticity for the axial expansion of a 1d quasi-BEC have been presented. While experimental heating prevents a direct verification of fast frictionless cooling, the results suggest that the shortcut ramp itself does not induce additional excitations, consistent with a constant heating rate during and after the control ramp. However, further measurements that provide a real proof of fast frictionless cooling in the future are called for.

It is interesting to consider whether the approach could be used within a closed-loop implementation directly on the experiment. In this context, it is important to consider the expected runtime in such a setting. The total number of cost function evaluations until convergence - the number of GPE simulations to estimate the breathing amplitude - amounts to ≈ 360 for decompression and ≈ 720 for compression. For a reliable experimental estimation of the breathing over a period of 100 ms to 200 ms, an average number of 10 data points per ramp is assumed. This results in 3600 or 7200 experimental runs, respectively, without taking into account additional statistics. In our experiment, with a cycle time of 30 seconds, this translates to a runtime of 30 or 60 hours per optimization, respectively. This is a challenging duration for a single optimization run, but feasible.

Another interesting question is whether the optimal control approach could be used on stochastic simulations that allow investigating finite temperature dynamics. Relying on quantities that can be calculated from a single stochastic field, or by averaging over a few realizations, the expected runtime is similar to the $T = 0$ case. Many observables require averaging over $\mathcal{O}(100)$ realizations however. In this case, extrapolating from the performance of the SGPE model presented in chapter 3 and used throughout this thesis, within its current implementation, an optimization run is estimated to take roughly 24 hours. Such optimal control studies on finite temperature simulations could open up interesting experiments, as using optimal control to create specific non-thermal states with tailored phononic occupation number distributions as initial conditions for the study of relaxation processes within a 1d Bose gas. So far, only very specific initial states can be created experimentally [205].

7. Cold atoms in a magnetic guide

> *"We have a habit in writing articles published in scientific journals to make the work as finished as possible, to cover up all the tracks, to not worry about the blind alleys or describe how you had the wrong idea first, and so on. So there isn't any place to publish, in a dignified manner, what you actually did in order to get to do the work."*
>
> RICHARD P. FEYNMAN, NOBEL LECTURE, 1996

The studies presented in chapters 5 and 6 were triggered by the investigation of ultracold atoms propagating in a 1d magnetic guide towards the integrated fluorescence detector presented in section 4.3.9. The goal of this chapter is to give a brief presentation of early studies on this topic, constituting a precursor to and additional motivation for the detailed analysis of quasi-1d BECs in time-dependent trapping potentials as presented in the chapters 5 and 6.

While recent measurements with the integrated fluorescence detector will mainly be subject of the thesis [188], the final part of this chapter summarizes some results considering the optimal parameters for the detection of ultracold atoms at temperatures below 1 μK. The main goal is to present an analysis of the kinematics of cold atoms in the detection region based on a numerical simulation contributed in the course of this thesis, and possible implications for the scattering properties and the estimation of the detection efficiency.

As such, this chapter is supposed to link the main results from this thesis to previous experiments on fluoresecence detection of non-degenerate thermal atoms [39] and the follow-up work which will be part of the thesis [188], and also to comment on loose ends and questions to be investigated within the next iteration of the experiment that is in the process of being set up, as summarized within chapter 8.

7.1. Introduction

Previous measurements (see the thesis [39] as well as [42] and references therein) performed with the experiment presented in chapter 4 focused on the properties of the integrated fluorescence detector outlined in section 4.3.9. Naturally, it is interesting to study the feasibility of using the fluorescence detector as a tool to investigate clouds at the temperatures necessary to reach degeneracy, as realized within the scope of this thesis.

Figure 7.1(b) sketches the geometry considered within this chapter: An atom cloud is prepared in a trap formed by external fields and the current I_Z through the Z-shaped wire structure in the centre of the chip. By subsequently ramping down I_Z while increasing the current I_G through the L-shaped wire structure marked in figure 7.1(b), the atom cloud is transferred into a tube-like potential, ideally able to freely propagate towards the detection region, with an axial confinement only present at the far end from the fluorescence detector's point of view. Note that to achieve optimal detection efficiency, the minimum of the tube-like potential needs to match the distance from the excitation fibre tip, as depicted in figure 4.11, to the chip surface. This distance is given by the fibre radius of 62.5 μm.

In the following, the transport of atom clouds with temperatures in the nanokelvin-regime along such a guide potential is discussed. The first section concentrates on the initial hydrodynamic propagation stage of a quasi-BEC. Note that the results presented as such do not allow to draw a full picture of the system; the questions raised in the course of this project lead to the investigation of quasi-BEC dynamics in a time-dependent trapping potential as presented in chapter 5. While, in this framework, the short-time expansion dynamics of a quasi-BEC in a homogeneous 1d potential is expected to be captured faithfully, the asymmetric shape of the guide wire complicates a clean experimental investigation of the expansion, leaving this project to the next iteration of the setup as presented within chapter 8. There, the axial confinement can be switched off symmetrically, allowing a description in terms of a scaling model as presented within section 5.3. Further, the scale invariance of the system is expected to be broken by sufficiently long expansion times even in a symmetric arrangement, with a potentially observable signature that is discussed in the framework of c-field simulations within section 7.3.

The second part of this chapter, section 7.4, examines the fluorescence detection of cold guided atoms. At low temperatures, the dependence of the signal strength on the properties of the detection light field is observed to deviate from the behaviour found at temperatures exceeding $T \gg \mathcal{O}(1)$ μK in reference [39]. Using a classical approximation to the dynamics of atoms in the vicinity of the detection region, an attempt to understand these deviations is presented, with possible implications for the design of a next generation fluorescence detector.

Beyond these contributions in the scope of the presented thesis, much work including additional experiments considering pulsed detection, the implementation of repulsive and attractive dipole potentials provided by the detection fibre and an analysis of the arrival time signal corresponding to a propagating quasi-BEC's density profile in terms of a Wigner function description, together with a discussion of the possible detection of flow correlations, will be contained in the thesis [188].

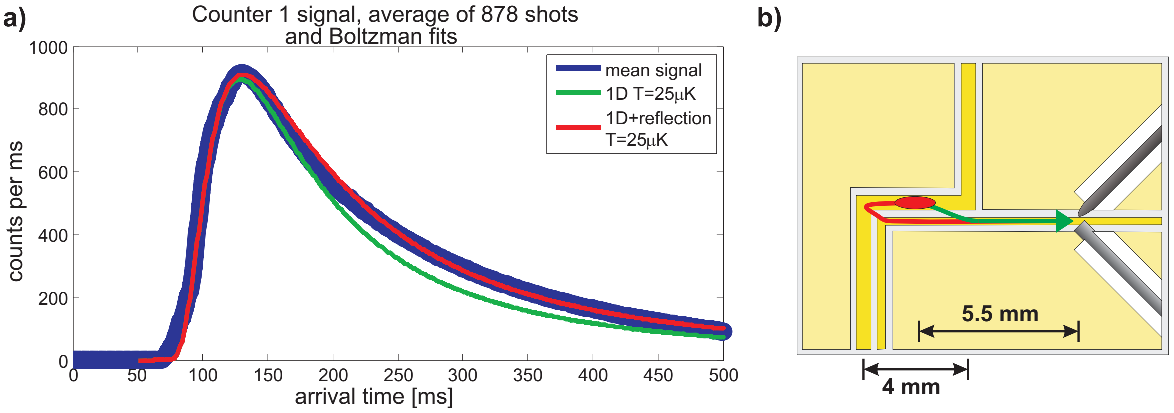

Figure 7.1.: Arrival time signal for hot atoms ($\geq 20\ \mu$K) and geometry of the transport. a) Comparison of an average arrival time signal (blue) with the 1d Boltzmann velocity distribution 7.1 (green line) and a fit based on the distribution 7.1 taking into account the contribution of atoms reflected by the closed end of the potential as denoted by the red path within panel b). b) Geometry of the transport: Atoms initially trapped by a current I_Z and external fields through the central Z-shaped wire structure are transferred into the magnetic guide potential given by the current I_G through the L-shaped guide wire, connecting the central chip region to the fluorescence detector. Figure adapted from [39].

7.2. Transport of quasi-BECs in a magnetic guide

Atom clouds with temperatures in the order of $\geq 20\ \mu$K have been observed to propagate smoothly along the guide potential. At such temperatures, the fluorescence signal is well-explained by ballistic propagation according to a 1d-Boltzmann velocity distribution,

$$f_{1d}(v) = \sqrt{\frac{m}{2\pi k_B T}} \exp - \left(\frac{mv^2}{2k_B T} \right) \tag{7.1}$$

plus a small additional contribution to correct for atoms with an initial velocity pointing away from the detector, reflected at the confined end of the guide potential. A detailed analysis of such arrival time signals from the fluorescence detector can be found in reference [39], while figure 7.1 serves as a demonstration.

In section 4.4.5, it was already noted that with decreasing distance of the trap minimum to the chip surface, corrugations in the potential can appear caused by irregularities of the current flow through the chip wires. These corrugations have little influence on the propagation of atoms with kinetic energies exceeding the 'waviness' of the potential $E_k \gg \Delta E_{pot}$. As shown in figure 4.19, the waviness can be in the order of the chemical potential of a quasi-BEC with $\mu <<$ a few $\hbar\omega_r$ for sufficiently small distances of the chip. Since interactions yield the dominant energy scale in the system, the expansion of such a cloud in a guide potential with corresponding waviness is expected to be influenced by the corrugations. Unfortunately, at the target distance of 62.5 μm between trap minimum and chip, this effect has observed to be sizeable in our experiment. To observe smooth propagation of a quasi-BEC along the full extension of the guide, distances between chip and trap minimum below $\sim 100\ \mu$m

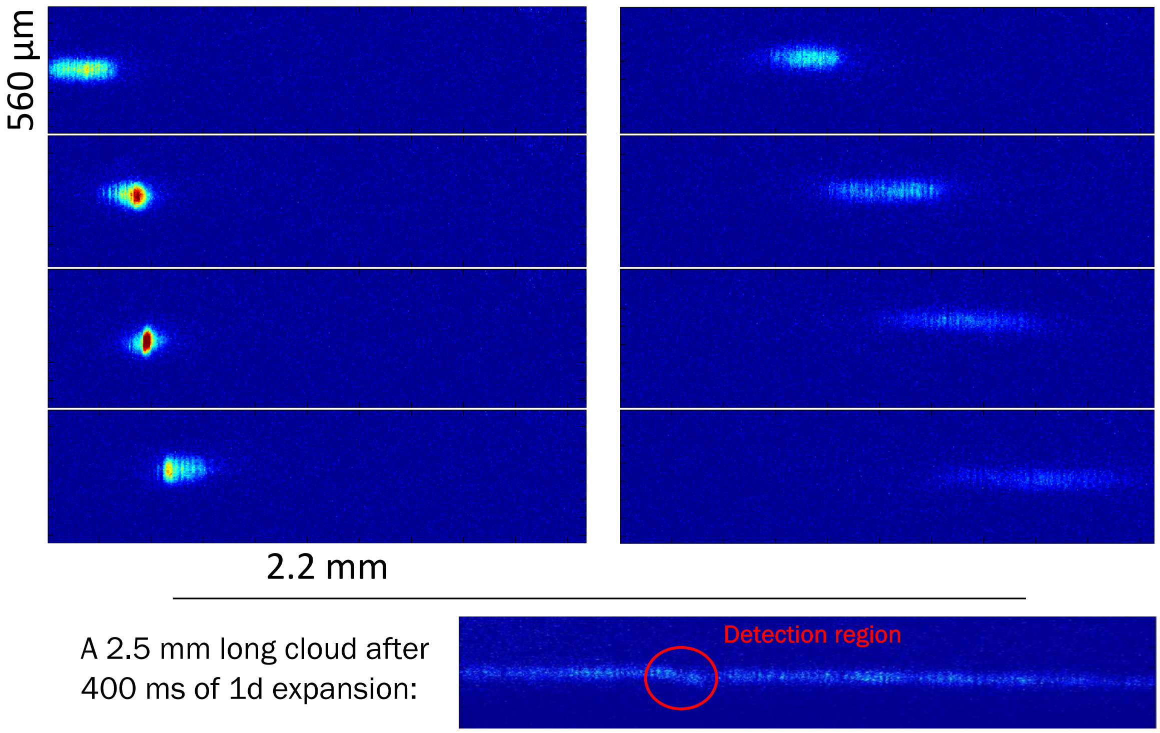

Figure 7.2.: Transport of a quasicondensate from ∼ 12000 atoms in a magnetic guide as discussed in the main text.

are to be avoided. Under these conditions, dynamics as shown in figure 7.2 can be observed. Here, a cloud of ≈ 12000 atoms is transferred from a trap with confinement characterized by $\omega_r, \omega_a \approx 2\pi \times (1400, 5)$ Hz into a guide potential with a radial trap frequency of $\omega_r^G \approx 2\pi \times 1600$ Hz within a timescale of 20 ms and imaged at intervals of 20 ms, each after an additional 10 ms of free expansion time. The first picture shows a quasicondensate within the initial trapping potential. After a subsequent compression phase that is not apparent in simple GPE descriptions of the process and is attributed to imperfections of the potential, the cloud proceeds to propagate and expand along the guide wire.

Figure 7.3 summarizes the time evolution of the average density profile. Figure 7.3(a) contains raw profiles (upper panel) and Gaussian fits (lower panel) to extract the RMS radius as a measure of the cloud with. The fit results are plotted in figure 7.3(b) and reveal an approximately linear expansion after the compression phase with a velocity of ≈ 4.2 mm/s, which roughly corresponds to twice the initial sound velocity $c_0 \approx 2.2$ mm/s. Revisiting the scaling equation 5.5 for a 1d quasicondensate in the Thomas-Fermi regime introduced in section 5.2, with vanishing axial trap frequency $\omega_a(t) = 0$,

$$\ddot{b}(t) = \sqrt{\frac{2g_{1d}n_0}{mR_0}}\frac{1}{b^2(t)}, \tag{7.2}$$

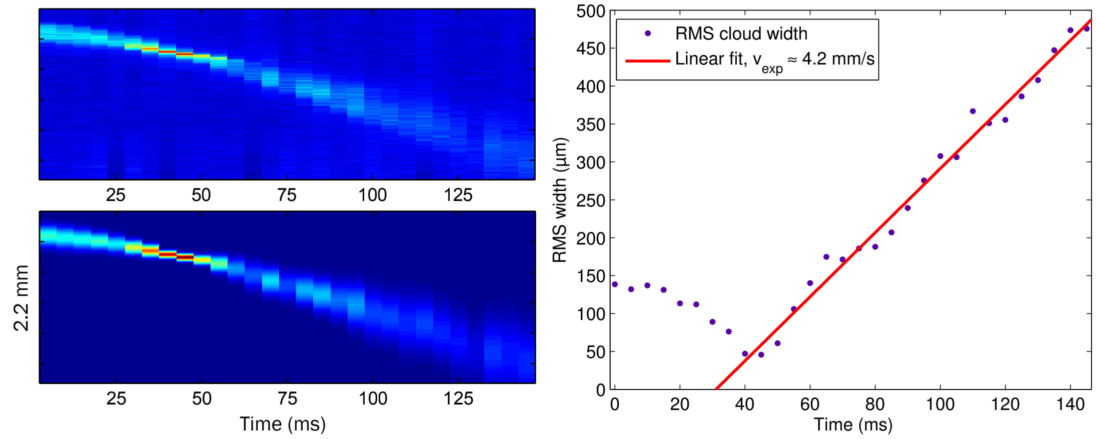

(a) Propagation: Density profiles.

(b) Propagation: Time evolution of the RMS width.

Figure 7.3.: Characterization of quasicondensate propagation in the magnetic guide. (a) Integrated density profiles from the dataset shown in figure 7.2 (upper panel) and Gaussian fits to these profiles (lower panel). (b) RMS radii corresponding to the Gaussian fits from (a), and linear fit to extract an expansion velocity of $v \approx 4.2$ mm/s.

one finds with $b(t) = R(t)/R_0$ and the initial Thomas-Fermi radius $R_0 = \sqrt{2g_{1d}n_0/m\omega_0^2}$ as well as the sound velocity $c_0 = \sqrt{g_{1d}n_0/m}$ the relationship

$$\ddot{R}(t) = \frac{2c_0^2 R_0}{R(t)}, \tag{7.3}$$

yielding for the expansion speed

$$\dot{R}(t) = 2c_0\sqrt{1 - \frac{R_0}{R(t)}}, \tag{7.4}$$

which, in the limit $R \gg R_0$ indeed converges to twice the sound velocity. The physically intuitive picture behind this circumstance is that, after sufficient time, the initial interaction energy, with c_0 being the characteristic velocity, should largely be transferred into kinetic energy. Hence, this basic result is expected to hold even if the asymmetry of the experimental setting breaks the validity of the scaling equation.

The axial propagation velocity induced by the change of the trapping potential and release of the cloud into the guide can also be deduced from the fits shown in figure 7.3(b), amounting to $v_p \approx 13.3$ mm/s.

The propagating cloud can be tracked by absorption imaging to make sure that no other defects in the trapping potential inhibit propagation towards the detection region. Since the atomic cloud eventually needs to pass the fibre detector at a distance of 62.5 μm from the chip surface, a second ramp reduces the guide wire current I_G after $\approx$ 250 ms of

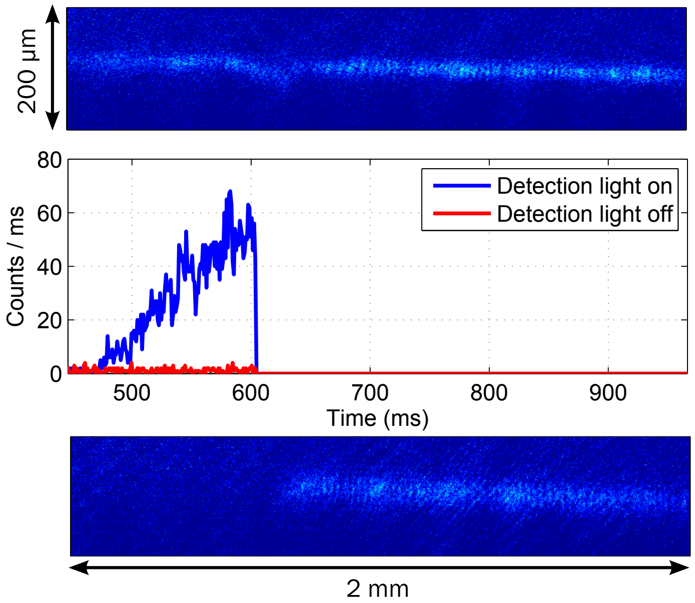

Figure 7.4.: Atom cloud passing the detection region. Upper panel: Absorption image of an atom cloud passing the detector in the absence of excitation light, after 600 ms of propagation and 7 ms of free expansion time. Lower panel: Picture for parameters identical as used to obtain the image shown in the upper panel, but in the presence of excitation light. Centre panel: Arrival time signals from the atom cloud depicted in the upper panel (red line) and the lower panel (blue line).

propagation time at constant external bias field with a ramp time of 50 ms from $I_G = 1$ A to $I_G = 0.65$ A, and from $\omega_r^G = 2\pi \times 1600$ Hz to $\omega_r^G = 2\pi \times 2200$ Hz. Fortunately, this second ramp does not disrupt the propagation, and atom clouds with sufficient initial density can be observed to pass the detection region. An example is given in figure 7.4. The central panel contains two arrival time signals from the fluorescence detector. The red signal corresponds to the upper panel, which shows an atom cloud passing through the detection region without any light coupled to the excitation fibre and, hence, no fluorescence. After switching off the trap at the time coinciding with the 600 ms mark in the arrival time plot and a free expansion time and 7 ms, the upper picture has been taken. In contrast, the blue signal denotes an atom cloud entering the detection region with the excitation light turned on, showing an increasing fluorescence rate until the switch-off time, after which the picture from the lower panel has been taken. Again, a free expansion time of 7 ms has been used. It is apparent from the image that the part of the cloud having entered the detection region has been removed from the trap by resonant scattering. Datasets like this show that it is possible to guide an initially degenerate atom cloud over a distance of 5.5 mm towards the fluorescence detector, and identify the corresponding arrival time signal.

7.3. Excitation spectrum of 1d-expanding quasi-BECs

Before turning to a further analysis of arrival time signals corresponding to ultracold atoms transported towards the integrated fibre detector as outlined within the previous section, here we discuss the excitation spectrum of a 1d quasicondensate during 1d expansion of an initial harmonically trapped cloud after switching off the axial confinement in an ideal symmetric setting. Such an experiment is expected to be realized within the next iteration of the experiment. Above, we already found an expression that allows to describe the density profile during expansion making use of the scaling equation 5.5. Hence, the time-evolution is self-similar, conserving the initial parabolic shape of a harmonically trapped cloud. Density and velocity fluctuations can then be described by the same linearised hydrodynamic equations 5.17 and 5.18 as used for the trapped system, since the external potential does not enter here and all modes scale with the spatial extension of the cloud via a well-defined scale parameter $b = R(t)/R_0$ with the time-dependent and initial Thomas-Fermi radii $R(t)$ and R_0, respectively, and one can use the exact same line of arguments as in section 5.3.2 to find an approximately adiabatic scaling of both the spectrum and temperature $\omega_l \propto T \propto b^{-3/2}$.

C-field approach: Temperature. Just as for the breathing dynamics from chapter 5, the time-evolution of the temperature can be investigated with the help of the SGPE-based c-field simulation introduced in chapter 3. The results for a corresponding simulation run for an initial cloud of ~ 16500 atoms at a temperature of $T = 100$ nK within a harmonic potential characterized by the trap frequencies $\omega_a, \omega_r = 2\pi \times (12, 1000)$ Hz, where the axial potential is removed within a ramp of 1 ms duration and the hydrodynamic expansion is observed for a time span of 100 ms, are displayed in figure 7.5. To confirm an initial equilibrium state, the confinement is kept for 100 ms of GPE evolution after the SGPE stage, before initiating the expansion. Figure 7.5(a) plots temperature values obtained by density ripple thermometry (see sections 2.5 and 4.6) against time, in comparison with the adiabatic scaling law and finds excellent agreement. Displaying the same data as a function of the scale parameter yields figure 7.5(b).

Scaling basis and adiabaticity. However, adiabaticity in the chosen basis of rescaled eigenmodes was not an exact result of the model derived in section 5.3, but only holds if the expansion speed 7.4 is bounded by

$$\frac{\dot{R}}{R} = \sqrt{2}\omega_a(0)\frac{R_0}{R}\sqrt{1 - \frac{R_0}{R}} \ll \omega_l(t) = \omega_l(0)\left(\frac{R_0}{R}\right)^{3/2}, \tag{7.5}$$

with $R := R(t)$ and the already encountered spectrum

$$\omega_l(0) = \frac{\omega_a}{\sqrt{2}}\sqrt{l(l+1)}. \tag{7.6}$$

The the expansion speed is always limited from above by $(\dot{R}/R)_{max} \approx \sqrt{2}\omega_a(0)R_0/R = 2c_0/R$ for $R \gg R_0$, as already noted in chapter 5. However, for the breathing dynamics,

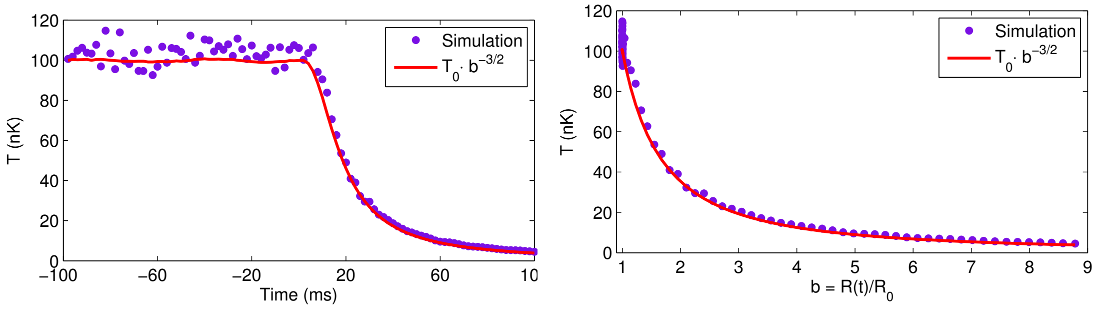

(a) Temperature vs. expansion time.

(b) Temperature vs. scale parameter.

Figure 7.5.: Temperature of a 1d-expanding quasicondensate in c-field simulations. 100 realizations of clouds of on average ~ 16500 atoms are prepared at a temperature of $T = 100$ nK within a harmonic potential characterized by the trap frequencies $\omega_a, \omega_r = 2\pi \times (12, 1000)$ Hz(a). To validate an initial equilibrium state, GPE propagation without any parameter change is performed for 100 ms, after which the axial potential is ramped down on a timescale of 1 ms to allow 1d expansion for a time span of 100 ms. (a) Temperatures measured by density ripple thermometry plotted against time (purple) compared with the scaling formula $T(t) = T_0 \cdot b^{-3/2}$ (red line). (b) Temperatures plotted against the scale parameter $b = R(t)/R_0$ (purple), again compared to the scaling formula (red line).

also R does not exceed values of $2 \times R_0$ to $3 \times R_0$, whereas for the expanding cloud, R can grow to arbitrary values. Substituting $(\dot{R}/R)_{max}$ and 7.6 into equation 7.5, one finds that $(\dot{R}/R) \ll \omega_l(t)$ only holds for

$$R \ll R_0 \, l(l+1). \tag{7.7}$$

This means that as the expansion process proceeds, more and more modes fall outside the adiabaticity criterion and mode mixing and corresponding changes of the occupation number distribution is expected to be observed in the rescaled basis.

Breakdown of adiabaticity and quasiparticle creation. Interestingly, during the work on this project we found that this scenario has already been discussed in reference [29] from a completely different viewpoint. There, the authors discuss several scenarios where the action of velocity fluctuations in degenerate quantum gases can be mapped to Friedmann-Robertson-Walker and de Sitter metrics to create analogue gravity scenarios, as pioneered Unruh's initial proposal [249]. While a detailed discussion of this mapping is beyond the scope of this thesis, the similarity of the description used by the authors of reference [29] to our approach as presented in section 5.3 warrants some comments. In particular, reference [29] considers parallels between the creation of quasiparticle excitations in expanding ultracold Bose and Fermi gases and ”cosmological” particle production in the early universe. To this end, a general scaling approach extremely similar to our description in section 5.3 is used, and the case of an expanding 1d quasi-BEC is even covered explicitly. Specifically, the authors recover the exact scale invariance discussed in reference [36] if interactions are tuned as $g_{1d} \rightarrow g_{1d}/b(t)$ in the form of an exact adiabaticity criterion in the basis of rescaled eigenmodes, while the

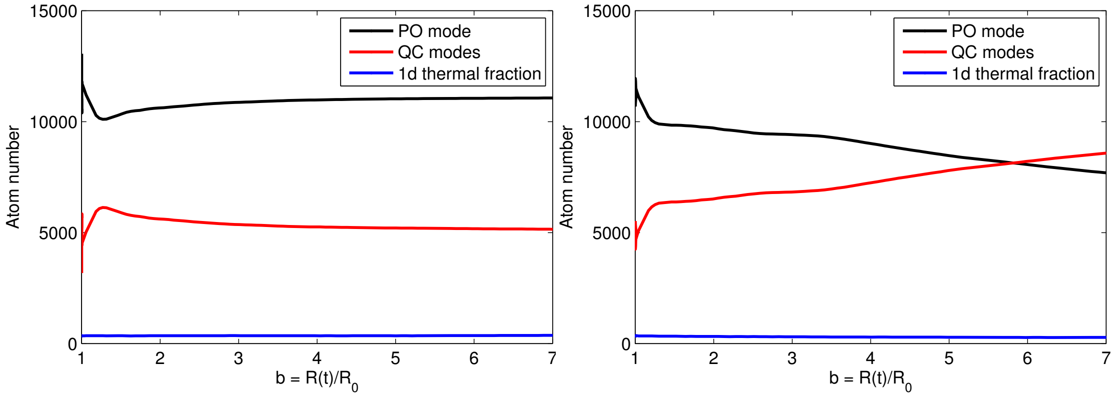

(a) Exact scaling: $g_{1d}(t) = \frac{g_{1d}(0)}{b(t)}$.

(b) Thomas - Fermi scaling: $g_{1d}(t) = g_{1d}(0)$.

Figure 7.6.: Density matrix decompositions from c-field simulations of 1d expanding quasicondensates. Parameters: $\sim$ 16500 atoms, T = 100 nK, trap frequencies: $\omega_a, \omega_r = 2\pi \times (12, 1000)$ Hz(a). (a) Occupation numbers in the Penrose-Onsager mode (black), quasicondensate modes (red) and decoherent modes (blue) for an expansion where exact scale invariance is guaranteed by tuning the 1d interaction constant as $g_{1d}(t) = g_{1d}(0)/b$. (b) As (a), but with constant g_{1d} given by the radial trap frequency of $\omega_r = 2\pi \times 1000$ Hz.

approximate scenario in the Thomas-Fermi limit as discussed above yields the creation of thermally distributed quasiparticle excitations in the scaling basis.

Since the instantaneous density matrix decomposition presented in section 3.3.5 yields a set of eigenmodes corresponding to the rescaled initial basis from the analytical approach, it is instructive to compare occupation numbers of these eigenstates for the expansion at stationary interaction constant (in the following called 'Thomas-Fermi scaling') with the exact case involving tuning of interactions. The results of such a comparison in the c-field approach are found in figure 7.6(b) and 7.6(a), respectively, both showing the decomposition into Penrose-Onsager mode, quasicondensate and incoherent fraction as functions of the scale parameter during expansion for identical parameters as used in figure 7.5 with the exception of a lower set temperature of 50 nK. Apart from some initial dynamics directly after switching off the axial potential (possibly inducing additional excitations, constituting some form of quench), the distribution of atoms among the different fractions is stationary for tuned interactions $g_{1d}(t) \to g_{1d}(0)/b(t)$ to conserve the exact scale invariance. In contrast, significant depletion of the Penrose-Onsager mode and correspondingly increasing occupation numbers in quasiparticle modes are observed for the Thomas-Fermi scaling, qualitatively in accordance with the predictions from reference [29] and our own observation that adiabaticity in the scaling basis is expected to break down in the limit $R \gg R_0$.

Observer dependence of the excitation spectrum and prospects for experiments. In references [28] and [27], the same authors raise interesting points about the observer dependence of measured quasiparticle occupation numbers, and draw analogies to the observer dependence of the black-body radiation spectrum in relativistic settings [250, 251, 249, 252]. In this context, it would be interesting to exploit a device like the fibre-based fluorescence detector as local observer, in contrast to global measurements performed with imaging methods. Further, reference [210] discussed signatures in the non-local phase and density correlation functions expected as a result of the quasiparticle creation process.

Both the exact implementation of such local measurements as well as studies concerning the feasibility of measuring predicted signatures on non-local correlation functions are left for future projects on the new experimental setup. Note, however, that the population of the Penrose-Onsager mode, defined as 3.29, is a well-defined quantity in terms of measurable correlation functions and can conceivably be detected by a combination of techniques to measure density fluctuations as used for instance in reference [16] and the analysis of phase fluctuations by the methods discussed within this thesis. Tuning the radial trap frequency over a factor of $b = 2$ to $b = 4$, either to satisfy or further violate the exact scale invariance during expansion by a factor b is realistic in atom chip experiments and is expected to yield an observable effect according to the results shown in figure 7.6.

Finally, let it be noted that it is not even necessary to explicitly induce an expansion process. Writing the Thomas-Fermi radius as

$$R_0 = \sqrt{\frac{4\hbar a n_0}{m}\frac{\sqrt{\omega_r}}{\omega_a}}, \tag{7.8}$$

one can immediately observe that, also in accordance with the scaling equation 5.9, keeping the ratio $\sqrt{\omega_r(t)}/\omega_a(t)$ constant keeps the cloud at a stationary radius R_0 while still changing the spectrum $\omega_l = (\omega_a/\sqrt{2})\sqrt{l(l+1)}$, allowing to perform similar experiments at stationary radius. This facilitates measurements where the time scale of the confinement change is varied, and connects naturally to quenches of the transverse confinement, leading to deviations from an adiabatic temperature change characterized by $T(t)/T_0 = \omega_l(t)/\omega_l(0)$.

Exact scaling and temperature. Note for completeness that the correct Ermakov equation for the exactly scale invariant Hamiltonian writes

$$\ddot{b}(t) + \omega_a^2(t)b(t) = \frac{\omega_0^2}{b^3(t)}, \tag{7.9}$$

as can easily be recovered following the steps outlined in section 5.2.1 from equation 5.3 with $d = 1$ and an interaction constant $\bar{U} \to \bar{U}/b(t)$. Since this tuned interaction

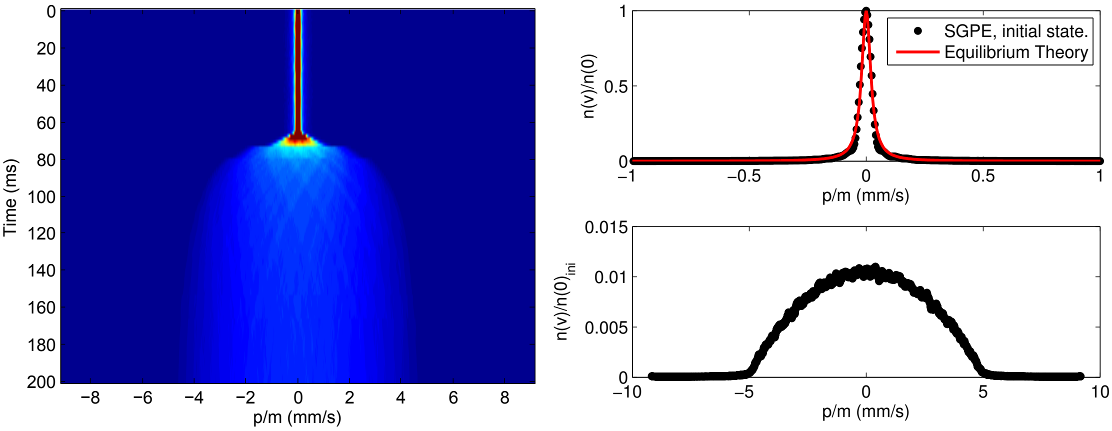

(a) Momentum distribution: Time evolution. (b) Momentum distribution: Initial and final state.

Figure 7.7.: Momentum distribution during the 1d expansion of quasicondensates from the c-field simulations yielding the results presented in figure 7.6(b).

constant changes the scaling of the sound velocity, the spectrum then scales as

$$\omega_l(t) = \frac{c(t)}{R(t)}\sqrt{l(l+1)} = \omega_l(0)b^{-2}, \tag{7.10}$$

yielding also a different temperature scaling $T(t) = T(0)b^{-2}$. While not explicitly demonstrated here, this scaling can also be validated by analysing the temperature corresponding to the simulated c-fields used for figure 7.6(a).

Momentum distribution of 1d expanding quasi-BECs. According to the Wiener-Khinchin theorem already invoked in section 2.3.2 for the homogeneous gas in thermal equilibrium, the time evolution of the momentum distribution is given by the Fourier transform of the rescaled density matrix or first order correlation function. The case of exact scaling is discussed in detail, also backed up by numerical results, in reference [36] and shows fast convergence against a stationary parabolic distribution. In the Thomas-Fermi limit, for moderate expansion times we can use the expression 5.31 deduced in chapter 5, repeated here for the sake of completeness:

$$\rho\left(z,z',t\right) \simeq \frac{\sqrt{n\left(z\right)n\left(z'\right)}}{b}\exp\left[-\frac{|z-z'|}{\sqrt{b}\lambda_T} + \frac{im\dot{b}}{2\hbar b}\left(z^2 - z'^2\right)\right]. \tag{7.11}$$

Similar to the results presented in [36], the parabolic term is expected to quickly dominate the shape of the momentum distribution during expansion. To demonstrate this, figures 7.7(a) and 7.7(b) show a carpet plot of the numerically calculated momentum distributions obtained from the simulation results also used to create figure 7.6(b), as well as a comparison of initial and final states, respectively. Note that due to the breakdown of adiabaticity discussed above, deviations from equation 7.11 are expected to arise for long expansion times, yielding another possible observable for future experiments.

Beyond the quasi-BEC regime. The expansion of a quasicondensate at constant 1d coupling parameter g_{1d} leads to decreasing density and thus to increasing interaction strength, parametrized by the Lieb-Liniger parameter γ defined by expression 2.34. Naturally, quasicondensate theory must break down as one approaches $\gamma \approx 1$. Several theoretical studies have been performed on this *dynamical fermionization* of the 1d gas and its influence on the shape of the density profile [253, 80], and correlation functions [254, 255], showing rich behaviour in the transition regime marked by $\gamma \approx 1$, connecting between the two by themselves scale-invariant Thomas-Fermi and Tonks-Girardeau regimes. Current experiments with initial states at $\gamma \approx 10^{-3}$ are far from this transition regime even for scale parameters around $b \approx 10$. However, in principle it is conceivable to combine low-density initial states and single-atom sensitive imaging techniques to probe the physics of the transition region in future experiments.

7.4. Fluorescence detection of cold atoms

Summary of previous results. Fluorescence detection of atoms at temperatures of order $\mathcal{O}(10)$ μK with the detection setup outlined in section 4.3.9 and depicted in 4.11 has been analysed in great detail within the theses [38] and [39]. In summary, using the $F = 2 \rightarrow F' = 3$ transition, optimal detection efficiency was found at total excitation light powers around 1 nW, corresponding to roughly 3 times the saturation power, yielding $\sim$ 120 scattered and on average $\sim$ 1.08 detected photons per atom, with an $1/e$ interaction time of $t_{int} = 12 \pm 1$ μs.

The optimal detection laser detuning to reach these conditions was determined by spectroscopy measurements. Since the atoms are radially trapped within a magnetic potential, they are subject to a position-dependent Zeeman shift, leading to a corresponding splitting visible on the spectroscopy data, as presented within figure 7.8. Due to the geometry of the detector, the atoms are likely to see a light field containing π, σ_+ and σ_--components with respect to the local quantization axis. Depending on the local Zeeman shift, the detuning of the light field from the zero-field resonance, as well on the unknown output polarization of the excitation fibre and the Doppler shift of a moving atom, either of these polarisation components can be resonant. Depending on the total detuning, atoms are likely to exhibit higher scattering rates for either of the circular components, leading to optical pumping into the $m_F = \pm 2$ states and subsequent driving of the closed closed $|2, 2\rangle \leftrightarrow |3, 3\rangle$ or $|2, -2\rangle \leftrightarrow |3, -3\rangle$ transitions, respectively, with the possible additional scattering of π polarized light. In total, this yields the spectroscopy data depicted in figure 7.8. The efficiency of the optical pumping depending on light intensity, detuning and relative intensity of the different polarization components has been estimated by Monte Carlo simulations in reference [38].

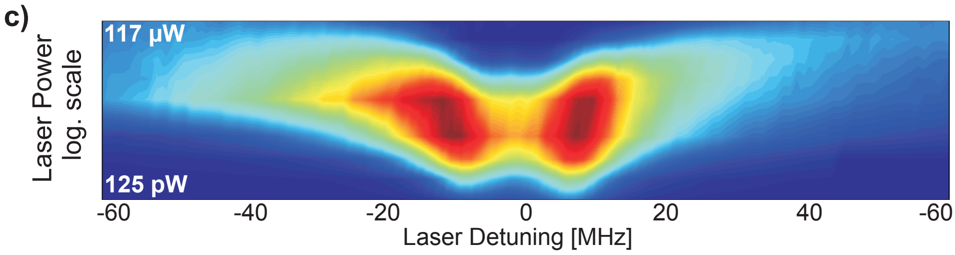

Figure 7.8.: Spectroscopy of the $|2, m_F\rangle \rightarrow |3, m'_F\rangle$, showing the number of detected counts per second of arrival time signals from atoms at temperatures of $\sim$ 50 μK normalized to the maximum count numbers, plotted against Laser detuning and power. The guide potential was characterized by a bias field of $B_b = 19.9$ G, a guide current $I_G = 0.627$ A and an external field defining the trap bottom of $B_I = 4.4$ G. The data clearly demonstrates a two-peaked structure caused by Zeeman splitting of the ground and excited hyperfine states, and corresponding resonance shifts between different polarization components in the excitation light field. Figure adapted from thesis [38].

At low intensities, the $|2, -2\rangle \leftrightarrow |3, -3\rangle$ was found to yield comparably less signal, which was attributed to low efficiency of the optical pumping process from the $|2, 2\rangle$ to the

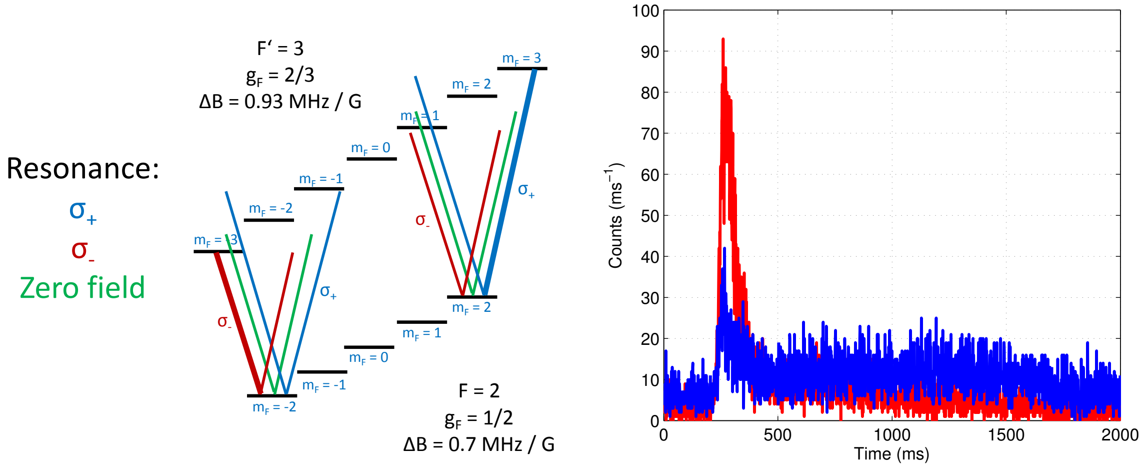

(a) (b)

Figure 7.9.: Zeeman splitting and polarization-dependent driving of transitions. (a) Sketch of the resonance conditions for different polarization components in the presence of a magnetic field for the $|2, m_F\rangle \rightarrow |3, m'_F\rangle$ transition of the ^{87}Rb D2-line. (b) Two fluorescence signals at different detunings of +5 MHz (blue line) and -25 MHz (red line) with respect to the zero-field resonance, demonstrating the difference in signal strength discussed within the main text.

$|2,-2\rangle$ ground states in the presence of sizeable local magnetic fields and corresponding differential Zeeman shifts in the $F = 2$ and $F' = 3$ hyperfine states. Therefore, it was concluded that this situation is best avoided, and scattering on the other closed transition is to be maximized.

Spectroscopy for cold atoms. For ultracold atoms, different behaviour is observed. Figure 7.9(b) contains two single-shot arrival time signals from initial atom clouds close to degeneracy. The blue line corresponds to data taken with a blue detuning of +5 MHz with respect to the zero-field transition, chosen to maximize scattering on the closed $|2,2\rangle \leftrightarrow |3,3\rangle$ transition, given a trap bottom of 3.3 G and an external Bias field of 26 G, yielding an overall trap depth of 23 G. Temperatures are below 1 μK. The initial peak that can be attributed to cold atoms guided towards the detection region visible on absorption images as discussed in the previous section, however, is only pronounced when using light at -25 MHz, far red detuned and expected to drive the $|2,-2\rangle \leftrightarrow |3,-3\rangle$ transition.

To put this effect under closer scrutiny, a spectroscopy varying power and detuning of the detection laser for atom clouds at $T < 1$ μK has been performed. The results are summarized in figure 7.10 and show that the total count number behaves similar to the results presented in the previous paragraph, with a minimum around the zero-field resonance and rising count numbers for both red and blue detuning. Figure 7.10(a) shows the peak count numbers as a measure for the contribution of the initial part of

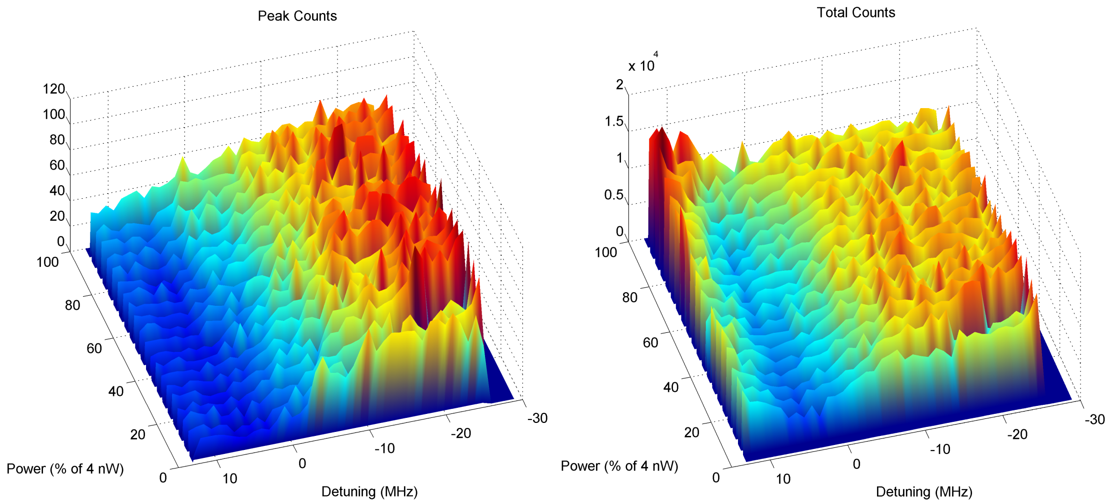

(a) (b)

Figure 7.10.: Spectroscopy of the $|2, m_F\rangle \rightarrow |3, m'_F\rangle$ transition for ultracold atoms. (a) Peak count numbers of arrival time distributions as shown in figure 7.9(b), corresponding to atom clouds with initial temperatures $T \leq 1\ \mu$K verified to pass the detection region by absorption imaging (see section 7.2). (b) Total counts of arrival time signals plotted against Laser detuning and power, similar to figure 7.8.

the arrival time signal that can actually be linked to a cold atom cloud passing the detector by absorption imaging, as presented previously in this chapter. It reveals that the peak is almost completely absent at blue detuning regardless of excitation power.

Simulation of atoms in the detection region. To better understand this behavior, a numerical simulation employing Monte Carlo methods to study the dynamics of single atoms in the vicinity of the detection region has been implemented. It considers the atoms as classical objects propagating individually along the magnetic potential formed by the guide wire, depending on their initial position and velocity. The motion is calculated by simply updating the velocity of each atom at each time step dt in the harmonic external potential

$$\boldsymbol{v}(\boldsymbol{r}, t) = \boldsymbol{v}(\boldsymbol{r}, t - dt) - \frac{\nabla V_{ext}(\boldsymbol{r})}{m}\, dt \qquad (7.12)$$

The interaction with the light field is modelled by the well-known expression of the total photon scattering rate of a two-level system (see e.g. [177]),

$$\gamma(\delta(\boldsymbol{r}, t), I(\boldsymbol{r})) = \frac{\Gamma}{2} \frac{I(\boldsymbol{r})/I_{sat}}{1 + \left(\frac{2\Delta(\boldsymbol{r},t)}{\Gamma}\right)^2 + \frac{I(\boldsymbol{r})}{I_{sat}}}, \qquad (7.13)$$

with the natural line width $\Gamma \approx 2\pi \times 6$ MHz, a detuning $\Delta(\boldsymbol{r}, t)$ and the saturation intensity for circularly polarized light

$$I_{sat} = \frac{\hbar\omega_0\Gamma}{12\pi c^2}. \tag{7.14}$$

Here, c denotes the vacuum speed of light, and ω_0 the frequency corresponding to the ^{87}Rb D2-line as given in [172]. Here, the intensity I is given as a Gaussian distribution on a numerical grid, defined by a beam waist of $w = 2.5$ μm, and for simplicity assumed to be axially homogeneous within its cross section with the volume considered for calculations, which is a cube of 60^3 $\mu\mathrm{m}^3$. The detuning is composed from contributions due to the local Zeeman shift, a possible detuning of the excitation laser frequency, and the Doppler shift of each atom,

$$\Delta(\boldsymbol{r}, t) = \Delta_m(\boldsymbol{r}) + \Delta_L - \Delta_D(t), \tag{7.15}$$

with $\Delta_m(\boldsymbol{r}) = \mu_B B(\boldsymbol{r})/h$ for the σ_+ transition and $\Delta_m = -\mu_B B(\boldsymbol{r})/3h$ for the σ_- transition, respectively, and $\Delta_D(t) = -v_L(t)\omega_0/2\pi c$ with the atom's velocity component along the light field $v_L(t)$. Note that the π transition is disregarded for the simulations presented in this section to isolate the dynamics induced by scattering on the closed transitions. Assuming photon scattering to be a Poisson process, the probability to scatter a photon in the time interval dt is given by

$$p_1(dt) = \gamma(\delta(\boldsymbol{r}, t) \cdot dt \quad | \quad p_1(dt) \ll 1, \tag{7.16}$$

allowing to compare a random number against this probability for each atom at each time step if it is made sure that $p_1(dt)$ is small enough. Upon scattering, the atom picks up a velocity $v_r = 5.8845$ mm/s [172] per photon along the direction of the light field $\hat{v}_L$, plus an additional recoil from emission into a random direction.

While with this, all ingredients to model scattering on the σ_+ transition are available, in order to describe the σ_- transition one needs to include optical pumping by repopulation of each atom's m_F state according to the transition probabilities for the $F = 2 \leftrightarrow F' = 3$ transitions as defined by the dipole matrix elements given in reference [172] upon each scattering event. Depending on the resulting m_F-state of the atom, the confinement in the magnetic potential changes, and becomes repulsive for negative values and hence crucially changing the atom trajectories, as will be seen below.

Finally, to model detection, one can roll a random number against the detection efficiency $\mathcal{N}_{ph}$ as defined in equation 4.15 for each scattered photon, taking into account the spatial dependence of the collection efficiency R_{coll} of the multimode fibre as indicated in figure 4.11 and discussed in the thesis [38].

Simulation results. With these steps, the trajectory of single independent atoms in the vicinity of the detection region as well as photon scattering and detection can be

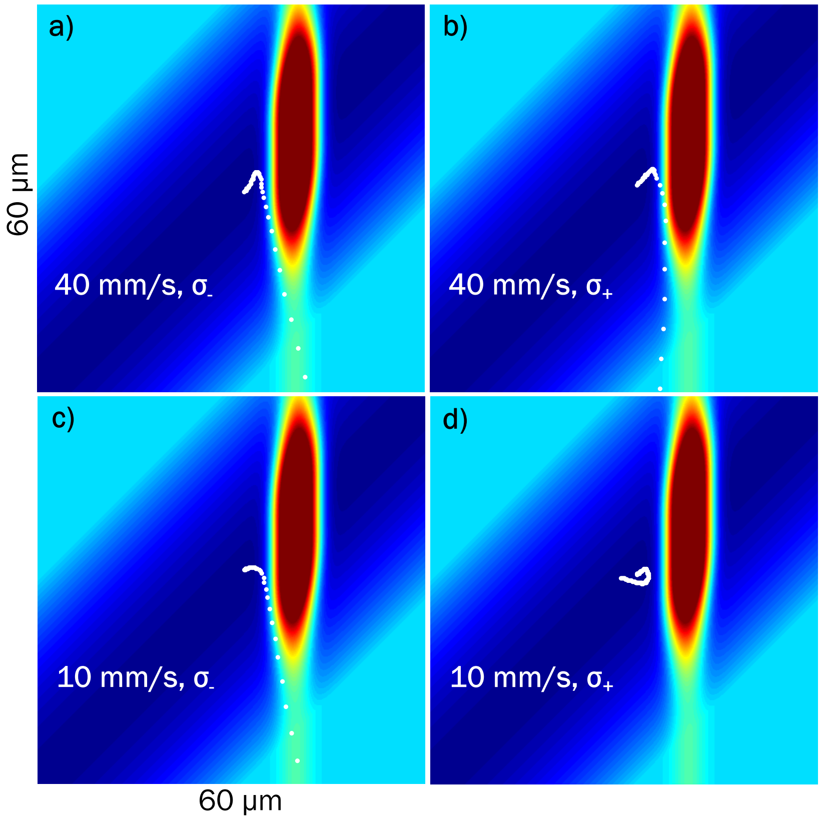

Figure 7.11.: Kinematics of atoms in the detection region. The plots show cuts through the magnetic guide potential, aligned along the diagonal, and the scattering rate (aligned along the horizontal x axis) due to a Gaussian excitation light field. The cuts lie in the $x - z$ plane at a distance $y = 62.5$ μm from the chip surface. Superimposed are trajectories (white dots) of single atoms, simulated by the Monte Carlo simulation presented within this section, projected onto this plane for different initial axial velocities in the potential as denoted within the images.

simulated. Figure 7.12 shows slices through the grid considered for a typical simulation run along the x-z direction, with the y-coordinate chosen in the plane defined by the center of the excitation fiber, and minimum of the guide potential. Here, the detection beam, marked by the red region in the pictures, is aligned along the x-direction, while the axis of the guide is lying in the x-z diagonal. Superimposed in white are projections of typical single-atom trajectories with an initial axial velocity of 10 mm/s at σ_+ (7.12(d)) and σ_- (7.12(c)) detection, as well as 40 mm/s at σ_+ (7.12(b)) and σ_- (7.12(a)) detection. These velocities are chosen, since they correspond to the average axial propagation speed of atom clouds close to degeneracy, as discussed in section 7.2 and the velocity of fast atoms from a 1d Boltzmann distribution 7.1, respectively. While for both velocities, using the σ_- transition, the atom trajectory crosses the detection beam, for σ_+ polarization scattering events take place only at the edge of the detection beam. For sufficient initial velocities, atoms still propagate deep enough into the light field in such a way that their dynamics is eventually dominated by scattering; for low

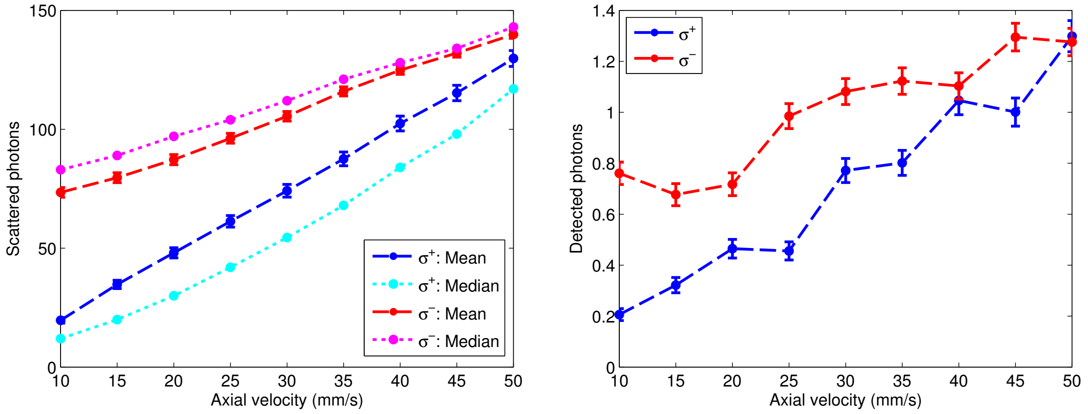

(a) (b)

Figure 7.12.: Total number of scattered and detected photons from the Monte Carlo simulation for atoms with different initial axial velocities. (a) Number of scattered photons at the σ_+ transition (means in blue, medians in cyan), and the σ_- transition (means in red, medians in purple), respectively. To correct for the influence of outliers, median values are provided in addition to means and standard errors from 6000 trajectories at identical parameters, each. (b) Average number of detected photons per atom for the σ_+ (red) and the σ_- transitions, respectively, from the same simulation yielding the scattered photon numbers shown in (a).

velocities, however, the combination of a few scattering events in the low-intensity tail of the light field and the confining potential lead to a reflection of the atom. Slow atoms interacting with σ_+ light, on the other hand, are optically pumped into untrapped states and subsequently pushed into the light field by the magnetic potential, increasing the number of scattering events.

To quantify these intuitive results, figures 7.12(a) and 7.12(b) contain statistics from 6000 individual trajectories for the number of scattered and detected events at different axial velocities between 10 mm/s and 50 mm/s, considering both σ_+ and σ_- light, at a total power of 1 nW ($3 \times P_{sat}$), as used in most experiments, providing evidence for the advantage of using the σ_- polarization for the detection of slow atoms, while providing realistic values for both scattered and detected photons numbers for fast atoms corresponding to the μK regime, although slightly underestimating the number of scattered photons compared to the measurements presented in reference [39].

Simulation versus reality. Of course, care has to be taken when comparing such a simple model to the experiment. On the one hand, atoms always see all polarization components present with different relative intensities depending on the local quantization axis in the experiment, affecting the efficiency of optical pumping for a low number of overall scattered photons. Further, atoms clouds in the μK regime have been measured to feature radial diameters in the order of 20 μm. Atoms at such distances from the trap centre are expected to feature significantly different dynamics in the detection region. Specifically, pumping such atoms into untrapped states is observed in corresponding simulations to decrease the interaction time with the light field, as intuitively expected, and therefore the signal strength on the σ_- transition relative to σ_+ polarized light.

In addition, while the interpretation offered for the measurements shown in figure 7.10 seems satisfactory with respect to the behaviour of cold atoms, the nature of the signal tails, apparently interacting more efficiently with σ_+ polarized light is an open question. Within the presented picture, it might be concluded that it consists of axially slow atoms with radial kinetic energies consistent with temperatures in the order of a few μK. The origin of such atoms, however, remains unclear and calls for future measurements characterizing the role of heating or residual corrugations in the guide potential during expansion.

7.5. Summary

The first part of this chapter presented some early results considering the propagation of atoms in a magnetic guide potential. It showed that it is crucial to perform such measurements at sufficiently far distances from the chip surface to minimize the effect of potential corrugations. Experience from different experiments across the group has shown that regardless of chip wire diameter, distances exceeding roughly 100 μm between chip and potential minimum are comparatively safe from corrugations for single surface layer atom chip designs. With respect to integrated fluorescence detection, the next iteration of this experiment as presented in chapter 8 is planned to include detectors where the excitation fibre tip is situated at ~ 100 μm distance from the chip surface as opposed to 62.5 μm within the previous setup, so that smooth propagation without intermediate current ramps complicating measurements is guaranteed.

With respect to the physics of 1d expansion, numerical results and a comparison with proposals to implement analogue gravity scenarios have been presented, opening up the opportunity to contribute experiments to this fascinating emerging field. Even disregarding these analogies, studying quasiparticle distributions with both global and local detection methods in expanding 1d quasicondensates could also contribute new insight into the non-equilibrium dynamics of this and similar systems that go beyond what can be calculated in terms of the exact solution from the Lieb-Liniger model. This is especially the case, if the transition regime to the strongly interacting Tonks-Girardeau state can be reached, where characteristic effects like deviations from the self-similar expansion are expected to set in already at values around $\gamma \approx 0.1$.

The final section outlined the velocity dependence of arrival time distributions in the limit of ultracold atom clouds with radial diameters in the order of merely ~ 1 μm. These results have entered the design for the next iteration of the fluorescence detector as presented in thesis [188], prompting the use of an arrangement where the excitation light is not directed against, but rather along the propagation axis of atoms in the guide to minimize the influence of the magnetic trap on the trajectory of scattering atoms.

Part III.

Outlook & Conclusion

8. Towards a novel light-matter interface

"Everything starts somewhere, although many physicists disagree."

Terry Pratchett

In parallel to the measurements presented in previous sections, a new experimental apparatus has been planned, prepared and partially set up during the final stage of this thesis. While the main part of this work will be contained in the two theses [188, 256] and within future publications, this chapter shortly summarizes the underlying ideas before presenting the next generation atom chip, with a focus on the layout of its wire structures and possible trap geometries. Finally, the stage of the project at the time of writing this thesis and the corresponding experimental apparatus is shortly outlined.

8.1. Overview

The goal of the experiment's next iteration is to integrate an optical nanofiber-based cavity on an atom chip. Optical fibers tapered to and shaped at sub-wavelength diameters have emerged as a powerful tool for the detection and manipulation of cold dilute atomic gases in recent years. Following the first experiments focusing on detection [257], neutral atom traps based on a combination of blue and red detuned light fields to form stable optical dipole traps for neutral atoms [258, 259] have soon been presented, as well as whispering gallery mode resonators [260] which recently have been demonstrated to allow strong coupling to single atoms [261, 262].

Another type of cavity can be realized by machining Bragg gratings into an optical fiber with the help of laser writing techniques, forming a Fabry-Pérot-type resonator [263]. Such a device is well-suited for integration within an atom chip setup, as will be seen in the following.

Fabry-Pérot resonator. The basis for this device is an optical single mode fiber[1], into which two Bragg mirrors are laser written[2] at a distance of ~ 2 cm to form a cavity with a center frequency at a suitable transition of the atom that is chosen to be coupled to the resonator. In our case, this is ^{87}Rb at a wavelength of $\lambda \sim 780.24$ nm. In the course of

---

[1] Thorlabs SM600, Thorlabs Inc., Newton, New Jersey, USA

[2] Laser writing is performed at the Leibnitz insitute of photonic technology, Jena, Germany

FSR (GHz)	Finesse	λ_0 (nm)	$\Delta\lambda$ (nm)	R1 (%)	R2 (%)
3.8	100	780.27	0.12	94.9	98.0

Table 8.1.: Parameters of the fiber Bragg resonator selected for first experiments. FSR denotes the free spectral range, λ_0 and $\Delta\lambda$ the center wavelength and stop band of the resonator, and R1 and R2 the reflectivities of the two Bragg mirrors, respectively.

this project, several resonators of this type have been tested, a thorough characterization of which will be found in future theses [188, 256] and publications. The parameters of the sample that has been selected for the first set of experiments are summarized in table 8.1.

Light propagation through a tapered nanofiber . The creation and the properties of fibers pulled to form tapers with diameters smaller than optical wavelengths is reviewed in detail within reference [264]. Their most important property considering our experiment is that at sub-wavelength diameters, light is not confined to propagate within the fiber core, but a significant fraction of the intensity is guided outside the fiber in the form of an evanescent field. To maximize this evanescent component, the fiber diameter should be given by $d \leq \lambda/2 \approx 400$ nm for a given optical wavelength of $\lambda = 780.24$ nm, with the field affecting distances of up to $\lambda/2$ from the fiber surface. Atoms in this region can couple to the optical field and are subject to dipole forces, resonant scattering with an enhanced probability to scatter into the fiber mode via the Purcell effect [265] or dispersive interaction [266].

While, similarly, coupling of atoms to guided light fields can also be accomplished in hollow-core photonic crystal fibers (PCF) [267], with the advantage that atoms can be placed in the region of maximum intensity, thus enhancing coupling strength, the latter approach suffers from poor coupling efficiency between PCF and other fibers or optical waveguides needed to extract the light from the experimental setup. Nanofibers, on the other hand, can achieve transmissions through the tapered region of close to 99% of the input intensity [264], and the ends can simply be spliced to single-mode fiber of the same type yielding an almost loss-less setup throughout. Coupling efficiency, on the other hand, can be improved by the use of a Fabry-Pérot resonator as discussed in the previous paragraph, rendering this approach ideal to create an atom-photon interface.

Nanofiber cavity on a chip: Schematics. While experiments coupling atoms to nanofibers already have been performed [259], these setups neither use Fabry-Pérot resonators to enhance coupling at the time of writing this thesis, nor an external trap to provide a cold gas at high phase space density, instead of relying on magneto-optical traps or optical dipole traps applied via the nanofiber. The trap geometries provided by an atom chip are ideally suited to produce elongated clouds at high phase space density to couple to the optical nanofiber field, opening up a number of novel experiments. The basic scheme of such a setup is found in figure 8.1. The waist of the nanofiber is posi-

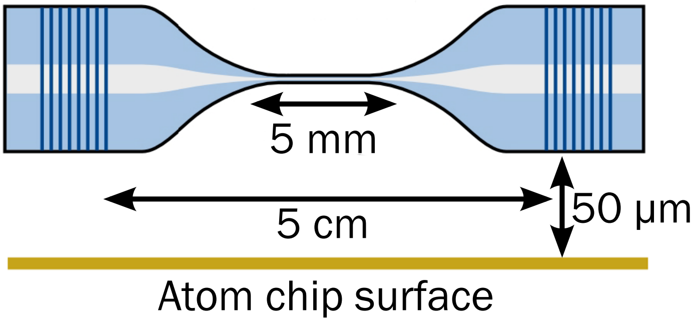

Figure 8.1.: Sketch of combined nano-fiber cavity atom chip setup presented in this section. A nanofiber is prepared with suitable Bragg mirrors to form a cavity with parameters similar to what is given in table 8.2. The fiber is then pulled to form a taper diameter of $\lambda/2 \approx 400$ nm and mounted at a distance of 100 μm between central taper and the surface of an atom chip that allows independent trapping of ultracold atoms at high phase space densities. Such a setup allows a high amount of control on both the light field as well as the atoms, which can be placed in the evanescent intensity distribution of light propagating along the fibre coupling them to the light field, while the cavity allows for an enhancement of interactions.

tioned at a distance of ~ 100 μm from the surface of the atom chip. After pulling, the distance between the Bragg mirrors amounts to 5 cm, while the elongation of the taper is 5 mm. As discussed in section 4.1.2, atoms can be trapped at distances between a few tens to hundreds of μm in atom chip traps. At degeneracy, the radial width of the cloud corresponds in good approximation to the transverse harmonic oscillator width, which is usually below 1 μm for realistic trap frequencies. This allows the precise positioning of an ultracold atom cloud with respect to the waist of the nanofiber and allows a wide variety of different trapping geometries. To prevent surface adsorption of atoms on the nanofiber, a blue-detuned dipole potential can be combined with a magnetic trap. Alternatively, the atom chip can be used as a source for a regular fiber-based dipole trap as presented in reference [259], or potentially to implement a novel proposal to trap atoms that can be found in reference [268]. Note that in the experiment, the fiber is externally mounted on a pair of shear piezos allowing to tune and lock the cavity.

Prospects for experiments. The main goal is to achieve strong coupling between atoms and photons in the evanescent field of the nanofiber. As a first step, it will be instructive to reproduce experiments to create electromagnetically induced transparency (EIT) and slow light within this system. For a comprehensive review on the topic, see [269]. This will be the starting point for similar experiments with the goal of deterministic storage of single photons within the atom cloud and subsequent retrieval.

If sufficient coupling strengths can be realized within the experiment, interacting atom-photon polariton states can be created, allowing to use the atom cloud to mediate effective photon-photon interactions. Experiments along this line would open up the

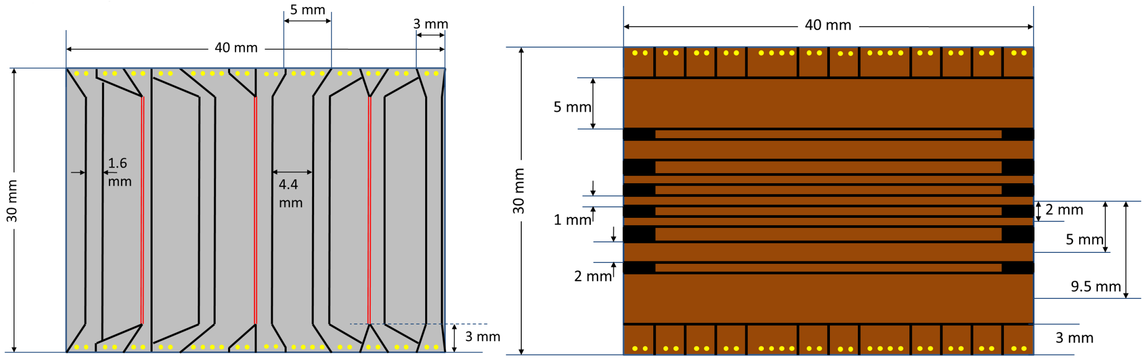

(a) New chip: Surface (b) New chip: Flipside

Figure 8.2.: Sketch of the structures on the new atom chip as discussed in the main text. (a) Chip surface, with wire structures applied by evaporation. (b) Flip side of the chip, with wire structures applied via electroplating.

possibility to implement gate operations on photonic states, allowing to test novel options for quantum computation with photonic qubits, which is otherwise restricted to linear operations and projective measurements [270].

In the limit of many photons and strong interactions, according to the proposal [271] it is possible to create a strongly interacting polariton gas, where the interaction strength can be controlled by the detuning of two Raman lasers involved in a 4-level EIT-like scheme.

8.2. The nanofiber atom chip

The next generation atom chip involves several changes to the currently used designs, both with respect to the wire layout, as well as to the fabrication procedure. As discussed within section 4.3.6, the previously used chip consists of a single 2 micron thick structured gold layer on top of a silicon substrate, which is connected to external current feedthroughs by sets of bonding wires. Only few specialised wire structures with widths between 50 μm and 200 μm are electrically connected. The macroscopic magnetic trap and MOT rely on a set of suitably shaped copper structures beneath the chip. (see section 4.3.5).

Notes considering the fabrication. The next generation chip will again feature a single metal layer on the surface of a silicon substrate. In contrast to a gold layer, however, a 2 to 3 micron thick copper layer covered with a thin gold layer to provide reflectivity and a 30 nm thick SiO_2 coating will be applied. The latter has been used in another experiment within the group (see [201]) to prevent surface adsorption of Rubidium. Here, the main reason is to provide better adsorption of a double layer SU-8 structure which will be used to support the next iteration of a fiber-based fluorescence detector, necessitating two layers to provide precise positioning of both a single-mode tapered excitation fiber of 125 μm diameter, as well as high-numerical aperture polymer fiber with a total diameter of 500 μm. This fiber detector, which has been briefly mentioned in section 7, will be explained in depth within the thesis [188]. The wires are not connected by bonding, but contacted to copper pads on the chip mounting with electrically conductive epoxy-based glue [3]. Surface wires are fed through the substrate via plated through-holes to contact pads on the flip-side of the chip.

Surface wire structures. As depicted in figure 8.2(a), and in contrast to previous designs, all structures form straight wires across the surface, with widths of 50 μm, 1600 μm and 4400 μm. The latter, together with the central 1600 μm wire are used to form a current-carrying plate for the magneto-optical trap stage, and support currents up to 15 A each. Together with two 5 mm plates on the flip-side, they replace the U-shaped copper structure used for the MOT within the previous setup as described in section 4.3.5. Similarly, the central 1600 μm wire can be used to create a macroscopic magnetic trap, together with both the 2 mm and 5 mm wide wires on the flip-side to provide axial confinement, with the parameters given in table 8.2.

The three 50 μm wires mark three distinct regions designed to produce the confinement needed to enter the 1d regime. Along the central wire, the nanofiber cavity is positioned as shown in the schematics 8.1. The other two 50 μm wires are planned to be used for the novel implementations of fiber-based fluorescence detectors and a test-setup for non-fiber-based optical waveguide structures, respectively. The wires are designed to support up to 4 A of current, allowing trap frequencies exceeding 4 kHz at a distance of 100 microns from the chip. Further tests need to confirm these current limits, however.

Flip-side wire structures. The flip-side of the substrate shown in figure 8.2(b) features 50 μm thick copper wires that are applied by electroplating, with widths between 1000 μm and 5000 μm, oriented orthogonally to the surface wires. They are used to create a U-shaped current flow for the MOT, and can generally be applied to provide axial confinement for both macroscopic and 1d microtraps.

8.2.1. Magnetic trap geometries.

Macroscopic trap. It is crucial to transfer as many atoms as possible from the MOT to the initial macroscopic magnetic trap to ensure sufficient phase space density for evaporative cooling to degeneracy. Heating due to limited mode-matching between MOT and magnetic trap necessitates sufficiently high trap depths to prevent sizeable losses by plain evaporation. Since the overall currents supported by the chip wires on the surface are smaller than what can be provided by the copper structures used up to

---

[3] Epotek EK2000, Epoxy Technology Inc., Billerica, Massachusetts, USA

B_{bias}	B_{Ioffe}	I (1.6 mm)	I (2 / 5 mm)
17 G	-5 G	15 A	15 A

Depth X	Depth Y	Depth Z
15 G	19 G	15 G

dB/dx	dB/dy	dB/dz	$\omega_x/2\pi$	$\omega_y/2\pi$	$\omega_z/2\pi$
70 G/cm	100 G/cm	40 G/cm	80 Hz	90 Hz	15 Hz

Table 8.2.: Possible configuration for a macroscopic magnetic trap produced via the double layer chip to be implemented within the new experiment. The first table contains the external fields as well as the currents through the central 1.6 mm wire and through both 2 mm and 5 mm wires on the flip-side of the chip. Second table: Trap depths along each spatial axis. Third table: Gradients and trap frequencies along each axis.

now, calculations have been performed to ascertain whether the new design is feasible to provide suitable trap geometries. A set of parameters that is similar to the initial configuration used in our old setup has been found by calculations based on finite-size solutions for the magnetic field produced by rectangular wires [145], and can be found in table 8.2. While the trap depth is slightly lower than in the current setup (15 G vs. 22 G), gradients and trap frequencies around the center are similar, and together with the option to produce more elongated MOT geometries by tuning the current flow through the chip surface accordingly, similar transfer efficiencies as in the current setup are expected.

Wire edge traps. Sufficiently strong bias fields B_y perpendicular to the chip surface can be used to rotate the minimum of a magnetic trap produced by a macroscopic wire towards its edges, as mentioned within section 4.1.2. By this means, the edges of the 1600 μm wires can be used to create 1d microtraps with high radial confinement. This circumstance will be used by positioning a regular tapered nanofiber without Bragg gratings in the vicinity of the centre-near edge of the main 1600 μm wire for various measurements not necessitating a cavity. Note that the macroscopic trap can as such be deformed into a 1d trap without any transfer of atoms between different wire structures.

On-chip bias fields. The vicinity of the 50 μm wires to other current carrying structures, together with the option to provide an axial Ioffe-component, defining the trap bottom, by the wires on the flip-side of the chip allows to test traps where all fields are provided by currents from the chip. This is advantageous, since external magnetic fields seem to be one of the major sources of noise[4] leading to heating in our setup.

RF dressed traps. While experiments involving RF-induced splitting of atom clouds are not planned within this experiment, applying RF fields to wires in the vicinity of the used trapping wire can still be used to dress the potential, for example to create anharmonic and anisotropic traps needed to generate twin-beam states [216], which

---

[4] This is based on the experience that heating rates in RF dressed traps where the trap bottom is defined by the RF field rather than external magnetic fields are observed to be lower than in static traps in other experiments.

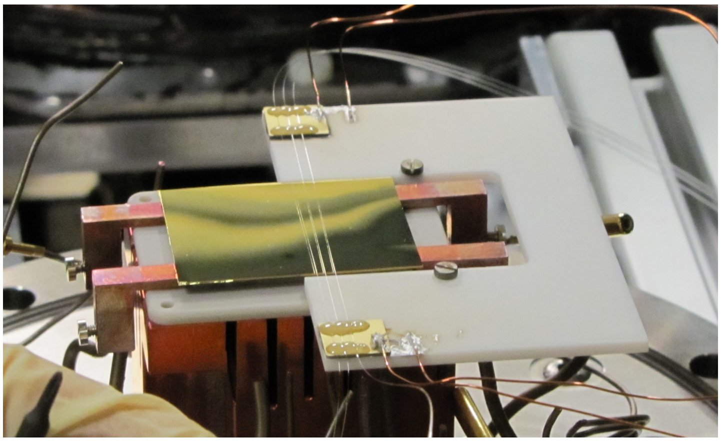

Figure 8.3.: Test setup built into the experiment at the time of writing this thesis. An unstructured gold mirror on top of an H-like copper structure allows for the creation of a chip MOT [139] as used within the finalized setup, while three tapered nanofibers, at this point without cavities, are mounted on a Macor structure attached to the chip mount, glued on top of two shear piezos which will allow to tune the cavity length in the next implementation with integrated Bragg mirrors. This test setup will allow to characterize the coupling of atoms from a ^{87}Rb MOT to the nanofibres.

would be interesting to investigate with a pair of fiber-based fluorescence detectors, which are planned to be integrated [188].

8.3. Current state of the project and outlook

At the time of writing this thesis, the vacuum chamber and coil setup as described in chapter 4 are already dismantled. In their place there is the new vacuum chamber[5] containing three nanofibers without Bragg mirrors, attached to a Macor mounting structure which is positioning the fiber waists at a distance of 3 mm to a gold mirror acting as place-holder for the final atom chip. The mounting with mirror and fibers is shown in figure 8.3. The vacuum chamber is pumped down to a pressure around 10^{-9} mbar and surrounded by new coils. At the moment, the lasers and optics are identical to what is presented in chapter 4. In this setup, a MOT is used to test the detection of ^{87}Rb atoms in the vicinity of the nanofiber. The next step will involve replacing the fibers by the first set of fiber cavities and demonstrate cavity-enhanced coupling to ^{87}Rb atoms.

First tests considering the maximally achievable currents on a sample chip with wire structures identical to those discussed in the previous section, have already been performed and resulted in supported currents of up to 15 A for the 4.4 mm and 2 mm wires without any signs of damage, as designed. However, practical issues with the mounting led to a redesign of some parts. The mounted test chip is shown in figure 8.4(b), while figure 8.4(a) contains a drawing of the device for comparison. In parallel to the measurements on the preliminary MOT setup, the new version of the chip mounting will

---

[5] Kimball Physics Inc., Wilton, New Hampshire, USA

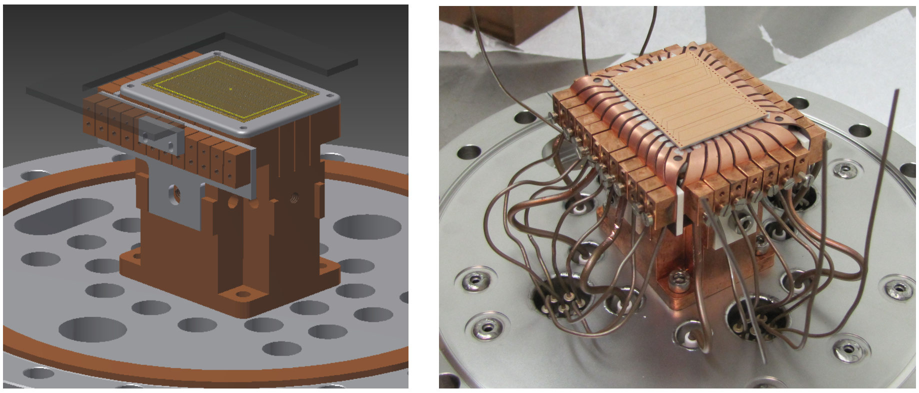

(a) Chip and mounting: drawing. (b) Chip and mounting: first test setup.

Figure 8.4.: Test setup with functioning chip. (a) Drawing of the chip mounting attached to flange, drawn and provided by Michael Trupke. (b) Test setup involving the mounting depicted in (a), with a test chip containing a set of electroplated copper wires before assembly in a vacuum chamber for the purpose of testing maximum currents through wires and feedthroughs.

be constructed and, upon successful completion of further tests, integrated within the experiment as soon as possible.

Naturally, there are several technical challenges to overcome on the way to the finalized setup, most prominently a strong temperature dependence of the cavity resonance, and the influence of optically active mechanical modes of the nanofiber on the cavity properties [272]. In addition, further work on the laser setup is necessary to prepare EIT measurements, and a reliable cavity locking scheme needs to be implemented.

Nevertheless, nanofibers and nanofiber cavities on an atom chip constitute a rich system that promises to enable a plethora of interesting experiments, both from the technological point of view of photon storage and from the implementation of nonlinear photonic quantum gates, to the investigation of strongly correlated polariton systems, combined with the unique option to directly perform correlation measurements on the transmitted photonic signal to analyse the polaritonic state in the trap. The different technological pieces for such an experiment have all been realized independently already, and a combination with currently available techniques seems feasible.

9. Conclusion

> *We have found it of paramount importance that in order to progress we must recognize our ignorance and leave room for doubt. Scientific knowledge is a body of statements of varying degrees of certainty — some most unsure, some nearly sure, but none absolutely certain.*
>
> Richard P. Feynman, The Value of Science, 1955

Recent years have seen the experimental realization of increasingly complex scenarios, such as multi-component spinor gases [273], experiments with mixtures of different atomic species with tunable interactions by means of Feshbach resonances [274], or, as a recent addition to the toolbox of ultracold atom physics, degenerate Lanthanide gases, featuring extremely rich collisional properties and long-range interactions due to their exotic electronic configurations [275, 276, 277]. While the one-dimensional Bose gas with short-range interactions, in contrast, is arguably one of the most well-understood quantum many-body systems, it is perhaps symptomatic for fundamental research that the investigation of this comparatively simple system keeps raising deep questions concerning the compatibility of concepts from classical statistical physics such as ergodicity, integrability or thermalization with quantum mechanics [278, 12, 279]. While the equilibrium properties of the 1d Bose gas have been studied extensively since the first experimental realization in 2001 [59], studies of non-equilibrium physics and relaxation processes, both theoretically and experimentally, have started to be conducted only recently.

Excitation spectrum of quasicondensates in time-dependent trapping potentials. Within this thesis, a very specific kind of non-equilibrium dynamics induced by a time-dependence of the harmonic external trapping potential has been investigated. Previous experiments in our group [205, 280] observed the relaxation of a non-equilibrium state towards a non-thermal steady state, in excellent agreement with a Luttinger liquid description for the quasicondensate. The spectrum of quasiparticle modes in these experiments is determined by the spatial extension and the local density of the cloud, and is considered to be static throughout the dynamics. In contrast, breathing yields a time-dependent set of eigenmodes. Still, the scaling symmetry of the Hamiltonian, as discussed in chapter 5 guarantees adiabaticity and hence constant occupation numbers within the rescaled basis. On the one hand, this is an interesting result on its own, providing a dynamical extension to the regular Luttinger liquid description of a trapped quasicondensate. On the other hand, this allows, in first approximation, to separate the dynamics due to collective oscillations from relaxation processes within the cloud which is helpful for measurements where it is difficult to suppress the axial breathing dynamics, such as several RF induced splitting protocols. Finally, the results from this thesis provide a means to determine the temperature of quasicondensates in the presence of collective excitations, constituting an extension to the density ripple thermometry method introduced for static clouds in references [30, 15, 31]. Note that a scale-invariant adiabatic breathing is, in this connection, also validated as a technique for condensate focussing [220, 97] to access the momentum distribution of a quasicondensate.

Of course both the Luttinger liquid description as well as the scale invariance in the Thomas-Fermi regime are approximations, and precise measurements considering the long-time dynamics of the system are expected to uncover experimental signatures from physics beyond these models. A route to investigate the effects of breaking the scale invariance is provided by studying the 1d expansion of quasicondensates as proposed in chapter 7. In principle, such measurements will be possible within the next iteration of the experimental setup introduced in chapter 8. However, in order to observe the depletion of the Penrose-Onsager mode, experimental means to determine the local second order correlation function $g^{(2)}(\Delta x = 0)$ will be necessary, either in terms of an improved integrated fluorescence detector or an in-situ absorption imaging system with sufficient resolution. Finally, significant deviations from the physics discussed within this thesis are expected in the vicinity to the crossover into the strongly interacting regime, for Lieb-Liniger parameters of $\gamma \geq 0.1$, providing a significant experimental challenge.

Shortcuts to adiabaticity and optimal control. The ability to manipulate the external trapping potential while suppressing spurious collective excitations is a powerful tool for future experiments. Especially, further studies with quasicondensates in double well potentials are expected to benefit from protocols that allow RF-splitting or recombining while controlling collective excitations.

The inverse approach, using optimal control to create specific non-equilibrium states, has already been used successfully within our group to engineer the radial state of the gas [216]. It would be interesting to apply such an approach in order to engineer the axial momentum distribution, replacing the GPE in the feedback loop by a c-field model. The closest existing experiments along this line involve a modulation of the radial confinement to create pairwise counterpropagating Bogolyubov-excitations with a momentum determined by the modulation frequency [281]. However, this approach has not been conclusive with respect to the excitation of modes deep in the phononic (low-energy) part of the Bogolyubov spectrum. Preparation of a sizeable occupation in a small band of phonon modes and studying momentum- and temperature-dependent decay rates would yield valuable information about extensions to the Luttinger liquid model allowing for phonon-phonon coupling processes.

Quasicondensates and integrated fibres. While the first experiments in the new setup will most probably focus on EIT and subsequently photon-storage and readout within an optical molasses, the finalized apparatus is planned to produce condensates and quasicondensates to be coupled to the evanescent field propagating along the nanofibre. In chapter 8, it was already mentioned that the far-reaching goal is the creation of a polaritonic quantum fluid with tunable interactions. However, from the viewpoint of quasicondensate physics adopted so far, one could also think of using the fibre to employ a 1d lattice perturbing the otherwise harmonic axial trapping potential and study the effect on relaxation processes in the cloud, or even introduce a means to apply Bragg pulses for momentum transfer or spectroscopy. The efficiency of such a scheme in the combined potential, however, is certainly a question open to future studies.

Finally, the next generation chip is planned to provide means to create stationary quasicondensates at the detection region, together with wire structures to move the cloud in the vicinity of this site in a controlled way. Using dipole potentials, as already tested and documented in reference [188], or resonant scattering, such a geometry will allow detection, but also to create localized defects in the density profile, providing an additional tool to manipulate the atom cloud and study relaxation processes.

Quasicondensates, solids and cosmology? Common characteristics of superficially different systems are one of the driving forces behind the explanatory power of modern science. While one obviously should not expect to capture the full complexity of high-TC superconductors, not to speak of the early universe, within simple cold-atom systems (”Don’t eat the menu!”), this is in fact not even a useful goal. After all, this complexity, at the moment, surpasses our ability to develop a satisfactory physical description. Rather, turning to a simpler system that might capture at least some aspects of the difficult one has often helped to isolate the important concepts, with the story of Feynman’s infamous ”wobbling plate” leading him down the path towards QED as an illustrative example [282].

Going beyond mere analogies, the idea to isolate useful common characteristics of different physical systems is known under the nowadays often-used term ”universality”. In many cases, one can disregard the microscopic structure of a certain physical system, since the process at hand is dominated by excitations corresponding to length scales exceeding the microscopic ones. The map between the behaviour of low-energy excitations in quasicondensates and spin chains provided by the same Luttinger liquid description, as an example, has already been commented on previously in this thesis. Most prominently, however, universality is established by the diverging correlation length in the vicinity of continuous phase transitions [54], allowing a classification of different systems according to their critical exponents.

Much effort has been invested in recent years to develop a similar picture for the non-equilibrium dynamics of many-body quantum systems. In the context of cold atom physics, universal and stable power-law distributions in momentum space are predicted to arise during the relaxation of ultracold Bose gases far from equilibrium, with connections to the creation and decay of topological defects [283] and, hence, the concept of superfluid turbulence[1]. The stability of these power-law distributions led to the concept of "non-thermal fixed points", similar to the fixed points encountered in equilibrium phase transitions. This description has also been applied to the one-dimensional Bose gas after an interaction quench [285].

By such mechanisms, the hope to uncover universal physics in the non-equilibrium dynamics of ultracold atoms, with predictive power for other, more complex systems, is arguably not misplaced, and other results, such as the recent experimental observation of Sakharov oscillations as known from cosmology in a 2d Bose gas [286] further strengthen this argument. In this sense, experiments as proposed within this section could yield valuable results with respect to the universality of decay processes from different non-equilibrium states prepared in 1d Bose gases.

The experimental observation of non-thermal fixed points would certainly point towards an interesting future, where cold atom experiments could indeed act not only as "wobbling plate", but to deduce general scaling laws that can be transferred to the non-equilibrium dynamics of other incarnations of many-body quantum systems - hence, advancing the frontier.

---

[1] Note that also this concept can be traced back to Feynman [284].

"At that subtle moment when man glances backward over his life, Sisyphus returning toward his rock, in that slight pivoting he contemplates that series of unrelated actions which become his fate, created by him; [...] A blind man eager to see who knows that the night has no end, he is still on the go. The rock is still rolling. [...] But Sisyphus teaches the higher fidelity that negates the gods and raises rocks. This universe henceforth without a master seems to him neither sterile nor futile. Each atom of that stone, each mineral flake of that night filled mountain, in itself forms a world. The struggle itself toward the heights is enough to fill a man's heart. One must imagine Sisyphus happy."

ALBERT CAMUS

Part IV.

Appendices

A. Nature constants

A.1. General constants

	Symbol	Value	Unit
Planck constant	h	$6.62606957(29) \times 10^{-34}$	J s
Vacuum speed of light	c	299792458	m s^{-1}
Boltzmann constant	k_B	$1.3806488(13) \times 10^{-23}$	J K^{-1}
Bohr magneton	μ_B	$927.400968(20) \times 10^{-26}$	J T^{-1}
Atomic mass unit	amu	$1.660538921(73) \times 10^{-27}$	kg
Bohr radius	a_0	$0.52917721092(17) \times 10^{-10}$	m
Earth standard gravity	g_0	9.80665×10^{-10}	m s^{-2}

Table A.1.: General nature constants according to [287], except earth standard gravity which is taken from [288].

A.2. ^{87}Rb D2 line

	Symbol	Value	Unit
Nuclear spin	I	3/2	
Mass	m	86.909180520(15)	amu
D2-line wavelength (vacuum)	λ_{D2}	780.241209686(13)	nm
Natural line width (FWHM)	Γ	$2\pi \times 6.0666(18)$	MHz
Recoil velocity	v_r	5.8845	mm s^{-1}
Doppler temperature	T_{DP}	145.57	μK

Table A.2.: Properties of ^{87}Rb and the D2 line according to [172].

B. Numerics: Odds and ends

B.1. Picking random points on a sphere

For the Monte Carlo simulation presented in chapter 7, to properly take into account uniform scattering of photons it is necessary to generate vectors pointing to uniformly distributed surface elements on the unit sphere. To this end, as outlined for instance in reference [289], one can either use Cartesian coordinates and create the vector

$$\boldsymbol{v}_R = \frac{1}{\sqrt{r_x^2 + r_y^2 + r_z^2}} \begin{pmatrix} r_x \\ r_y \\ r_z \end{pmatrix}, \tag{B.1}$$

where r_x, r_y and r_z are standard Gaussian random numbers. Alternatively, using spherical coordinates where the solid angle is given by $d\Omega = \sin\phi \; d\theta \; d\phi$, one can use

$$\theta = 2\pi r_\theta \tag{B.2}$$

$$\phi = \arccos\left(2r_\phi - 1\right). \tag{B.3}$$

Here, r_θ and r_ϕ denote uniform random numbers on the interval $[0, 1]$.

B.2. GPGPU with Matlab

The abbreviation GPGPU stands for *General Purpose computation on Graphics Processing Unit.* Using graphics cards can significantly speed up calculations relying heavily on point-wise matrix operations, fourier transforms, or in general easily parallelizable code. Hence, split-operator methods as presented in chapter 3.2 lends itself very well to gain speed-ups of a factor $\mathcal{O}(10)$ over the CPU. At the moment, there are two interfaces available to use the GPU for calculations. OpenCL is an open standard supported by all suppliers, while CUDA is a set of libraries for NVidia graphics cards. The latter is directly supported by Matlab and Mathematica, rendering it very easy to port existing code into GPU - ready versions. Initializing the graphics card, performing a point-wise matrix multiplication between two predefined matrices A and B, and reading out the result with Matlab and a CUDA - enabled GPU is as simple as

```
gpuDevice(1)                             % initialize GPU
gA = gpuArray(A); gB = gpuArray(B);      % push A, B to GPU as gA, gB
gC = gA.*gB;                             % matrix operation as usual
C = gather(gC);                          % pull gC to RAM as C
```

In a similar manner, many Matlab operations directly work with GPU variables.

C. Publications

- *Stochastic optimization of a cold atom experiment using a genetic algorithm*
  W. Rohringer, R. Bücker, S. Manz, T. Betz, C. Koller, M. Göbel, A. Perrin, J. Schmiedmayer and T. Schumm
  Appl. Phys. Lett. **93**, 264101 (2008)

- *A single atom detector integrated on an atom chip: fabrication, characterization and application*
  D. Heine, W. Rohringer, D. Fischer, M. Wilzbach, T. Raub, S. Loziczky, XiYuan Liu, S. Groth, B. Hessmo and J. Schmiedmayer
  New J. Phys. **12**, 095005 (2010)

- *Stochastic optimization of Bose-Einstein condensation using a genetic algorithm*
  W. Rohringer, D. Fischer, M. Trupke, J. Schmiedmayer and T. Schumm
  Stochastic Optimization - Seeing the optimal for the uncertain
  InTech Publishing, ISBN:978-953-307-829-8 (2011)

- *Scale invariance and shortcuts to adiabaticity in a one-dimensional Bose gas*
  W. Rohringer, D. Fischer, F. Steiner, I. E. Mazets, J. Schmiedmayer and M. Trupke
  submitted

- *Evaporative cooling of 1D Bose gases*
  B. Rauer, P. Grisins, R. Geiger, T. Langen, T. Schweigler, W. Rohringer, M. Gring, D. Adu Smith, I. Mazets and J. Schmiedmayer
  in preparation

Acknowledgements

Obviously, a thesis project in this field of physics does not (only) exist in a vacuum. The successful realization of cold atom experiments is first and foremost teamwork, and I would like to express my gratitude towards the following people for their crucial contributions to this thesis.

My supervisors: Jörg Schmiedmayer, for the chance to work on this fascinating project, for letting me visit various international conferences and workshops, and for sharing his insight - especially concerning how a defocused BEC looks like. Michael Trupke, for his admirable effort to focus the work performed in our team, and for his unswerving calmness and his crisis management skills in the face of the incessant series of bad news from the lab. Björn Hessmo, for supervision in the early stages of the project, and for his advice considering all kinds of fancy lab equipment.

My fellow PhD students on team μ-optics, Dominik Fischer and Florian Steiner, for all the hours of building, aligning, repairing, troubleshooting, bugfixing, analysing and being confused together. Sorry for the buggy code and the bad music. Special thanks to Dominik for the collaborative realization of the first sunshine BEC in the group, and to Florian for his assistance in the development of the prototype nanofiber-vacuum-cleaner.

The former members on team μ-optics, Marco Wilzbach and Dennis Heine for their previous work on the experiment, and especially for providing us with the group's best laser setup. The TA has survived several commercial ones, by now. Also, thank you for the pictures you left on the lab computers.

The diploma students of team μ-optics: Sebastian Loziczky and Thomas Raub for their early support, Michaela Trimmel for her work on the absorption imaging system, and Georg Winkler for his various contributions to the setup.

Thorsten Schumm, for being a mentor and for his continuing support after introducing me to this group, especially in the times when our experiment was somewhat low on personnel. Also, thank you for teaching me how to build these lasers and assigning this genetic algorithm topic to me, back then.

Igor Mazets for his work on the theory underlying the projects presented in this thesis, and for his patience in explaining this work to me. Repeatedly.

Jean-François Schaff for introducing me to the topic of shortcuts to adiabaticity.

Stephan Schneider for his help on fixing the test chamber, for sharing his knowledge on arcane vacuum equipment and for his administrative support.

The first generation Rb-II crew: Stephanie Manz, Robert Bücker (who will both cringe at the wordplay in the first sentence of this section even more than other people), Christian Koller, Thomas Betz and Aurélien Perrin for supporting me in my first steps towards optimal control of BEC machines. Also, thank you for all the chocolate cookies.

Max Kuhnert for providing his data analysis tools, Bernhard Rauer and Pjotrs Grisins for their collaboration and help in developing the c-field numerics, Tim Langen and Tarik Berrada for many discussions and various pieces of code, Fritz Diorico and Stephan Minniberger for all the lent lab equipment, all the people of the "magnificent seven" office for the peaceful coexistence and the entire atom chip group for the friendly and supportive atmosphere as well as the most amazing discussions at the coffee corner. Everybody has provided valuable help at some point in time, which I am grateful for.

The electronics workshop of the ATI for replacing countless Darlington transistors and the mechanical workshop for manufacturing the chip and coil mountings for the new setup.

Sebastian Erne for many helpful discussions considering theory and numerics.

Martin Plenio and Arno Rauschenbeutel, for joining my thesis advisory commitee.

Thomas Gasenzer for his willingness to act as my thesis referee.

My friends and family, especially my mother and my late father for their unconditional support throughout all these years.

I thank Tina for being the best wife in the world, even though I was often absent in these years, at least mentally.

Bibliography

[1] Lambert, N., Chen, Y.-N., Cheng, Y.-C., Li, C.-M., Chen, G.-Y. & Nori, F. Quantum biology. *Nat. Phys.* **9**, 10–18 (2013).

[2] Anderson, M. H., Ensher, J. R., Matthews, M. R., Wieman, C. E. & Cornell, E. A. Observation of Bose-Einstein Condensation in a Dilute Atomic Vapor. *Science* **269**, 198–201 (1995).

[3] Davis, K. B., Mewes, M.-O., Andrews, M. R., van Druten, N. J., Durfee, D. S., Kurn, D. M. & Ketterle, W. Bose-Einstein condensation in a gas of sodium atoms. *Phys. Rev. Lett.* **75**, 3969–3973 (1995).

[4] Bradley, C. C., Sackett, C. A., Tollett, J. J. & Hulet, R. G. Evidence of Bose-Einstein Condensation in an Atomic Gas with Attractive Interactions. *Phys. Rev. Lett.* **75**, 1687–1690 (1995).

[5] Sachdev, S. *Quantum Phase Transitions* (Cambridge University Press, 2001).

[6] Greiner, M., Mandel, O., Esslinger, T., Hansch, T. W. & Bloch, I. Quantum phase transition from a superfluid to a Mott insulator in a gas of ultracold atoms. *Nature* **415**, 39–44 (2002).

[7] Srednicki, M. Chaos and quantum thermalization. *Phys. Rev. E* **50**, 888–901 (1994).

[8] Rigol, M., Dunjko, V. & Olshanii, M. Thermalization and its mechanism for generic isolated quantum systems. *Nature* **452**, 854–8 (2008).

[9] Caux, J.-S. & Mossel, J. Remarks on the notion of quantum integrability. *J. Stat. Mech. Theory Exp.* **2011**, P02023 (2011).

[10] Lieb, E. H. & Liniger, W. Exact Analysis of an Interacting Bose Gas. I. The General Solution and the Ground State. *Phys. Rev.* **130**, 1605–1616 (1963).

[11] Lieb, E. H. Exact Analysis of an Interacting Bose Gas. II. The Excitation Spectrum. *Phys. Rev.* **130**, 1616–1624 (1963).

[12] Cazalilla, M. A., Citro, R., Giamarchi, T., Orignac, E. & Rigol, M. One dimensional bosons: From condensed matter systems to ultracold gases. *Rev. Mod. Phys.* **83**, 1405–1466 (2011).

[13] Haller, E., Gustavsson, M., Mark, M. J., Danzl, J. G., Hart, R., Pupillo, G. & Nägerl, H.-C. Realization of an Excited, Strongly Correlated Quantum Gas Phase. *Science* **325**, 1224–1227 (2009).

[14] Esteve, J., Trebbia, J.-B., Schumm, T., Aspect, A., Westbrook, C. I. & Bouchoule, I. Observations of Density Fluctuations in an Elongated Bose Gas: Ideal Gas and Quasicondensate Regimes. *Phys. Rev. Lett.* **96**, 130403 (2006).

[15] Manz, S., Bücker, R., Betz, T., Koller, C., Hofferberth, S., Mazets, I. E., Imambekov, A., Demler, E., Perrin, A., Schmiedmayer, J. & Schumm, T. Two-point density correlations of quasicondensates in free expansion. *Phys. Rev. A* **81**, 1–4 (2010).

[16] Jacqmin, T., Armijo, J., Berrada, T., Kheruntsyan, K. V. & Bouchoule, I. Sub-Poissonian Fluctuations in a 1D Bose Gas: From the Quantum Quasicondensate to the Strongly Interacting Regime. *Phys. Rev. Lett.* **106**, 230405 (2011).

[17] Perrin, A., Bucker, R., Manz, S., Betz, T., Koller, C., Plisson, T., Schumm, T. & Schmiedmayer, J. Hanbury Brown and Twiss correlations across the Bose-Einstein condensation threshold. *Nat. Phys.* **8**, 195–198 (2012).

[18] Mazets, I. E., Schumm, T. & Schmiedmayer, J. Breakdown of Integrability in a Quasi-1D Ultracold Bosonic Gas. *Phys. Rev. Lett.* **100**, 210403 (2008).

[19] Mazets, I. E. Integrability breakdown in longitudinaly trapped, one-dimensional bosonic gases. *Eur. Phys. J. D* **65**, 43–47 (2011).

[20] Kollar, M., Wolf, F. A. & Eckstein, M. Generalized Gibbs ensemble prediction of prethermalization plateaus and their relation to nonthermal steady states in integrable systems. *Phys. Rev. B* **84**, 54304 (2011).

[21] Caux, J.-S. Correlation functions of integrable models: A description of the ABACUS algorithm. *J. Math. Phys.* **50**, – (2009).

[22] Blakie, P. B., Bradley, A. S., Davis, M. J., Ballagh, R. J. & Gardiner, C. W. Dynamics and statistical mechanics of ultra-cold Bose gases using c-field techniques. *Adv. Phys.* **57**, 363–455 (2008).

[23] Proukakis, N. P. & Jackson, B. Finite-temperature models of Bose–Einstein condensation. *J. Phys. B At. Mol. Opt. Phys.* **41**, 203002 (2008).

[24] Giamarchi, T. *Quantum Physics in One Dimension.* International Series of Monographs on Physics (Clarendon Press, 2004).

[25] José, J. Sine-Gordon theory and the classical two-dimensional x-y model. *Phys. Rev. D* **14**, 2826–2829 (1976).

[26] Uhlmann, M., Xu, Y. & Schützhold, R. Aspects of cosmic inflation in expanding Bose–Einstein condensates. *New J. Phys.* **7**, 248–248 (2005).

[27] Fedichev, P. O. & Fischer, U. R. Gibbons-Hawking Effect in the Sonic de Sitter Space-Time of an Expanding Bose-Einstein-Condensed Gas. *Phys. Rev. Lett.* **91**, 240407 (2003).

[28] Fedichev, P. & Fischer, U. Observer dependence for the phonon content of the sound field living on the effective curved space-time background of a Bose-Einstein condensate. *Phys. Rev. D* **1**, 1–9 (2004).

[29] Fedichev, P. & Fischer, U. "Cosmological" quasiparticle production in harmonically trapped superfluid gases. *Phys. Rev. A* **69**, 033602 (2004).

[30] Imambekov, A., Mazets, I. E., Petrov, D. S., Gritsev, V., Manz, S., Hofferberth, S., Schumm, T., Demler, E. & Schmiedmayer, J. Density ripples in expanding low-dimensional gases as a probe of correlations. *Phys. Rev. A* **80**, 1–14 (2009).

[31] Manz, S. *Density correlations of expanding one-dimensional Bose gases.* Ph.d. thesis, Vienna University of Technology (2010).

[32] Kagan, Y., Surkov, E. L. & Shlyapnikov, G. v. Evolution of a Bose-condensed gas under variations of the confining potential. *Phys. Rev. A* **54**, R1753–R1756 (1996).

[33] Castin, Y. & Dum, R. Bose-Einstein Condensates in Time Dependent Traps. *Phys. Rev. Lett.* **77**, 5315–5319 (1996).

[34] Pitaevskii, L. P. & Rosch, A. Breathing modes and hidden symmetry of trapped atoms in two dimensions. *Phys. Rev. A* **55**, 853–856 (1997).

[35] Minguzzi, A. & Gangardt, D. M. Exact Coherent States of a Harmonically Confined Tonks-Girardeau Gas. *Phys. Rev. Lett.* **94**, 240404 (2005).

[36] Gritsev, V., Barmettler, P. & Demler, E. Scaling approach to quantum non-equilibrium dynamics of many-body systems. *New J. Phys.* **12**, 113005 (2010).

[37] Schaff, J.-F., Capuzzi, P., Labeyrie, G. & Vignolo, P. Shortcuts to adiabaticity for trapped ultracold gases. *New J. Phys.* **13**, 113017 (2011).

[38] Wilzbach, M. *Single atom detection on an atom chip with integrated optics.* Ph.d. thesis, University of Heidelberg (2007).

[39] Heine, D. *Single Atom Detection and Nonclassical Photon Correlations.* Ph.d. thesis, University of Heidelberg (2008).

[40] Wilzbach, M., Heine, D., Groth, S., Liu, X., Raub, T., Hessmo, B. & Schmiedmayer, J. Simple integrated single-atom detector. *Opt. Lett.* **34**, 259–261 (2009).

[41] Heine, D., Wilzbach, M., Raub, T., Hessmo, B. & Schmiedmayer, J. Integrated atom detector: Single atoms and photon statistics. *Phys. Rev. A* **79**, 21804 (2009).

[42] Heine, D., Rohringer, W., Fischer, D., Wilzbach, M., Raub, T., Loziczky, S., Liu, X., Groth, S., Hessmo, B. & Schmiedmayer, J. A single-atom detector integrated on an atom chip: fabrication, characterization and application. *New J. Phys.* **12**, 095005 (2010).

[43] Planck, M. Über eine Verbesserung der Wienschen Spektralgleichung. *Verhandlungen der Dtsch. Phys. Gesellschaft* **2**, 202–204 (1900).

[44] Planck, M. Zur Theorie des Gesetzes der Energieverteilung im Normalspektrum. *Verhandlungen der Dtsch. Phys. Gesellschaft* **2**, 237 (1900).

[45] Bose, S. N. Plancks Gesetz und Lichtquantenhypothese. *Zeitschrift für Phys.* **26**, 178–181 (1924).

[46] Landau, L. D. & Lifshitz, E. M. *Quantum Mechanics: Non-relativistic Theory.* Butterworth Heinemann (Butterworth-Heinemann, 1977).

[47] Stoof, H. T. C., Gubbels, K. B. & Dickerscheid, D. B. M. *Ultracold Quantum Fields.* Theoretical and mathematical physics (BPR Publishers, 2008).

[48] Fierz, M. Über die relativistische Theorie kräftefreier Teilchen mit beliebigem Spin. *Helv. Phys. Acta* **12** (1939).

[49] Pauli, W. The Connection Between Spin and Statistics. *Phys. Rev.* **58**, 716–722 (1940).

[50] Weinberg, S. Feynman Rules for Any Spin. *Phys. Rev.* **133**, 1318–1332 (1964).

[51] Weinberg, S. Feynman Rules for Any Spin. II. Massless Particles. *Phys. Rev.* **134**, 882–896 (1964).

[52] Weinberg, S. Feynman Rules for Any Spin. III. *Phys. Rev.* **181**, 1893–1899 (1969).

[53] Einstein, A. *Zur Quantentheorie des idealen Gases*, vol. 3 of *Sitzungsberichte der Preussischen Akademie der Wissenschaften. Physikalisch-mathematische Klasse* (Verlag der Akademie der Wissenschaften, in Kommission bei Walter de Guyter u. Company, 1925).

[54] Landau, L. D. & Lifshitz, E. M. *Statistical Physics.* Bd. 5 (Elsevier Science, 1996).

[55] Smith, R. P., Campbell, R. L. D., Tammuz, N. & Hadzibabic, Z. Effects of Interactions on the Critical Temperature of a Trapped Bose Gas. *Phys. Rev. Lett.* **106**, 250403 (2011).

[56] Hohenberg, P. C. Existence of Long-Range Order in One and Two Dimensions. *Phys. Rev.* **158**, 383–386 (1967).

[57] Mermin, N. D. & Wagner, H. Absence of Ferromagnetism or Antiferromagnetism in One- or Two-Dimensional Isotropic Heisenberg Models. *Phys. Rev. Lett.* **17**, 1133–1136 (1966).

[58] Ketterle, W. & van Druten, N. J. Bose-Einstein condensation of a finite number of particles trapped in one or three dimensions. *Phys. Rev. A* **54**, 656–660 (1996).

[59] Görlitz, A., Vogels, J. M., Leanhardt, A. E., Raman, C., Gustavson, T. L., Abo-Shaeer, J. R., Chikkatur, A. P., Gupta, S., Inouye, S., Rosenband, T. & Ketterle, W. Realization of Bose-Einstein Condensates in Lower Dimensions. *Phys. Rev. Lett.* **87**, 130402 (2001).

[60] Bagnato, V., Pritchard, D. E. & Kleppner, D. Bose-Einstein condensation in an external potential. *Phys. Rev. A* **35**, 4354–4358 (1987).

[61] Penrose, O. & Onsager, L. Bose-Einstein Condensation and Liquid Helium. *Phys. Rev.* **104**, 576–584 (1956).

[62] Pitaevskii, L. P. & Stringari, S. *Bose-Einstein Condensation.* International Series of Monographs on Physics (Clarendon Press, 2003).

[63] Bogolyubov, N. N. On the Theory of Superfluidity. *J. Phys.* **11**, 23–32 (1947).

[64] Olshanii, M. Atomic Scattering in the Presence of an External Confinement and a Gas of Impenetrable Bosons. *Phys. Rev. Lett.* **81**, 938–941 (1998).

[65] Salasnich, L., Parola, A. & Reatto, L. Effective wave equations for the dynamics of cigar-shaped and disk-shaped Bose condensates. *Phys. Rev. A* **65**, 43614 (2002).

[66] Deshpande, V. V., Bockrath, M., Glazman, L. I. & Yacoby, A. Electron liquids and solids in one dimension. *Nature* **464**, 209–216 (2010).

[67] Kheruntsyan, K., Gangardt, D., Drummond, P. & Shlyapnikov, G. Pair Correlations in a Finite-Temperature 1D Bose Gas. *Phys. Rev. Lett.* **91**, 040403 (2003).

[68] Kheruntsyan, K., Gangardt, D., Drummond, P. & Shlyapnikov, G. Finite-temperature correlations and density profiles of an inhomogeneous interacting one-dimensional Bose gas. *Phys. Rev. A* **71**, 1–17 (2005).

[69] Sykes, A. G., Gangardt, D., Davis, M., Viering, K., Raizen, M. & Kheruntsyan, K. Spatial Nonlocal Pair Correlations in a Repulsive 1D Bose Gas. *Phys. Rev. Lett.* **100**, 2–5 (2008).

[70] Deuar, P., Sykes, A. G., Gangardt, D. M., Davis, M. J., Drummond, P. D. & Kheruntsyan, K. V. Nonlocal pair correlations in the one-dimensional Bose gas at finite temperature. *Phys. Rev. A* **79**, 43619 (2009).

[71] Reichel, J. & Vuletic, V. *Atom Chips.* Atom Chips (Wiley, 2010).

[72] Yang, C. N. & Yang, C. P. Thermodynamics of a One-Dimensional System of Bosons with Repulsive Delta-Function Interaction. *J. Math. Phys.* **10**, 1115–1122 (1969).

[73] Naraschewski, M. & Glauber, R. Spatial coherence and density correlations of trapped Bose gases. *Phys. Rev. A* **59**, 4595–4607 (1999).

[74] Srednicki, M. *Quantum Field Theory* (Cambridge University Press, 2007).

[75] Stimming, H.-P., Mauser, N. J., Schmiedmayer, J. & Mazets, I. E. Fluctuations and Stochastic Processes in One-Dimensional Many-Body Quantum Systems. *Phys. Rev. Lett.* **105**, 015301 (2010).

[76] Girardeau, M. D., Wright, E. M. & Triscari, J. M. Ground-state properties of a one-dimensional system of hard-core bosons in a harmonic trap. *Phys. Rev. A* **63**, 33601 (2001).

[77] Paredes, B., Widera, A., Murg, V., Mandel, O., Fölling, S., Cirac, I., Shlyapnikov, G. V., Hänsch, T. W. & Bloch, I. Tonks–Girardeau gas of ultracold atoms in an optical lattice. *Nature* **429**, 277–281 (2004).

[78] Bouchoule, I., Kheruntsyan, K. & Shlyapnikov, G. Interaction-induced crossover versus finite-size condensation in a weakly interacting trapped one-dimensional Bose gas. *Phys. Rev. A* **75**, 2–5 (2007).

[79] Panfil, M. & Caux, J.-S. Finite-temperature correlations in the Lieb-Liniger one-dimensional Bose gas. *Phys. Rev. A* **89**, 33605 (2014).

[80] Pedri, P., Santos, L., Öhberg, P. & Stringari, S. Violation of self-similarity in the expansion of a one-dimensional Bose gas. *Phys. Rev. A* **68**, 1–6 (2003).

[81] Rauer, B., Grisins, P., Geiger, R., Langen, T., Schweigler, T., Rohringer, W., Gring, M., Adu Smith, D., Mazets, I. & Schmiedmayer, J. Evaporative cooling in 1d Bose gases. *Prep.* (2014).

[82] Petrov, D. S., Shlyapnikov, G. V. & Walraven, J. T. M. Regimes of Quantum Degeneracy in Trapped 1D Gases. *Phys. Rev. Lett.* **85**, 3745–3749 (2000).

[83] de Gennes, P. G. *Superconductivity of metals and alloys.* Frontiers in physics (W.A. Benjamin, 1966).

[84] Mora, C. & Castin, Y. Extension of Bogoliubov theory to quasicondensates. *Phys. Rev. A* **67**, 053615 (2003).

[85] Cladé, P., Ryu, C., Ramanathan, A., Helmerson, K. & Phillips, W. D. Observation of a 2D Bose Gas: From Thermal to Quasicondensate to Superfluid. *Phys. Rev. Lett.* **102**, 170401 (2009).

[86] Hellweg, D., Dettmer, S., Ryytty, P., Arlt, J., Ertmer, W., Sengstock, K., Petrov, D., Shlyapnikov, G., Kreutzmann, H., Santos, L. & Lewenstein, M. Phase fluctuations in Bose-Einstein condensates. *Appl. Phys. B Lasers Opt.* **73**, 781–789 (2001).

[87] Gangardt, D. M. & Shlyapnikov, G. V. Stability and Phase Coherence of Trapped 1D Bose Gases. *Phys. Rev. Lett.* **90**, 10401 (2003).

[88] Haldane, F. D. M. Effective Harmonic-Fluid Approach to Low-Energy Properties of One-Dimensional Quantum Fluids. *Phys. Rev. Lett.* **47**, 1840–1843 (1981).

[89] Andersen, J. O., Al Khawaja, U. & Stoof, H. T. C. Phase Fluctuations in Atomic Bose Gases. *Phys. Rev. Lett.* **88**, 70407 (2002).

[90] Al Khawaja, U., Andersen, J. O., Proukakis, N. P. & Stoof, H. T. C. Low dimensional Bose gases. *Phys. Rev. A* **66**, 13615 (2002).

[91] Y. Castin. Simple theoretical tools for low dimension Bose gases. *J. Phys. IV Fr.* **116**, 89–132 (2004).

[92] Whitlock, N. K. & Bouchoule, I. Relative phase fluctuations of two coupled one-dimensional condensates. *Phys. Rev. A* **68**, 53609 (2003).

[93] Gerbier, F., Thywissen, J. H., Richard, S., Hugbart, M., Bouyer, P. & Aspect, A. Momentum distribution and correlation function of quasicondensates in elongated traps. *Phys. Rev. A* **67**, 1–4 (2003).

[94] Richard, S., Gerbier, F., Thywissen, J., Hugbart, M., Bouyer, P. & Aspect, A. Momentum Spectroscopy of 1D Phase Fluctuations in Bose-Einstein Condensates. *Phys. Rev. Lett.* **91**, 10–13 (2003).

[95] Armijo, J., Jacqmin, T., Kheruntsyan, K. V. & Bouchoule, I. Probing Three-Body Correlations in a Quantum Gas Using the Measurement of the Third Moment of Density Fluctuations. *Phys. Rev. Lett.* **105**, 230402 (2010).

[96] Armijo, J., Jacqmin, T., Kheruntsyan, K. & Bouchoule, I. Mapping out the quasicondensate transition through the dimensional crossover from one to three dimensions. *Phys. Rev. A* **83**, 21605 (2011).

[97] Amerongen, A. H. V., Es, J. J. P. V., Wicke, P., Kheruntsyan, K. V. & Druten, N. J. V. Yang-Yang Thermodynamics on an Atom Chip. *Phys. Rev. Lett.* **090402**, 13–15 (2008).

[98] Menotti, C. & Stringari, S. Collective oscillations of a one-dimensional trapped Bose-Einstein gas. *Phys. Rev. A* **66**, 043610 (2002).

[99] Krüger, P., Hofferberth, S., Mazets, I. E., Lesanovsky, I. & Schmiedmayer, J. Weakly Interacting Bose Gas in the One-Dimensional Limit. *Phys. Rev. Lett.* **105**, 265302 (2010).

[100] Gerbier, F. Quasi-1D Bose-Einstein condensates in the dimensional crossover regime. *Europhys. Lett.* **66**, 771–777 (2004).

[101] Ketterle, W., Durfee, D. S. & Stamper-Kurn, D. M. Making, probing and understanding Bose-Einstein condensates. In Inguscio, M., Stringari, S. & Wieman, C. E. (eds.) *Bose-Einstein Condens. At. gases*, 76–176 (IOS Press, Amsterdam, 1999).

[102] Petrov, D., Shlyapnikov, G. & Walraven, J. Phase-Fluctuating 3D Bose-Einstein Condensates in Elongated Traps. *Phys. Rev. Lett.* **87**, 050404 (2001).

[103] Hutchinson, D. A. W., Burnett, K., Dodd, R. J., Morgan, S. A., Rusch, M., Zaremba, E., Proukakis, N. P., Edwards, M. & Clark, C. W. Gapless mean-field theory of Bose-Einstein condensates. *J. Phys. B At. Mol. Opt. Phys.* **33**, 3825 (2000).

[104] Zaremba, E., Nikuni, T. & Griffin, A. Dynamics of Trapped Bose Gases at Finite Temperatures. *J. Low Temp. Phys.* **116**, 277–345 (1999).

[105] Stoof, H. T. C. Coherent Versus Incoherent Dynamics During Bose-Einstein Condensation in Atomic Gases. *J. Low Temp. Phys.* **114**, 11–109 (1999).

[106] Stoof, H. T. C. & Bijlsma, M. J. Dynamics of Fluctuating Bose–Einstein Condensates. *J. Low Temp. Phys.* **124**, 431–442 (2001).

[107] Gardiner, C., Anglin, J. & Fudge, T. The stochastic Gross-Pitaevskii equation. *J. Phys. B At. Mol. Opt. Phys.* **35**, 1555–1582 (2002).

[108] Davis, M. J., Morgan, S. A. & Burnett, K. Simulations of Bose Fields at Finite Temperature. *Phys. Rev. Lett.* **87**, 160402 (2001).

[109] Gardiner, C. W. & Davis, M. J. The stochastic Gross–Pitaevskii equation: II. *J. Phys. B At. Mol. Opt. Phys.* **36**, 4731 (2003).

[110] Steel, M. J., Olsen, M. K., Plimak, L. I., Drummond, P. D., Tan, S. M., Collett, M. J., Walls, D. F. & Graham, R. Dynamical quantum noise in trapped Bose-Einstein condensates. *Phys. Rev. A* **58**, 4824–4835 (1998).

[111] Sinatra, A., Lobo, C. & Castin, Y. The truncated Wigner method for Bose-condensed gases : limits of validity and applications *. *J. Phys. B At. Mol. Opt. Phys.* **35**, 3599–3631 (2002).

[112] Gasenzer, T., Berges, J., Schmidt, M. G. & Seco, M. Nonperturbative dynamical many-body theory of a Bose-Einstein condensate. *Phys. Rev. A* **72**, 63604 (2005).

[113] Pethick, C. & Smith, H. *Bose-Einstein Condensation in Dilute Gases* (Cambridge University Press, 2002).

[114] Proukakis, N., Schmiedmayer, J. & Stoof, H. Quasicondensate growth on an atom chip. *Phys. Rev. A* **73**, 053603 (2006).

[115] Witkowska, E., Gajda, M. & Rzazewski, K. Monte Carlo method, classical fields and Bose statistics. *Opt. Commun.* **283**, 671–675 (2010).

[116] Davis, M. J., Morgan, S. A. & Burnett, K. Simulations of thermal Bose fields in the classical limit. *Phys. Rev. A* **66**, 53618 (2002).

[117] Rooney, S. J., Blakie, P. B. & Bradley, a. S. Stochastic projected Gross-Pitaevskii equation. *Phys. Rev. A* **86**, 053634 (2012).

[118] Duine, R. & Stoof, H. Stochastic dynamics of a trapped Bose-Einstein condensate. *Phys. Rev. A* **65**, 013603 (2001).

[119] Steck, D. A. *Quantum and Atom Optics* (2007).

[120] Blanes, S. & Moan, P. C. Practical Symplectic Partitioned Runge–Kutta and Runge–Kutta–Nystr&#x00F6;M Methods. *J. Comput. Appl. Math.* **142**, 313–330 (2002).

[121] Bücker, R., Perrin, A., Manz, S., Betz, T., Koller, C., Plisson, T., Rottmann, J., Schumm, T. & Schmiedmayer, J. Single-particle-sensitive imaging of freely propagating ultracold atoms. *New J. Phys.* **11**, 103039 (2009).

[122] Cockburn, S. P., Nistazakis, H. E., Horikis, T. P., Kevrekidis, P. G., Proukakis, N. P. & Frantzeskakis, D. J. Matter-Wave Dark Solitons: Stochastic versus Analytical Results. *Phys. Rev. Lett.* **104**, 174101 (2010).

[123] Cockburn, S. P., Negretti, A., Proukakis, N. P., Henkel, C., Introduction, I. & Wigner, A. T. A comparison between microscopic methods for finite temperature Bose gases. *Phys. Rev. A* **83**, 1–35 (2011).

[124] Cockburn, S. P., Gallucci, D. & Proukakis, N. P. Quantitative study of quasi-one-dimensional Bose gas experiments via the stochastic Gross-Pitaevskii equation. *Phys. Rev. A* **84**, 023613 (2011).

[125] Wright, T. M., Proukakis, N. P. & Davis, M. J. Many-body physics in the classical-field description of a degenerate Bose gas. *Phys. Rev. A* **84**, 023608 (2011).

[126] Cockburn, S. P. *Bose Gases In and Out of Equilibrium within the Stochastic Gross-Pitaevskii Equation*. Ph.D. thesis, Newcastle University (2010).

[127] Gardiner, C. W., Lee, M. D., Ballagh, R. J., Davis, M. J. & Zoller, P. Quantum Kinetic Theory of Condensate Growth: Comparison of Experiment and Theory. *Phys. Rev. Lett.* **81**, 5266–5269 (1998).

[128] Prokof'ev, N., Ruebenacker, O. & Svistunov, B. Critical Point of a Weakly Interacting Two-Dimensional Bose Gas. *Phys. Rev. Lett.* **87**, 270402 (2001).

[129] Galluci, D. *Ab Initio Modelling of Quasi-one-dimensional Bose Gase Experiments via the Stochastic Gross-Pitaevskii Equation.* Ph.D. thesis, Newcastle University (2013).

[130] Langen, T., Erne, S., Rauer, B., Schweigler, T., Kuhnert, M., Rohringer, W., Gasenzer, T. & Schmiedmayer, J. Experimental observation of a generalized Gibbs ensemble. *Prep.* (2014).

[131] Kuhnert, M., Langen, T., Rauer, B., Adu Smith, D., Geiger, R. & Schmiedmayer, J. Thermalization of a coherently split Bose gas. *Prep.* (2014).

[132] Uhlenbeck, G. E. & Ornstein, L. S. On the Theory of the Brownian Motion. *Phys. Rev.* **36**, 823–841 (1930).

[133] Gillespie, D. T. Exact numerical simulation of the Ornstein-Uhlenbeck process and its integral. *Phys. Rev. E* **54**, 2084–2091 (1996).

[134] Schmiedmayer, J. Guiding and trapping a neutral atom on a wire. *Phys. Rev. A* **52**, R13—-R16 (1995).

[135] Weinstein, J. D. & Libbrecht, K. G. Microscopic magnetic traps for neutral atoms. *Phys. Rev. A* **52**, 4004–4009 (1995).

[136] Denschlag, J., Cassettari, D., Chenet, A., Schneider, S. & Schmiedmayer, J. A neutral atom and a wire: towards mesoscopic atom optics. *Appl. Phys. B* **69**, 291–301 (1999).

[137] Denschlag, J., Cassettari, D. & Schmiedmayer, J. Guiding Neutral Atoms with a Wire. *Phys. Rev. Lett.* **82**, 2014–2017 (1999).

[138] Reichel, J., Hänsel, W. & Hänsch, T. Atomic Micromanipulation with Magnetic Surface Traps. *Phys. Rev. Lett.* **83**, 3398–3401 (1999).

[139] Folman, R., Krüger, P., Cassettari, D., Hessmo, B., Maier, T. & Schmiedmayer, J. Controlling cold atoms using nanofabricated surfaces: atom chips. *Phys. Rev. Lett.* **84**, 4749–52 (2000).

[140] Hansel, W., Hommelhoff, P., Hansch, T. W. & Reichel, J. Bose-Einstein condensation on a microelectronic chip. *Nature* **413**, 498–501 (2001).

[141] Ott, H., Fortagh, J., Schlotterbeck, G., Grossmann, a. & Zimmermann, C. Bose-Einstein Condensation in a Surface Microtrap. *Phys. Rev. Lett.* **87**, 230401 (2001).

[142] Groth, S., Krüger, P., Wildermuth, S., Folman, R., Fernholz, T., Schmiedmayer, J., Mahalu, D. & Bar-Joseph, I. Atom chips: Fabrication and thermal properties. *Appl. Phys. Lett.* **85**, 2980 (2004).

[143] Groth, S. *Development, Fabrication and Characterisation of Atom Chips.* Ph.d. thesis, University of Heidelberg (2006).

[144] Folman, R., Kruger, P., Cassettari, D., Hessmo, B., Maier, T. & Schmiedmayer, J. Controlling cold atoms using nanofabricated surfaces: atom chips. *Phys. Rev. Lett.* **84**, 4749–52 (2000).

[145] Reichel, J. Microchip traps and Bose–Einstein condensation. *Appl. Phys. B* **74**, 469–487 (2002).

[146] Wildermuth, S. *One-dimensional Bose-Einstein condensates in micro-traps.* Ph.d. thesis, University of Heidelberg (2005).

[147] Schumm, T. *Bose-Einstein condensates in magnetic double well potentials.* Ph.D. thesis, University of Heidelberg (2006).

[148] Wing, W. H. On neutral particle trapping in quasistatic electromagnetic fields. *Prog. Quantum Electron.* **8**, 181–199 (1984).

[149] Earnshaw, S. On the Nature of the Molecular Forces which Regulate the Constitution of the Luminiferous Ether. *Trans. Cambridge Philos. Soc.* **7**, 97 (1848).

[150] Majorana, E. Atomi orientati in campo magnetico variabile. *Nuovo Cim.* **9**, 43–50 (1932).

[151] Gott, Y. V., Ioffe, M. S. & Tel'kovsky, V. G. Some new results on confining plasmas in a magnetic trap. *Nucl. Fusion Suppl.* **3**, 1045 (1962).

[152] Pritchard, D. E. Cooling Neutral Atoms in a Magnetic Trap for Precision Spectroscopy. *Phys. Rev. Lett.* **51**, 1336–1339 (1983).

[153] Bergeman, T., Erez, G. & Metcalf, H. J. Magnetostatic trapping fields for neutral atoms. *Phys. Rev. A* **35**, 1535–1546 (1987).

[154] Trinker, M., Groth, S., Haslinger, S., Manz, S., Betz, T., Schneider, S., Bar-Joseph, I., Schumm, T. & Schmiedmayer, J. Multilayer atom chips for versatile atom micromanipulation. *Appl. Phys. Lett.* **92**, – (2008).

[155] Schneider, S. *Bose-Einstein Kondensation in einer magnetischen Z-Falle.* Ph.D. thesis, University of Heidelberg (2003).

[156] Cohen-Tannoudji, C., Grynberg, G. & Dupont-Roc, J. *Atom-Photon Interactions: Basic Processes and Applications* (Wiley, New York, 1992).

[157] Gericke, T., Wurtz, P., Reitz, D., Langen, T. & Ott, H. High-resolution scanning electron microscopy of an ultracold quantum gas. *Nat. Phys.* **4**, 949–953 (2008).

[158] Stibor, a., Bender, H., Kühnhold, S., Fortágh, J., Zimmermann, C. & Günther, a. Single-atom detection on a chip: from realization to application. *New J. Phys.* **12**, 065034 (2010).

[159] Vassen, W., Cohen-Tannoudji, C., Leduc, M., Boiron, D., Westbrook, C. I., Truscott, A., Baldwin, K., Birkl, G., Cancio, P. & Trippenbach, M. Cold and trapped metastable noble gases. *Rev. Mod. Phys.* **84**, 175–210 (2012).

[160] Kuhr, S., Alt, W., Schrader, D., Müller, M., Gomer, V. & Meschede, D. Deterministic Delivery of a Single Atom. *Science* **293**, 278–280 (2001).

[161] Nelson, K., Li, X. & Weiss, D. Imaging single atoms in a three-dimensional array. *Nat. Phys.* **3**, 556–560 (2007).

[162] Bakr, W. S., Gillen, J. I., Peng, A., Folling, S. & Greiner, M. A quantum gas microscope for detecting single atoms in a Hubbard-regime optical lattice. *Nature* **462**, 74–77 (2009).

[163] Sherson, J. F., Weitenberg, C., Endres, M., Cheneau, M., Bloch, I. & Kuhr, S. Single-atom-resolved fluorescence imaging of an atomic Mott insulator. *Nature* **467**, 68–72 (2010).

[164] Thompson, R. J., Rempe, G. & Kimble, H. J. Observation of normal-mode splitting for an atom in an optical cavity. *Phys. Rev. Lett.* **68**, 1132–1135 (1992).

[165] Childs, J. J., An, K., Otteson, M. S., Dasari, R. R. & Feld, M. S. Normal-Mode Line Shapes for Atoms in Standing-Wave Optical Resonators. *Phys. Rev. Lett.* **77**, 2901–2904 (1996).

[166] Münstermann, P., Fischer, T., Maunz, P., Pinkse, P. W. H. & Rempe, G. Observation of Cavity-Mediated Long-Range Light Forces between Strongly Coupled Atoms. *Phys. Rev. Lett.* **84**, 4068–4071 (2000).

[167] Trupke, M., Goldwin, J., Darquié, B., Dutier, G., Eriksson, S., Ashmore, J. & Hinds, E. A. Atom Detection and Photon Production in a Scalable, Open, Optical Microcavity. *Phys. Rev. Lett.* **99**, 63601 (2007).

[168] Gehr, R., Volz, J., Dubois, G., Steinmetz, T., Colombe, Y., Lev, B. L., Long, R., Estève, J. & Reichel, J. Cavity-Based Single Atom Preparation and High-Fidelity Hyperfine State Readout. *Phys. Rev. Lett.* **104**, 203602 (2010).

[169] Volz, J., Gehr, R., Dubois, G., Estève, J. & Reichel, J. Measurement of the internal state of a single atom without energy exchange. *Nature* **475**, 210–213 (2011).

[170] Gring, M. *Prethermalization in an Isolated Many Body System.* Ph.d. thesis, Vienna University of Technology (2012).

[171] Trimmel, M. *Design and construction of an absorption imaging system for Bose - Einstein condensates.* Diploma thesis, Vienna University of Technology (2011).

[172] Steck, D. A. *Rubidium 87 D Line Data.* Url: http://steck.us/alkalidata/, Revision 2.1.4 (2010).

[173] Erhard, M. *Experimente mit mehrkomponentigen Bose-Einstein-Kondensaten.* Ph.d. thesis, Hamburg University (2004).

[174] Rohringer, W., Bücker, R., Manz, S., Betz, T., Koller, C., Göbel, M., Perrin, A., Schmiedmayer, J. & Schumm, T. Stochastic optimization of a cold atom experiment using a genetic algorithm. *Appl. Phys. Lett.* **93**, 264101 (2008).

[175] Reinaudi, G., Lahaye, T., Wang, Z. & Guéry-Odelin, D. Strong saturation absorption imaging of dense clouds of ultracold atoms. *Opt. Lett.* **32**, 3143–3145 (2007).

[176] Phillips, W. D. Laser cooling and trapping of neutral atoms. *Rev. Mod. Phys.* **70**, 721–741 (1998).

[177] Metcalf, H. J. & van der Straten, P. *Laser Cooling and Trapping* (Springer-Verlag, New York, 1999).

[178] Katori, H., Ido, T., Isoya, Y. & Kuwata-Gonokami, M. Magneto-Optical Trapping and Cooling of Strontium Atoms down to the Photon Recoil Temperature. *Phys. Rev. Lett.* **82**, 1116–1119 (1999).

[179] Honda, K., Takahashi, Y., Kuwamoto, T., Fujimoto, M., Toyoda, K., Ishikawa, K. & Yabuzaki, T. Magneto-optical trapping of Yb atoms and a limit on the branching ratio of the 1P1 state. *Phys. Rev. A* **59**, R934—-R937 (1999).

[180] McClelland, J. J. & Hanssen, J. L. Laser Cooling without Repumping: A Magneto-Optical Trap for Erbium Atoms. *Phys. Rev. Lett.* **96**, 143005 (2006).

[181] Sané, S. S., Bennetts, S., Debs, J. E., Kuhn, C. C. N., McDonald, G. D., Altin, P. A., Close, J. D. & Robins, N. P. 11 W narrow linewidth laser source at 780nm for laser cooling and manipulation of Rubidium. *Opt. Express* **20**, 8915–8919 (2012).

[182] Egorov, M., Opanchuk, B., Drummond, P., Hall, B. V., Hannaford, P. & Sidorov, A. I. Measurement of s-wave scattering lengths in a two-component Bose-Einstein condensate. *Phys. Rev. A* **87**, 53614 (2013).

[183] Bücker, R. *Twin-atom beam generation in a one-dimensional Bose gas.* Ph.D. thesis, Vienna University of Technology (2013).

[184] Schünemann, U., Engler, H., Grimm, R., Weidemüller, M. & Zielonkowski, M. Simple scheme for tunable frequency offset locking of two lasers. *Rev. Sci. Instrum.* **70** (1999).

[185] Wilzbach, M. *Aufbau eines Experiments zur miniaturisierten und integrierten Detektion neutraler Atome.* Ph.D. thesis, University of Heidelberg (2002).

[186] Wildermuth, S., Krüger, P., Becker, C., Brajdic, M., Haupt, S., Kasper, A., Folman, R. & Schmiedmayer, J. Optimized magneto-optical trap for experiments with ultracold atoms near surfaces. *Phys. Rev. A* **69**, 030901 (2004).

[187] Fischer, D. *Fabrication of optic and electromagnetic devices for experiments with ultra cold atoms.* Diploma thesis, Vienna University of Technology (2008).

[188] Fischer, D. *t.b.a.* Ph.D. thesis, Vienna University of Technology (2014).

[189] Hetesi, Z. & Regaly, Z. A New Interpretation of Drake-Equation. *J. Br. Interplanet. Soc.* **59**, 11–14 (2006).

[190] Brajdic, M. *Entwicklung einer Computersteuerung und ihre Anwendung in einem Experiment zur vereinfachten Bose-Einstein Kondensation in einer Oberflächenfalle.* Diploma thesis, University of Heidelbert (2003).

[191] Rohringer, W. *Stochastic Optimization in an Ultracold Atom Experiment.* Diploma thesis, Vienna University of Technology (2008).

[192] Rohringer, W., Fischer, D., Trupke, M., Schumm, T. & Schmiedmayer, J. Stochastic Optimization of Bose-Einstein Condensation Using a Genetic Algorithm (2011).

[193] Luiten, O. J., Reynolds, M. W. & Walraven, J. T. M. Kinetic theory of the evaporative cooling of a trapped gas. *Phys. Rev. A* **53**, 381–389 (1996).

[194] Ketterle, W. & Druten, N. J. V. Evaporative Cooling of Trapped Atoms. vol. 37 of *Advances In Atomic, Molecular, and Optical Physics*, 181–236 (Academic Press, 1996).

[195] Snoke, D. W. & Wolfe, J. P. Population dynamics of a Bose gas near saturation. *Phys. Rev. B* **39**, 4030–4037 (1989).

[196] Burt, E. A., Ghrist, R. W., Myatt, C. J., Holland, M. J., Cornell, E. A. & Wieman, C. E. Coherence, Correlations, and Collisions: What One Learns about Bose-Einstein Condensates from Their Decay. *Phys. Rev. Lett.* **79**, 337–340 (1997).

[197] Söding, J., Guéry-Odelin, D., Desbiolles, P., Chevy, F., Inamori, H. & Dalibard, J. Three-body decay of a rubidium Bose–Einstein condensate. *Appl. Phys. B* **69**, 257–261 (1999).

[198] Esry, B. D., Greene, C. H. & Burke, J. P. Recombination of Three Atoms in the Ultracold Limit. *Phys. Rev. Lett.* **83**, 1751–1754 (1999).

[199] Härter, A., Krukow, A., Deisz, M., Drews, B., Tiemann, E. & Denschlag, J. H. Population distribution of product states following three-body recombination in an ultracold atomic gas. *Nat. Phys.* **9**, 512–517 (2013).

[200] Schaff, J.-F., Song, X.-L., Capuzzi, P., Vignolo, P. & Labeyrie, G. Shortcut to adiabaticity for an interacting Bose-Einstein condensate. *EPL (Europhysics Lett.* **93**, 23001 (2011).

[201] Kuhnert, M. *Thermalization and Prethermalization in an ultracold Bose Gas.* Ph.d. thesis, Vienna University of Technology (2013).

[202] Trebbia, J.-B., Garrido Alzar, C. L., Cornelussen, R., Westbrook, C. I. & Bouchoule, I. Roughness Suppression via Rapid Current Modulation on an Atom Chip. *Phys. Rev. Lett.* **98**, 263201 (2007).

[203] Bouchoule, I., Trebbia, J.-B. & Garrido Alzar, C. L. Limitations of the modulation method to smooth wire-guide roughness. *Phys. Rev. A* **77**, 23624 (2008).

[204] Saleh, B. E. A. & Teich, M. C. *Fundamentals of Photonics.* Wiley Series in Pure and Applied Optics (Wiley, 2007).

[205] Gring, M., Kuhnert, M., Langen, T., Kitagawa, T., Rauer, B., Schreitl, M., Mazets, I., Smith, D. A., Demler, E. & Schmiedmayer, J. Relaxation and prethermalization in an isolated quantum system. *Science* **337**, 1318–22 (2012).

[206] Efron, B. & Tibshirani, R. J. *An Introduction to the Bootstrap.* Chapman & Hall/CRC Monographs on Statistics & Applied Probability (Taylor & Francis, 1994).

[207] Hughes, I. & Hase, T. *Measurements and Their Uncertainties: A Practical Guide to Modern Error Analysis* (OUP Oxford, 2010).

[208] Barcelo, C., Liberati, S. & Visser, M. Analogue Gravity. *Living Rev. Relativ.* (2005).

[209] Carusotto, I., Fagnocchi, S., Recati, A., Balbinot, R. & Fabbri, A. Numerical observation of Hawking radiation from acoustic black holes in atomic Bose–Einstein condensates. *New J. Phys.* **10**, 103001 (2008).

[210] Prain, A., Fagnocchi, S. & Liberati, S. Analogue cosmological particle creation: Quantum correlations in expanding Bose-Einstein condensates. *Phys. Rev. D* **82**, 105018 (2010).

[211] Finazzi, S., Liberati, S. & Sindoni, L. Cosmological Constant: A Lesson from Bose-Einstein Condensates. *Phys. Rev. Lett.* **108**, 71101 (2012).

[212] Chen, X., Lizuain, I., Ruschhaupt, A., Guéry-Odelin, D. & Muga, J. G. Shortcut to Adiabatic Passage in Two- and Three-Level Atoms. *Phys. Rev. Lett.* **105**, 123003 (2010).

[213] Lewis, H. R. Class of Exact Invariants for Classical and Quantum Time-Dependent Harmonic Oscillators. *J. Math. Phys.* **9**, 1976 (1968).

[214] Ermakov, V. P. Transformation of differential equations. *Univ. Izv. Kiev.* **20**, 1 (1880).

[215] Leach, P. G. L. & Andriopoulos, K. The Ermakov equation: a commentary. *Appl. Anal. Discret. Math.* **2**, 146 (2008).

[216] Bücker, R., Grond, J., Manz, S., Berrada, T., Betz, T., Koller, C., Hohenester, U., Schumm, T., Perrin, A. & Schmiedmayer, J. Twin-atom beams. *Nat. Phys.* **7**, 608–611 (2011).

[217] Moritz, H., Stöferle, T., Köhl, M. & Esslinger, T. Exciting Collective Oscillations in a Trapped 1D Gas. *Phys. Rev. Lett.* **91**, 1–4 (2003).

[218] Werner, F. & Castin, Y. Unitary gas in an isotropic harmonic trap: Symmetry properties and applications. *Phys. Rev. A* **74**, 053604 (2006).

[219] Abramowitz, M. & Stegun, I. A. *Handbook of mathematical functions with formulas, graphs, and mathematical tables*, vol. 55 of *National Bureau of Standards Applied Mathematics Series* (For sale by the Superintendent of Documents, U.S. Government Printing Office, Washington, D.C., 1964).

[220] Shvarchuck, I., Buggle, C., Petrov, D., Dieckmann, K., Zielonkowski, M., Kemmann, M., Tiecke, T., von Klitzing, W., Shlyapnikov, G. & Walraven, J. Bose-Einstein Condensation into Nonequilibrium States Studied by Condensate Focusing. *Phys. Rev. Lett.* **89**, 1–4 (2002).

[221] Jacqmin, T., Fang, B., Berrada, T., Roscilde, T. & Bouchoule, I. Momentum distribution of one-dimensional Bose gases at the quasicondensation crossover: Theoretical and experimental investigation. *Phys. Rev. A* **86**, 043626 (2012).

[222] Kuhnert, M., Geiger, R., Langen, T., Gring, M., Rauer, B., Kitagawa, T., Demler, E., Adu Smith, D. & Schmiedmayer, J. Multimode Dynamics and Emergence of a Characteristic Length Scale in a One-Dimensional Quantum System. *Phys. Rev. Lett.* **110**, 090405 (2013).

[223] Born, M. & Fock, V. Beweis des Adiabatensatzes. *Zeitschrift für Phys.* **51**, 165–180 (1928).

[224] Kato, T. On the Adiabatic Theorem of Quantum Mechanics. *J. Phys. Soc. Japan* **5**, 435–439 (1950).

[225] Avron, J. E. & Elgart, A. Adiabatic Theorem without a Gap Condition. *Commun. Math. Phys.* **203**, 445–463 (1999).

[226] Farhi, E., Goldstone, J., Gutmann, S., Lapan, J., Lundgren, A. & Preda, D. A Quantum Adiabatic Evolution Algorithm Applied to Random Instances of an NP-Complete Problem. *Science* **292**, 472–475 (2001).

[227] Peng, X., Liao, Z., Xu, N., Qin, G., Zhou, X., Suter, D. & Du, J. Quantum Adiabatic Algorithm for Factorization and Its Experimental Implementation. *Phys. Rev. Lett.* **101**, 220405 (2008).

[228] Chen, X., Ruschhaupt, A., Schmidt, S., Ibanez, S. & Muga, J. G. Shortcut to adiabaticity in harmonic traps. *J. At. Mol. Sci.* **1**, 1–17 (2010).

[229] Schaff, J.-F., Song, X.-L., Vignolo, P. & Labeyrie, G. Fast optimal transition between two equilibrium states. *Phys. Rev. A* **82**, 5–9 (2010).

[230] del Campo, A. Shortcuts to Adiabaticity by Counterdiabatic Driving. *Phys. Rev. Lett.* **111**, 100502 (2013).

[231] del Campo, A. Frictionless quantum quenches in ultracold gases: A quantum-dynamical microscope. *Phys. Rev. A* **84**, 4–7 (2011).

[232] Chen, X., Ruschhaupt, A., Schmidt, S., del Campo, A., Guéry-Odelin, D. & Muga, J. G. Fast Optimal Frictionless Atom Cooling in Harmonic Traps: Shortcut to Adiabaticity. *Phys. Rev. Lett.* **104**, 1–4 (2010).

[233] Caneva, T., Calarco, T. & Montangero, S. Chopped random basis quantum optimization. *Phys. Rev. A* **84** (2011).

[234] Rosi, S., Bernard, A., Fabbri, N., Fallani, L., Fort, C., Inguscio, M., Calarco, T. & Montangero, S. Fast closed-loop optimal control of ultracold atoms in an optical lattice. *Phys. Rev. A* **88**, 021601 (2013).

[235] Wolpert, D. H. & Macready, W. G. No Free Lunch Theorems for Search. Tech. Rep. SFI-TR-95-02-101, Santa Fe Institute, Santa Fe, NM (1995).

[236] Wolpert, D. H. & Macready, W. G. No free lunch theorems for optimization. *Evol. Comput. IEEE Trans.* **1**, 67–82 (1997).

[237] Rabitz, H. A., Hsieh, M. M. & Rosenthal, C. M. Quantum optimally controlled transition landscapes. *Science* **303**, 1998–2001 (2004).

[238] Rabitz, H., Ho, T.-S., Hsieh, M., Kosut, R. & Demiralp, M. Topology of optimally controlled quantum mechanical transition probability landscapes. *Phys. Rev. A* **74**, 012721 (2006).

[239] Roslund, J. & Rabitz, H. Experimental quantum control landscapes: Inherent monotonicity and artificial structure. *Phys. Rev. A* **80**, 013408 (2009).

[240] Spall, J. C. *Introduction to Stochastic Search and Optimization: Estimation, Simulation, and Control.* Wiley Series in Discrete Mathematics and Optimization (Wiley, 2005).

[241] Herrera, F., Lozano, M. & Verdegay, J. L. Tackling Real-Coded Genetic Algorithms Operators and Tools for Behavioural Analysis. *Artif. Intell. Rev.* **12**, 265–319 (1998).

[242] Baker, J. E. Adaptive Selection Methods for Genetic Algorithms. In *Proc. 1st Int. Conf. Genet. Algorithms*, 101–111 (L. Erlbaum Associates Inc., Hillsdale, NJ, USA, 1985).

[243] Baker, J. E. Reducing Bias and Inefficiency in the Selection Algorithm. In *Proc. Second Int. Conf. Genet. Algorithms Genet. Algorithms Their Appl.*, 14–21 (L. Erlbaum Associates Inc., Hillsdale, NJ, USA, 1987).

[244] Pohlheim, H. *Evolutionäre Algorithmen: Verfahren, Operatoren und Hinweise* (Springer, Berlin, 2000).

[245] Mühlenbein, H. & Schlierkamp-Voosen, D. Predictive Models for the Breeder Genetic Algorithm I. Continuous Parameter Optimization. *Evol. Comput.* **1**, 25–49 (1993).

[246] Mühlenbein, H. & Schlierkamp-Voosen, D. Analysis of selection, mutation and recombination in genetic algorithms. In Banzhaf, W. & Eeckman, F. (eds.) *Evol. Biocomput.*, vol. 899 of *Lecture Notes in Computer Science*, 142–168 (Springer Berlin Heidelberg, 1995).

[247] Betz, T., Manz, S., Bücker, R., Berrada, T., Koller, C., Kazakov, G., Mazets, I. E., Stimming, H.-P., Perrin, A., Schumm, T. & Schmiedmayer, J. Two-Point Phase Correlations of a One-Dimensional Bosonic Josephson Junction. *Phys. Rev. Lett.* **106**, 20407 (2011).

[248] Berrada, T., van Frank, S., Bücker, R., Schumm, T., Schaff, J.-F. & Schmiedmayer, J. Integrated Mach–Zehnder interferometer for Bose–Einstein condensates. *Nat. Commun.* **4** (2013).

[249] Unruh, W. G. Experimental Black-Hole Evaporation? *Phys. Rev. Lett.* **46**, 1351–1353 (1981).

[250] Fulling, S. A. Nonuniqueness of Canonical Field Quantization in Riemannian Space-Time. *Phys. Rev. D* **7**, 2850–2862 (1973).

[251] Davies, P. C. W. Scalar production in Schwarzschild and Rindler metrics. *J. Phys. A. Math. Gen.* **8**, 609 (1975).

[252] Crispino, L. C. B., Higuchi, A. & Matsas, G. E. A. The Unruh effect and its applications. *Rev. Mod. Phys.* **80**, 787–838 (2008).

[253] Öhberg, P. & Santos, L. Dynamical Transition from a Quasi-One-Dimensional Bose-Einstein Condensate to a Tonks-Girardeau Gas. *Phys. Rev. Lett.* **89**, 1–4 (2002).

[254] Buljan, H., Pezer, R. & Gasenzer, T. Fermi-Bose Transformation for the Time-Dependent Lieb-Liniger Gas. *Phys. Rev. Lett.* **100**, 80406 (2008).

[255] Jukic, D., Pezer, R., Gasenzer, T. & Buljan, H. Free expansion of a Lieb-Liniger gas: Asymptotic form of the wave functions. *Phys. Rev. A* **78**, 16–18 (2008).

[256] Florian, S. *t.b.a.* Ph.D. thesis, Vienna University of Technology (2015).

[257] Sagué, G., Vetsch, E., Alt, W., Meschede, D. & Rauschenbeutel, A. Cold-Atom Physics Using Ultrathin Optical Fibers: Light-Induced Dipole Forces and Surface Interactions. *Phys. Rev. Lett.* **99**, 163602 (2007).

[258] Sagué, G., Baade, A. & Rauschenbeutel, A. Blue-detuned evanescent field surface traps for neutral atoms based on mode interference in ultrathin optical fibres. *New J. Phys.* **10**, 113008 (2008).

[259] Vetsch, E., Reitz, D., Sagué, G., Schmidt, R., Dawkins, S. T. & Rauschenbeutel, A. Optical interface created by laser-cooled atoms trapped in the evanescent field surrounding an optical nanofiber. *Phys. Rev. Lett.* **104**, 203603 (2010).

[260] Pöllinger, M., O'Shea, D., Warken, F. & Rauschenbeutel, A. Ultrahigh-Q Tunable Whispering-Gallery-Mode Microresonator. *Phys. Rev. Lett.* **103**, 53901 (2009).

[261] Junge, C., O'Shea, D., Volz, J. & Rauschenbeutel, A. Strong Coupling between Single Atoms and Nontransversal Photons. *Phys. Rev. Lett.* **110**, 213604 (2013).

[262] O'Shea, D., Junge, C., Volz, J. & Rauschenbeutel, A. Fiber-Optical Switch Controlled by a Single Atom. *Phys. Rev. Lett.* **111**, 193601 (2013).

[263] Wuttke, C., Becker, M., Brückner, S., Rothhardt, M. & Rauschenbeutel, A. Nanofiber Fabry–Perot microresonator for nonlinear optics and cavity quantum electrodynamics. *Opt. Lett.* **37**, 1949–1951 (2012).

[264] Garcia-Fernandez, R., Alt, W., Bruse, F., Dan, C., Karapetyan, K., Rehband, O., Stiebeiner, A., Wiedemann, U., Meschede, D. & Rauschenbeutel, A. Optical nanofibers and spectroscopy. *Appl. Phys. B* **105**, 3–15 (2011).

[265] Purcell, E. M. Proceedings of the American Physical Society. *Phys. Rev.* **69**, 674 (1946).

[266] Dawkins, S. T., Mitsch, R., Reitz, D., Vetsch, E. & Rauschenbeutel, A. Dispersive Optical Interface Based on Nanofiber-Trapped Atoms. *Phys. Rev. Lett.* **107**, 243601 (2011).

[267] Bajcsy, M., Hofferberth, S., Peyronel, T., Balic, V., Liang, Q., Zibrov, A. S., Vuletic, V. & Lukin, M. D. Laser-cooled atoms inside a hollow-core photonic-crystal fiber. *Phys. Rev. A* **83**, 63830 (2011).

[268] Schneeweiss, P., Kien, F. L. & Rauschenbeutel, A. Nanofiber-based atom trap created by combining fictitious and real magnetic fields. *New J. Phys.* **16**, 13014 (2014).

[269] Fleischhauer, M., Imamoglu, A. & Marangos, J. P. Electromagnetically induced transparency: Optics in coherent media. *Rev. Mod. Phys.* **77**, 633–673 (2005).

[270] Kok, P., Munro, W. J., Nemoto, K., Ralph, T. C., Dowling, J. P. & Milburn, G. J. Linear optical quantum computing with photonic qubits. *Rev. Mod. Phys.* **79**, 135–174 (2007).

[271] Chang, D. E., Gritsev, V., Morigi, G., Vuletic, V., Lukin, M. D. & Demler, E. A. Crystallization of strongly interacting photons in a nonlinear optical fibre. *Nat Phys* **4**, 884–889 (2008).

[272] Wuttke, C., Cole, G. D. & Rauschenbeutel, A. Optically active mechanical modes of tapered optical fibers. *Phys. Rev. A* **88**, 61801 (2013).

[273] Stamper-Kurn, D. M. & Ueda, M. Spinor Bose gases: Symmetries, magnetism, and quantum dynamics. *Rev. Mod. Phys.* **85**, 1191–1244 (2013).

[274] Chin, C., Grimm, R., Julienne, P. & Tiesinga, E. Feshbach resonances in ultracold gases. *Rev. Mod. Phys.* **82**, 1225–1286 (2010).

[275] Fukuhara, T., Sugawa, S. & Takahashi, Y. Bose-Einstein condensation of an ytterbium isotope. *Phys. Rev. A* **76**, 51604 (2007).

[276] Lu, M., Burdick, N. Q., Youn, S. H. & Lev, B. L. Strongly Dipolar Bose-Einstein Condensate of Dysprosium. *Phys. Rev. Lett.* **107**, 190401 (2011).

[277] Aikawa, K., Frisch, A., Mark, M., Baier, S., Rietzler, A., Grimm, R. & Ferlaino, F. Bose-Einstein Condensation of Erbium. *Phys. Rev. Lett.* **108**, 210401 (2012).

[278] Cazalilla, M. A. & Rigol, M. Focus on Dynamics and Thermalization in Isolated Quantum Many-Body Systems. *New J. Phys.* **12**, 055006 (2010).

[279] Polkovnikov, A., Sengupta, K., Silva, A. & Vengalattore, M. Colloquium: Nonequilibrium dynamics of closed interacting quantum systems. *Rev. Mod. Phys.* **83**, 863–883 (2011).

[280] Langen, T., Geiger, R., Kuhnert, M., Rauer, B. & Schmiedmayer, J. Local emergence of thermal correlations in an isolated quantum many-body system. *Nat. Phys.* **9**, 640–643 (2013).

[281] Jaskula, J.-C., Partridge, G. B., Bonneau, M., Lopes, R., Ruaudel, J., Boiron, D. & Westbrook, C. I. Acoustic Analog to the Dynamical Casimir Effect in a Bose-Einstein Condensate. *Phys. Rev. Lett.* **109**, 220401 (2012).

[282] Feynman, R. P., Hutchings, E. & Leighton, R. *"Surely You're Joking, Mr. Feynman!": Adventures of a Curious Character.* Arrow Books (Vintage, 1992).

[283] Nowak, B., Schole, J., Sexty, D. & Gasenzer, T. Nonthermal fixed points, vortex statistics, and superfluid turbulence in an ultracold Bose gas. *Phys. Rev. A* **85**, 43627 (2012).

[284] Feynman, R. P. Application of quantum mechanics to liquid helium. *II. Prog. Low Temp. Phys.* **1** (1955).

[285] Schmidt, M., Erne, S., Nowak, B., Sexty, D. & Gasenzer, T. Non-thermal fixed points and solitons in a one-dimensional Bose gas. *New J. Phys.* **14**, 075005 (2012).

[286] Hung, C.-L., Gurarie, V. & Chin, C. From cosmology to cold atoms: observation of Sakharov oscillations in a quenched atomic superfluid. *Science* **341**, 1213–5 (2013).

[287] Mohr, P. J., Taylor, B. N. & Newell, D. B. CODATA recommended values of the fundamental physical constants: 2010. *Rev. Mod. Phys.* **84**, 1527–1605 (2012).

[288] Taylor, B. N. & Thompson, A. The international system of units (SI). Tech. Rep., United States Department of Commerce, NIST (2008).

[289] Kolonko, M. *Stochastische Simulation: Grundlagen, Algorithmen und Anwendungen.* Vieweg Studium (Vieweg Verlag, Friedr, & Sohn Verlagsgesellschaft mbH, 2008).

D. I. Wolfgang Rohringer
Erdbergstraße 30/6
1030 Wien, Austria
+43 699 12767329
rohringer@ati.ac.at

Curriculum Vitae

Personal Information

Date of birth: 18.1.1982
Place of Birth: Hall in Tirol, Austria
Citizenship: Austrian
Employment: Projektassistent, TU Wien

Education

Since 2009: PhD student at Atominstitut, TU Wien / CoQuS doctoral programme
June 2008: Diploma in Technical Physics
2007 – 2008: Diploma thesis at Atominstitut, TU Wien (group of Jörg Schmiedmayer)
Thesis topic: *Stochastic Optimization in an Ultracold Atom Experiment*
2001 – 2008: Technical Physics studies, TU Wien
2000 – 2001: Military service
June 2000: Matura, Öffentliches Gymnasium der Franziskaner, Hall in Tirol

Scholarships

2009 Admission to the doctoral programme for complex quantum systems (CoQuS)

Volunteer work

April 2012: *Lange Nacht der Forschung*, University of Vienna
September 2011: Physics workshop for children at the *Ars Electronica 2011*, Linz
06/2009 – 06/2011: Elected student representative for doctoral studies, TU Wien
06/2005 – 06/2007: Student faculty representative, Faculty of Physik, TU Wien
06/2003 – 06/2005: Elected student representative for Technical Physics studies, TU Wien
10/2003 – 10/2007: Member of the curriculum commission for Technical Physics studies, TU Wien

Other activities

2007 – 2009: Web development and IT – administration in the group of Jörg Schmiedmayer at Atominstitut, TU Wien (http://www.atomchip.org)